# THE EFFECT OF TRANSITION METAL ADDITIONS ON DOUBLE OXIDE FILM DEFECTS IN AL ALLOY CASTINGS

## by

## QI CHEN

A thesis submitted to the University of Birmingham for the degree of

DOCTOR OF PHILOSOPHY

School of Metallurgy and Materials

College of Engineering and Physical Science

University of Birmingham

September, 2016

**UNIVERSITY**OF
**BIRMINGHAM**

**University of Birmingham Research Archive**

**e-theses repository**

*To my mum and dad*

# Abstract

This work investigated the effect of transition metal additions on the double oxide film defects in Al alloys.

A bubble trapping experiment was initially conducted, which deliberately trapped an air bubble inside the aluminium melt for a period of time in three different Al alloys (Commercial purity aluminium, 2L99(Al-7Si-0.35Mg) and Al-5Mg alloy), as an analogy of the consumption of the entrapped atmosphere in double oxide film defects in castings. Several elements, namely, Mo, Ti, Zr, Hf, Sc were selected and added into the aluminium melt. The result suggested that the three different alloys behaved differently with regard to the consumption of the entrapped bubble and the different oxide/nitride layers formed. Only the addition of Sc and Mo altered the structure of the oxide surface and promoted the consumption of the air in the trapped bubble in the 2L99 aluminium alloy melt.

Sand casting was subsequently conducted for 2L99 alloy with different element additions. Mo and W were found to improve the Weibull moduli of the UTS. Statistical analysis confirmed that such improvement was significant. For the castings with Mo addition, a nitride was found in some double oxide film defects, on the fracture surface of the tensile testbars. This was unusual, as bi-film defects in aluminium castings usually have a short solidification time and do not have enough time to consume the majority of their entrapped oxygen. The formation of the nitride on the surface of bi-film defects in +Mo castings, suggested that the majority of the oxygen was depleted and a reaction was going on between nitrogen and liquid aluminium. The formation of the permeable nitride surface layer on the bifilm defect might promote the consumption of the entrapped gas. This should lead to reductions in the bi-film size and an improvement in mechanical properties. For +W casting, W containing intermetallic compound might be nucleated on the sides of the bifilm and drag the bi-film to the bottom of the casting, resulting in a clean melt and improving mechanical properties.

The effect of Si modifier addition on the bi-film defect (Na, Sr and Ba) in 2L99 sand castings was also investigated, which suggested the addition of modifiers resulted in a reduction in the mechanical properties of the 2L99 castings while the bi-film defect content in the casting was high but significantly improved the Weibull moduli of the UTS of 2L99 castings while the bi-film defect content was reduced. The results suggested that the modifier addition tended to aggravate the effect of bi-film defects on mechanical properties by increasing the defect size.

Ti and Mn additions into 2L99 alloy were found to not significantly affect the mechanical properties of the casting. A porous oxide structure was found on only one of the fracture surfaces (out of ten) of Ti containing testbar examined, which hardly affect the mechanical properties of the casting. For the +Mn casting, the composition and structure of the oxide was not affected by the addition. The reduction of the mean value of the UTS for both element additions could be due to bi-film defects being introduced during master alloy preparation, master alloy addition and during degassing before casting.

# Acknowledgement

I would like to express my sincere thanks to my supervisor W.D. Griffiths for his patient guidance and supervision. His unparallel help make this work possible.

Thanks also go to Mr. Adrian Caden and Mr. Peter Canner, for their careful assistance with the experimental work.

I would also like to thank my colleague and friends, for their help during this research work, in particularly, Dr. Keehyun Kim and Ms. Jing Wu for their help with FIB (Focused Ion beam milling) and TEM.

Finally I would like to thank my parents for their continuous support and encouragements during this research work.

# Contents

# Chapter 1 Introduction

Research into double oxide film defects has been going on for decades. Since first mentioned by Campbell in the 1990s, their effects on casting properties of light alloys have drawn increasing attention, (although it was ignored for a long time previously due to the nature of this extremely thin film, which escaped the detection by traditional non-destructive detection methods).

A large amount of work has been conducted previously investigating the nature of this defect and its effect on the mechanical properties of light alloys. A critical ingate velocity was determined both theoretically and experimentally which allowed redesign and improvement of castings, to produce castings with less surface turbulence in the melt during metal transfer or mould filling. However, during some casting processes, severe surface turbulence of the liquid metal and entrainment of larger amounts of double oxide film defects inside the aluminium melt are inevitable. This includes industrial processes like high pressure die casting or metal recycling. Therefore, it is important to figure out the best way to deactivate bi-film defects once they have already formed.

A healing mechanism has been put forward which suggested that the internal atmosphere in a double oxide film can be consumed to reduce its size. However, no research work has found a healing process in bi-film defects by experimental observation in the normal casting process, probably due to the short lifetime of the double oxide film defects. In this work here, transition metal additions are proposed with the aim of changing the structure of the oxide in the bi-film defect, which may change the consumption of the internal atmosphere in the defect. Elements that are commonly added to Al-Si alloys like Sr, Na and Ti have been

1

selected and their effect on double oxide film defects and the reproducibility of the properties of Al-Si alloys have been investigated. In addition, Mo, W, Mn, Zr, Hf, Ba and Sc have all been trialled in this research work.

The behaviour of air bubbles trapped in three different Al alloy melts (CPAl, 2L99 and Al-5Mg) with the addition of different elements has been clarified in a bubble trapping experiment. Based on these results, the effect of the element additions on the reproducibility of the mechanical properties reproducibility of 2L99 alloy (Al-7Si-0.35Mg) has been investigated. The change in the mechanical properties of the casting was attributed to the change of the morphology and composition of the oxide film defect inside the casting and the relevant mechanism was evaluated. The employment of Focused Ion Beam milling (FIB) helped to understand the structure of the double oxide film defect which naturally formed inside the casting and Transmission Electron Microscopy (TEM) has helped to understand the composition of the phases formed of double oxide film defects during the casting process.

# Chapter 2   Literature Review

## 2.1   Double oxide film defects in Al alloys

### 2.1.1   The formation of oxide film defects

A double oxide film defect is formed by folding over of the oxidised skin on a liquid metal, due to the surface turbulence of the liquid metal caused by pouring or mould filling. A pocket of gas, predominantly air, is entrapped inside the two unwetted sides of the oxide skin, forming a gas filled crevice. This defect is then carried into the casting and forms a double oxide film defect after solidification. A sketch for the formation of this defect is shown in Figure 2-1[1]
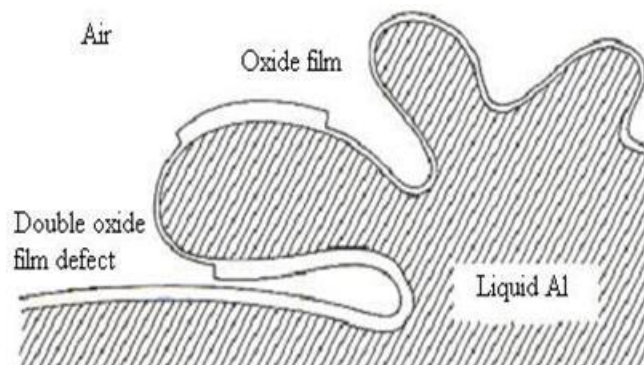


Figure 2-1 Formation of double oxide film defect [1].

Campbell[1] suggested that surface turbulence during any liquid metal transfer process was the direct reason of the entrainment behaviour and the formation of double oxide film defects. He calculated the theoretical gate velocity above which surface turbulence will occur. The turbulence of the melt is driven by the internal pressure, which is defined as $1/2v^2\rho$ ($\rho$ and $v$ are the density and the velocity of the liquid metal, respectively). This pressure is balanced by surface tension (the maximum pressure is achieved when the liquid

metal forms a spherical shape, which is $\frac{2\gamma}{r}$. r is the radius of a sphere and $\gamma$ is the surface tension), see Figure 2-2. In this case:

$$1/2v^2\rho=2\gamma/r \qquad (1)$$

$$v^* = 2\sqrt{\frac{\gamma}{\rho r}} \qquad (2)$$
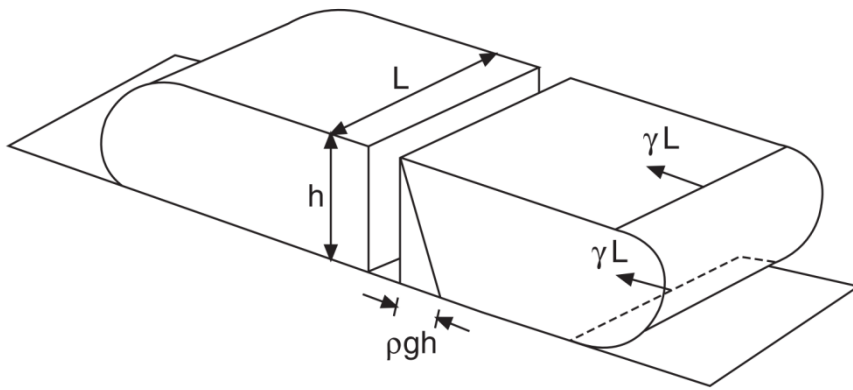


**Figure 2-2 The sketch showing the boundary condition which the sensile drop on a flat plate was kept still[1].**

For the radius r, the author [1] assumed the value of a sessile drop on a plate. There are two forces balanced to keep the drop, gravity which tends to flatten the drop and surface tension which keeps it from flattening. The pressure caused by gravity is derived by $0.5\rho gh^2L$ and the surface tension is defined by $2\gamma L$. For the critical situation where the drop is balanced by the two forces, we have:

$$0.5\rho gh^2L=2\gamma L \qquad (3)$$

The author [1] assumed that the value of h was equal to 2r and suggested:

4

$$v^* = 2\sqrt[4]{g\gamma/\rho} \qquad\qquad (4)$$

Using the data for liquid aluminium, $\rho = 2.4 \times 10^3$ Kg/m$^3$ and surface tension=0.9 Nm$^{-1}$, the ingate velocity was calculated to be 0.5 m/s. This gate velocity in aluminium was confirmed by Runyoro et al.[4] using a high speed camera. The author [1] suggested that, with a gate velocity higher than 0.55 m/s, the dry side of the rising melt wave would start to fold over upon the opposing dry side which is likely to form a double oxide structure with a bubble of gas entrapped. The result is consistent with Lai [7], who compared the effect on the liquid metal with a gate velocity of 0.5m/s and 1.1m/s. The images recorded suggested that for a gate velocity of 1.1 m/s, liquid metal will fold over upon itself and the oxide film is expected to be incorporated into the melt, while for a gate velocity of 0.5m/s, no folding over action occurs. Lai [7] also confirmed this gate velocity by Computational Fluid Dynamic (CFD) modelling.
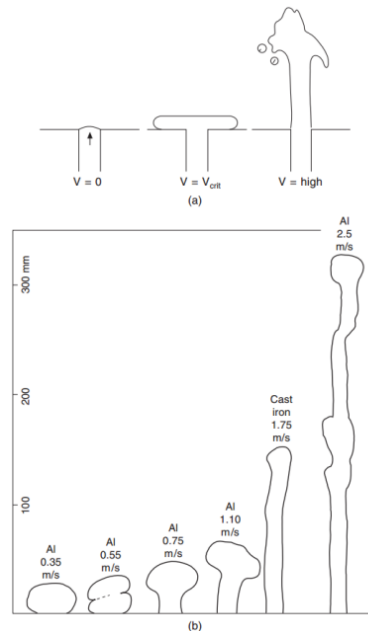


**Figure 2-3 (a) A Diagram showing that the surface turbulence will occur on liquid metal when V>V$_{critical}$ and (b) the experimental observation by Runyoro [4].**

5

Campbell suggested that turbulence in the casting can be described by three dimensionless quantities: the Weber number (We) and the Froude number (Fr) are used to describe surface turbulence, while the Reynolds number (Re) is used to describe bulk turbulence.

$$We = v^2 L\rho/\gamma \qquad (5)$$

$$Fr = v^2/(gh) \qquad (6)$$

$$Re = vL\rho/\mu \qquad (7)$$

v: the velocity of the liquid metal

L: characteristic length, normally assumed to be the hydraulic radius of the channel

h: wave height

g: gravity

μ: dynamic viscosity of the melt

γ: surface tension of the liquid metal

The We number is shown in Equation (5) and is defined as the ratio of the pressure of the melt to the surface tension. The We number is used to assess the surface turbulence in small quantities, such as small droplets. When the We number is larger than 1, surface turbulence is very likely to occur[8].

The Fr number is similar to We, but is used to describe the surface turbulence in a larger scale. Fr number is defined as the ratio of the internal pressure (trying to break the surface)

to the pressure caused by gravity (trying to restrain the surface) as shown in Equation (6). Turbulence is likely to occur when the Fr number is larger than 2000[8].

The Re Number is different from these two numbers in that it is used to assess bulk liquid behaviour. It is described as the ratio between the internal pressure to the viscous pressure, as shown in Equation (7). This has nothing to do with the process of incorporation of the double oxide film defect into the liquid melt but it is important to show that the double oxide film being carried into the casting by the liquid metal underneath the surface film is subject to bulk turbulence. Even with a carefully designed running system which minimizes the bulk turbulence, the Re number can still reach 7000. In a normal industrial casting, the Re number could be as high as $10^6$[8].

The double oxide film defect was initially discovered by Campbell in pure aluminium, it was then reported by other researchers, in various Al alloys ( e.g. Al-Si-Mg alloy[9-11], Al-Mg [12] alloy, Al-Cu alloy [13]and A319 [14] alloy, etc.) and Mg alloys(commercial pure Mg [15], AZ91[16, 17] et. al.). Campbell and Tiryakioglu [18] suggested that oxide film effects also occur in Ni based alloys. This defect is usually $mm^2$ in area but the thickness of this defect varies from a few hundred nm to a few μm(as shown in Table 1)[1].

**Table 1 The table shows the types of oxide film based on their lifetime[1].**

| Type of film | Growth time | Thickness (μm) | Description |
|---|---|---|---|
| Young oxide films | <0.01 s | 0.056 – 0.127 | Observed only as change in apparent colour of melt surface |
| | 0.01-1 s | 0.05 – 0.50 | Delicate, transparent, thin film, with sharp creases or wrinkles |
| Old oxide films | 10 s to 1 min | 10 | Flexible, extensive films |
| | 10 min to 1 hr. | 100 | Thicker films, less flexible |
| | 10 hr. to 10 days | 1000 | Rigid lumps and plates |

### 2.1.2   The evidence for double oxide film defects

The oxide film defect is so thin that it cannot be discovered by traditional non-destructive detection methods[1]. They are also not revealed by X-ray examination. However, there is still much evidence that points to the existence of this defect. Figure 2-4 shows the fracture surface of a tensile test bar of commercial pure Mg alloy, where an oxide film was located symmetrically on both sides which showed the doubled nature of this defect. EDX analysis suggested that a small oxygen peak was detected in addition to the peak from the matrix indicating a thin oxide film located on the metal matrix[5]. Many researchers also observed the expanded double oxide film defects with the aid of X-ray tomography and a reduced pressure test. Fox and Campbell [2] were the first to use this technique for the examination of the quality of liquid metal. In this test, liquid metal was allowed to solidify under an atmosphere ranging from 0.005 atm to 0.25 atm. The negative internal pressure should allow the internal atmosphere in an oxide film defect to expand, leading to the unfolding of the defect itself, so that the oxide film defect becomes visible in the X-ray image. In addition to that, the hydrogen content in the melt might also migrate into the internal atmosphere in a double oxide film defect under a reduced pressure, which would cause the expansion of

the bi-film. Figure 2-5 shows how, with a reduced pressure, the oxide film can become

clearer in the X-ray image.
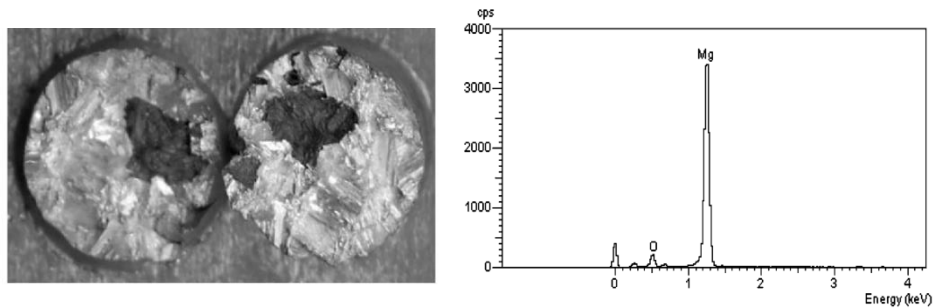


**Figure 2-4 The fracture surface showing the oxide film defect located symmetrically on both sides of tensile test bar[5].**



(a) 1000 mbar

(b) 200 mbar

(c) 100 mbar

(d) 50 mbar

10 mm

(e) 25 mbar

(f) 12.5 mbar
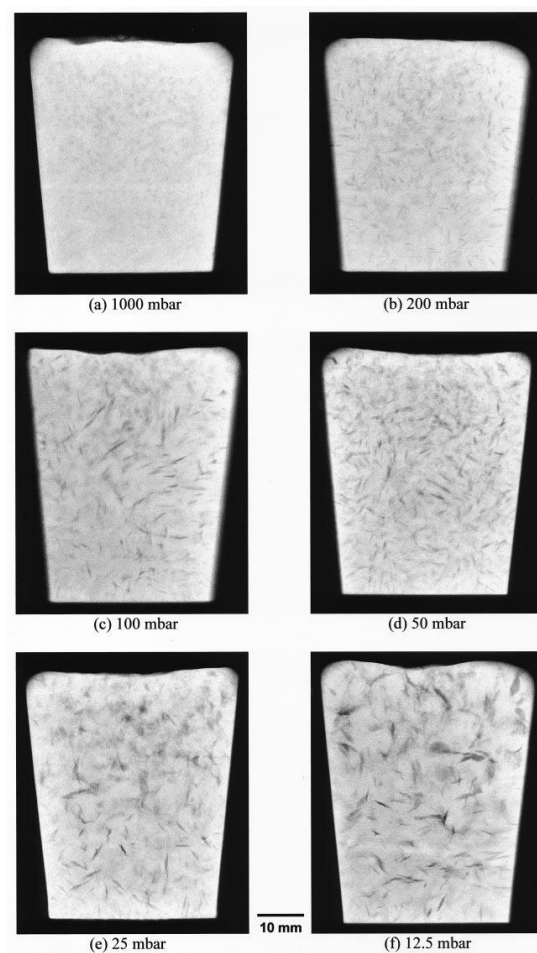
**Figure 2-5 The graph showing the oxide film under the X-ray tomography with reduced pressure[2].**

Divandari and Campbell [19] also suggested that an oxide containing defect can be observed with a "sandwich structure", as shown in Figure 2-6. Bubbles were deliberately introduced into an aluminium melt, and two bubbles were seen by X-ray tomography sticking together, and a high magnification image of this area showed a "sandwich structure" which consisted of two oxide layers and a layer of metal in between.

The author [20] also observed the formation of a bubble trail, which is another type of oxide defect, but with a long oxide tail in the casting. When an air bubble becomes trapped inside a casting, the oxide layer around the bubble can prevent its further motion, trapping bubbles with a small size, smaller than 5mm diameter. For a larger sized bubble, buoyancy overcomes the resistance of the oxide layer allowing the bubble to float upward. During this process, the gas bubble frequently breaks the oxide on the surface, and a new oxide layer is reformed. This floating up process leaves a long bubble trail which might reduce mechanical properties after solidification, even though the bubble itself has escaped by floatation up and through the surface of the metal melt. A sketch of the bubble trail is shown in Figure 2-7.

**Upper Bubble Oxide Film**

**Metal-Oxide Sandwich**

**Lower Bubble Oxide Film**

(a)



*Oxide-Metal Sandwich*

A

10 mm

(b)



18 mm
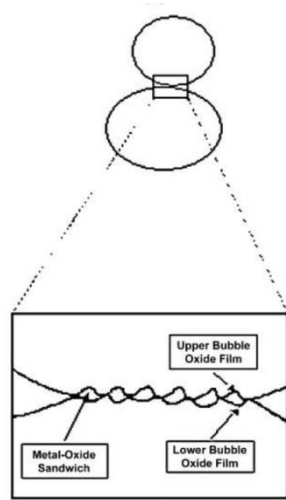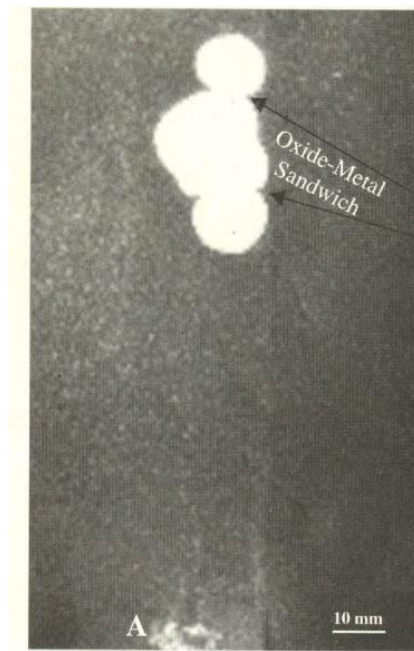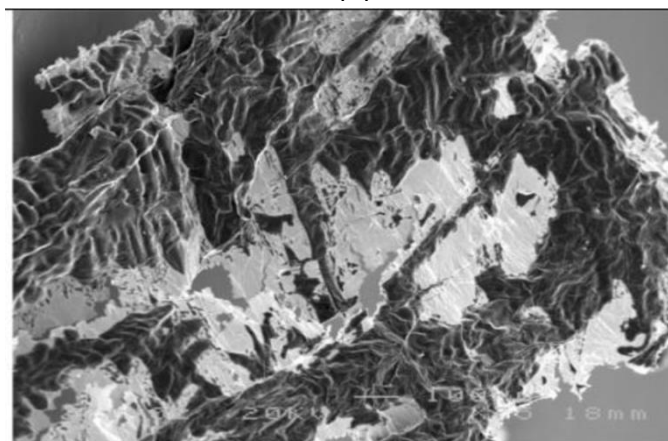
(c)

**Figure 2-6 (a) The sketch showing the "sandwich structure"; (b) the X-ray tomography and (c) the SEM image of the intersection point between two bubbles. White layers are double oxide film while the darker area is the aluminium dendrite with oxide film above[19].**

(a)



(b)
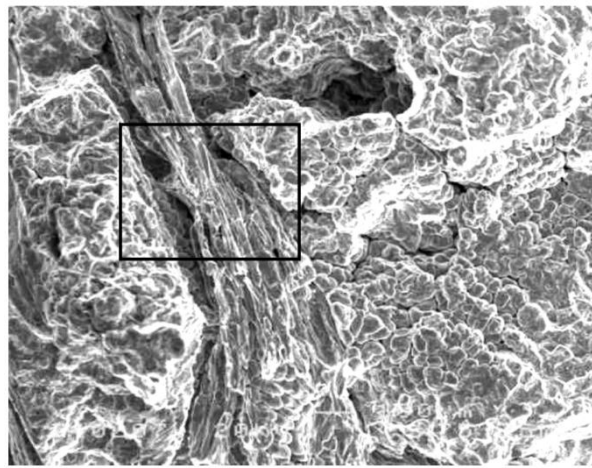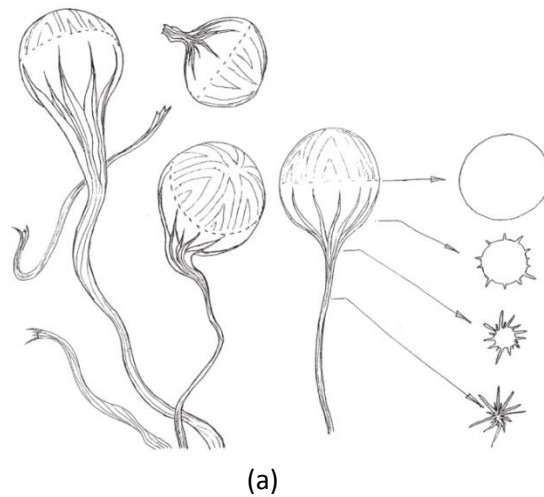
**Figure 2-7 (a) The sketch and (b) the SEM image of the bubble trail [20].**

In order to produce oxide film free castings, two methods have been suggested. The first one is the redesign of the casting component so that the gate velocity is controlled to below 0.5 m/s. Cox et al. [21] suggested that a top-filled casting contained more oxide film defect compared to a bottom-filled casting and thus had reduced mechanical properties and a reduced Weibull moduli, compared with a bottom-filled casting. Dai [22] investigated three different types of running system design, as shown in Figure 2-8 (a), (b) and (c), (labelled VR (with a cylindrical shape); RR (with a rectangular shape) and TR (with a triangular cross-section), respectively). Figure 2-8 shows the simulation results for the metal flow in the three different castings with different running system designs. The authors suggested that

the VR system can effectively control the gate velocity to below 0.5 m/s and cause the least surface turbulence in the casting.

Another method for the control of the bifilm content in an aluminium melt is the use of a filter. Aubrey et al. [23] suggested that the use of a filter before liquid metal entered the casting will filter out inclusions to give a relatively clean melt. However Sirrell et al. [24] suggested that the use of a filter would not necessarily filter out oxide film defects, but would reduce the velocity of the liquid metal entering the running system, and reduce the splashing and surface turbulence of the liquid metal surface. In this case, less new oxide film defects would be produced. This idea was confirmed by Bäckman [25] by experiment. The author suggested that the back pressure caused by filter led to better filling of the downsprue prior to casting and after the filter; the velocity of the liquid metal would be reduced and the filling of the casting become smoother. Arish and Raiszadeh [26] suggested that, in a commercial purity aluminium, the size and number of double oxide film defects was reduced when a filter was used.
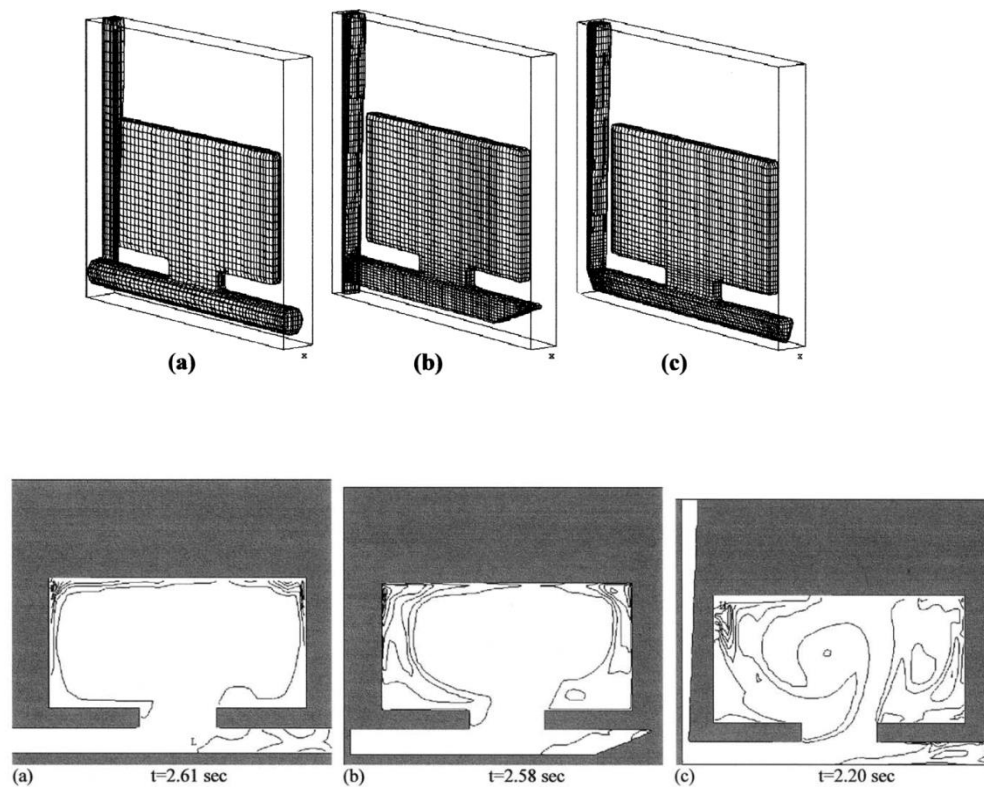
**Figure 2-8 The effect of different runner system design of the turbulence of the liquid metal inside the casting pieces.(a) VR; (b) RR and (c) TR [22].**

### 2.1.3 The deactivation of double oxide film defects

However, the oxidation of the liquid metal and the formation of an oxide skin is inevitable and, in industrial processes like degassing, and injection in high pressure die casting, surface turbulence and the folding over of the oxide skin cannot be avoided. Therefore, it is necessary to understand the life-cycle of a double oxide film defect before solidification and perhaps determine ways to deactivate the defect once formed.

A hypothesis was proposed by Nyahumwa et al. [27], who suggested that a double oxide film defect can be ruptured due to the stress caused by the transformation of the oxide structure, the stress caused by solidification or the nucleation of intermetallic phases on the

films. The entrapped atmosphere will react with the liquid metal resealing the rupture point. The repeated rupturing and resealing process will consume the entrapped atmosphere, consisting initially of oxygen, and then nitrogen. When the majority of the atmosphere is depleted, only a small amount of argon would be left and the oxide layers might have a chance to bond together. A sketch of this hypothesis is shown in Figure 2-9 [27].
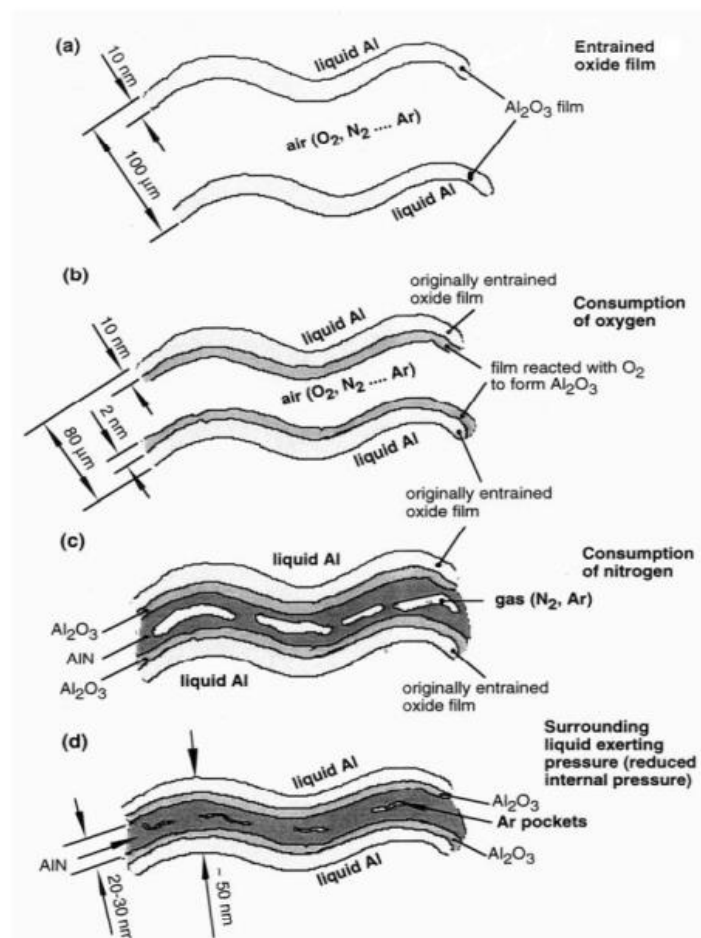


**Figure 2-9 The sketch of the healing mechanism of the double oxide film defect with time which was proposed by Nyahumwa [27].**

Based on this assumption, Raeiszadeh[28] trapped a bubble of air inside an aluminium melt for about 8h, in a Sialon tube with a blind hole at one end, immersed into an aluminium melt (as shown in Figure 2-10 (a)). The consumption of the entrapped atmosphere was

monitored using real-time X-ray tomography, as shown in Figure 2-10(b). The reaction

product between the entrapped gas and the liquid metal was also analysed by SEM/EDX.

The author found that, for 3-4h, reaction occurred between oxygen and the Al melt forming

aluminium oxide. Then the reaction between $N_2$ and Al took place, which formed AlN, (as

show in Figure 2-10(d)).



(a)



(b)



(c)
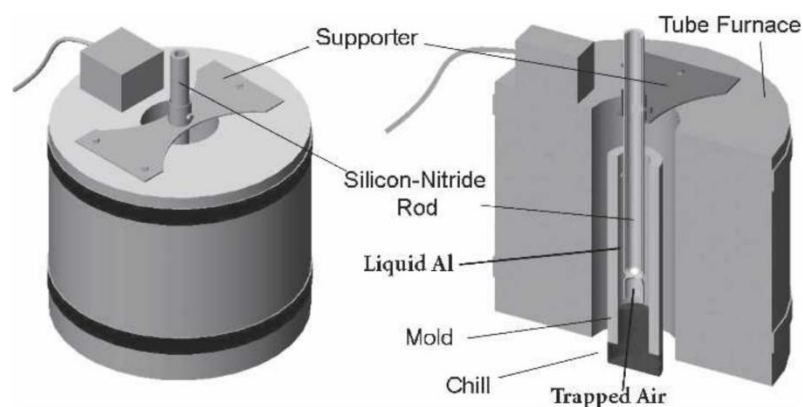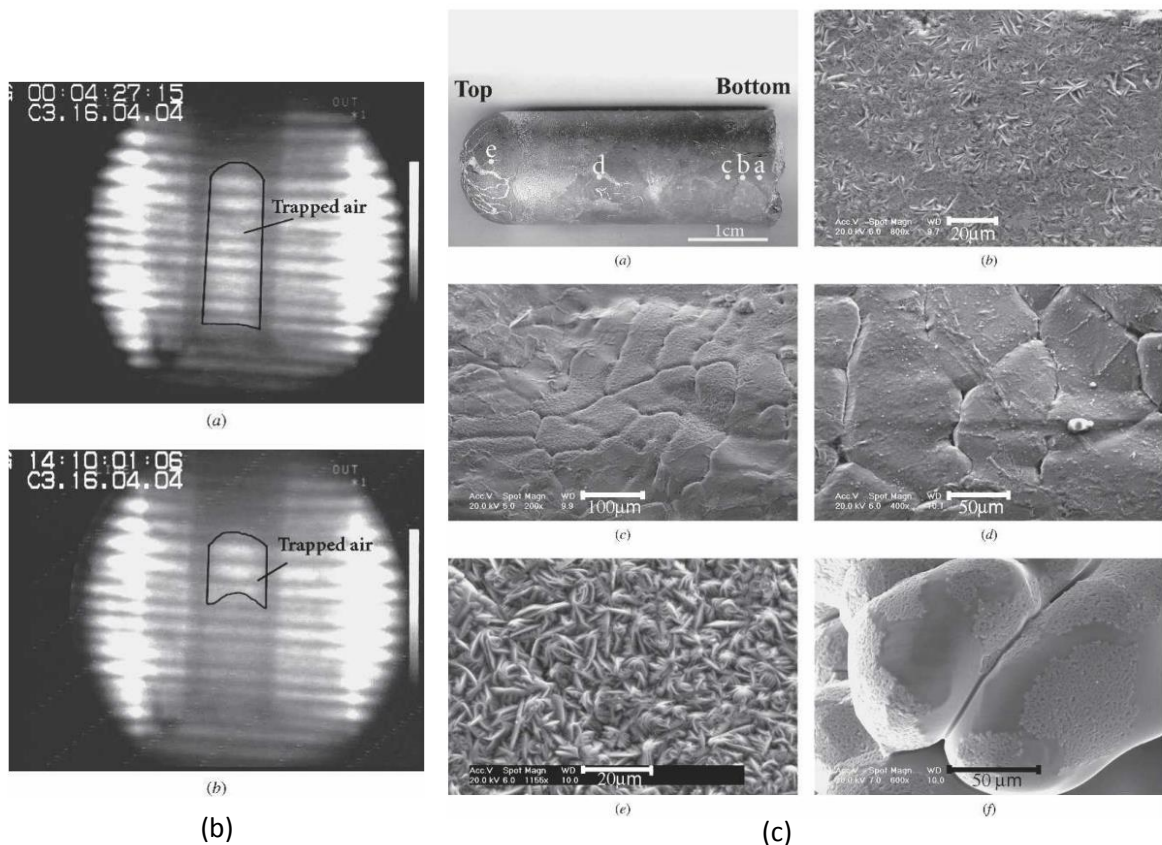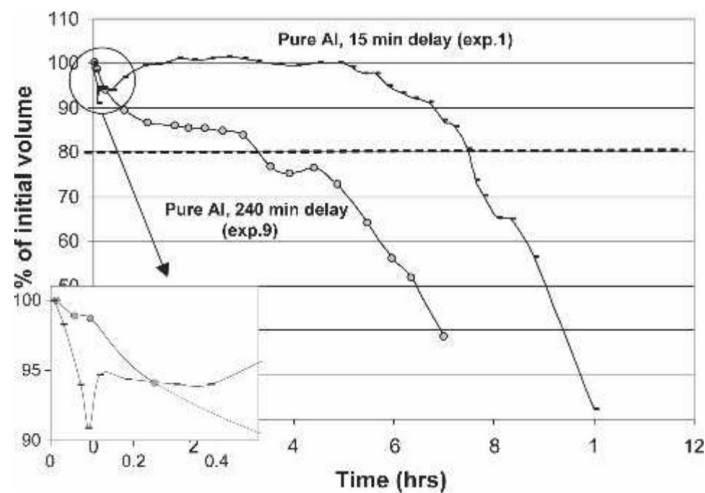
**Figure 2-10 (a) The experimental apparatus for the bubble capturing experiment by Rahzadeh; (b) The X-ray tomography showing the reacting process between the liquid metal and the entrap atmosphere inside the bubble; (c) The reactant between the liquid metal and entrap atmosphere and (d) the curve shows the consumption rate of the entrapped atmosphere [28].**

Mahmoud [29] used a Pore Gas analyser to investigate the change in composition of a trapped bubble with time, in three different alloys (commercial purity aluminium, 2L99 and Al-5Mg alloy). The author immersed steel strips with a blind hole on each side into the aluminium melt, as shown in Figure 2-11(a). The entrapped bubbles were allowed to react with the melt before solidification and their composition was then analysed using a Pore Gas Analyser. The same conclusion was reached, that the $O_2$ was initially consumed in the entrapped atmosphere, and then $N_2$ as shown in Figure 2-38 (b). It was also suggested that Al-5Mg had the fastest gas consumption rate of all three alloys, for both $O_2$ and $N_2$, while pure aluminium came second and 2L99 last, as shown in Figure 2-11(b). The author also suggested that the H continued to diffuse into the double oxide film defect: Al-5Mg has the fasted diffusion rate, followed by pure Al and then 2L99, as shown in 2-11(c).

(a)



(b)



(c)
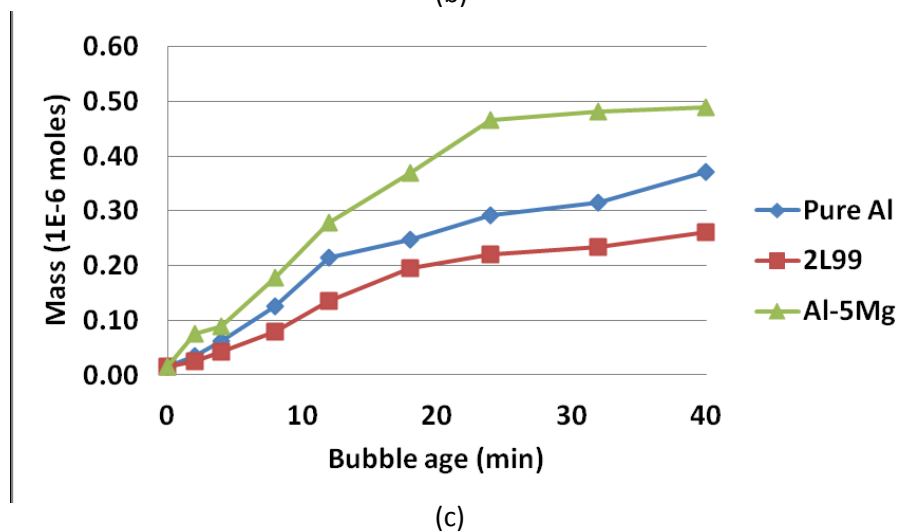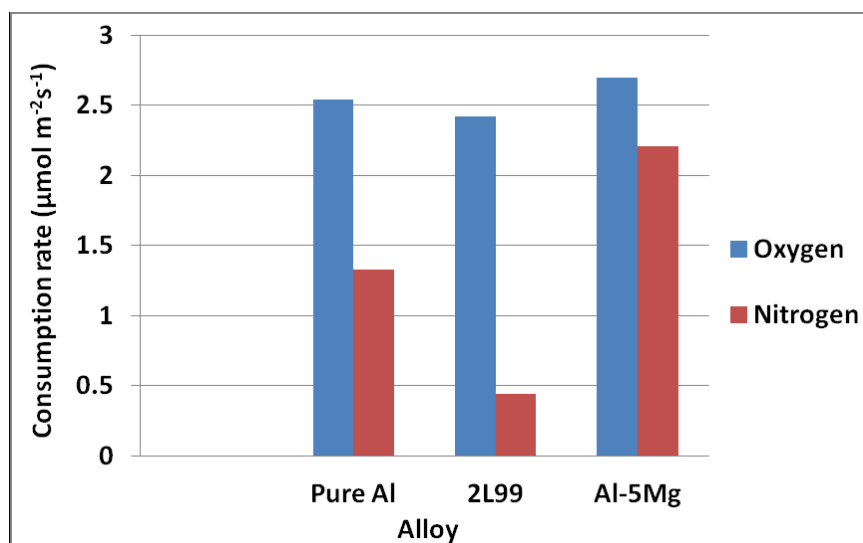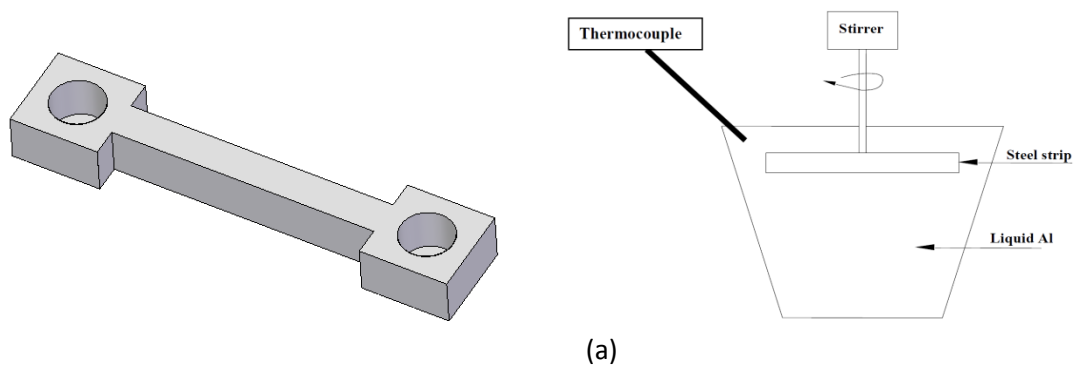
**Figure 2-11 (a) The sketch for the Pore Gas Analyser sample; (b) the consumption rate of oxygen and nitrogen by liquid metal reacting with entrapped atmosphere and (c) the consumption rate of H in the experiment [29].**

18

If the majority of the entrapped $O_2$ and $N_2$ could be consumed, the un-wetted oxide/nitride layers might have a chance to bond together. The occurrence of this bonding will reduce the deleterious effect caused by double oxide film defects. This bonding effect has proved to be feasible according to Raihzadeh et al. in A356 alloy[30].

In the case of Raihzadeh, two aluminium bars with the same dimensions were prepared with both ends oxidised. The oxidised surfaces were placed face-to-face, into a stainless steel container, and the aluminium bars were then melted and held for a period of time before solidification, as shown in Figure 2-12. With only 13min holding time, the two aluminium bars were easily detached from each other after solidification and SEM examination showed that there was little bonding. However, after a holding time of 8h (A356 alloy), some bonding was observed on the oxide surface and about 1.5 kN was required in order to separate the two aluminium bars.

Amirinejhad and Najafzadeh[31, 32] expanded the experiment, with different amounts of Mg content, which led to a decrease in the time needed for the occurrence of bonding between the two  unwetted oxide layers. They also suggested that phase transformations and atomic rearrangement were a necessary condition for the bonding to occur in Al alloys containing various Mg contents.
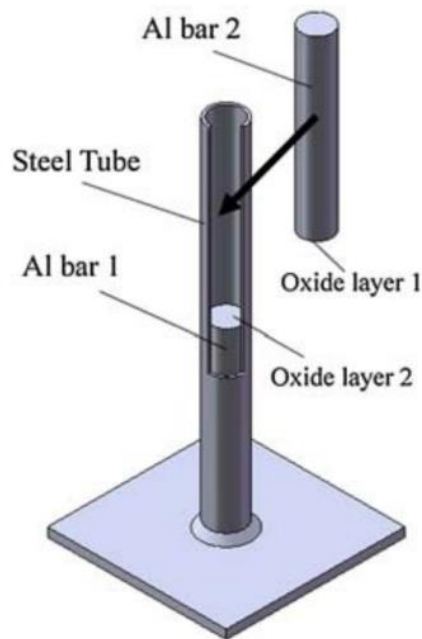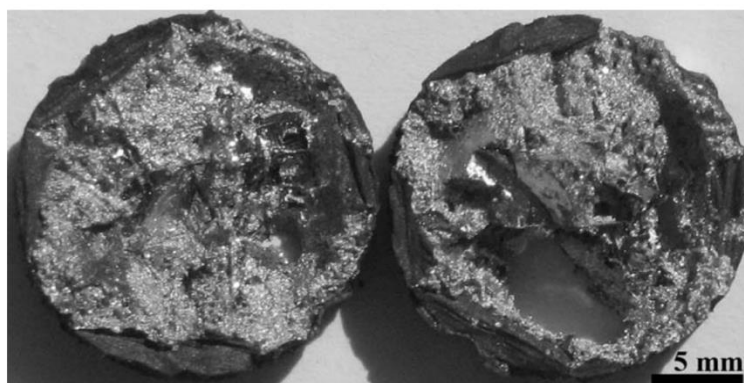
Figure 2-12 The experiment shows the effect of holding time on the bonding of two alumina layer in the aluminium melt. (a) Experimental apparatus; (b) The effect of bonding after 18 min; and (c) The effect of bonding after 8h[31].

### 2.1.4 Effect of different elements on the double oxide film defect

#### 2.1.4.1 The effect of Si addition on double oxide film defect in Al alloys

The addition of Si to Al reduces the melting point and improves its fluidity and castability. The addition of Si, however, is not supposed to affect the formation of the double oxide film defect due to the low Gibbs Free energy for the formation of $SiO_2$ ( $\Delta G^o_{1000K}$=-730.26 kJ/mol $O_2$) compared with $MgAl_2O_4$ and $Al_2O_3$ (which are -939.97 kJ/mol and -907.55 kJ/mol respectively)[33]. Campbell[34] suggested that primary Si could be nucleated on the sides of a double oxide film defect. The Si phase was initially nucleated on $AlP_3$, which is a known nucleation site for primary Si phase in Al-Si alloy[35]. The author suggested that $AlP_3$ was nucleated on the wetted side of oxide film defects, therefore the Si phase was in turn growing on the bi-film defect. The Si phase might grow into a plate-like shape and stretch the crumpled bifilm defect. This stretching phenomenon might lead to the formation of cracks between an oxide film and the Si phase.
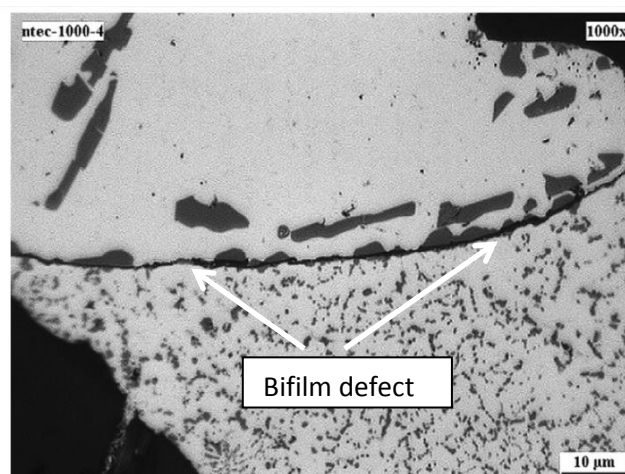


**Figure 2-13 The microstructure of the Al-Si alloy with superfast cooling rate showing the areas separated by oxide film defect. Si phase was seen growing on the side of double oxide film defect [6].**

Dispinar et al. [6] investigated the effect of cooling rate on the microstructure of an Al-Si alloy. He observed an area which was separated by a double oxide film defect and contained a much finer grain structure, as shown in Figure 2-13. Larger sized Si particles were observed growing on the other side of the bifilm defect.

### 2.1.4.2 The effect of Fe content on double oxide film defect in Al alloy

Fe is the main impurity in foundry Al alloys. Al-Fe-Si intermetallic phases can be formed and cause a reduction in the mechanical properties of the alloy. 3 common types of Fe-containing intermetallic phases are: $\alpha$, $\beta$ and $\pi$ phases ($\alpha$-Al$_8$Fe$_2$Si, $\beta$-Al$_5$FeSi and $\pi$-Al$_8$Mg$_3$FeSi$_6$). The morphology of the intermetallic phase is shown in Figure 2-14. As can be seen, $\alpha$ will usually have a plate-like structure, while the $\beta$- state has a needle-like structure. The $\pi$ phase however, was shown to be in a porous structure[36]. Bangyikhan[11] suggested that an 11% improvement in the tensile properties was achieved when the Fe content was reduced from 0.5 wt.% to 0.1 wt.% in Al-7Si-0.3Mg alloy. Of all three phases, $\beta$-Al$_5$FeSi is supposed to have the most detrimental effect to mechanical properties due to its morphology[37].

Cao et al.[9, 38-40], observed the $\alpha$-Fe intermetallic phases growing on alumina, as shown in Figure 2-15. The author suggested that the lattice disregistry between the $\alpha$-Fe intermetallic phase and oxides ($\gamma$-Al$_2$O$_3$, $\alpha$-Al$_2$O$_3$, MgAl$_2$O$_4$ and MgO) were all <12%, which suggested that the wetted side of the oxide film can serve as a substrate for the nucleation of the Fe-containing intermetallic phase. Bangyikhan[11] investigated the behaviour of Fe in Al-7Si-0.3Mg alloy and suggested that, by SEM observation, $\beta$-Fe phase could also be nucleated on the bi-film defect.

Backenrud[41] suggested that, during the solidification process the Fe containing intermetallic phase initially formed( >575 °C) would be β-Al$_5$FeSi, before transformation to a π-Al$_8$FeMg$_3$Si$_6$ phase (<575 °C). Bangyikhan[11] suggested that, for an Fe phase nucleated on the bi-film defect, this transformation will introduce stress into the double oxide film defect and cause it rupture locally. This rupture point will enable the H content of the intermetallic phase to migrate into the double oxide film effect, causing its expansion.



(a)                                          (b)
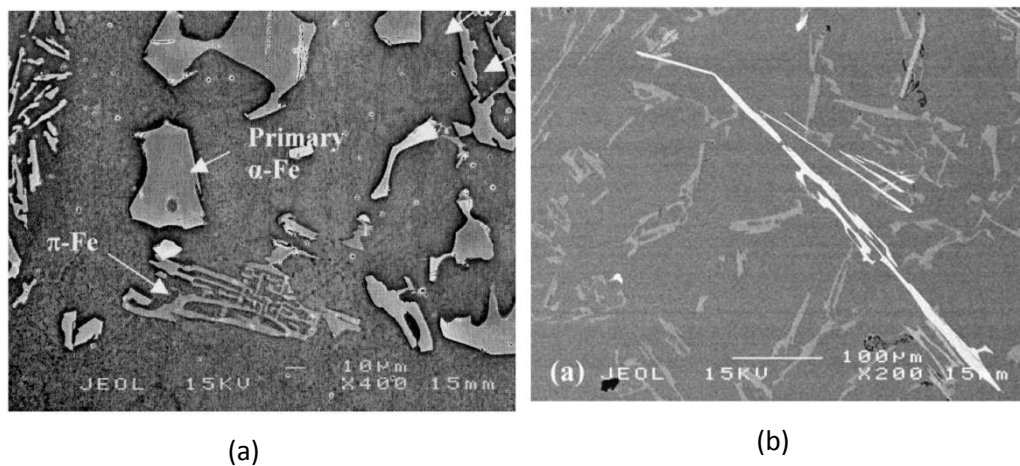
**Figure 2-14 The SEM image showing the (a) α and π; (b) β Fe-containing phases in Al-Si-Mg alloy [41].**
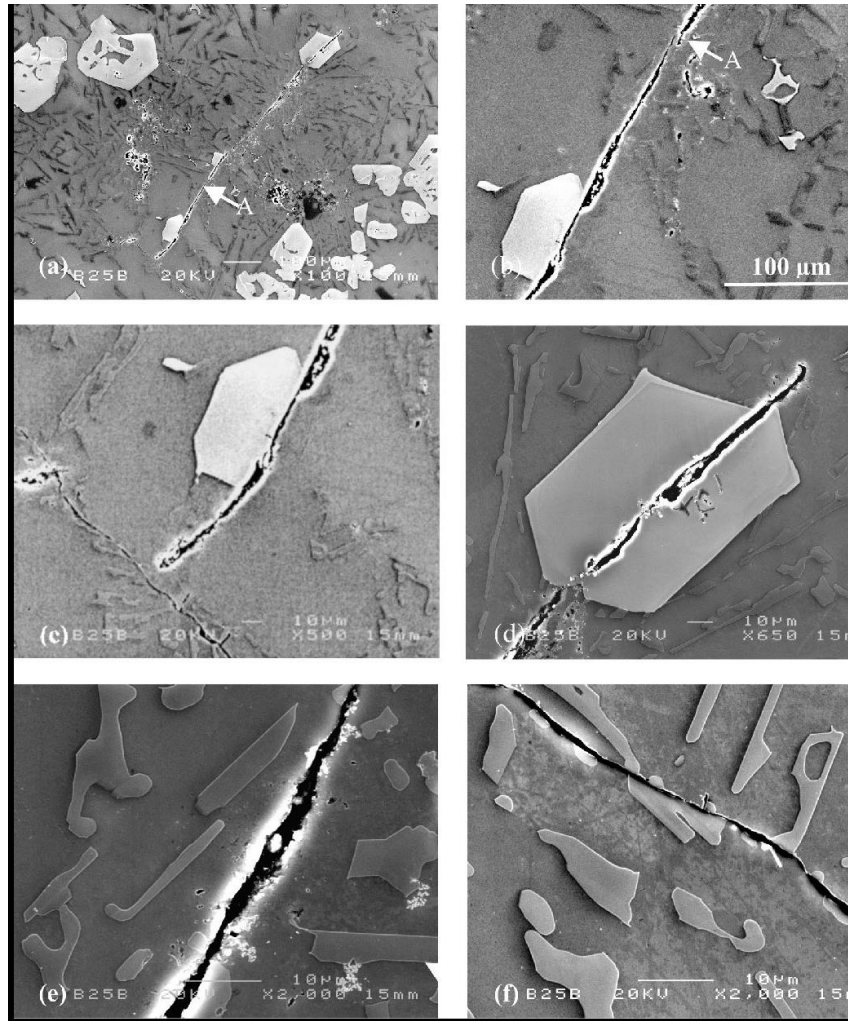
**Figure 2-15 The α-Fe phase found growing on the sides of double oxide film defect in Al alloy [41].**

### 2.1.4.3 *Effect of H on double oxide film defects*

In aluminium alloy, hydrogen is a soluble gas. Hydrogen comes from the reaction between the liquid aluminium and $H_2O$ vapour, according to Equation (8).[42]:

$$2Al + 3H_2O = Al_2O_3 + 3H_2 \qquad\qquad (8)$$

According to Talbot[43], monatomic hydrogen will be stored at interstitial points in the solid aluminium and will stay at inter-atomic points in the liquid aluminium. The author

calculated the largest vacancy available for the hydrogen to be 0.059nm in solid FCC aluminium. This space is increased by 4% when the metal is in a liquid state and it is sufficient for one hydrogen atom (0.053nm). However, the available space will not be able to accommodate molecular H. Molecular H has to be dissociated before having dissolved into the aluminium melt as shown in Equation (9).

$$H_2(gas) = 2H(in\ the\ melt) \hspace{3cm} (9)$$

Jakes and Pasturel[44] studied the self-diffusion of H atoms in the aluminium melt and suggested that  H will not be trapped at stationary interatomic sites, and that vibration would occur in the area which would lead to the capability of long jumps of H atoms into nearby vacancies. The distance for this jump was estimated to be as long as 15 times the distance of the Al-H interatomic spacing (3nm) and will allow the hydrogen to gradually diffuse throughout the liquid metal.
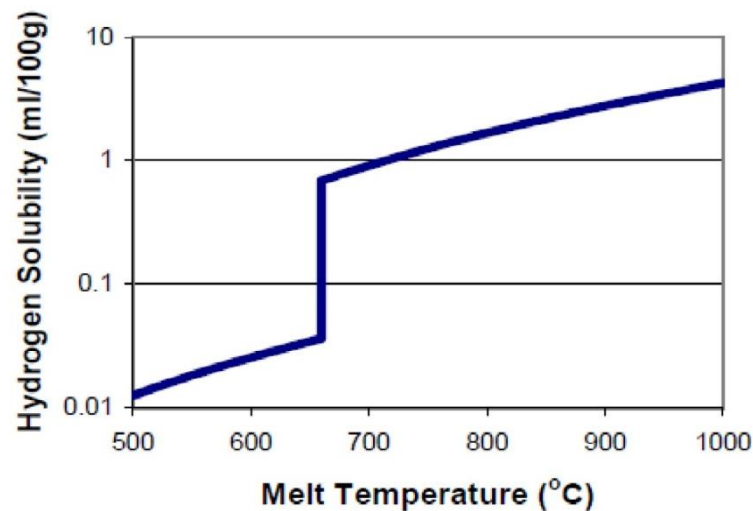


**Figure 2-16 Solubility of H in pure aluminium with temperature [45].**

Ransley and Neufeld[45] studied the solubility of H in the aluminium melt and they suggested that solubility was temperature dependent, as shown in Figure 2-16. As can be seen, the hydrogen solubility in the liquid state is much higher than in the solid state. During the solidification, as the dendritic front advances, the hydrogen at the solid-liquid interface was rejected into the liquid leading to an increase in the hydrogen content in the remaining liquid. Zhou et al[46], suggested that the hydrogen content in the melt during solidification was directly proportional to the fraction of solid.

H is shown to affect the mechanical properties of a casting, El-Sayed [47] suggested that, increasing the H content from 0.05 $cm^3$/100g to 0.18 $cm^3$/100g decreased the Weibull moduli of the UTS of 2L99 alloy from 21 to 5.

Hydrogen in aluminium is often accused of causing the formation of porosity[48], however, according to Campbell[1], both homogeneous and heterogeneous nucleation of hydrogen porosity are very difficult.

Fisher[49] and Campbell[1] suggested that the energy required for the homogeneous formation of the gas bubble is:

$$\Delta G = \gamma A + P_e V - P_i V$$

$$= 4\pi r^2 \gamma + 4/3\pi r^3 (P_e - P_i) \qquad (10)$$

Where $P_e$ is the pressure in the melt in which the gas bubble was generated. In order to produce a gas bubble with volume V, work equal to $P_e V$ is required. In addition to this, the formation of the interfacial area A between the bubble and melt requires work $\gamma A$, where $\gamma$ is the surface tension of the liquid metal. The hydrogen gas, with pressure $P_i$, will help the

formation of the bubble by reducing the required work $P_iV$. The equation of the required work is shown in Equation (10). The maximum value of is $\Delta G$ is derived at:

$$R = 2\ \gamma/(\ P_e - P_i) \tag{11}$$

This $\Delta G$ value suggests the minimal energy required for the homogeneous nucleation of the gas bubble. Campbell used the data from the A356 alloy ($\gamma$=0.9 Nm$^{-1}$ , the diameter of Al atom: 0.3nm) and reached the conclusion that the minimal pressure required for the hydrogen bubble was 31,000 atm, a value too high to be achieved in normal casting conditions.

Fisher[49] then investigated the heterogeneous nucleation of a gas bubble and he suggested that there was a relationship between homogeneous and heterogeneous nucleation based on the wetting angle between the porosity and the matrix.

$$P_{\text{homogeneous}}/P_{\text{heterogeneous}} = 1.12\sqrt{\frac{(2-con\theta)(1+cos\theta)^2}{4}} \tag{12}$$
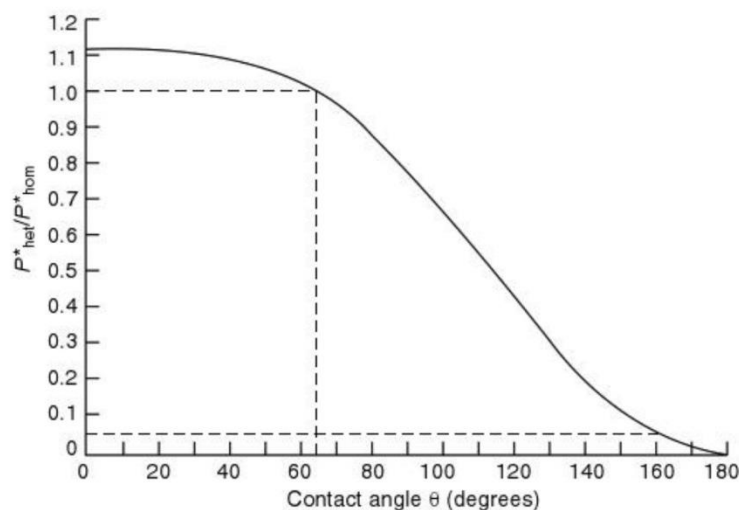


Figure 2-17 The difficulty for the H gas formation for heterogeneous nucleation compared with homogeneous nucleation[1].

Figure 2-17 shows the difficulty for formation of heterogeneous nucleation of H pores based on Equation (12). It has been proposed that a wetting angle larger than 160° is unlikely in a real experiment [1]. Therefore, the pressure required for the heterogeneous nucleation of the hydrogen bubble would be 1500 atm (at 160°), which is also too high to happen in practice.

Therefore Campbell[1] suggested that the only possibility for the formation of a hydrogen bubble was that the H penetrated through an oxide film defect and inflated it. El-Sayed [47] suggested that, a smaller sized oxide film defect can be observed on the fracture surface of Al-7Si-0.37Mg alloy with low H content compared with the casting containing high H content. This provided evidence for the effect of H in expanding oxide film defects.

Weigel and Fromm [50] suggested that the oxide layer could be an effective barrier to hydrogen. The author suggested that the hydrogen absorption rate for a pure aluminium melt at 700°C, with the protection of an oxide layer, was only a few ml/m$^2$h but this was increased $10^4$-$10^5$ times when the oxide layer is removed.

Gerrard and Griffiths [51] suggested that both continuous aluminium oxide and feather-like aluminium nitride would allow the hydrogen to diffuse through, but that the H absorption rate into the melt for the latter was twice as much as for the former.

Raeizadeh and Griffiths [28]suggested that H could diffuse into the oxide film defect by a rupture point or through the permeable nitride formed to reseal the rupture point.

### 2.1.5 Statistical analysis of the effect of double oxide film defects on mechanical properties

The Weibull distribution is an empirical statistical distribution initially mentioned by Weibull[52] in 1951. Originally, the author used this to describe the probability of the failure of a chain involving many links, with the failure of any of those links resulting in the failure of the whole chain (the weak chain theory). The cumulative function for the probability of failure is expressed in Equation (13).

$x_u$, m, and $x_0$ are all Weibull parameters, where $x_u$ stands for the lower boundary of the value x; m is the Weibull modulus of the data set and $x_0$ is the position parameter within which 1- 1/e (~63%) of the data might fail.

$$F(x) = 1 - e^{-\left(\frac{x-x_u}{x_0}\right)^m}$$
(13)

This distribution is used widely in engineering to model the lifetime of a component or the reliability of an engineered piece[53]. It is different from the normal distribution in that the data set is not distributed symmetrically on both sides of an axis; more data in this distribution tends to accumulate at the higher end.

Campbell[54] suggested that the Weibull distribution was ideal to describe the failure of a defect-containing casting in that there is a cut-off at the higher end of this distribution which is consistent with casting behaviour where a limit to the tensile strength exists which represents the limit of the material itself. The tensile test results tend to accumulate at the higher end, but there are also several tensile test bars that would contain large defects

giving poor mechanical properties. This is consistent with the Weibull distribution in that a long tail exists at the lower end.

Green and Campbell[55] used a Weibull distribution to describe the properties of Al-7Si-0.35Mg alloy, and suggested that the use of a Weibull distribution have a better data fit compared with a Normal distribution or a Type I extreme distribution. A similar conclusion was reached by Byczynski [14], who suggested that tensile test results for A319 alloy (Al-Si-Cu-Mg) fitted a Weibull distribution better compared with a Normal distribution or a log normal distribution.

To simplify the data fitting process, the Weibull parameters are estimated by a 2 parameter Weibull distribution with a linear regression method used. In this simplified equation, shown in Equation (14), $x_u$ is taken as zero:

$$P = 1 - e^{-\left(\frac{x}{x_0}\right)^m} \tag{14}$$

The above equation can be rewritten as:

$$\ln\left[\ln\left(\frac{1}{1-P}\right)\right] = m * lnx_n - m * lnx_0 \tag{15}$$

For mechanical property test results from castings (e.g., UTS or %Elongation), the values are sorted into an ascending order, as shown in Equation (16). A probability of failure (0<P<1), as shown in Equation (17), is assigned to each value of the mechanical property test results.

$$x_1 < x_2 < x_3 < \cdots < x_{n-1} < x_n \tag{16}$$

$$P_1 < P_2 < P_3 < \cdots < P_{n-1} < P_n \tag{17}$$

The probability value P needs to be estimated. The probability estimator is often written as shown in equation (18). And four commonly used equations[56, 57] are shown in Equations (19-22).

$$P_n = \frac{n-a}{N+b} \tag{18}$$

$$P_n = \frac{n-0.5}{N} \tag{19}$$

$$P_n = \frac{n}{N+1} \tag{20}$$

$$P_n = \frac{n-0.3}{N+0.4} \tag{21}$$

$$P_n = \frac{n-0.5}{N+0.25} \tag{22}$$

For the four equations shown above, Khalili [58] suggested that the use of equation (22), gave a better estimation, while equation (20) had the least reliable outcome. Tiryakioğlu et al. [59]further suggested that, with the help of a Monte Carlo simulation, a series combination of a and b in Equation (18) can be used to produce an unbiased estimation with different sample sizes.

While the a and b values are determined, $\ln\left[\ln\left(\frac{1}{1-P}\right)\right]$ can be plotted against $\ln x_n$, and the other parameters can be easily obtained. To determine if the mechanical property test results really followed the Weibull distribution, a criteria needed to be met. Tiryakioğlu et al. [60]suggested that, with a sample size range of 5-100, Equation (23) can be used as a criteria of $R^2$ for 95% confidence, above which the data set can be treated as following the Weibull distribution. n is the sample size of the data set.

$$R_{0.05}^2 = 1.0637 - \frac{0.4174}{n^{0.3}} \qquad\qquad (23)$$
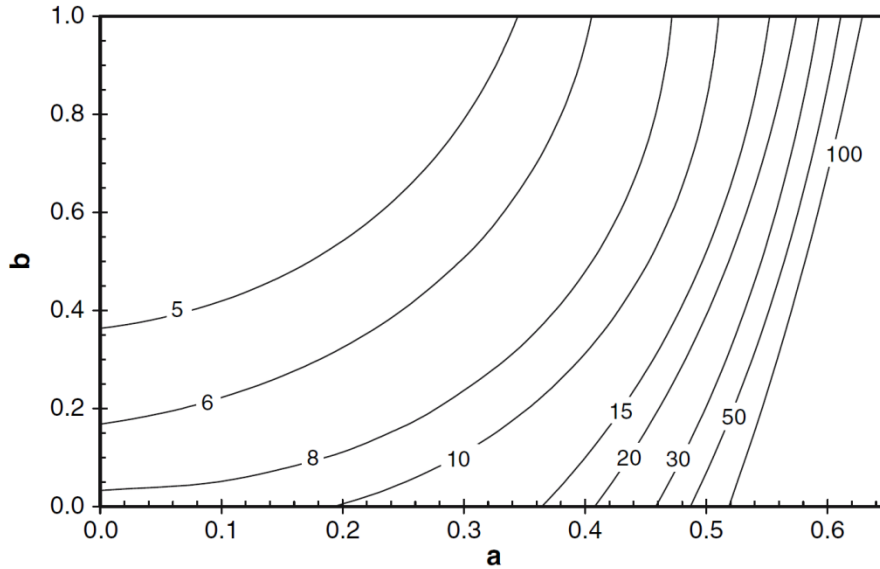


**Figure 2-18 The a, b value for the unbiased estimation of the probability estimator P [60].**

It was suggested that only when the above criteria were satisfied then the data set can be accepted as a Weibull distribution. However in some castings a bimodal distribution might exist [61], caused by the presence of more than one type of defect, which would lower the $R^2$ value. Nyahumwa et al [62] suggested that , when investigating the fatigue life of the alloy, in an Al-7Si-0.35Mg alloy, multiple types of defect existed. This showed as different slopes on the Weibull plot rather than a single straight line, as shown in Figure 2-19. The author also suggested that the different types of failure in the alloy were old oxide film defects, young oxide film defects, pores inflated from oxide film and the slip planes, (the metallurgical strength of the alloy). Cox et al.[63] observed the difference in the slope of the Weibull plot for HIPed Ni IN939 alloy, above and below 1100MPa, and suggested the existence of a bi-model distribution.

(a)



(b)
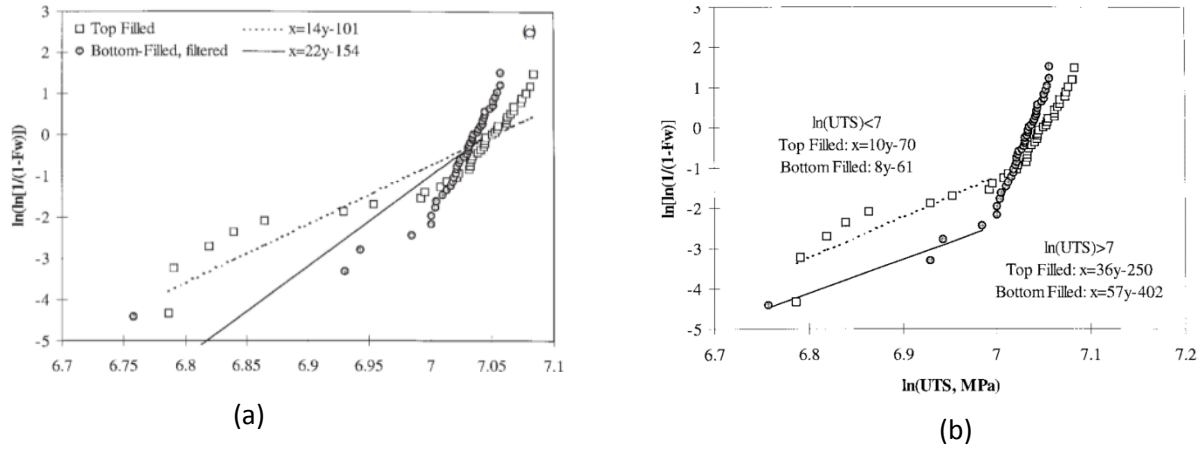
**Figure 2-19 Result from Mahumwa et. al. shows the exist of bi-distribution in the tensile test result [62].**

Hudak and Tiryakioğlu[64] tried to compare two different Weibull moduli. The authors used a Monte-Carlo simulation to generate 2 groups of data points, which contained $n_1$ and $n_2$ ($n_1 > n_2$) data points. The Weibull modulus was estimated with a 2 parameter Weibull distribution to give a Weibull modulus of $m_1$ and $m_2$, respectively. The ratio for $m_1/m_2$ was recorded and this process repeated 10,000 times for a clear distribution. For a sample size ranging from 10-100, 2.5 and 97.5 percentiles of the distribution was shown in Figure 2-20. In practice, if the $m_1/m_2$ value for the Weibull moduli of the tensile test results of two castings, containing $n_1$ and $n_2$ test bars fell outside the percentile range, then the two castings can be treated as having different Weibull moduli.

**Figure 2-20 2.5 and 97.5 percentile of m1/m2 when comparing the Weibull moduli of two data set.**

Each cell shows the 2.5 percentile / 97.5 percentile of m1/m2.

| n2 \ n1 | 10 | 15 | 20 | 25 | 30 | 35 | 40 | 50 | 60 | 70 | 80 | 90 | 100 |
|---|---|---|---|---|---|---|---|---|---|---|---|---|---|
| 10 | 0.412 / 2.434 | 0.453 / 2.262 | 0.475 / 2.222 | 0.4888 / 2.151 | 0.494 / 2.124 | 0.505 / 2.1 | 0.507 / 2.089 | 0.517 / 2.058 | 0.524 / 2.09 | 0.535 / 2.042 | 0.534 / 2.027 | 0.536 / 2.011 | 0.54 / 2.03 |
| 15 |  | 0.489 / 2.069 | 0.511 / 1.976 | 0.531 / 1.951 | 0.543 / 1.906 | 0.55 / 1.881 | 0.559 / 1.877 | 0.574 / 1.854 | 0.581 / 1.827 | 0.591 / 1.821 | 0.594 / 1.823 | 0.599 / 1.798 | 0.595 / 1.798 |
| 20 |  |  | 0.526 / 1.889 | 0.553 / 1.851 | 0.571 / 1.799 | 0.575 / 1.798 | 0.585 / 1.767 | 0.6 / 1.722 | 0.609 / 1.708 | 0.614 / 1.703 | 0.621 / 1.69 | 0.629 / 1.693 | 0.629 / 1.693 |
| 25 |  |  |  | 0.567 / 1.771 | 0.581 / 1.728 | 0.598 / 1.72 | 0.599 / 1.677 | 0.615 / 1.661 | 0.624 / 1.647 | 0.632 / 1.63 | 0.639 / 1.62 | 0.644 / 1.618 | 0.649 / 1.6 |
| 30 |  |  |  |  | 0.596 / 1.677 | 0.608 / 1.662 | 0.621 / 1.622 | 0.634 / 1.612 | 0.643 / 1.597 | 0.653 / 1.583 | 0.66 / 1.573 | 0.661 / 1.559 | 0.668 / 1.549 |
| 35 |  |  |  |  |  | 0.614 / 1.624 | 0.632 / 1.605 | 0.643 / 1.568 | 0.658 / 1.56 | 0.671 / 1.545 | 0.674 / 1.523 | 0.683 / 1.516 | 0.684 / 1.5 |
| 40 |  |  |  |  |  |  | 0.636 / 1.569 | 0.655 / 1.552 | 0.668 / 1.531 | 0.674 / 1.515 | 0.685 / 1.51 | 0.693 / 1.492 | 0.694 / 1.489 |
| 50 |  |  |  |  |  |  |  | 0.665 / 1.504 | 0.678 / 1.483 | 0.689 / 1.466 | 0.694 / 1.458 | 0.702 / 1.447 | 0.708 / 1.432 |
| 60 |  |  |  |  |  |  |  |  | 0.69 / 1.444 | 0.702 / 1.439 | 0.709 / 1.42 | 0.713 / 1.412 | 0.721 / 1.402 |
| 70 |  |  |  |  |  |  |  |  |  | 0.71 / 1.445 | 0.714 / 1.399 | 0.724 / 1.389 | 0.731 / 1.38 |
| 80 |  |  |  |  |  |  |  |  |  |  | 0.722 / 1.384 | 0.731 / 1.382 | 0.739 / 1.36 |
| 90 |  |  |  |  |  |  |  |  |  |  |  | 0.737 / 1.361 | 0.741 / 1.355 |
| 100 |  |  |  |  |  |  |  |  |  |  |  |  | 0.752 / 1.331 |

## 2.2 Oxidation of liquid aluminium

### 2.2.1 Oxidation of pure aluminium

Liquid aluminium, when exposed to air, will form a layer of oxide which will instantly reform when broken, due to the high Gibbs Free Energy for the formation of alumina [$G^0_{1000K}$ =-907.55 kJ/mole $O_2$ [33]]. Researchers have identified that the originally formed alumina is in an amorphous state [3, 65], which can then crystallize to a γ-$Al_2O_3$ structure after a period of time and then stabilize in the α state [66]. If the oxide film stays in a static situation during oxidation, then this transformation time could be as long as 5 hours[66]. However, if the oxidation is dynamic, the transformation time could be shortened by as much as 60 times (according to Wightman and Fray [67], by comparing the oxidation of high purity aluminium under dynamic and quiescent conditions, with carbon dioxide).
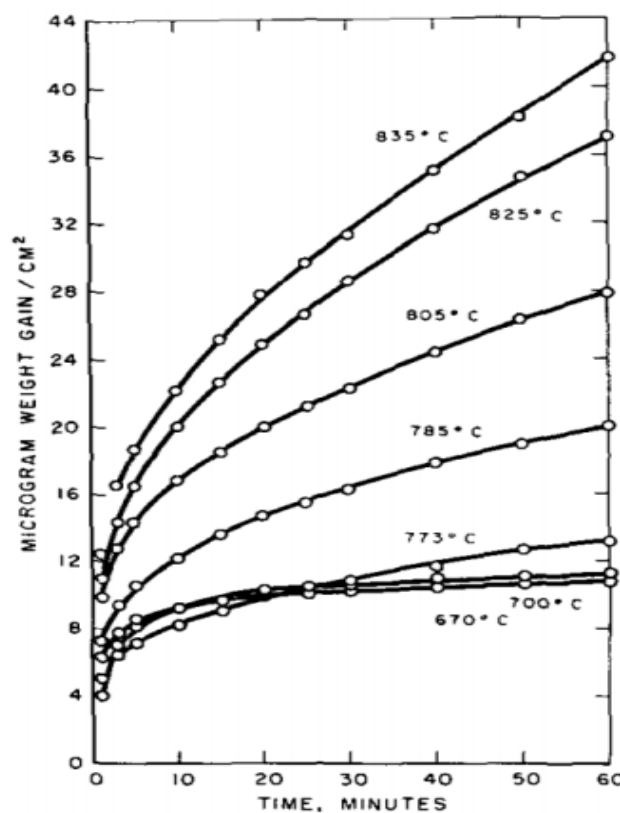


**Figure 2-21 The weight gain of liquid aluminium after a period of time under different temperatures[3].**

35

Sleppy[3] suggested that the oxidation rate for pure aluminium is temperature dependant, as shown in Figure 2-21. For oxidation of the liquid metal below 700 °C, a logarithmic trend was followed which is shown by the mass gain of the system. However, with the temperature above 700 °C, a parabolic trend was followed.

The author used a different theory in explaining the oxidation behaviour below or above 700 °C. At the higher temperature, higher activation energy allows metal ions to penetrate through the existing crystallized oxide layer and react with the oxygen in the atmosphere, leading to the continuous thickening of the oxide. For the temperature below 700 °C, the low temperature makes it less likely for the metal ions to penetrate through the oxide layer, instead pores, loose structure, or cracks provide convenient means for the oxygen ions to penetrate through the oxide and react with the liquid metal. The author also suggested that the volume change caused by the transformation of the oxide layer and the rearrangement of the oxide atoms might provide a chance for the continuous reaction[3].

Impey et. al. [68] suggest that hydroxyl ions play an important role in stabilizing $\gamma$-$Al_2O_3$ state. The author compared the oxidation rate of commercial purity aluminium under dry air or humid air and the result is shown in Figure 2-22. As can be seen, the liquid metal oxide had a much higher oxidation rate, under dry air, compared with humid air. The author attributed this to transformation of the $\gamma$ into $\alpha$ alumina.  For the metal oxide under dry air, the hydroxyl ion, which stabilizes $\gamma$-$Al_2O_3$, was absorbed by the liquid metal in the form of hydrogen and the oxide was then transformed into $\alpha$-alumina. The cubic alumina ($\gamma$-$Al_2O_3$) to rhombohedral structure ($\alpha$-$Al_2O_3$) transformation was accompanied by a 24% volume change which introduces stress into the existing oxide layer, causing local failure. The liquid metal can then penetrate through the oxide layer and react with oxygen in the atmosphere.

Therefore the oxidation rate will be greatly increased. However, for oxidation under humid air, a continuous supply of the hydroxyl ions will allow the aluminium oxide to stay in the γ state for a longer period.
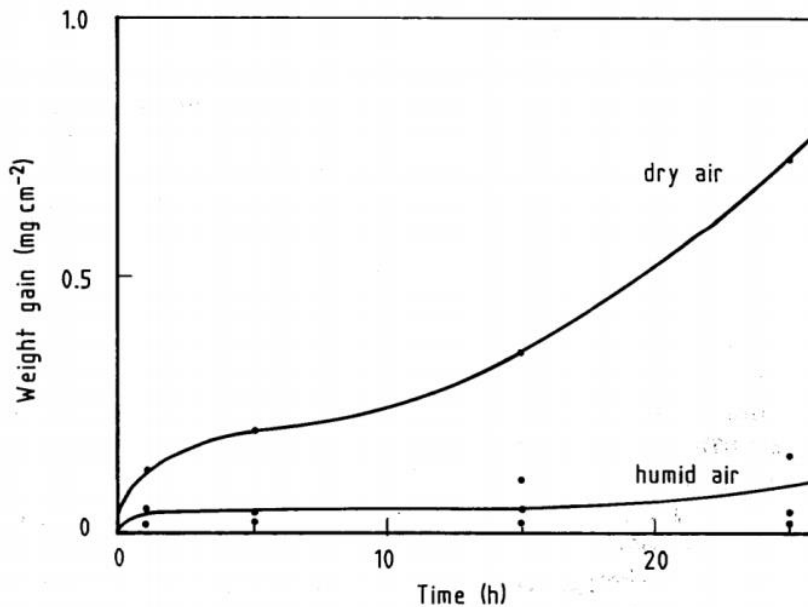


**Figure 2-22 The weight gain of the commercial pure aluminium under dry air and humid air [68].**

The morphology of the newly formed oxide layer on the top of the liquid aluminium is shown in Figure 2-23 (a) [69]. Figure 2-23 (b) shows a "nodule growth" which is formed by the solidified liquid metal penetrating through the rupture points in the crystalline oxide layer, after oxidation for 5h. Figure 2-23 (b) shows that the nodules grew in number and size with time, after 70h.

(a)

(b)

(c)
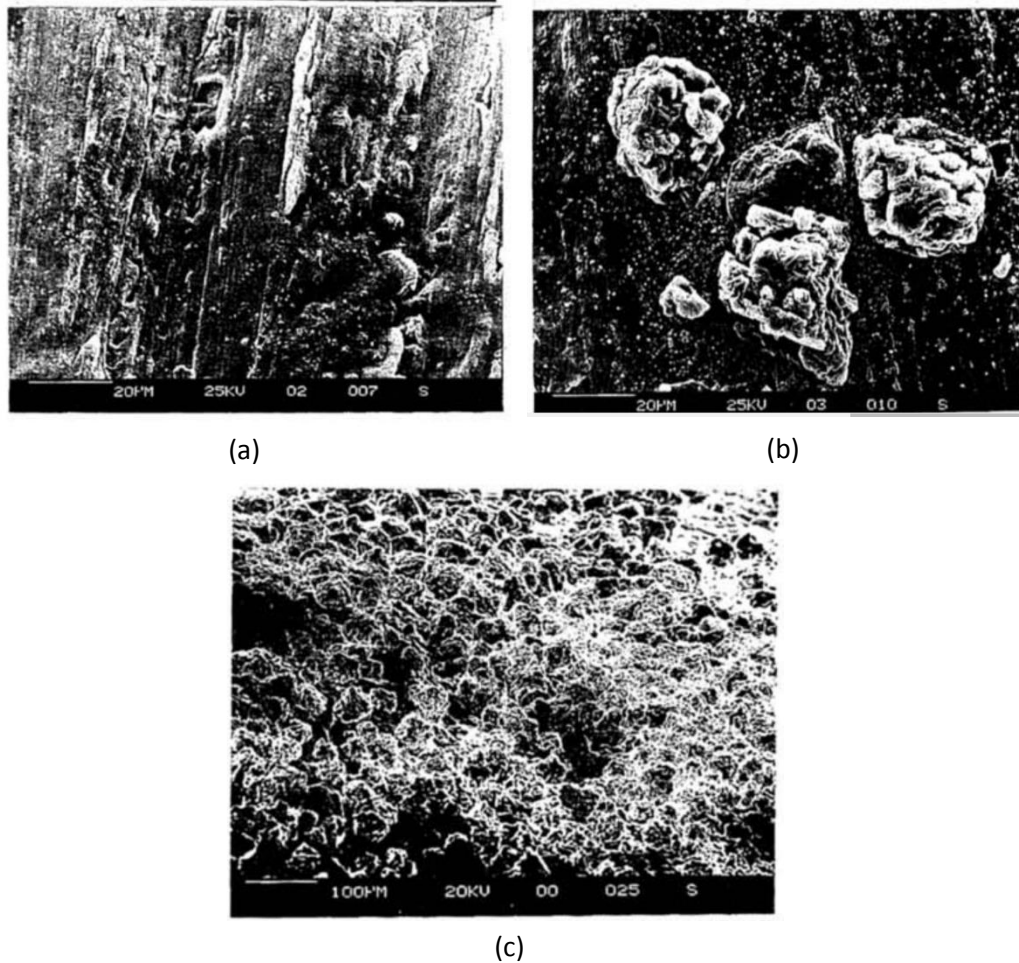
**Figure 2-23 The morphology of the oxide layer in CP-Al; (a) newly formed oxide, (b) the oxide formed by holding liquid aluminium for 5h and (c) the oxide formed by holding liquid metal for 70h.**

## 2.2.2 The effect of the addition of Mg into alloy

Mg is one of the most common additions in aluminium alloys, improving the strength by solution hardening and improving work hardening. However, it is also suggested that the addition of Mg changes the oxidation behaviour of the aluminium oxide and causes a loss of Mg in the aluminium melt[70].

Impey et. al.[69] investigated the behaviour of oxide in both commercial purity aluminium and Al-5Mg alloy, at 750 °C. The author suggested that the oxidation behaviour for both

alloys were similar but the addition of Mg accelerated the oxidation rate by 30 times, as shown in Figure 2-24.
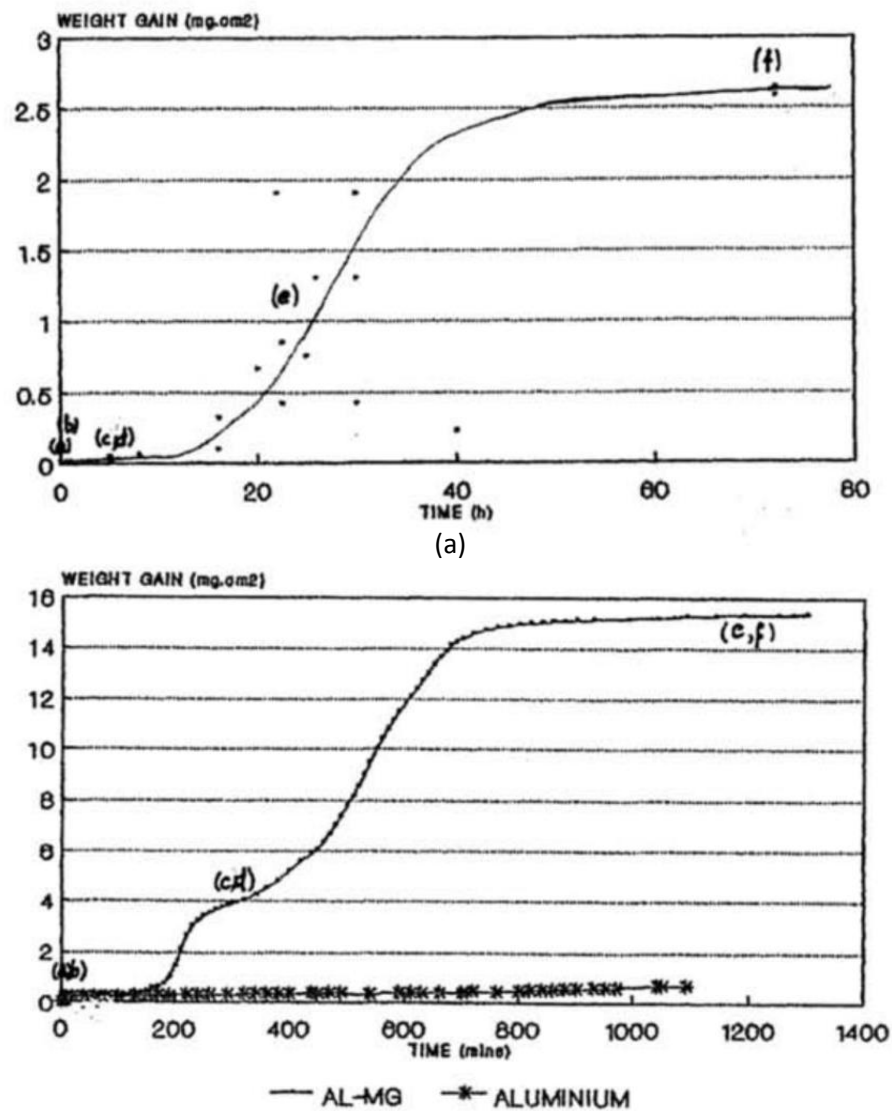


Figure 2-24 The weight gain of liquid (a) commercial pure aluminium and (b) Al-5Mg alloy with time at 750°C [69].

Silva and Talbot[71] suggested that the addition of different amounts of Mg into the aluminium melt resulted in a different oxide layer formed. Their thermodynamic calculations, at 725 °C, (shown in Figure 2-25), suggested that with a Mg content lower than

39

0.15 wt.%, $Al_2O_3$ is favoured. However, when the content of Mg was between 0.15 wt. % to

1.5 wt.% Mg, the most favoured reactant was spinel ($MgAl_2O_4$). For Mg content higher than

1.5 wt.%, MgO was formed preferentially.
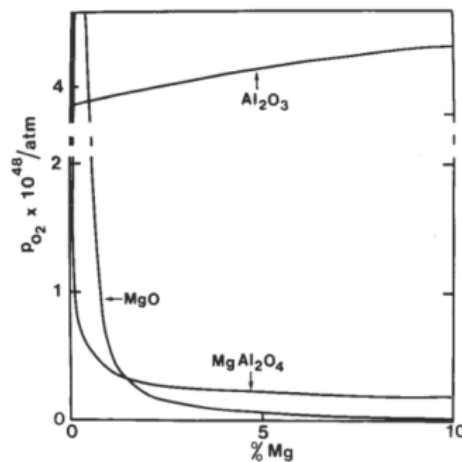


**Figure 2-25 The thermodynamic calculation of the favorited oxide formed in Al alloy with different Mg content at 725°C [69].**

However, many researchers suggested that the oxide layer on the Al-Mg melt is more than a

single oxide phase. $Al_2O_3$, $MgAl_2O_4$ and MgO could co-exist simultaneously under various Mg

contents (0.05%-10%) and temperature ranges (600 °C-1000°C) [72].

Like commercial purity aluminium, the Mg containing oxide also experienced a

transformation (amorphous structure to crystalline structure transition) which involved an

incubation time. However, the composition of this amorphous layer was not determined.

Belitskus [73] suggested that this oxide layer could be amorphous MgO (as only crystalline

MgO was detected by XRD after the incubation time). Impey [69], however, suggested that

this layer was an amorphous $Al_2O_3$ layer identical to that in the oxidation of pure aluminium.

The incubation time depended on the Mg content in the melt and its temperature.

Cochran[70] investigated the incubation time, for a crystalline oxide to form, for Al-1.8 wt.%

Mg alloy. It was found that this period was one hour at 800 °C, but prolonged by 30 times

when the temperature decreased to 660 °C. Belitskus[73] suggested that, at 750 °C, the incubation time was 5h for  Al-4.5Mg. The incubation time at this temperature could be further decreased to around 10 minutes in Al-10Mg[74].

The transformation of the amorphous oxide layer into a crystalline structure introduces volume changes and stresses into the oxide layer which can result in the rupture of the existing oxide and the formation of a new oxide phase. Field et  al. [75], and Impey et  al. [76] suggested that the rupture of the existing amorphous alumina layer in Al-Mg alloy allowed the formation of MgO according to Equation (24). Newly formed MgO then aggregated and formed nodule shapes, while at the same time smaller secondary MgO was formed, according to Equation (25). Spinel crystals were later formed when the Mg content in the melt was reduced, according to Equation (26).

$$Mg + 1/2O_2 \rightarrow MgO \qquad\qquad (24)$$

$$3Mg + Al_2O_3 \rightarrow 3MgO + 2\ Al \qquad\qquad (25)$$

$$MgO + 2Al + \frac{3}{2}O_2 = MgAl_2O_4 \qquad\qquad (26)$$
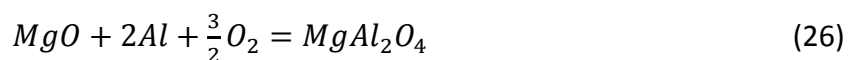
Belitsku [73] however, suggested that the original amorphous layer was MgO and it was then transformed into a crystalline structure until the Mg content in the melt was mostly depleted, whereupon the formation of spinel (MgAl$_2$O$_4$) became favoured.

Hanginoya and Fukusako [74] agreed that  MgO was initially formed, and suggested that the oxide was then transformed into a spinel structure according to Equation (26). The amount

of MgO was initially increased due to the initial oxidation but then gradually consumed by the transformation into MgAl$_2$O$_4$ (spinel). The amount of MgAl$_2$O$_4$ formed, however, increased continuously.

Impey[69] suggested that the spinel on the oxide layer might gradually grow into large particles at the oxide-metal interface, as shown in Figure 2-26. The large particles might introduce extra stresses into the existing oxide layer which caused rupture to become easier.
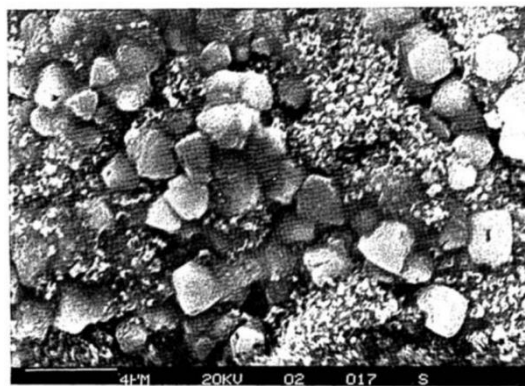


**Figure 2-26 The large granular shaped spinel particles growing on the oxide layer of Al-Mg alloy [69].**

Later, Salas[77] investigated the oxidation behaviour and mechanism of 3 wt. % Mg in commercial purity aluminium and the author explained the important role of microchannels and permeability within the oxide layer at different stages of oxidation behaviour. The author suggested that there could be three stages for oxidation. (1) The aluminium melt experienced a short but rapid oxidation in the initial period.  A layer of dense spinel was formed with MgO growing on the top. The author suggested that such a structure was not stable thermodynamically but its formation was feasible from kinetics point of view. It was suggested that, for a melt which contained both metal atoms A and B, the oxidation of the

metal will be as the follows: the AO will be formed on the side of $AB_2O_4$ if the diffusion rate followed Equation (27)

$$D_A > D_B > D_O \tag{27}$$

The author suggested that the formation of MgO satisfied the above description and the formation was due to the fast diffusion of the Mg ions compared with Al ions through the dense spinel layer. A sketch of the oxide layer formed during the initial incubation period is shown in Figure 2-27.
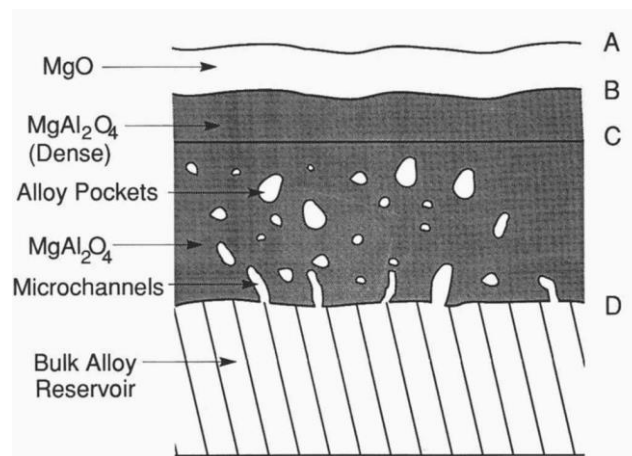


**Figure 2-27 The sketch of the oxide layer formed during the initial incubation period in Al-3Mg alloy metal melt [77].**

During this period, Mg might be evaporated as MgO, or the Mg penetrating through the dense spinel layer might react with oxygen in the atmosphere and form additional MgO (according to Equation (24)). Both the spinel layer and the MgO layer are thickened in this stage.

$$3MgO + 2Al = Al_2O_3 + 3Mg \tag{28}$$

$$4MgO + 2Al = MgAl_2O_4 + 3Mg \tag{29}$$
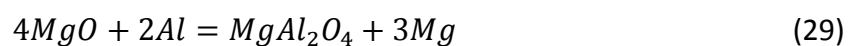
The author suggested that, after the initial stage, microchannels provide an effective way of transporting the liquid metal, as well as oxygen, to the interface between the liquid metal and the spinel layer, ( D in Figure 2-27), or the MgO and spinel layer, (B in Figure 2-27). A SEM image of the cross-section of the oxide and alloy is shown in Figure 2-28, which showed the presence of the microchannels.

The microchannels allow the continuous thickening of the existing spinel layer at point D of Figure 2-27. At point B, however, the liquid metal passing through the micro-channels reacts with MgO and forms either more spinel, (initially), or $Al_2O_3$ nodules, (while the concentration of the Mg content in the melt is decreased), according to Equation (28) or Equation (29). The MgO layer therefore is reduced in thickness.
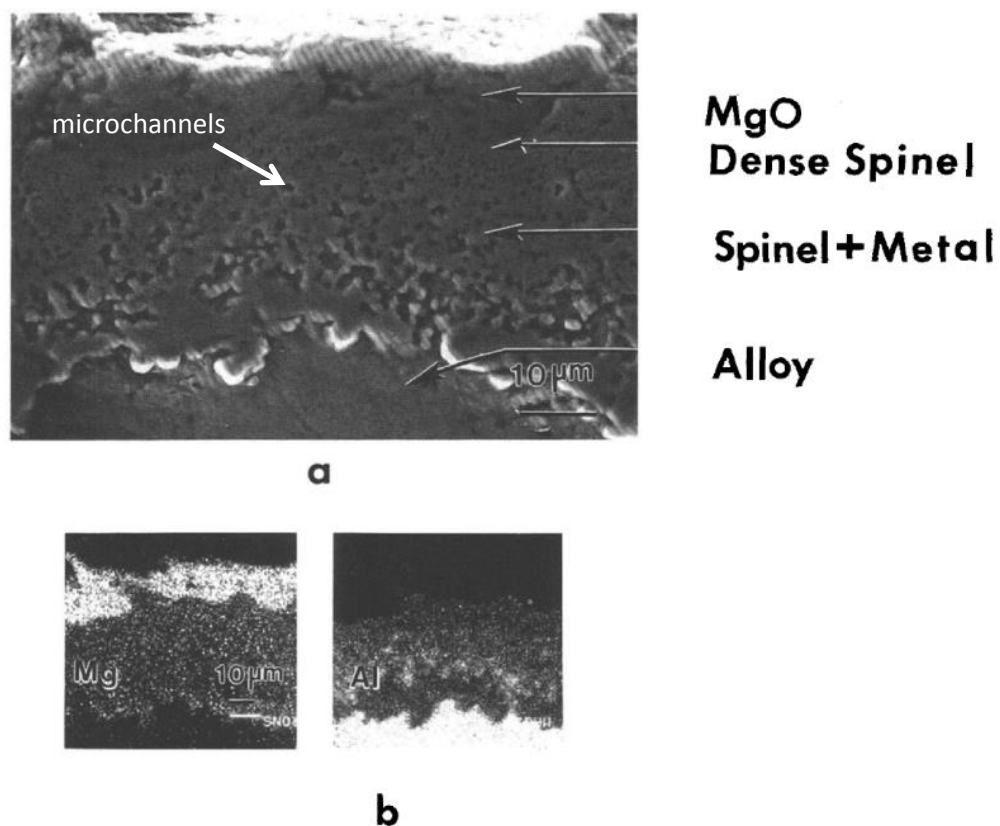


Figure 2-28 Cross-section of the oxidised Al-Mg alloy [77].
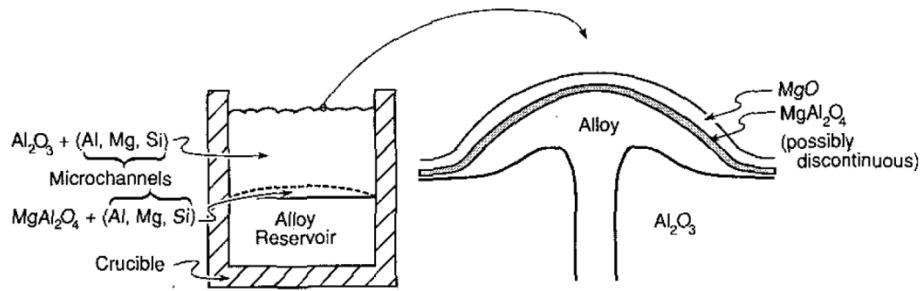
**Figure 2-29 The sketch of the third stage of oxidation of Al-Mg alloy as supposed by Salas [77].**

Third stage, bulk oxidation, is shown in Figure 2-29. A thin layer of MgO exists with a thin layer of $MgAl_2O_4$ underneath. The liquid metal is transported to the interface between the spinel layer and the $Al_2O_3$ particles through micro channels. The microchannels between the $Al_2O_3$ particles allow the liquid metal trapped between $MgAl_2O_4$ and $Al_2O_3$ to connect to the bulk liquid metal. At this stage, a continuous supply of evaporated or ionic Mg allows the maintenance of a thin MgO layer, though part of the MgO oxide layer might react and transform into the spinel layer. It is possible that both MgO and $MgAl_2O_4$ are partly dissolved by the liquid metal while the $Al_2O_3$ experiences the continuous growth.

Kim[78] used focused ion beam (FIB) milling, with a lift-out technique, to investigate the oxide layer in an Al-Mg alloy. The author observed that both MgO and $MgAl_2O_4$ occured on the cross-section of an Al-4%Mg alloy, oxidised at 750 °C [79]. However, the author observed that a thin layer of $Al_2O_3$ with a thickness of only 50nm existed between the aluminium matrix and the spinel layer (as shown in Figure 2-30). This aluminium oxide layer could come from the remaining part of the initial amorphous $Al_2O_3$ oxide layer, (as observed by Field and Impey), but not yet converted into MgO or $MgAl_2O_4$.
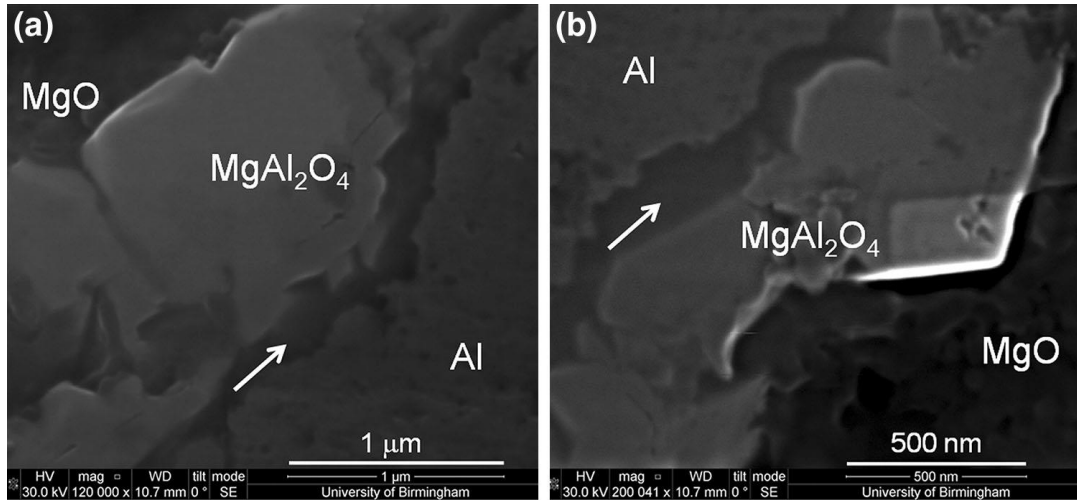
**Figure 2-30 The Al$_2$O$_3$ layer observed by KeeyHum between MgAl$_2$O$_4$ and aluminium matrix [78].**

The author further suggested that the reason for the formation of spinel[80] was that porous MgO which initially formed might provide a means for oxygen to penetrate; MgO might then react with liquid aluminium and oxygen according to Equation (30) and Equation (31) and form the spinel layer as shown in Figure 2-31.

$$MgO + 2Al + 3/2\ O_2\ \rightarrow MgAl_2O_4 \tag{30}$$

$$MgO + Al_2O_3 \rightarrow MgAl_2O_4 \tag{31}$$
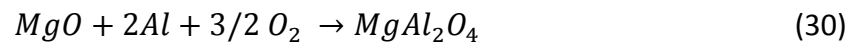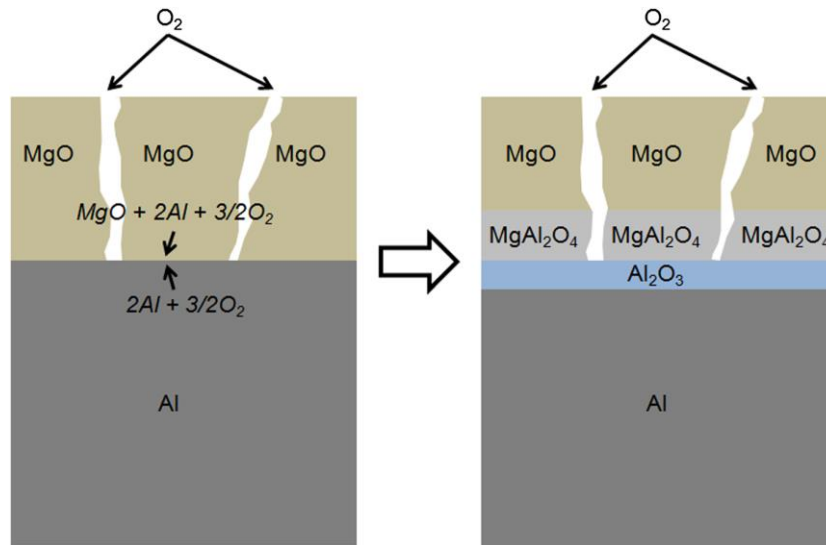
**Figure 2-31 The sketch of the formation of the oxide layer in Al-Mg alloy described by KeeyHum [80].**

## 2.3 The formation of aluminium nitride

According to the hypothesis of Nyahumwa et al. [27], the entrapped atmosphere might gradually be consumed by reacting with the surrounding liquid metal, when the majority of oxygen was consumed, the liquid might start to react with nitrogen in the entrapped atmosphere and thus forming the relevant nitride. This nitride might serve as a sealing point to the rupture of the oxide layer in the double oxide film defect and the formation of nitride might play an important role in reducing the size of double oxide film defects and deactivate their negative effect on mechanical properties.

Aluminium nitride can be formed by the reaction between liquid Al and nitrogen gas, by Equation (32). *In situ* formation of AlN in the aluminium melt to produce a reinforced metal matrix Composite (MMC) has proved to be feasible by bubbling nitrogen gas into the aluminium melt[81], or through a pressureless infiltration method[82, 83].

$$2Al + N_2 \rightarrow AlN \qquad\qquad (32)$$

Zheng et al.[81] claimed that aluminium nitride particles, of size less than 10μm, were successfully produced by a direct bubbling method as shown in Figure 2-32(a). Swaminathan [84] claimed that they have produced AlN uniformly inside the aluminium melt at up to 64 vol.% by the pressureless infiltration method, as shown in Figure 2-32 (b).



(a)                                           (b)
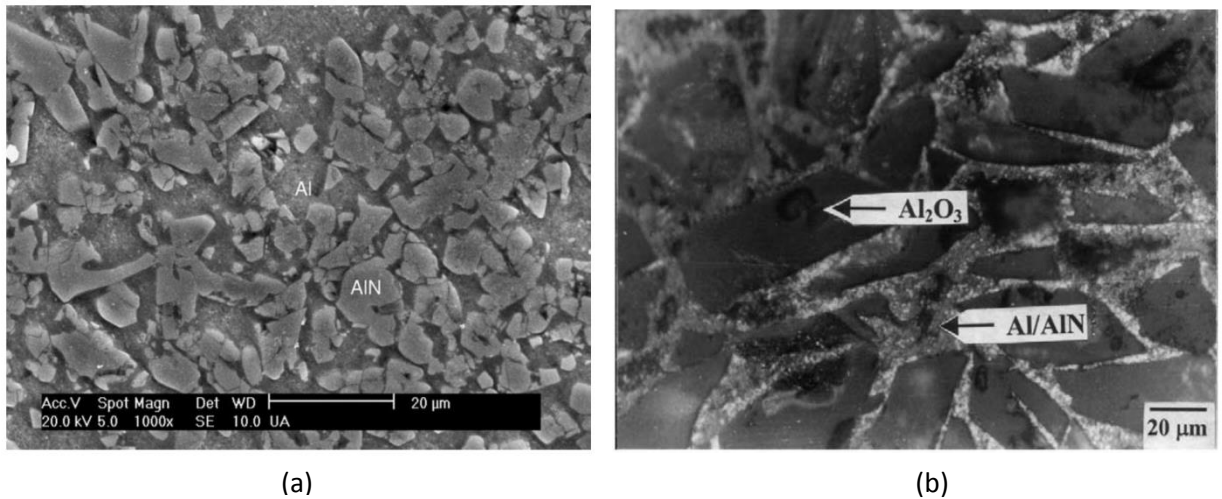
**Figure 2-32 The AlN formed in (a) direct bubbling method [81] and (b) pressur less infiltration method [82].**

### 2.3.1    The effect of O on the formation of AlN

The presence of oxygen has been reported to cause deleterious effects on the formation of AlN[82, 84-87]. Zheng et. al. [87] compared the effect of nitrogen bubbling between commercial purity nitrogen and high purity nitrogen, and suggested that AlN was only formed in the experiment when the partial pressure of the oxygen was low.

Swaminathan[84] further suggested that increasing the oxygen content to higher than 10 ppm would result in a decrease of the content of AlN particles from 64 vol. % to 6 vol. %.

Zheng et al.[87] realized that the explanation of this inhibiting effect of O was not feasible from a thermodynamic point of view, as suggested in Figure 2-33, an oxygen partial pressure of less than $10^{-25}$ was required for the formation of AlN, at 1073K. In the experiment, however, AlN was observed to be formed at a partial pressure of $10^{-6}$ Pa.
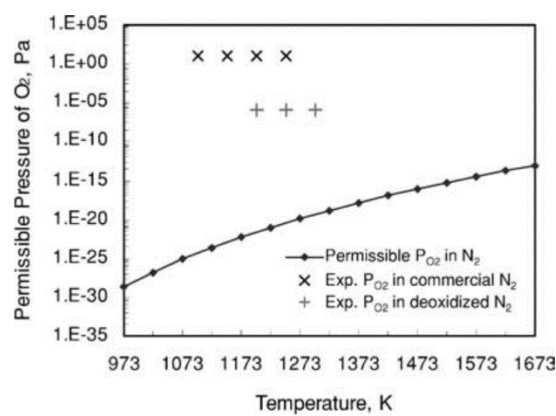


**Figure 2-33 Permeability of the oxygen partial pressure calculated by Zheng et.al. [87].**

The author then tried to explain this effect from a kinetic point of view. Four steps were proposed for the formation of AlN, as shown in Figure 2-34. In the first step, nitrogen molecules migrate towards the intersection area between gas and liquid metal (Equation (33)). In the second step, $N_2$ molecules dissociate into atoms and are chemisorbed at the liquid boundary (Equation (34)). In the third stage, the nitrogen atoms penetrate through the liquid boundary (Equation (35)) and, in the last step, the nitrogen atoms react with aluminium atoms and form AlN (Equation (36)).
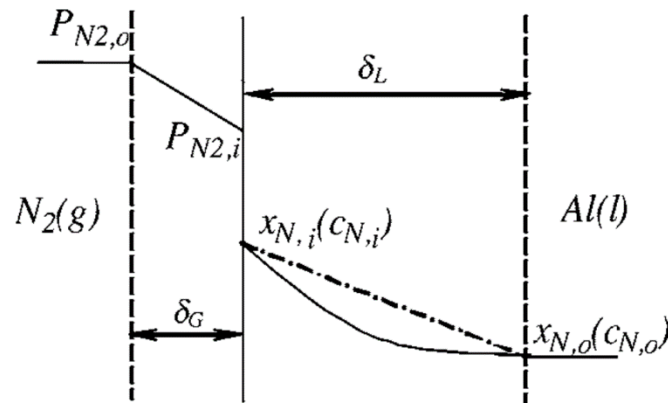
**Figure 2-34 The graph shows the penetration of the nitrogen through the gas-liquid boundary and react with Al melt in the formation of AlN [87].**

$$N_2(P_{N_2,o}) \rightarrow N_2(P_{N_2,i}) \tag{33}$$

$$N_2(g) \rightarrow 2N \; (chemisorbed) \tag{34}$$

$$N(x_{N,i}) \rightarrow N(x_{N,o}) \tag{35}$$

$$N(in \; Al \; melt) + Al(l) \rightarrow AlN(s) \tag{36}$$
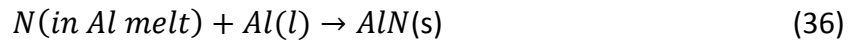
The author suggested that, during this process, stage 2 was supposed to be the slowest and reaction rate-determining step. It is also easily affected by oxygen impurities. This process is further explained in Figure 2-35. The nitrogen molecules, when passing through the gas boundary, might be di-polarised with one side and physisorbed by the liquid surface. This physical bonding might then transform into a chemical bond if sufficient energy is available to overcome the activation energy barrier to form AlN.
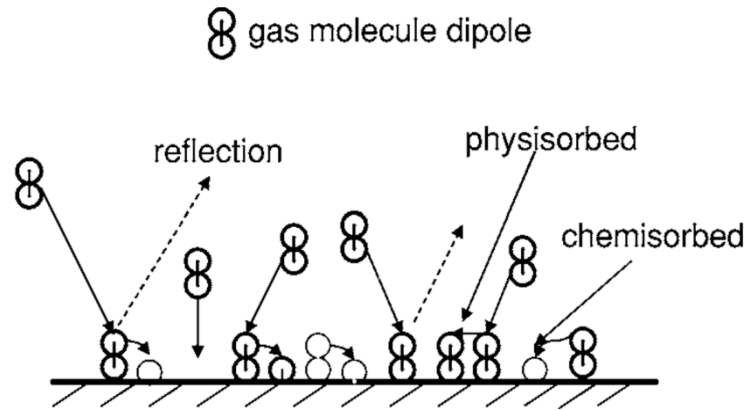
**Figure 2-35 The graph shows the chemisorption step in the formation of AlN proposed by Zheng et.al [87].**

If oxygen molecules were present in this process, the oxygen will compete with the molecular nitrogen and be chemisorbed by the surface instead, as shown in Equation (37). The change in the Gibbs Free Energy for the formation of AlN and $Al_2O_3$ are shown in Figure 2-36. As can be seen, the change of the physisorbed $N_2$(a) to the chemisorbed $N_2$(b) required the overcoming of an activation energy of $E_{ap}$ (308 kJmol$^{-1}$), where no such barrier existed for the chemisorption of oxygen(c).
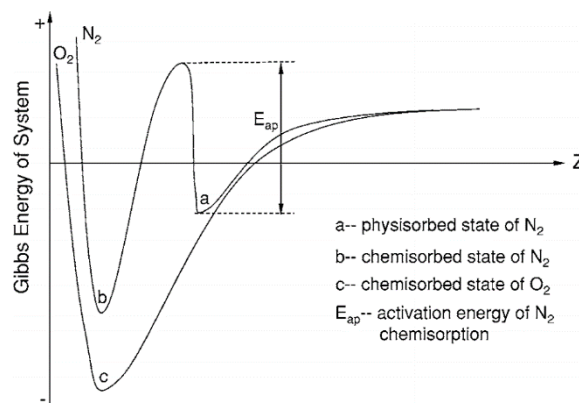


**Figure 2-36 The change in the Gibbs Free Energy for the physical and chemical absorption of oxygen and nitrogen in aluminium [87].**

$$2N + O_2(g) \rightarrow N_2 + 2O \qquad (37)$$

Swaminathan[84] further suggested that there were two rate determining oxygen levels during his infiltration experiment, producing Al-AlN MMC when high purity nitrogen was used. Below the lower boundary, a significant amount of AlN could be formed. When the oxygen content reached the lower boundary, the infiltration process could still proceed but the formation of AlN was reduced, (i.e. liquid metal came into contact with the nitrogen gas but little reactant was formed). However, when the oxygen content reached the higher limit, oxide particles were formed regardless of the nitrogen content in the gas. The author did not give the exact value for the above two oxygen contents but assumed that, by using a kinetic calculation, there existed a relationship as shown in Equation (38).

$$P \approx 2 * 10^4 f \qquad (38)$$

Where P is the partial pressure of oxygen and f is the O:Al ratio where the poisoning effect of oxygen on the nitridisation process will occur. The author took f to be $10^{-6}$ Pa, thus when the nitrogen atmosphere was 1 atm, the value of P was about 0.02 Pa.

### 2.3.2 Effect of Mg on the formation of AlN

Mg additions were suggested to affect the formation of AlN. Scholz[85] investigated the formation of AlN in an Al-Si-Mg alloy and suggested that the increase in the Mg content in the aluminium melt resulted in an increased amount of AlN being formed.

Hou[88] suggested that the Mg in the aluminium melt could act as a catalyst in the formation of AlN. Vaporised Mg in the aluminium melt will react with nitrogen gas to form $Mg_3N_2$, according to Equations (39-40). $Mg_3N_2$ will then be deposited and react with the Al melt to form AlN according to Equation (41). However, this assumption was questioned by

other researchers as no $Mg_3N_2$ phase was reported in an Al alloy melt [84]. It only existed in a Mg-Al alloy where $Mg_3N_2$ was detected in addition to AlN[89].

$$Mg(l) \rightarrow Mg(g) \tag{39}$$

$$3Mg + N_2 \rightarrow Mg_3N_2 \tag{40}$$

$$2Al(l) + Mg_3N_3(s) = 2AlN(s) + 3Mg(l) \tag{41}$$
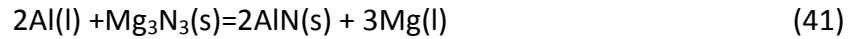
Some other researchers [84, 90, 91] suggested that the role of Mg in affecting the formation of AlN could be due to its effect on oxygen. Mg might react with oxygen in forming MgO or spinel and reduce the O content in the Al alloy and thus effectively improve the possibility of the formation of AlN .

### 2.3.3 Formation of AlN by other methods

Raeiszadeh[28] observed feather-like aluminium nitride (as shown in Figure 2-37) when trying to investigate the reaction rate between an air gas bubble and an aluminium melt. He used a sialon rod to trap a bubble of gas inside liquid aluminium and suggested that after about 2h, the aluminium nitride was formed. However, the author also suggested, based on Auger spectroscopy, that at the time N was detected in the reactant, an O peak was seen as well, which suggested that the $N_2$ started to be consumed while the $O_2$ content is not completely depleted.
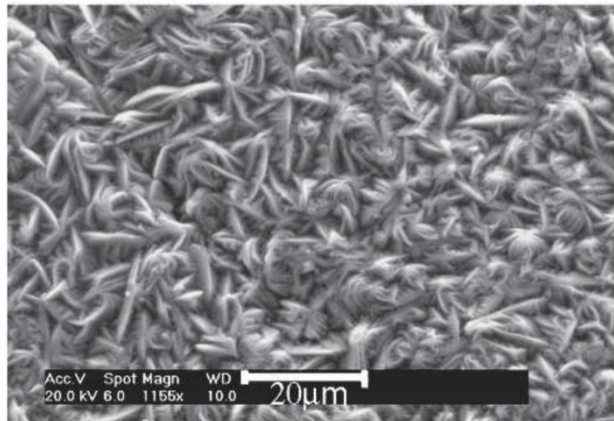
**Figure 2-37 The AlN found by Rahzadeh by a bubble trapping method [28].**

A similar result was also obtained by El-Sayed et al.[92] who used a Pore Gas Analyser (PGA) to identify the composition of the gas bubble after reacting with an aluminium melt for a period of time. The author observed aluminium nitride in the reactant and his plot from the Pore Gas Analyser suggested a detectable amount of oxygen when the nitrogen content in the gas bubble was in the process of being consumed (as shown in Figure 2-38).
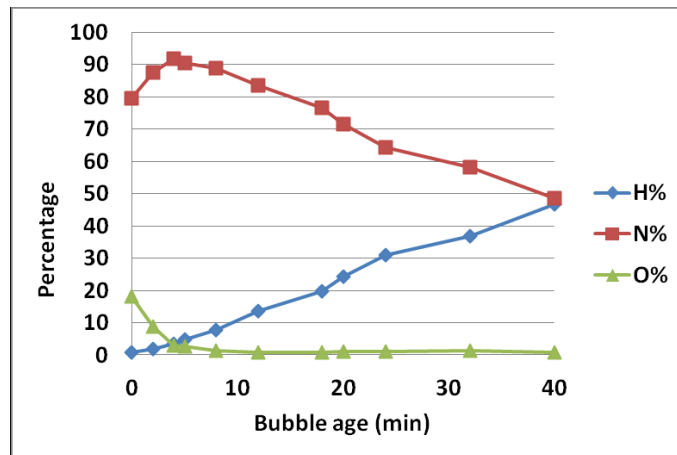
(a)
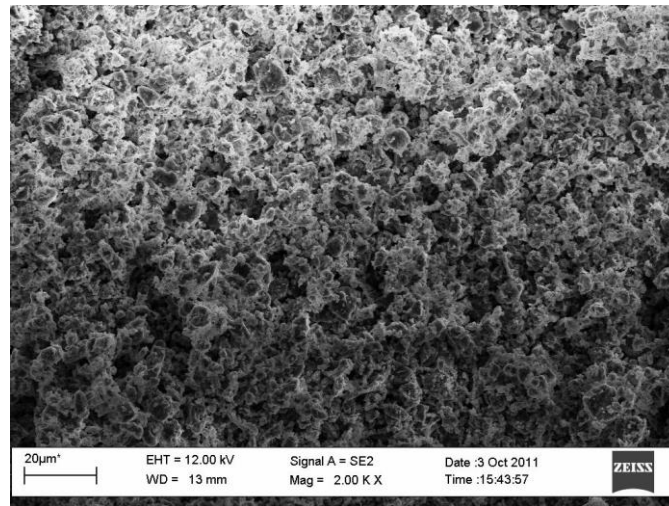


(b)

**Figure 2-38 (a) The result from the Pore Gas Analyser showing the consumption of first oxygen and then nitrogen inside the air bubble which was deliberately introduced into the melt.(b) The SEM image showing the aluminium nitride found by the author [92].**

## 2.4 The modification of Al-Si alloy

The modification of Al-Si refers to the flake-to-fibre transition of the Si phase, which improves mechanical properties, especially the %Elongation of the alloy. First introduced by Aldar [93] , who accidently introduced NaF into an Al-Si melt, the addition of Na to modifiy the Si phase of Al-Si alloys has become a commonly used technique.

Various elements are reported to have a modification effect on Si, among which Sr and Na are the most commonly used [94-97], Sb, Ba, Ca and some other rare earth elements [98, 99] are also reported to have a similar effect on Si. For the commonly used modifers, Sr is most stable, but it is well known for the production of gas porosity. Na modification is less sensitive to cooling rate during casting and there is no incubation time needed for the Na addition. However, Na evaporates and there is a risk of detrimental over modification which coarsening the eutectic Si phase.
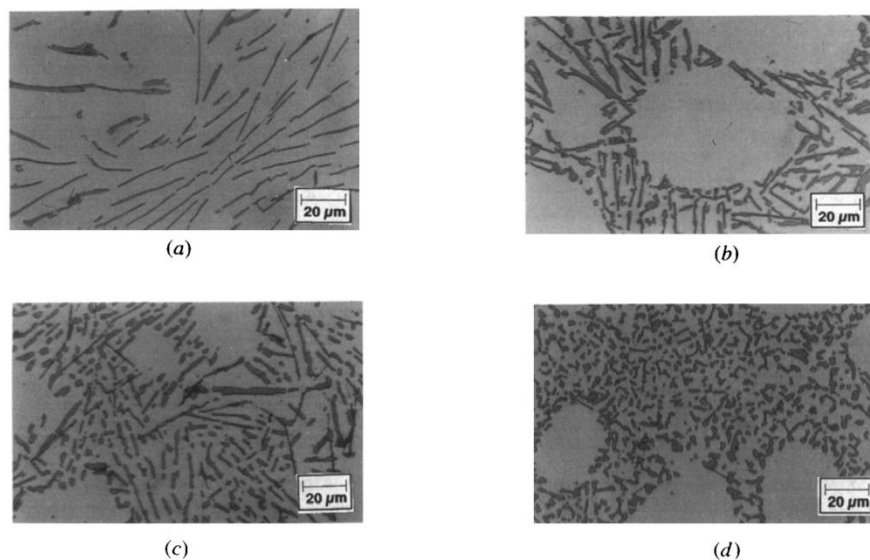


**Figure 2-39 (a) Al-10Si alloy; (b)Al-7Si alloy; (c) Na modified Al-7Si alloy and (d) Sr modified Al-7Si alloy[95].**

Lu et al. [100], suggested that the twinning density in Na modified Al-Si alloy is much higher than that in unmodified alloy. The author suggested a model called Impurity Induced Twinning to explain the high twinning defect density of the alloy and the modification mechanism. In this model, Si initially grew by extending its multiple layers through the step motion direction shown in Figure 1-41. Modifier atoms (determined by the author with the ratio r(modifier):r(silicon)= 1.646) are adsorbed at the interface of the advancing solid,

which blocks the continuous growth of the Si phase. However, the author suggested that the interface undercooling is high which resulted in the change of the growing direction as shown in Figure 1-41 which provides the conditions for twining of Si.

The author further stated a possible process for the twinning to occur. When a deactivated step was later reactivated, the modification atom might lead the Si atoms to miss their original position and fall on the next available vacancy, as shown in Figure 2-41. This process creates twinning.
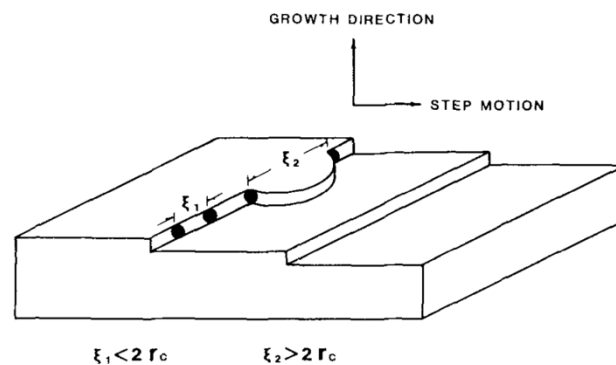


**Figure 2-40 Model showing the sketch of Impurity Induced Twining [100].**



**Figure 2-41 The formation of a twining of Si.**

Campbell [34] suggested that the addition of a modifier into an Al-Si alloy deactivated the possible nuclei of the Si phase, which are two, AlP and the wetted side of an oxide film defect. In this case, eutectic Si is forced to nucleate at a later stage at a lower temperature and restricted spacing (due to the increased solidification). The Si phase will need to re-orientate its growth direction constantly so that it will not be in contact with or collision with a solidifying dendrite or another Si precipitated.

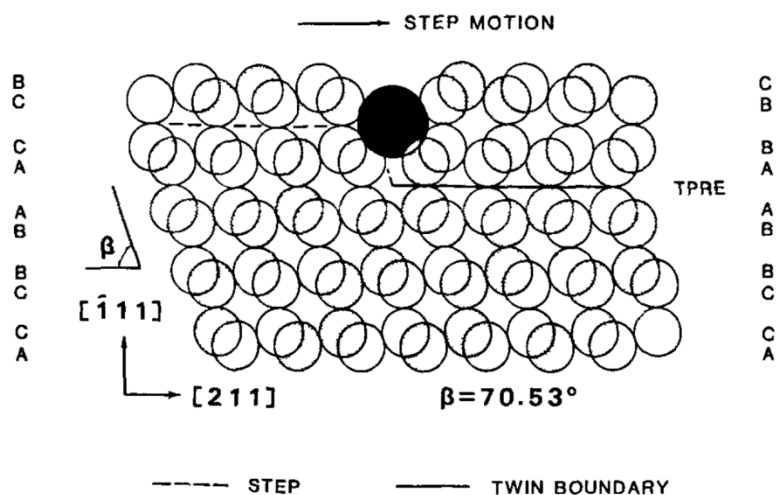The addition of Sr and Na in Al-Si alloys are often associated with an increase in the porosity of castings. The increase in the porosity number was initially attributed to an increase in hydrogen content in the melt with the addition of modifiers[101, 102]. However, Shahani [103] did not detect a change of the hydrogen content with Sr addition. Those controversial results might suggest that the addition of modifier does not have a direct relationship with hydrogen content in the aluminium melt. It is suggested that the process of modifier addition, which involves the continuous breaking of the oxide surface of the aluminium melt by stirring, thus removing the barrier for H absorption into the melt, might increase the hydrogen content of the castings.

Some researchers suggested that the addition of modifiers into Al-Si alloys affected the feedability of the alloy and thus promoted the formation of shrinkage porosity. Fuoco et.al. [104, 105] suggested that the addition of Sr reduce the fluidity of the liquid metal by the experiment shown in Figure 2-42. The liquid aluminium silicon alloy was poured in a sand mould, with one end sealed by a piece of stainless steel. The steel was removed when the fraction solid reached a certain extent. As can be seen, a good fluidity can be seen up to 55% solid when no modifiers were added. However, when modifiers were added, no mobility can be seen at 55% solid fraction during the solidification.
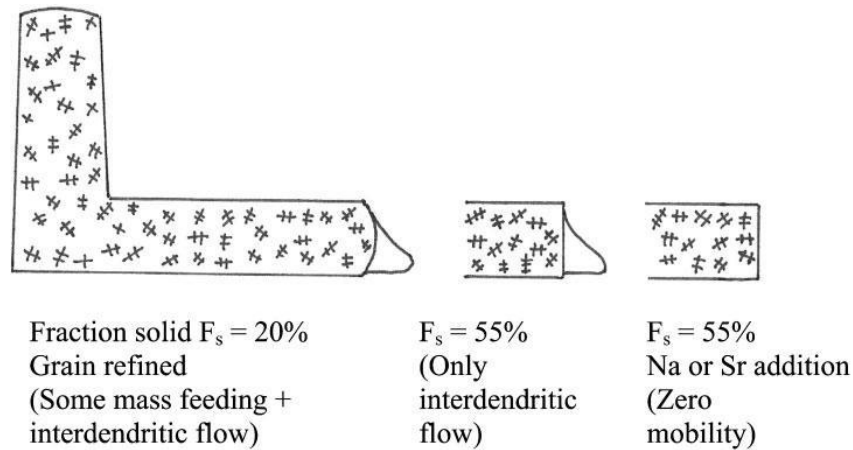
**Figure 2-42 Result from Fouco et. al showing the effect of modifiers on restricting the mobility of the liquid metal [104].**
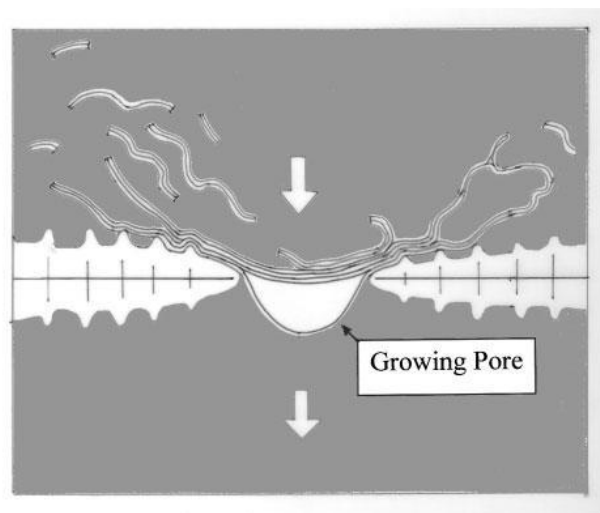


**Figure 2-43 The sketch showing the oxide film defect as an inter-dendritic barrier during the solidification and the formation of shrinkage porosity [34].**

Campbell[34] suggested that the reduced feedability can be attributed to an increased amount of oxide film defects in the casting with modifier additions. These oxides can serve as a barrier to interdendritic growth during solidification. As shown in Figure 2-43, tangled oxide film defects might become suspended between the α-aluminium dendrites. During solidification, the volume deceased locally cannot be compensated for by the surrounding liquid due to the existence of this barrier. The volume decrease was, on the other hand,

compensated by the expansion of the oxide film defect due to the local hydrostatic pressure. The expanded oxide film defect might then become a shrinkage pore after solidification.

Researchers also suggested that the addition of modifiers might change the oxidation behaviour of the liquid aluminium-silicon alloy. Iwahori[106] suggested that the formation of Sr related oxide on an Al-Si alloy. Emadi et al.[107] suggested that the oxidation rate was increased by 3 times when Sr was added. Jacob et.al.[108] suggested that the oxide in a Sr modified Al-Si alloy is thick and inhomogeneous. In an area containing Sr-related oxide, it could be as thick as 500 μm. However, such changed oxidization was not observed by Lee[109], who used an x-ray temperature gradient stage to *in situ* observe the formation of porosity in Sr modified Al-Si alloy. The author suggested that no Sr-containing oxide was observed.

## 2.5   The addition of elements into Al

Aluminium alloys are classified as wrought or cast. Each category was divided into several series.  The series and the main compositions for cast alloys and wrought alloys are shown in Table 2-2 and Table 2-3[110].

**Table 2-2 the table showing the series of cast Al alloy and its main elements addition [110].**

| Series | Main alloying elements |
|--------|------------------------|
| 1xx.x  | Al>=99.0%              |
| 2xx.x  | Cu                     |
| 3xx.x  | Si; with Cu or Mg addition |
| 4xx.x  | Si                     |
| 5xx.x  | Mg                     |
| 7xx.x  | Zn                     |
| 8xx.x  | Tn                     |
| 9xx.x  | other elements         |

**Table 2-3 the table showing the series of wrought Al alloys and their main elements addition [110].**

| Series | Main alloying elements |
|--------|------------------------|
| 1xxxx  | Al>=99.0%              |
| 2xxxx  | Cu                     |
| 3xxxx  | Mn                     |
| 4xxxx  | Si                     |
| 5xxxx  | Mg                     |
| 6xxxx  | Mg and Si              |
| 7xxxx  | Zn                     |
| 8xxxx  | other elements         |
| 9xxxx  | unused                 |

Effect of Si

Silicon is one of the common alloying elements in aluminium alloy. The addition of silicon lowers the solidification temperature and improves its fluidity and castability. The primary and eutectic Si phase is usually brittle, which might have a negative effect on mechanical properties of Al alloys, and decrease machinability. In this case, the modification of Si is needed, as discussed in previous section. The addition of Mg in addition to Si makes the alloy heat-treatable by forming the $MgSi_2$ strengthening phase [111, 112]

Effect of Cu

Cu is usually added into aluminium at around 2-10 wt.%. The addition of Cu improves the strength by precipitation hardening $Al_2Cu$, or $Al_2CuMg$, if Mg is present. The addition of Mg together with Cu further improved its strength [110, 113, 114]. However, Cu in Al might precipitate in the grain boundaries and lead to poor corrosion behaviour[115, 116].

The effect of Mn

The addition of Mn in Al improves strength by the precipitate of $Al_6Mn$. Nam and Lee[117] suggested that an addition of Mn greater than 0.5 wt.%, improved the UTS significantly. It was also reported that the addition of Mn had an effect on modifying the detrimental plate-like $\alpha\text{-}Al_5FeSi$ phase into a less harmful $\pi\text{-}Al_{15}(MnFe)_3Si_2$, thus improving mechanical properties in Fe containing Al-Si alloys[118-120].

The effect of Mg

Mg is a common addition into Al in the range of ~0.1% to ~13%. Al-Mg alloys are non-heat-treatable and their strength is derived from solid solution strengthening. The corrosion resistance of Al-Mg alloy is also improved compared to the alloy without addition of Mg[110, 121].

The effect of Zn

Zn is usually added into Al with Mg, Si and Cu to strengthen the material by precipitaion hardening. However, research suggests that increasing Zn content can lead to a reduction in electrochemical properties[111].

In addition to these main alloying additions, there are also some minority addition elements, added in a smaller amount or present as impurities.

Effect of Mo

Mo has a limited solubility in Al at both room temperature and casting temperatures (around 700 °C-850 °C). Mo is not widely used as an addition into Al but there are some applications. Bourkhina[122] suggested that the addition of 0.3 wt.% Mo and /or Co would result in a change in shape of Fe-containing phases into a compact Fe-Mo-Co phase and reduce the detrimental effects of the Fe containing phases. Kawahara[123] suggested that with a Mo addition of between 0.05 wt.% to 0.3 wt.% there will be a reduction in the oxidation rate of an solid Al-Mg alloy. A patent from Sumitomo Aluminium Smelting Co.[124] suggested that the addition of Mo between 0.05 wt.%-2 wt.% would improve the heat-resistance of an Al-Si-Cu-Mg alloy.

Effect of Sc

Ahmad[125] suggested that the addition of 0.2 wt.%~0.6 wt.% Sc would significantly improve the strength of pure Al or Al-Mg alloy by solution hardening and precipitation of fine scale $Al_3Sc$ particles. The author also suggested that the addition of Sc increases recrystallization temperatures of aluminium alloys up to greater than 600 °C which is much higher than the normal heat-treatment temperature. Tack[126] suggested that the addition of Sc together with Zr will result in improvement in the strength of the aluminium alloy by promoting the precipitation of thermostable $Al_3Zr_xSc_{1-x}$ particles.

Effect of W

W is also not a common addition into aluminium. However, there are reports showing that the addition of W improved the corrosion behaviour of the alloy[127]. W or WC particles are

also reported to be added into Al as a reinforced phase in Al-based metal matrix composites. Considerable improvements in strength and hardness for these metal matrix composite were reported[128, 129].

## 2.6 Grain refinement of Al and Al-Si alloys

Grain size is an important feature of alloys. It is recognised that smaller sized, equaxied grain structures will result in improved UTS and better fatigue performance[130]. Decreased grain size will allow an increase in the number of grains and thus increased number of grain boundaries in a unit volume of a casting. These grain boundaries can slow down the movement of dislocations and the crack formation process.

The addition of an inoculant is an effective way to decrease the grain size. McCartney[131] suggested that the addition of an inoculant can change the columnar or twinned columnar grain structure into a fine equiaxed structure, as shown in Figure 2-44. The most common inoculant is an Al-Ti-B master alloy, (5%Ti, 1%B).
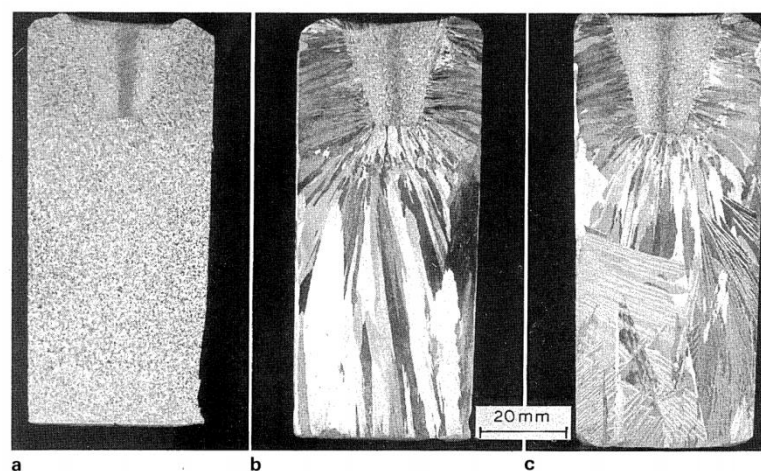


**Figure 2-44 the grain structure of commercial pure aluminium showed (a) a equiaxed fine structure with the grain refiner addition; (b) the columnar grain structure in the casting without grain refiner addition and (c) twinned columnar grain structure in the casting without grain refiner addition [130].**

Several theories have been put forward to explain the mechanism of grain refinement. An early theory suggested that the presence of $Ti_2B$ or $AlB_2$ would lead to nucleation as their lattice parameters vary little compared with that of $\alpha$-Al[132]. However, later results suggested that $TiB_2$ or $AlB_2$ alone might not make an effective nucleant[133, 134]. The orientation relationship between $TiB_2$ or $AlB_2$ and Al was not determined. It was also confirmed that the grain refinement effect will not occur for $TiB_2$ or $AlB_2$ if no excess Ti was in solution. $TiB_2$ was, on the other hand, pushed to the grain boundaries in these cases[135].

It was later suggested that $Al_3Ti$ could be a better nucleation site[136, 137]. It was observed located in the central part of the grains and its orientation relationship with the Al matrix is well known. However, in the Al-Ti phase diagram, $Al_3Ti$ is not a stable phase at the hypoperitectic concentration of Ti (i.e. <0.15 wt.% of Ti addition, as show in Figure 2-45). The normal Ti addition rate in Al alloy for the grain refinement purpose will not usually exceed this amount. It was then suggested that the presence of B in the aluminium melt might lead to a change in the peritectic reaction point to a lower concentration (around 0.05 wt.% Ti), which stabilized $Al_3Ti$[138]. Other researchers pointed out that solidification was occuring under non-equilibrium conditions due to Ti segregation, which would leave part of the $Al_3Ti$ particles undissolved and available for the nucleation of the Al grains. However there is no strong evidence to support these opinions[139].
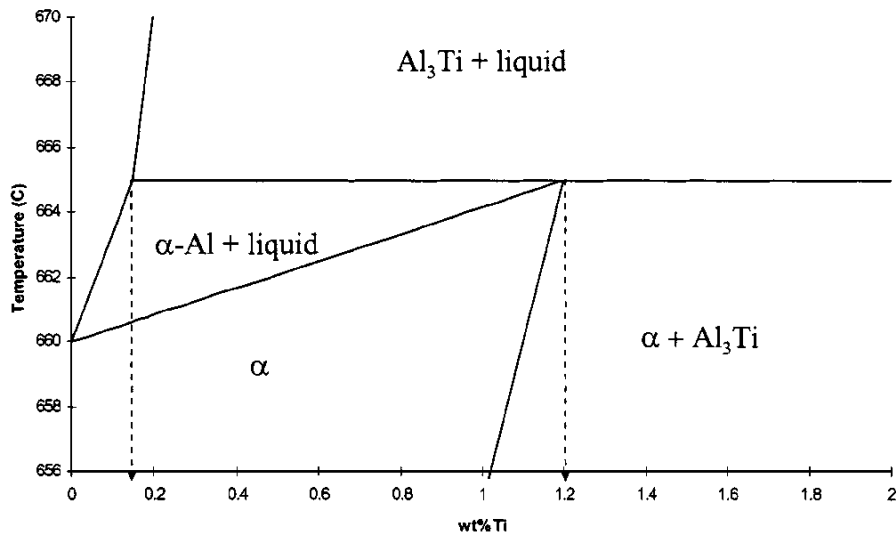
**Figure 2-45 The phase diagram for Al-Ti alloy with the Ti concentration between 0-2%[136].**

Mohanty et al.[140] and Schumacher et al.[141] suggested that nucleation could be more complicated and involve duplex particles. They suggested that $TiB_2$ could be the original nucleation site where excess Ti will segregate and form a layer of $Al_3Ti$ on the $TiB_2$ particle. The $TiB_2$ would stabilize the $Al_3Ti$ phase and α-Al grains are then able to nucleate on the $Al_3Ti$.

The development of the theory of the growth restriction factor Q further explains the effect of solute on grain refinement [137, 142-144]. This theory quantifies the effect of solute elements in the grain refining process. Nucleants still play an important role including $TiB_2$, $Al_3Ti$, and duplex particles as mentioned above, or any other particles in the aluminium melt ( e.g. $(Al_x, Ti_{1-x})B_2$). However, these nucleation points require a certain degree of undercooling for nucleation to be activated. The presence of solute elements, such as Ti, plays two roles in the solidification process. The solute elements might segregate to the liquid-solid interface and inhibit the growth of the solidification front. This provides time for nucleation and growth of other grains. The second role is that segregated elements at the

solidification front will form a constitutional undercooling zone. This will be the driving force to activate nucleation by particles in the undercooled zone. The ability of the melt to inhibit grain growth and the undercooling they provide is expressed as the growth restriction factor, Q [145]:

$$Q = m(k-1)c_0 \tag{42}$$

Where:

m is the slope of the liquidus line;

k = $C_s/C_L$ at the solidification front;

$C_o$ is the concentration of the solute element.

Greer et al[146] suggested that, for a Si-containing Al alloy, a high Q value is not always associated with a decrease in the grain size. The authors investigated the result of the grain refinement effect in several Al-Si alloys [143] and suggested that the grain size was decreased initially, but then increased, after a Q value higher than about 20 (as shown in Figure 2-46). The author then suggested that there was a poisoning effect by Ti, with a Si content higher than 3 wt.%. Easton et al. [145] suggested that Si has the same role as a segregating element as Ti, which is why $TiB_2$ can serve as an effective nucleant in an Al-Si alloy without excess Ti. However, there is a limiting effect of the segregating elements, beyond which no further grain refinement effect will occur. The author attributed this to different Al dendrite growth mechanisms with different Grain Restriction Factors. While the Q value is low, the solute elements at the tip of the solidification front will reduce its growth rate. However, when the Q value becomes high, the growth of the solidification front will

reject solute elements into the melt in the direction normal to the solidification front and thus growth will not be affected.

On the other hand, a high concentration of solute segregating elements might have an adverse effect, which causes an increase in the grain size, as shown in Figure 2-46. However, this effect was not observed in every alloy system, for Al-Zn or Al-Cu systems, such an effect will not happen. When excess solute elements were added, the grain size will not be affected.
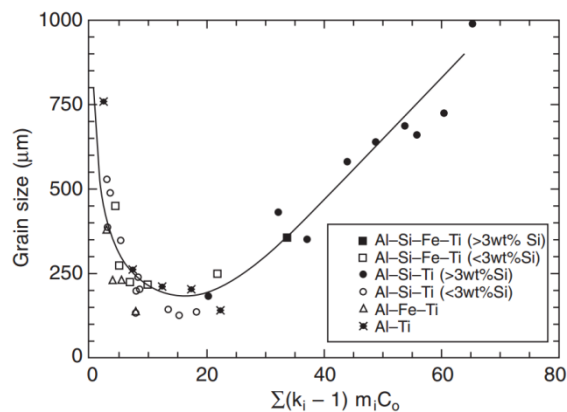


**Figure 2-46 The change in grain size with the change of growth restriction factor in several Al alloys [145].**

In addition to TiB$_2$, it is also suggested that the addition of 0.3 wt.% Mo[110, 147], Nb, Zr [148] and small amount of Chromium[149] will have a grain refinement effect in pure aluminium. Nowak et al. [150]suggested that a Nb-B masteralloy could be an ideal grain refiner for Al-Si alloys. Some researchers also indicated that in addition to these elements, the Al and Mg related oxides, namely alumina, spinel or MgO, might also be nucleation sites for Al grains [80, 151].

## 2.7  Summary

In this work, a detailed survey of the formation of the double oxide film defect, the evidence for its formation, the characterization method with the use of Weibll distributions and methods for minimising the formation of this defect has been conducted. The hypothesis is proposed that consumption of the oxygen and nitrogen in a double oxide film defect, will reduce its size. In order to further understand this, a literature survey about the oxidation and nitridisation process of the liquid aluminium has been conducted.

The literature survey about the effect of different element additions on the double oxide film defect and Al alloy castings has also been conducted, which includes the Si modifiers, grain refiners, and other non-commonly used transition elements.

# Chapter 3   Experimental Procedure

## 3.1   Materials

Three alloys were used, commercial purity aluminium (LMO), 2L99 (Al-7Si-0.3Mg) and Al-5Mg alloy. The compositions of the three alloys are shown in Table 3-1. The Al-5Mg alloy was prepared by adding 5 wt.% CP-Mg into commercial purity aluminium.

Table 3-1 The composition of different alloys used.

|  | Element | Cu | Mg | Si | Fe | Mn | Ni | Zn | Pb | Sn | Ti | Al |
|---|---|---|---|---|---|---|---|---|---|---|---|---|
| | Pure Aluminium | 0.01 | 0.01 | 0.1 | 0.1 | 0.01 | 0.01 | 0.01 | 0.01 | 0.01 | 0.02 | Bal. |
| wt.% | 2L99 | 0.01 | 0.38 | 7.04 | 0.09 | 0.01 | 0.01 | 0.00 | 0.00 | 0.01 | 0.11 | Bal. |
| | Al-5Mg | 0.01 | 5.00 | 0.11 | 0.1 | 0.01 | 0.01 | 0.01 | 0.01 | 0.02 | 0.02 | Bal. |

## 3.2   The experiment with an entrapped air bubble inside the aluminium melt

In this experiment, 750g aluminium was melted in a 45 kW induction furnace before being transferred to a 4 kW cylindrical resistance furnace and held at 725 °C. A steel rod with a 13mm dia., 40mm deep blind hole at one end was placed above the aluminium melt, which heated up the gas in the blind hole to 300 °C (measured by a thermocouple), before being gradually plunged into the aluminium melt. The steel rod was then placed at a depth of 85mm inside the melt. During the plunging process, an oxide layer might become attached to the side of the steel rod, which would connect the entrapped air bubble to the outside atmosphere. To solve this problem, the steel rod was made to rotate at 90 rpm during the plunging process and, after the steel rod was in the correct position inside the aluminium melt, a 6mm steel rod was inserted into the aluminium melt, touching the rotating steel rod at the side, to break the leak path manually.
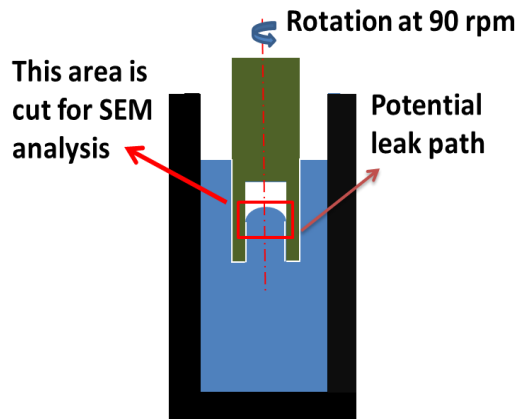
**Figure 3-1 The sketch of the experiment setup for bubble trapping experiment.**

The air bubble was held for 1h before the furnace was switched off and the metal allowed to solidify within the furnace (over 20min). As shown in Figure 3-1, the red circled area was cut off for SEM analysis after the solidification and the height of the liquid metal inside the blind hole was measured.

5 elements, Ti, Zr, Hf, Sc and Mo were selected and added into the aluminium melt (with an addition rate of 0.4 wt.%). Ti, Zr and Sc were added in the form of Al-10Ti/Al-10Zr/Al-2Sc waffle plate that was purchased. Hf and Mo were added in the form to Al-5Hf/Al-10Mo master alloy ingot pre-prepared by adding 50g Hf/100g Mo into 950g/900g CPAl at 1300 °C for 40min.

The element additions to the aluminium melt might change the morphology or composition of the oxide layer, which might affect the consumption rate of the entrapped atmosphere. From this the effect of changes in melt composition on a bifilm defect and on mechanical properties of the castings might be determined. The elements selected were all added to the 3 different alloys (CPAl, 2L99 and Al-5Mg).

## 3.3   Testbar casting experiment

### 3.3.1   Sand Mould preparation

The test bar castings in this work were all made in sand casting. A sketch of the mould is shown in Figure 3-2. For the castings with reduced bi-film defect content, the mould shown in Figure 3-3 was used. The sand moulds were made 2 weeks before casting, to allow the resin inside the sand mould to reduce its H content, to minimise H pick-up by the liquid metal poured into the mould. Two types of resin, 5112 and 5230 (each with 0.6 wt.% addition) were used for the the sand moulds.
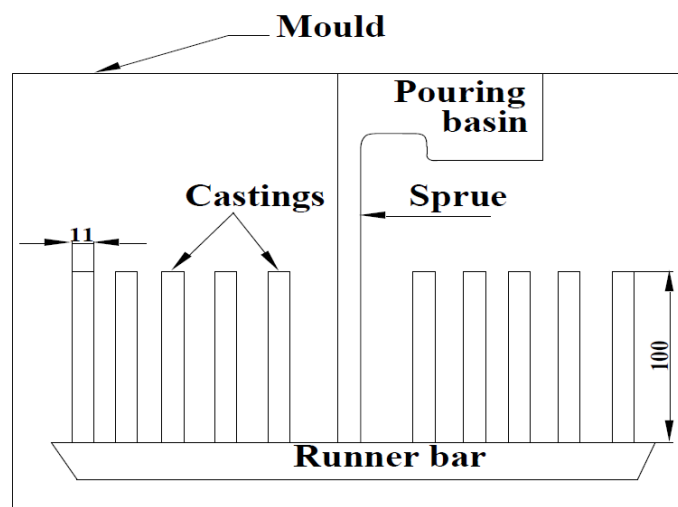

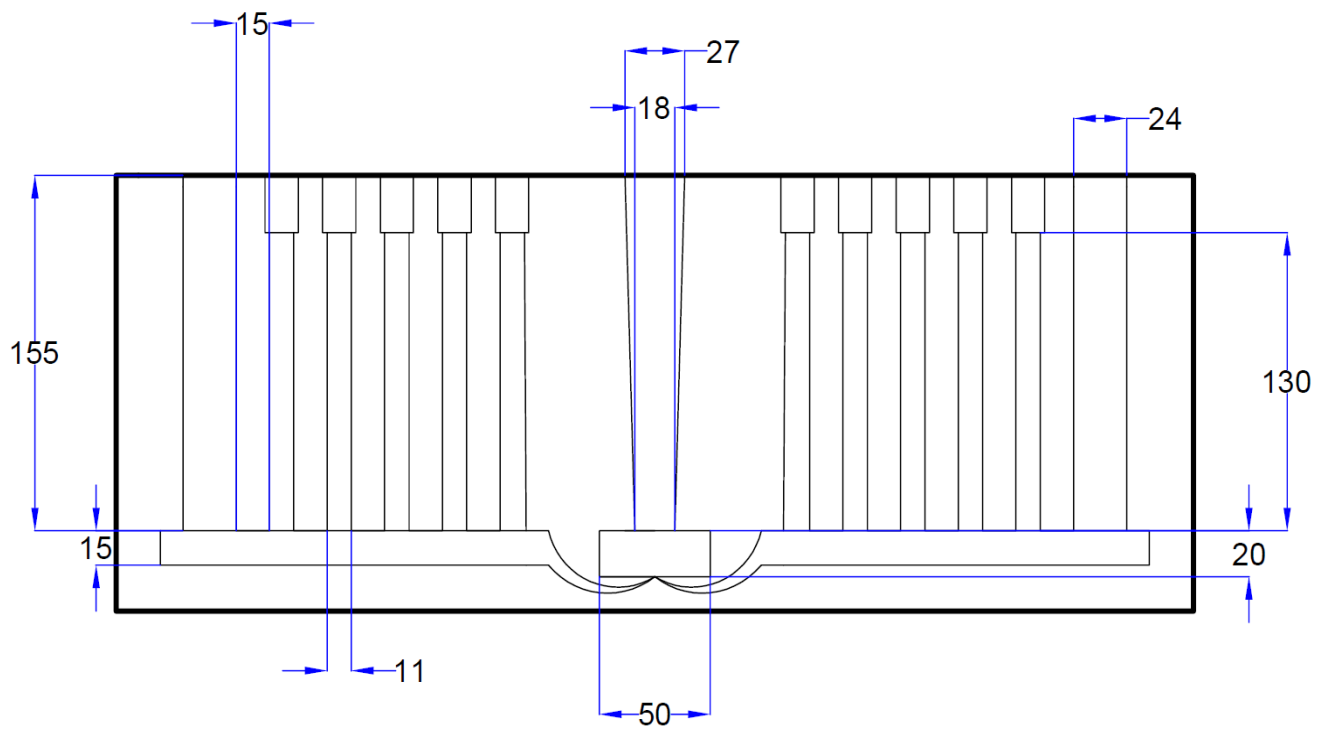
**Figure 3-2 The sketch of the sand mould.**

**Figure 3-3 The sketch of the mould with reduced bi-film defect content.**

### 3.3.2 Master Alloy preparation

For the Mo, W and Mn additions, 2L99-10Mo, 2L99-10W and 2L99-10Mn masteralloys were made. The masteralloys were made by adding 200g pure Mo/W/Mn (purity:99.9%, confirmed by the supplier) into 1800g of 2L99 alloy, held at 1300 °C in a 45 kW induction furnace, The melt was held for 40min before being cast into an ingot mould.

For the modifier additions, Ba and Na were added in the form of pure elements (99.9% purity). Sr was added in the form of Al-10Sr rod purchased from a supplier.

Ti was added in the form of an Al-10Ti rod with 250g Al-10Ti rod added into 9.75kg 2L99 alloy. During the casting, 1.5g of pure magnesium was added into the metal melt to compensate for the loss of Mg with the master alloy addition.

### 3.3.3 Casting

12 kg of 2L99 alloy was melted in a 90 kW induction furnace and the addition of masteralloy or pure elements made when the temperature of the melt reached 730 °C. At the same time, Ar degassing was used to reduce the hydrogen content of the melt. 20 min was allowed for degassing. During this time the hydrogen content was measured by a Severn Science instrument. When the H content was reduced to below 0.1 mm$^3$/100g, the liquid metal was cast.

In order to minimise possible shrinkage porosity in the tensile test bars, a roll-over device was used. An Al rod, serving as a stopper, was inserted into the downsprue of the casting as soon as the mould was filled. The casting was then rolled over 180° immediately, as show in Figure 3-3.

### 3.3.4 Heat–treatment

All the castings were then given a T6 heat-treatment before machining. This consisted of a 540°C solution treatment for 12h, followed by a quench in 65 °C water and aging at 155°C for 3.5h[110]. The temperature during the heat-treatment processes was controlled within +/- 3 °C.

### 3.3.5 Roll over process

The use of the roll-over device was aimed at reducing the possibility of the formation of the shrinkage porosity. A sketch of the roll over device has been shown in Figure 3-4. As can be seen, 3 moulds were fixed on the roll-over device before casting. A long chill, made of the same composition as the metal cast, was inserted into the downsprue as long as the liquid metal was in the mould. The moulds are rolled over by 180° after casting and the runner system will provide feeding to the test bar to minimize the formation of shrinkage porosity.



**Figure 3-4 the rollover device used for minimise the formation of shrinkage porosity in the casting**

### 3.3.6   XRF measurements

The composition of the masteralloys and the composition of the castings after solidification, were measured by XRF (BRUKER S8 Tiger wavelength dispersive X-ray fluorescence) usually on a section of the runner bar. The sample to be tested was ground to 800 grit prior to the test. In the test, an area of 50.24 mm$^2$ of the ground sample surface was measured with a 8mm dia. mask. The test for each sample ran for 8 min.

### 3.3.7 LECO™ hydrogen content analysis

To obtain the H content of the actual castings, a section of the runner bar, of length 100 mm and 8 mm dia., was taken from each casting. During the LECO[TM] test, the sample was heated in a closed chamber and the hydrogen released from the sample was carried in a $N_2$ carrier stream through a thermal conductivity cell used to determine the amount of hydrogen.

### 3.3.8 Tensile test bar machining and testing

The castings were machined into tensile test bars, according to ASTM E8/E8M-15a[152]. The dimensions of the tensile test bars are shown in Figure 3-5. The total length of the test bar was 100mm, with 37mm in the gauge length and 26mm radius.

The tensile test machine used was a Zwick[TM], equipped with a micro extensometer, with a strain rate of 1 mm/min being used.
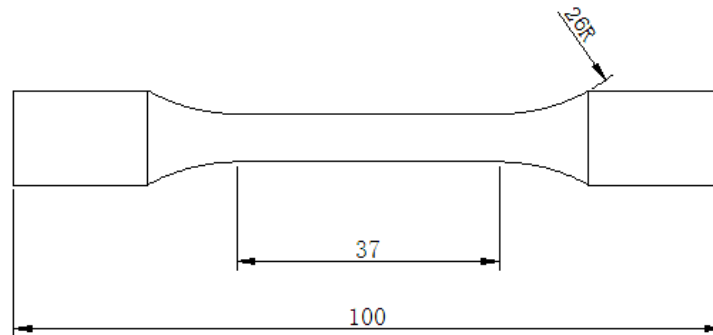


**Figure 3-5 The sketch of the tensile test bar.**

## 3.4 SEM/TEM imaging

The observation of the fracture surface was carried out using a JOEL 7000 SEM equipped with an INCA Oxford Electron Dispersive X-ray spectrometer (EDS). Some cross-sections were milled using a Focused Ion Beam (FIB), using a dual beam FIB-SEM, FEI Quanta 3D,

equipped with an Electron Dispersive X-ray spectrometer (EDS). A layer of Pt was initially coated on the surface of the sample, and a Ga beam was used for cross-sectional milling. TEM samples were fabricated by Ga beam milling on both sides of the selected area to obtain a thin section. The thin section was then lifted out with an FIB lift-out technique for analysis using a FEI Tecani F20 TEM.

## 3.5 Optical microscopy of the sample surface

Samples for optical imaging were initially cut from the runner bars of the casting and then mounted in conductive Bakelite. This was followed by grinding with 240#, 400#, 800#, 1200#, and 2500# SiC paper. Samples were then polished with 9μm, 3μm and 1μm diamond paste to obtain a mirror-like surface. The microstructure was observed under a LEICA LEITZ DMRX optical microscope.

## 3.6 The TP-1 test to determine the grain size with Mo addition

10 kg of commercial purity or 2L99 alloy was melted in a 90 kW induction furnace, and element additions were made at 718 °C. A Mo addition was made by adding the Al-10Mo or 2L99-10Mo masteralloy prepared before casting. $TiB_2$ was added in the form of 5(wt.% Ti):1( wt.% B) rod. After the addition, the surface layer in the melt was skimmed off and the melt was stirred for 15s to better dissolve the additions. After 5 min, the ladle, as shown in Figure 3-6, was lowered beneath the surface of the melt for 30s and then taken out and placed vertically onto the ring of the quenching fixture for solidification at a standardised rate. After solidification, a sample was cut 38mm from the base and polished to 3μm.

For CPAl, CPAl+0.5 wt. % Mo, a sample was etched with Poulton's solution (60% concentrated HCl, 30% concentrated $HNO_3$, 5% HF and 5% $H_2O$). Images of the grain structure were then taken using an AxioCam MRc 5 camera.

For CPAl + 100 ppm $TiB_2$, CPAl+100 ppm $TiB_2$ + 0.125 Mo, CPAl+100 ppm $TiB_2$ + 0.25 Mo and CPAl+100 ppm $TiB_2$ + 0.5 wt.% Mo, samples were electro-etched to reveal grain boundaries for clear grain size measurements. The electro-etching was done by placing the polished sample surface at the anode and a piece of stainless steel at the cathode. The sample on the anode and the stainless steel piece in the cathode were placed in Barker's solution (8ml 48% $HBF_4$ with 192ml $H_2O$) with a 50mm distance between them. A constant current supply of 20V and 2A was used. The etching was completed in 60s. After etching, the sample was washed immediately with water. Grain boundaries were clearly revealed and images were taken using a LEICA LEITZ DMRX optical microscope equipped with an automatic adjustable stage so that 25 50X images could be combined together for grain size measurements.

The grain size of 300 adjacent grains were measured with Image J. The average grain size was calculated and grain distribution graphs determined.

For the sample of 2L99 alloy (grain refined with 300ppm $TiB_2$) + Mo, the sample preparation steps were the same as electro etching except for the microscope used for analysis. Here, a Carl Zeiss Axioskop 2 MAT optical microscope, equipped with a polarised light filter and a $\lambda$ plate was used to reveal the grains in different colours. 5 50X images were taken from each sample (of 2L99 and 2L99 +0.5 wt. % Mo) and their grain size distribution determined.
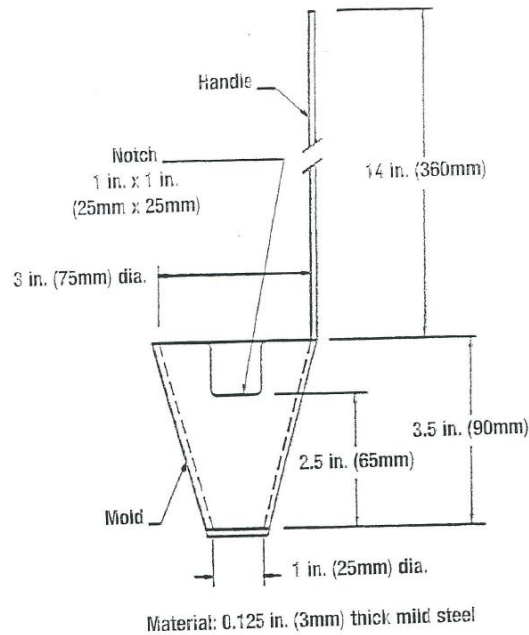
**Figure 3-6 Dimension of the TP-1 test ladle[181].**

## 3.7 Experiment to determine the floatation of the bi-film defects

In this experiment, a 4-point bend test was used to investigate the position of the double oxide film defects in a rectangular test bar. In a 4-point bend test, the surface of the testbar which faced downward will be subjected to the maximum tensile stress, and the testbar is likely to fracture if a bi-film defect is near this surface. From this casting, 60 testbars were divided into 2 groups, with 30 of them conducted with the bend test with top surface under the maximum tensile load while the other 30 of them with the bottom surface placed under the maximum tensile load. By comparing the tensile test results, it can be concluded if the bifilm defect floated to the top surface of the bend test bar or settled to the bottom.

The sketch of the bend testbar mould is shown in Figure 3-5 during the bend test, the distance between the two bottom rollers was 90mm and 60mm for the top rollers. The rollers had a diameter of 12mm. The test was conducted with a Ziwick[TM] mechanical test machine and the compression strain rate was 1 mm/min.
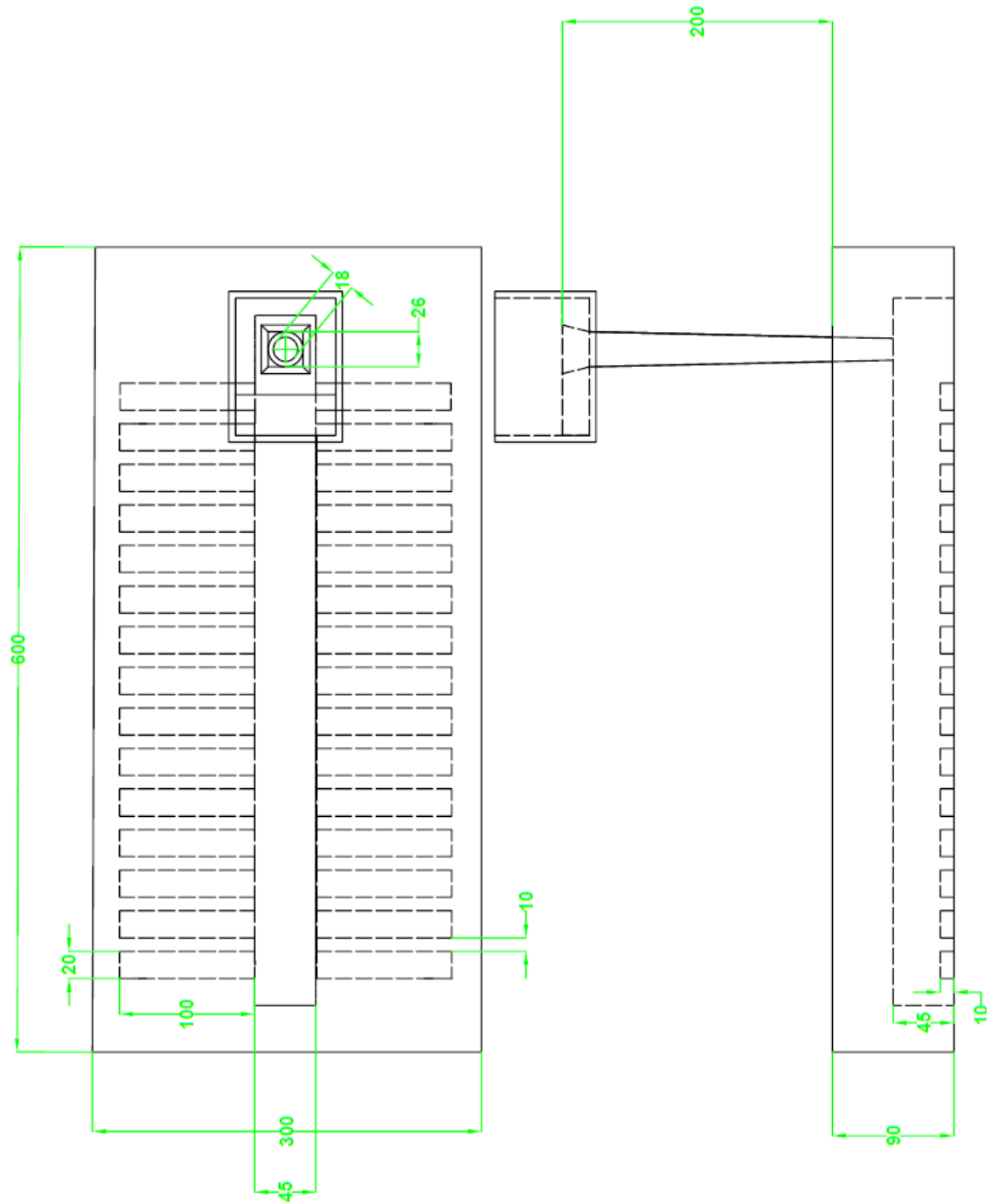
**Figure 3-5 Sketch of the bend testbar mould (top view and front view).**

## 3.8 Flow chat for the results in this work
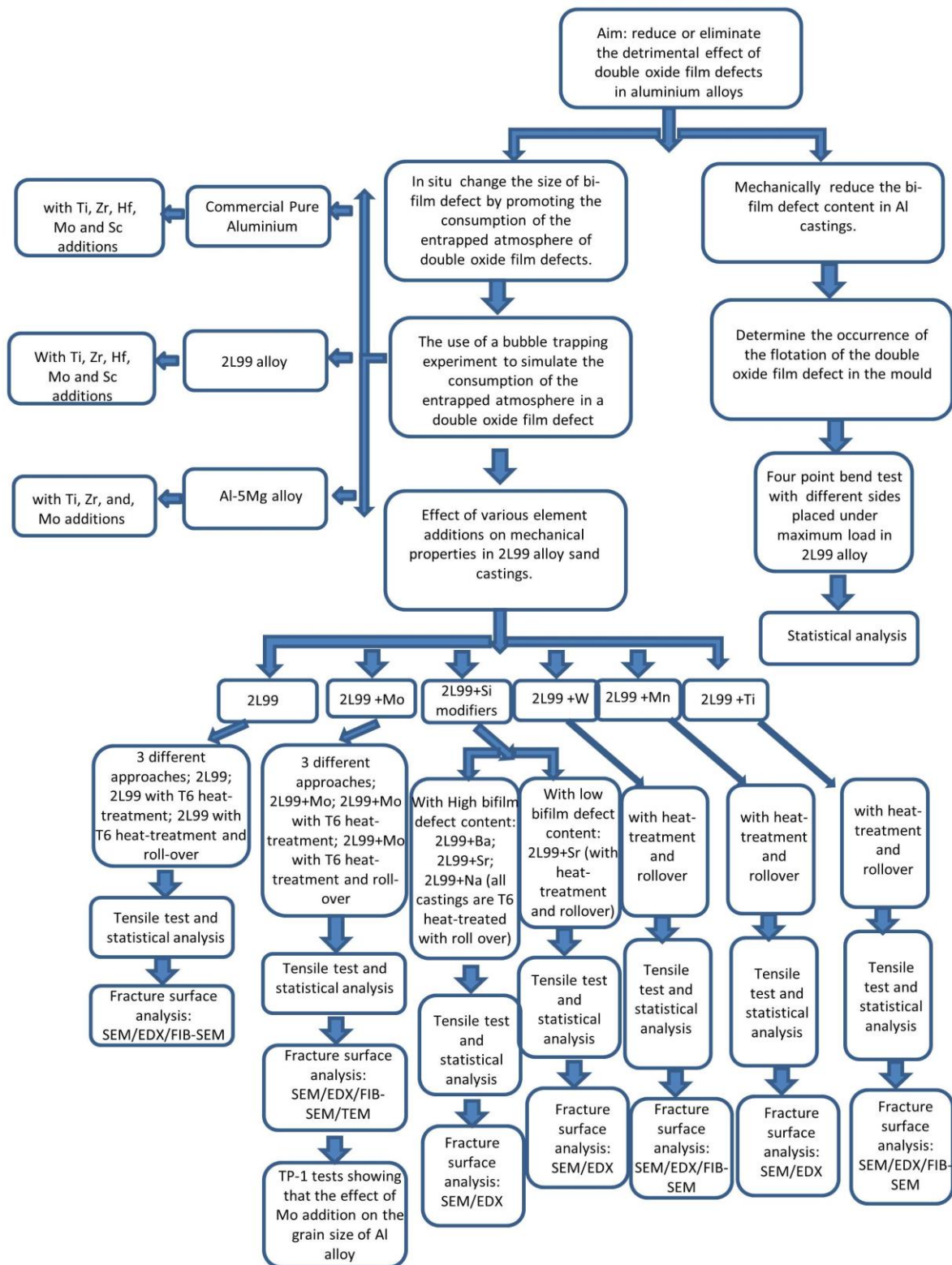
# Chapter 4   Results

## 4.1   The effect of different element additions on the behaviour of a trapped air bubble in liquid aluminium

In this experiment, a steel rod with a blind hole at one end was plunged into an aluminium alloy melt for a period of time. The air bubble trapped inside the blind hole reacted with the melt and its oxygen and nitrogen was consumed, with oxide and nitride formed on the upper surface of the liquid aluminium inside the blind hole, which was then analysed by SEM/EDX after solidification. In this experiment, several different elements were selected and added into 3 different alloys (commercial purity Al, Al-7Si-0.35Mg (2L99) alloy and Al-5Mg alloy). The aim of this work was to investigate how the element additions affected the formation of oxide or nitride for those alloys, and whether the additions accelerated the consumption rate of the trapped air bubble. If this happened to the trapped atmosphere of an oxide film defect in Al castings, the bonding between the two unwetted oxide layers in this defect might be promoted, which might result in a beneficial effect on mechanical properties of the alloys and improvement in the reproducibility of properties of Al castings.

In the experiment, the transition metals to be added were selected due to their low Gibbs Free energy for the formation of an oxide or nitride, compared with Al. The elements added to the melt might compete with aluminium in the formation of oxide/ nitride, and accelerate the consumption of the entrapped atmosphere in the aluminium. Mo was added based on results from Hinton[151]  which suggested the possibility for the formation of a permeable oxide layer when Mo was added into aluminium alloy.

### 4.1.1 Air bubble trapping experiment in commercial pure Al

Five elements were selected and added to commercial purity aluminium alloy (Ti, Zr, Hf, Sc and Mo). For all experiments, 0.5 wt.% of the transition metal was added. All experiments lasted for 1h except in the case of Ti, when the solidified metal height inside the blind hole was quite low after 1 h, and the experiment time was increased to 3 h. The reference sample of CP-Al was repeated three times to ensure the reproducibility of the experiment. The chemical composition of the element recovery was analysed by XRF and has been shown in Table 4-1. Ti and Sc had the best recovery rate (0.4 wt. %-0.5 wt. %), while about 0.35 wt.% Mo, Hf and 0.3 wt.% Zr was recovered. In addition to the element recovery, there was also 1.5-2 wt. % Fe picked up, due to the dissolution of the iron rod into the melt during the experiment.

After the experiment, the height of metal solidified inside the blind hole was measured and is also shown in Figure 4-1. The full height of the blind hole was 40 mm.

**Table 4-1 XRF results showing the recovery rate for elements addition into commercial purity aluminium.**

| Element addition | Duration | Recovery (wt. %) | Fe recovery (wt. %) |
|---|---|---|---|
| N/A | 1h | N/A | 1.85% |
| Zr | 1h | 0.30% | 1.87% |
| Ti | 1h | 0.40% | 1.58% |
| Ti | 3h | 0.52% | 1.74% |
| Mo | 1h | 0.35% | 1.60% |
| Hf | 1h | 0.35% | 1.65% |
| Sc | 1h | 0.50% | 1.70% |
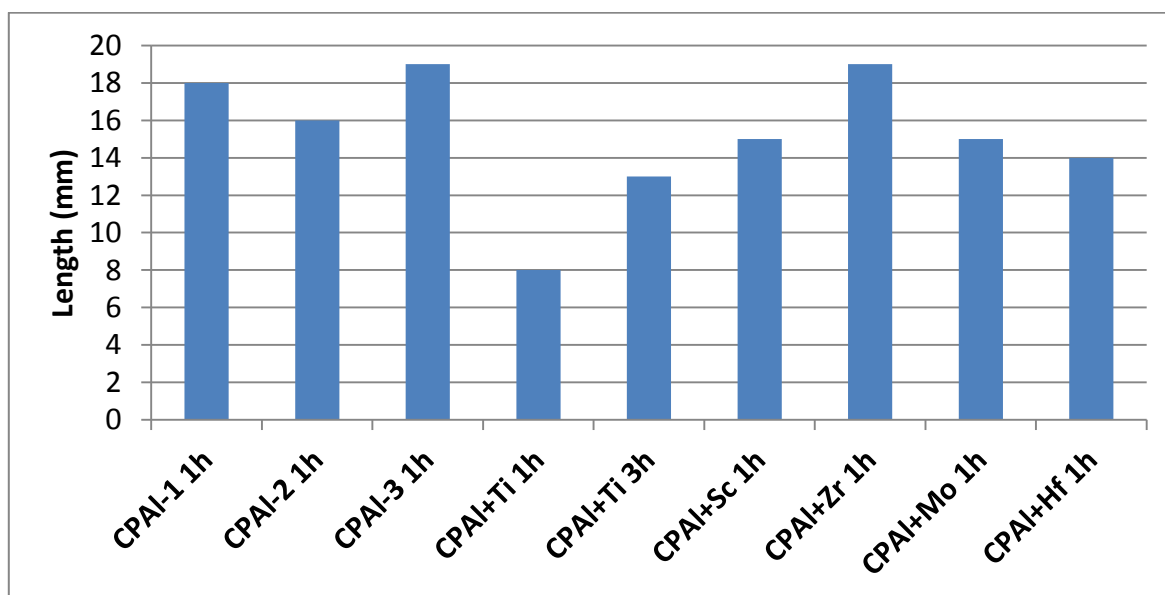


**Figure 4-1. Length of sample solidified inside the blind hole for commercial pure aluminium and additions.**

#### 4.1.1.1 Commercial purity Al

For commercial purity aluminium without any addition, the liquid metal solidified inside the blind hole with a mean height of 18 mm. SEM examination of the top surface of the solidified sample surface suggested the presence of both oxide and nitride, (see Figure 4-2 and Figure 4-3).

EDX analysis of the oxide layer showed an oxygen peak in addition to the aluminium peak (16 at. % oxygen and 83 at. % aluminium), suggesting $Al_2O_3$.

Two forms of nitride were found on the sample surface, one with a coarse feather-like structure, shown in Figure 4-3, and the other a thin nitride layer, which might have grown on the existing oxide layer, as shown in Figure 4-4.

In Figure 4-3, a small oxygen peak (3.21 at.%) can be seen at X2, which suggested that this area contained a thin oxide layer. The oxygen content, however, was doubled to 7.8 at. % at X1 and the nitrogen content was 35 at.%. The feather-like structure was probably AlN as similar structures have been seen by Raeiszadeh [153] and Gerrad[51].

Spectrum X1 in Figure 4-4 ( from CPAl-2) showed a weaker nitrogen peak (10 at.%) compared with Figure 4-3 (CPAl-3), which suggested that the nitride shown in Figure 4-4 could be at an initial stage of the formation of the nitride, i.e. the sample solidified before the nitride could grow thicker. This idea was also confirmed by the sample height measurements which showed that CPAl-2 had a 16% lower sample height than CPAl-3.
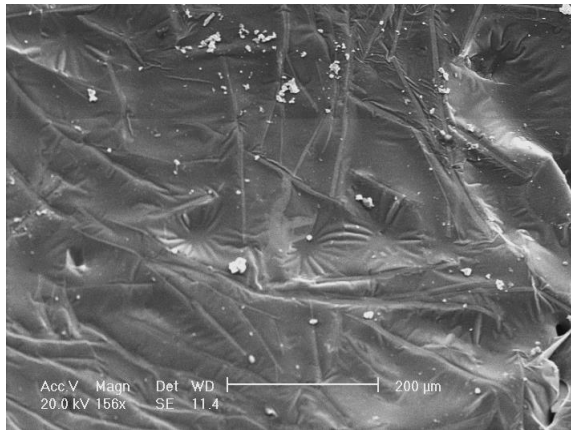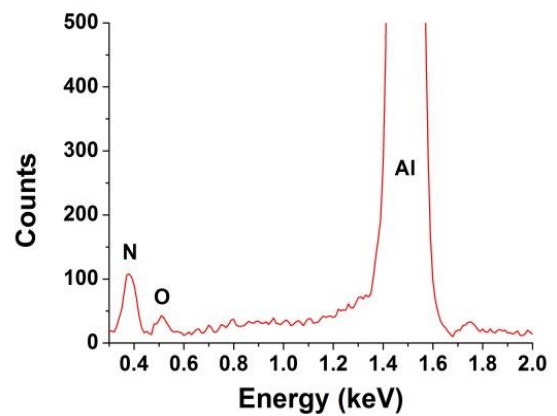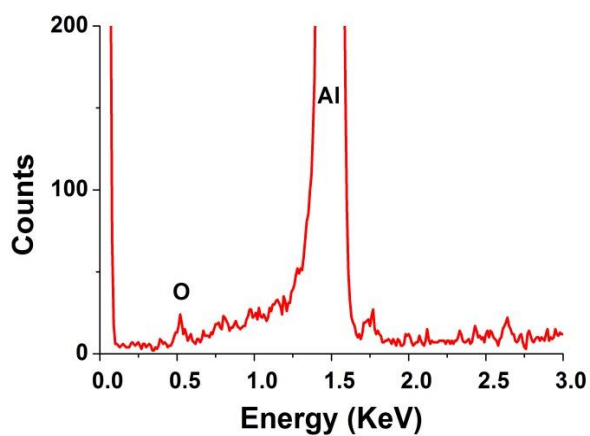
(a)
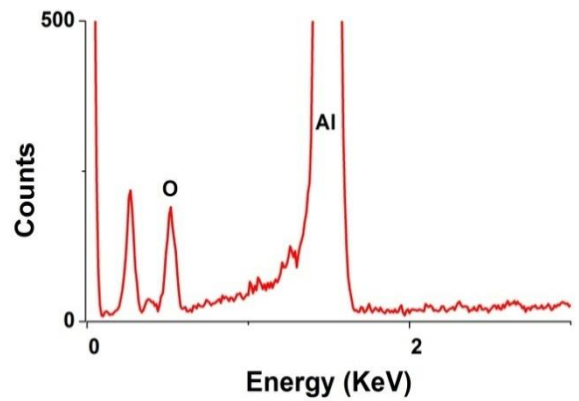
(b)

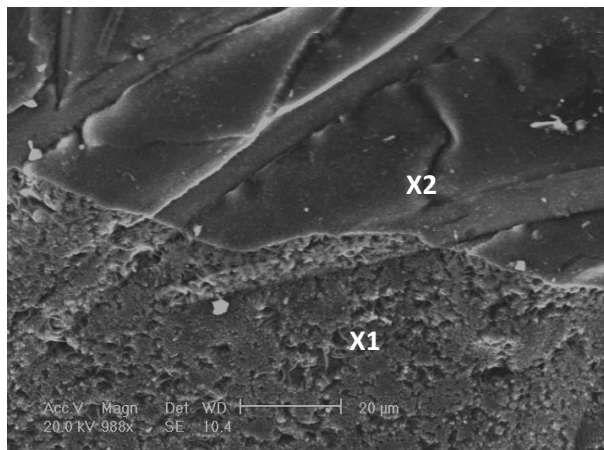**Figure 4-2 Continuous oxide layer on the sample for CPAl-2.**
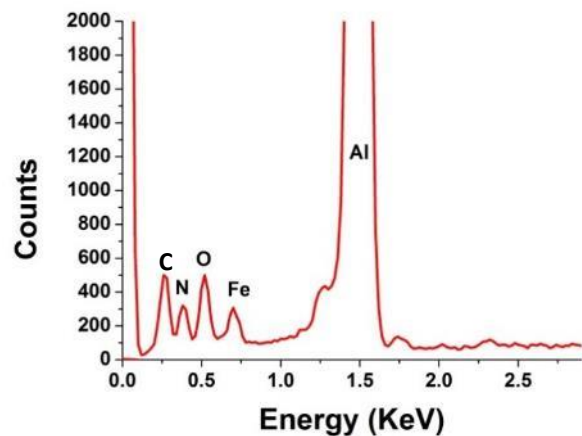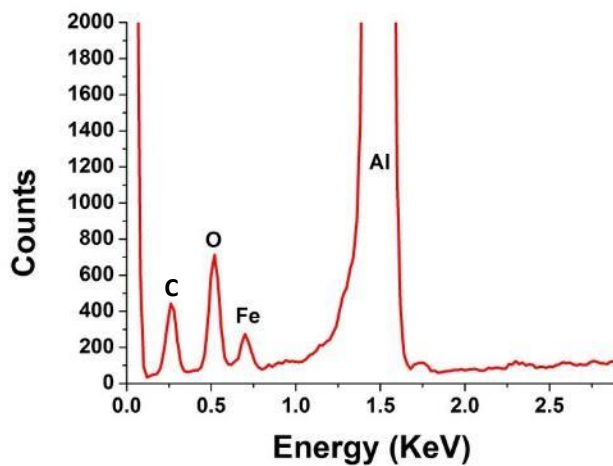


(a)

(b)
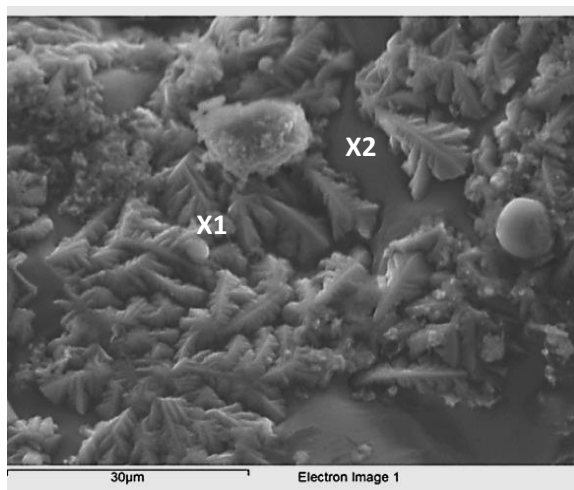
**Figure 4-3. (a) Feather like nitride layer found on the sample of CPAl-3; (b) EDX spectrum for X1 and (c) EDX spectrum for X2.**



(c)

87

(a)



(b)



Figure 4-4. (a) The nitride layer growing on the oxide layer in CPAl-2; (b) EDX spectrum for X1; (c) EDX spectrum for X2.

(c)

## 4.1.1.2   The effect of the addition of Ti into commercial pure aluminium

Two experiments with Ti added to commercial pure Al were carried out. The first for 1h, in which the liquid metal reached a height of 8 mm in the blind hole, which increased to 13 mm when the holding time of the liquid metal was increased to 3 h. SEM examination showed only oxide on both of the sample surfaces. The oxide was not affected by the Ti

addition as no Ti peak was detected by EDX. The morphology and composition of the oxide layer is shown in Figure 4-5. Figure 4-6 showed iron containing particles (containing 21% Fe) dispersed on the surface of the oxide layer.
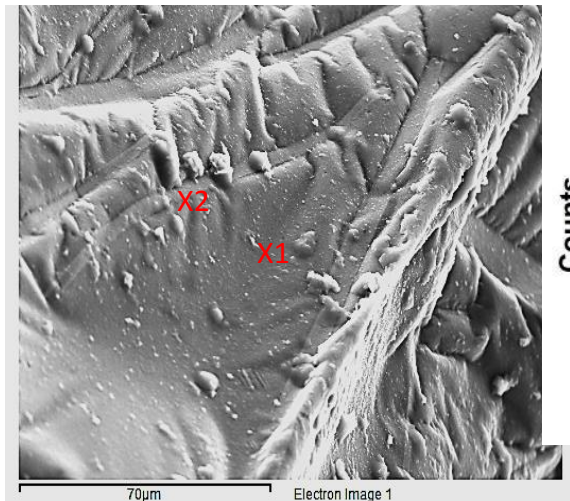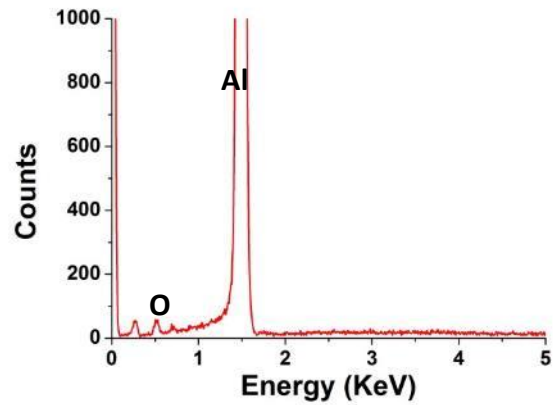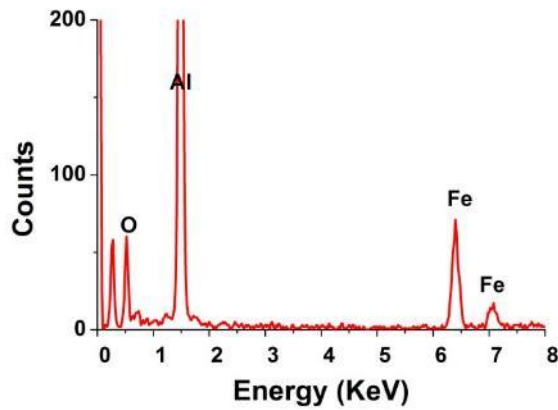


(a)

(b)

(c)

(d)
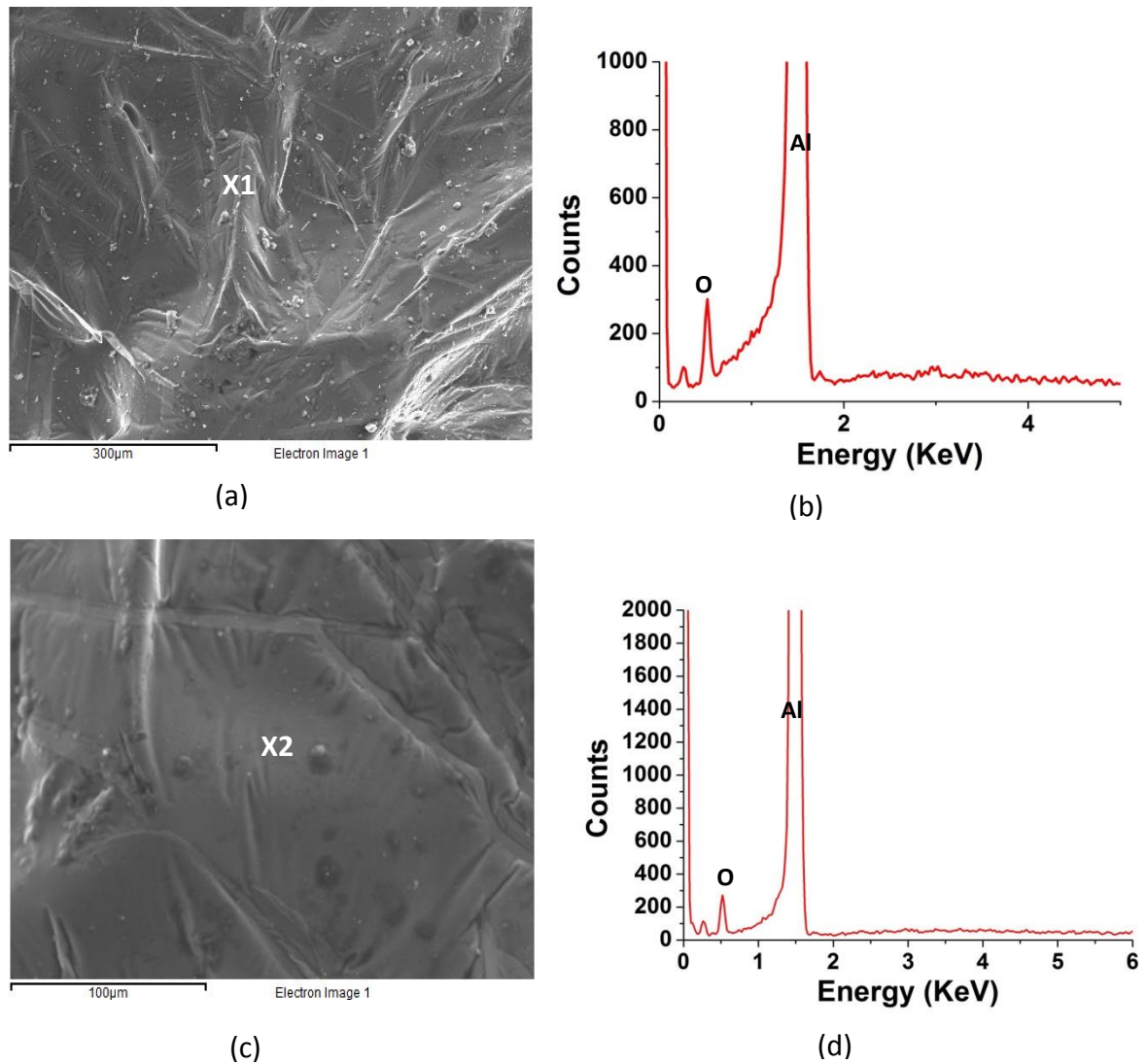
**Figure 4-5. (a) (c) SEM/EDX investigation of the sample surface with CPAl+Ti; (b)EDX for spectrum 1 and (d) EDX for spectrum 2.**

Figure 4-6 (a)SEM/EDX image showed that the iron particles on the surface of CPAl-Ti sample; (b) and (c) EDX spectrum of X1 and X2 respectively.

### 4.1.1.3   The addition of Zr into commercial pure aluminium

With Zr, the liquid metal reached a height of 19 mm into the blind hole. SEM investigation of the sample surface suggested that both oxide and nitride had formed on the sample surface, but there was no sign of Zr precipitates. Figure 4-7 showed the oxide found on the sample surface, which formed a continuous alumina layer with Fe-rich particles dispersed on it. Figure 4-8 showed a nitride layer. Quantification of the spectrum suggested that this nitride
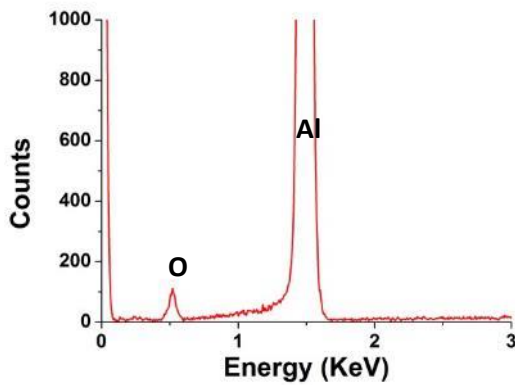
layer contained 17.6 at. % oxygen and 9.72 at. % nitrogen. There was no sign of Zr participating into the oxide or nitride formation.
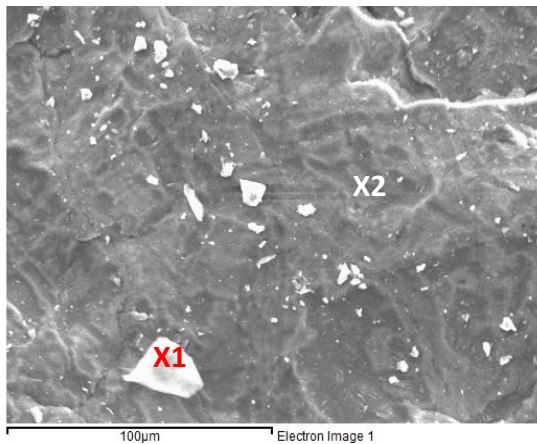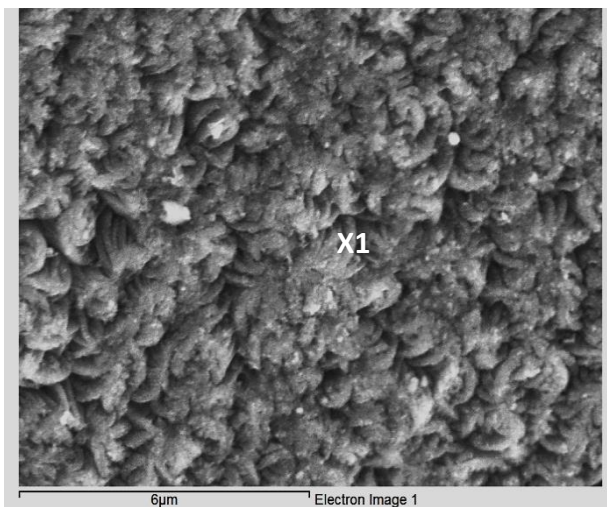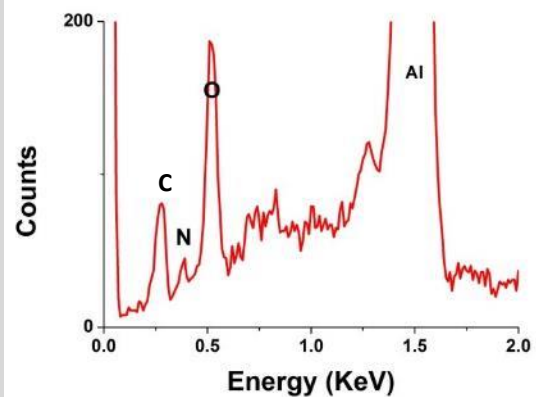

(a)
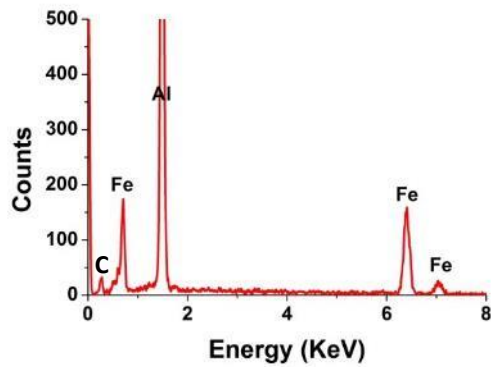

(b)


(c)

**Figure 4-7 (a) Oxide layer found on the sample surface with CPAl+Zr; (b)EDX for spectrum 1 and (c) EDX for spectrum2.**


(a)


(b)

**Figure 4-8. (a) SEM image of the feather like nitride layer growing on the surface of sample with CPAl +Zr and (b) EDX spectrum for X1.**

#### *4.1.1.4 The addition of Hf into commercial pure aluminium*

In this experiment, the liquid metal height was 14 mm inside the blind hole, and investigation of the sample surface showed no sign of Hf in the reaction to form an oxide layer.

On the sample surface, however, some Hf containing intermetallic particles were observed, which also contained Fe and Al (72.4 at. % Al, 5.54 at. % Hf and 22.06 at. % Fe), (in addition to the Fe-containing intermetallic on the sample surface, as shown in Figure 4-9).

Hf did not affect the composition of the oxide layer on the sample surface, the consumption of the entrapped atmosphere was also not affected. It could be possible that Hf in the aluminium melt might react with Iron and aluminium and form an Al-Hf-Fe intermetallic compound. Yildirim [178] and Gaydosh [179] suggested that an $HfFe_6Al_6$ phase could be formed in FeAl alloy with Hf addition. Al-Hf phase diagram [180] suggested that a mixture of $Al_3Hf$ and $Al_2Hf$ will be formed at the concentration used in this work (0.4 wt.%), at the casting temperature. The formation of the intermetallic compounds might significantly reduce the Hf content in the aluminium melt and, therefore, a Hf-containing oxide layer would be less likely to form.
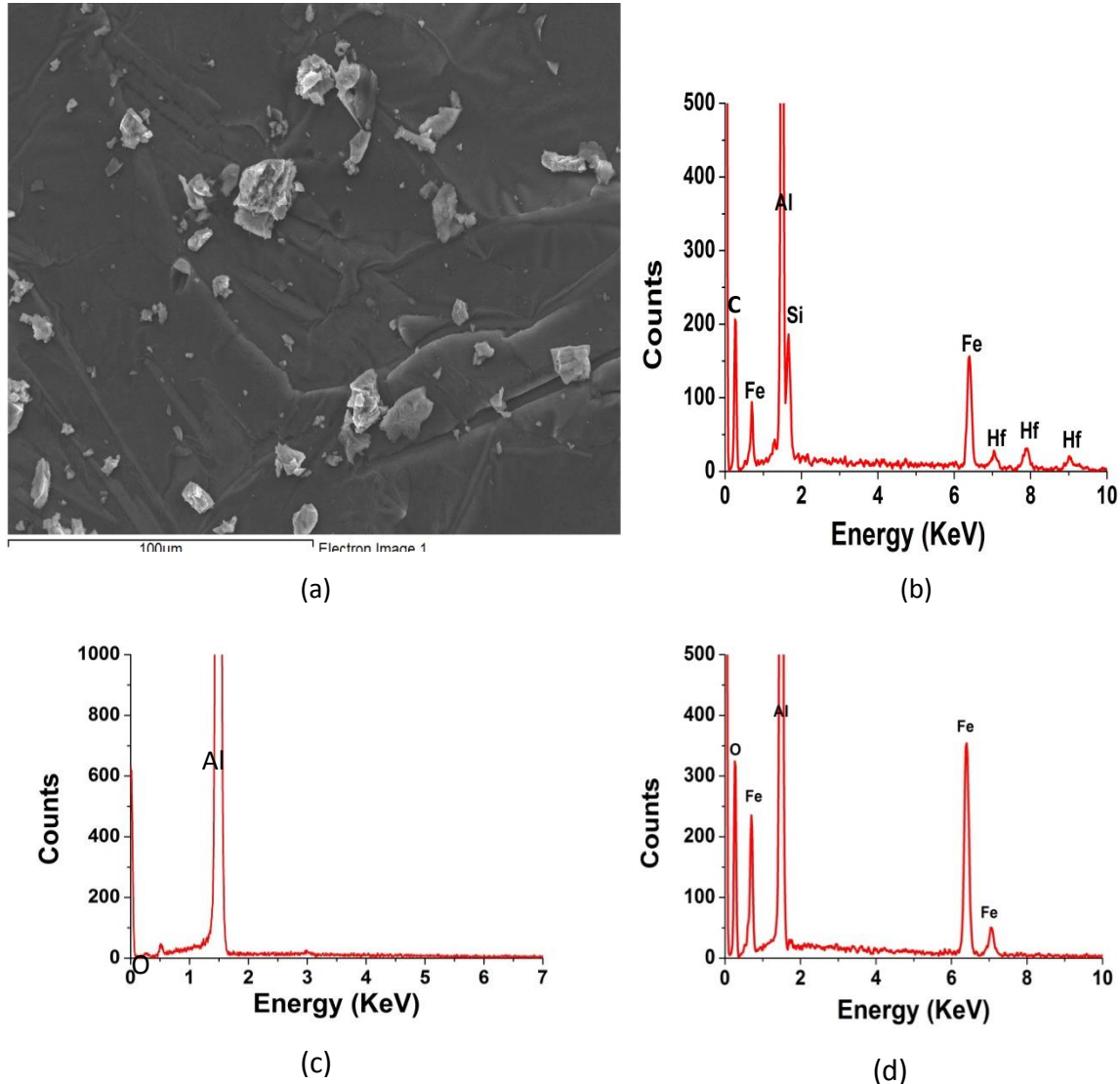
(a)

(b)

(c)

(d)

**Figure 4-9. (a) The morphology of the sample surface with CPAl+Hf; (b) EDX spectrum from X1; (c) EDX spectrum from X2 and (d) EDX spectrum from X3.**

### 4.1.1.5 The addition of Sc into commercial pure aluminium

In this experiment, the liquid metal entered 15 mm into the blind hole. SEM/EDX analysis of the sample surface indicated that only oxide was formed. Figure 4-10 shows the oxide layer observed on the sample surface. A Sc peak was detected in spectrum 1 (Figure 4-10). A higher magnification of the oxide layer in the area is shown in Figure 4-11, suggesting a Sc

containing intermetallic compound underneath the oxide in the nearby region or Sc participated in the oxide formation process.
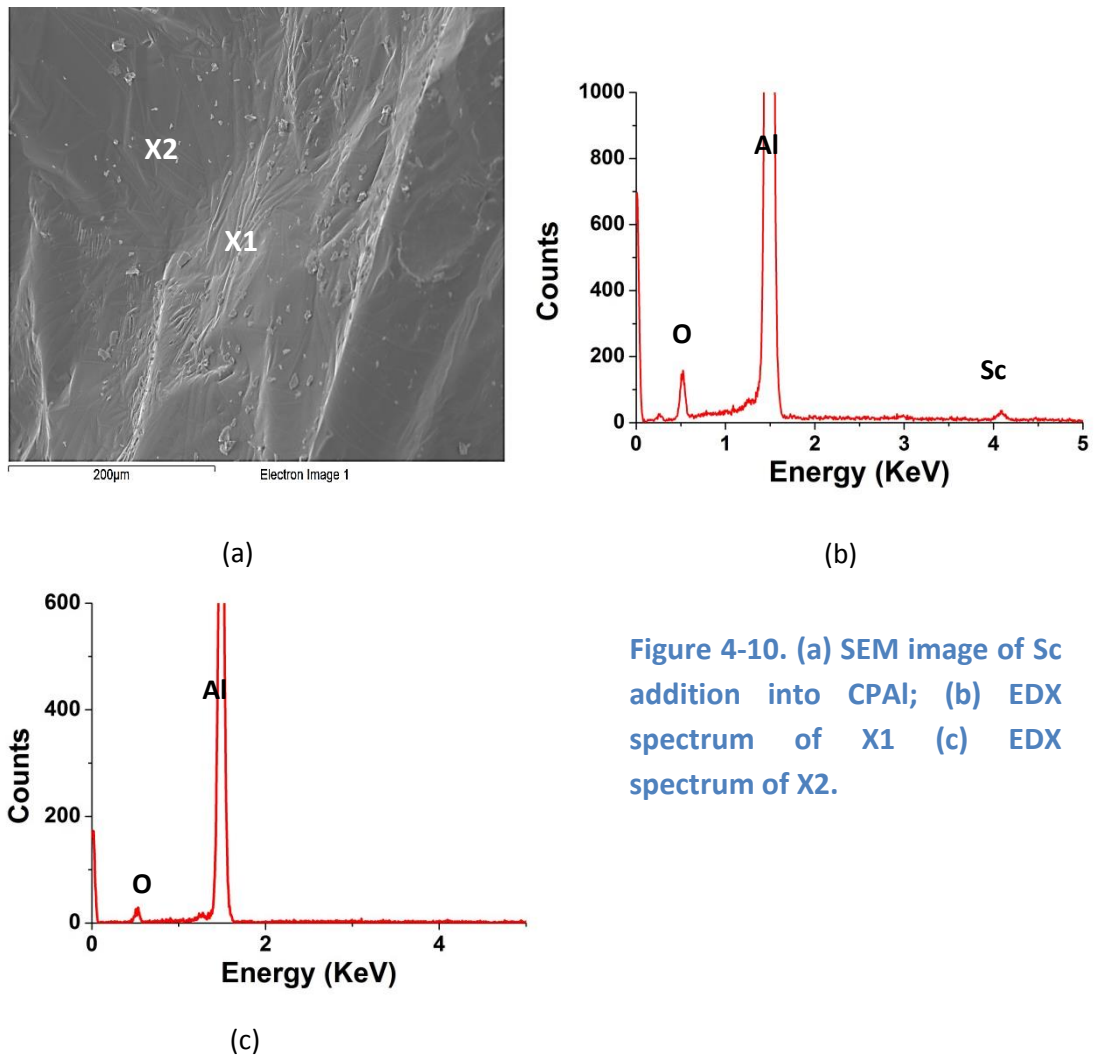


(a)



(b)



(c)

**Figure 4-10. (a) SEM image of Sc addition into CPAl; (b) EDX spectrum of X1 (c) EDX spectrum of X2.**
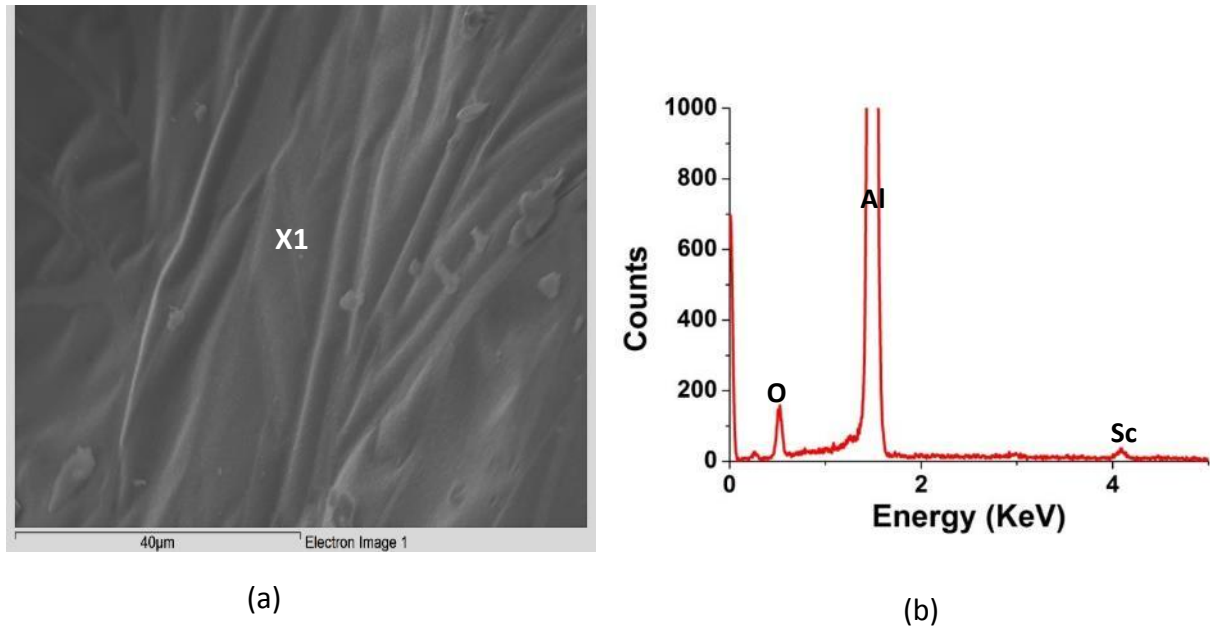
(a)

(b)

**Figure 4-11. Higher magnification image of the oxide layer on the sample surface of CPAl+Sc.**

### 4.1.1.6  The addition of Mo into commercial pure aluminium

In this experiment, the solidified metal height inside the blind hole was 15 mm. EDX analysis showed an oxide layer detected on the sample surface, and the surface morphology of the oxide was wrinkled (see Figure 4-12). EDX analysis showed a very small amount of Mo (0.17 at. %) associated with the oxide layer, as shown in Figure 4-12 (d). In this spectrum, 7.56 at. % N and 7.21 at. % O was also formed.
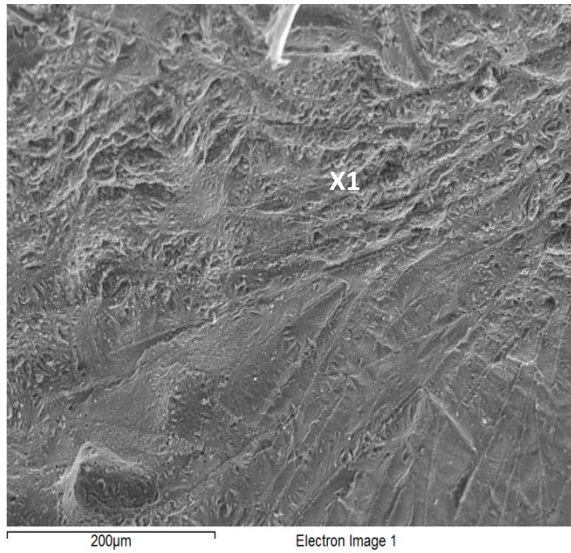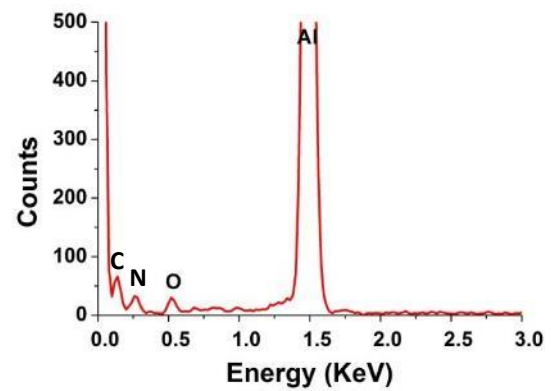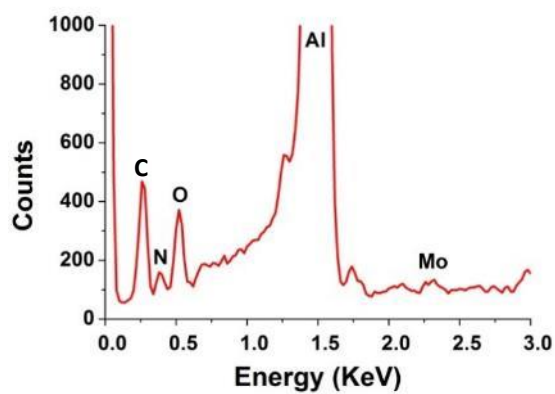
(a)
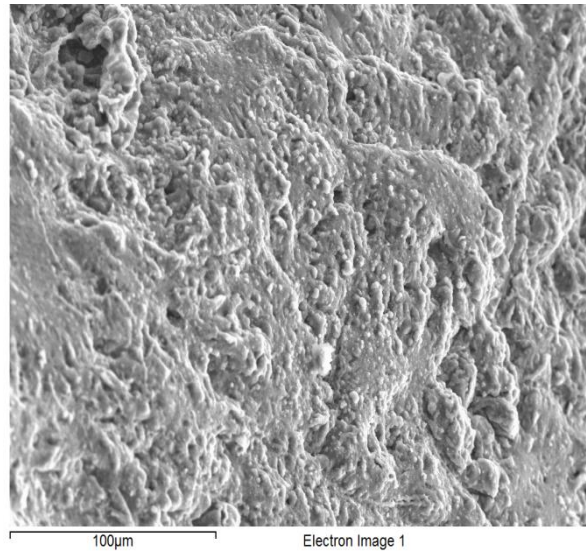


(b)
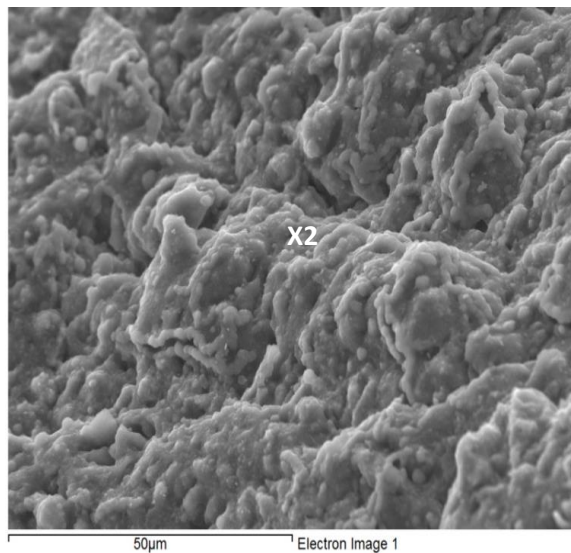


(c)



(d)



(e)

Figure 4-12 (a), (b) and (c) Oxide found on the surface of solidified metal inside the blind hole of the experiment with CPAl+Mo. (d) EDX spectrum for X1 and (e) EDX spectrum for X2.

### 4.1.2   An entrapped air bubble in 2L99 alloy

In these experiments, the same amount of the transition metal as in the experiment with commercial purity Al alloy (0.5 wt. %) was added to the castings. The element recovery for the addition into 2L99 is shown in Table 4-2. The depth of the metal solidified inside the blind hole is shown in Figure 4-13.
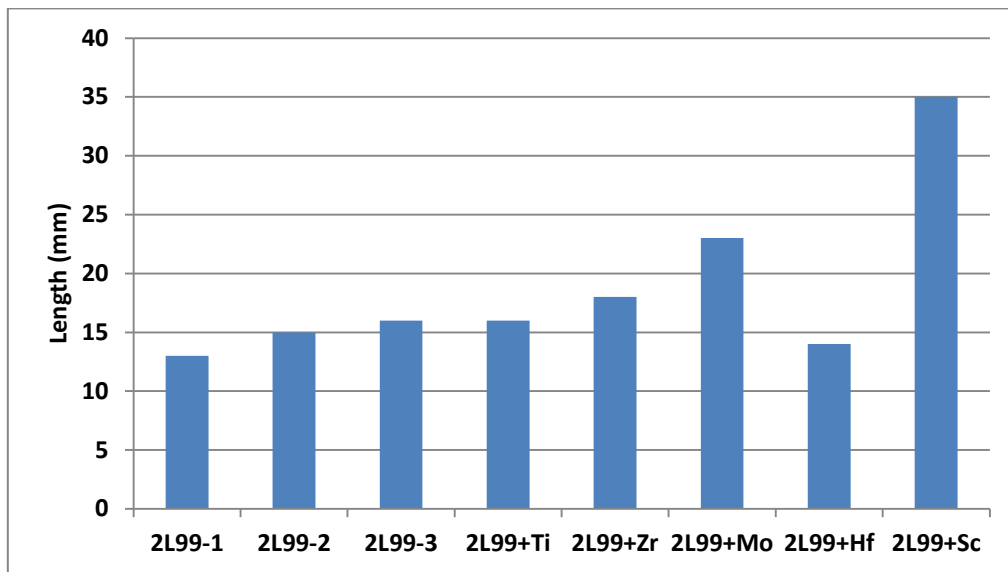


**Figure 4-13 The depth of metal solidified inside the blind hole for element additions into 2L99.**

**Table 4-2 Element pickup for different element addition into 2L99.**

| No | Duration | Element | Pickup (wt.%) | Fe pick up(wt.%) |
|----|----------|---------|---------------|------------------|
| 1  | 1h       | N/A     | N/A           | 1.35%            |
| 2  | 1h       | Zr      | 0.41%         | 1.32%            |
| 3  | 1h       | Ti      | 0.51%         | 1.69%            |
| 4  | 1h       | Mo      | 0.39%         | 0.95%            |
| 5  | 1h       | Hf      | 0.51%         | 1.21%            |
| 6  | 1h       | Sc      | 0.58%         | 1.69%            |

In the experiment with Sc addition into 2L99, much more metal entered inside the blind hole compared with the other additions, which means that more entrapped gas was

consumed. This is followed by Mo addition with the sample height of 23mm. No significant differences in the consumption of the entrapped gas were seen for the other element additions.

The experiments with Sc, Hf and Ti had a recovery rate of around 0.5wt.%, and 0.4 wt.% for Mo and Zr.

### 4.1.2.1 The experiment with 2L99

For 2L99, without any addition, the liquid metal entered the rod to a mean height of 15 mm inside the blind hole. SEM Investigation of the sample surface suggested that only an oxide layer was formed. A typical oxide layer found on the sample surface is shown in Figure 4-14.

The EDX spectrum in Figure 4-15 X2 showed a high O peak compared with X1, which suggested a thicker oxide. In addition to the oxygen peak, a high Mg peak was also seen in X2. This suggests that Mg was participating in the formation of the oxide layer, which was probably $MgAl_2O_4$.



80µm    Electron Image 1

(a)

(b)
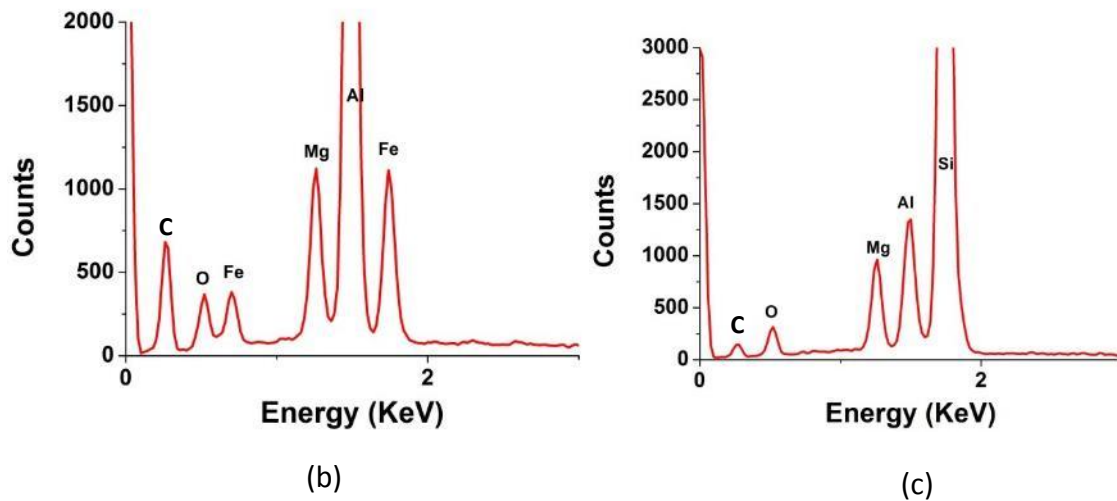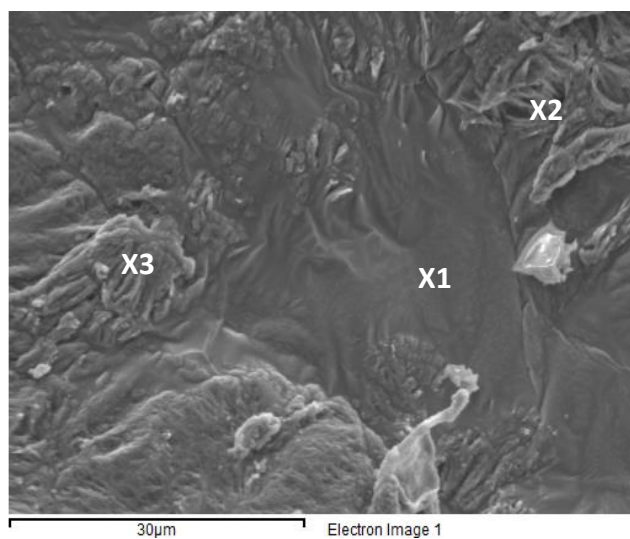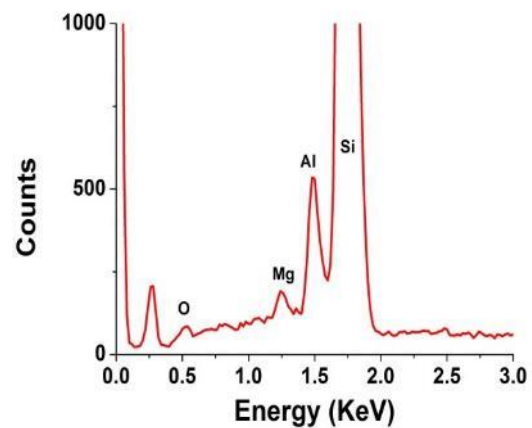


(c)
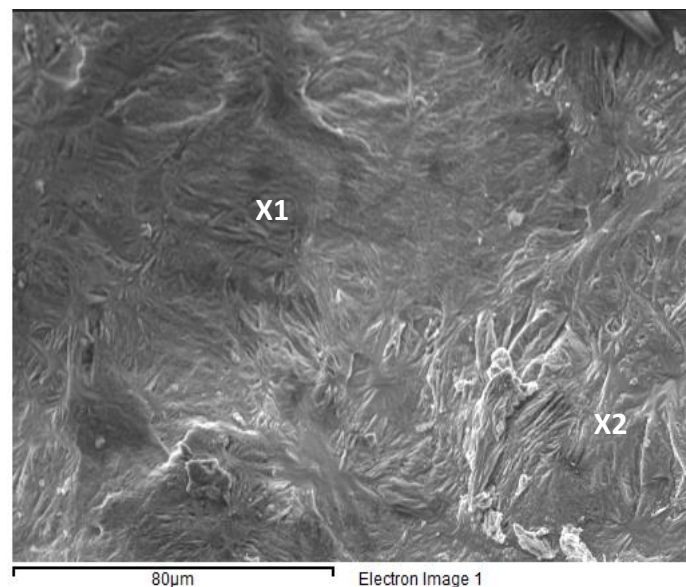
Figure 4-14 (a) Oxide layer found on sample with 2L99; (b) EDX spectrum for X1 and (c) EDX spectrum for X2.

Table 4-3 Quantity of the EDX spectrum shown in Figure 4-14.

|  | Spectrum 1 | spectrum 2 |
|---|---|---|
| Element | Concentration (at.%) | Concentration (at.%) |
| O | 9.95 | 5.24 |
| Mg | 9.34 | 4.03 |
| Al | 58.12 | 12.13 |
| Si | 13.95 | 78.6 |
| Fe | 7.86 | |



(a)



(b)

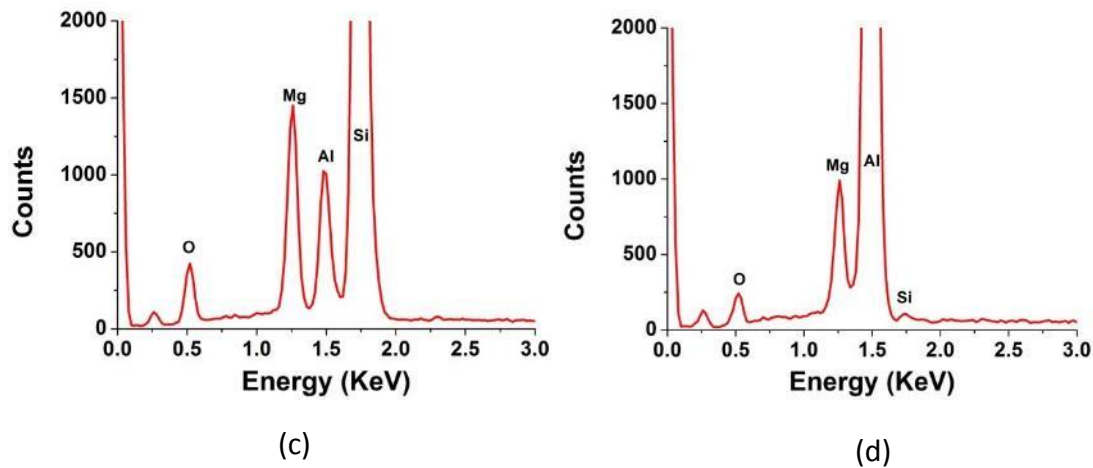(c)                                                    (d)

**Figure 4-15. (a) SEM investigation of the sample surface for the experiment with 2L99; (b)EDX spectrum for X1; (C) EDX spectrum for X2; and (d) EDX spectrum for X3.**

**Table 4-4 The Quantity of the EDX spectrum for X1 and X2 in Figure 4-15.**

|  | spectrum 1 | spectrum 2 |
|---|---|---|
| Element | Composition (atomc.%) | Composition (atomic%) |
| O | 1.06 | 10.03 |
| Mg | 0.47 | 6.97 |
| Al | 2.45 | 6.13 |
| Si | 96.02 | 74.87 |

### 4.1.2.2  The addition of Ti into 2L99 alloy

In the experiment with the Ti addition to 2L99, the liquid metal entered 17 mm into the blind hole. SEM examination failed to show nitride on the sample surface. However, a porous and Ti containing oxide was shown in Figure 4-16 and Figure 4-17.  The porous oxide was present in relatively small areas of around 0.01 to 0.05 mm$^2$. Higher magnifications of the porous oxide structure are shown in Figure 4-18 and Figure 4-19.

100

The composition of the spectra in Figure 4-16 are shown in Table 4-4. Table 4-5 shows the composition of two more oxidised areas containing Ti, from Figure 4-18. The oxygen content in the Ti-containing oxide layer was usually 33 at.%-35 at.% three times the amount in the Ti-free oxide layer discovered ( as show in Figure 4-16 X2), which might suggested a thicker oxide. The Mg content was similar in the oxide layer, with or without Ti. In the Ti containing oxide layer, the Ti composition varied between 10% to 15%, which showed a Ti:O ratio of about 1:2.5 to 1:3. Thermodynamic calculation in 5.2 suggested that $Ti_3O_5$ and $Ti_4O_7$ can be formed preferentially to $MgAl_2O_4$ or $Al_2O_3$. However, both oxides have a Ti:O ratio<1:2. This area might therefore consist of a mixture of both Ti containing oxide, aluminium oxide and spinel.



(a)

(b)



(c)
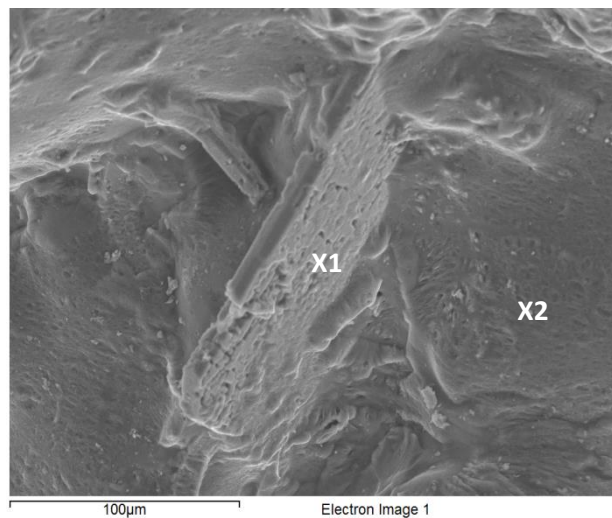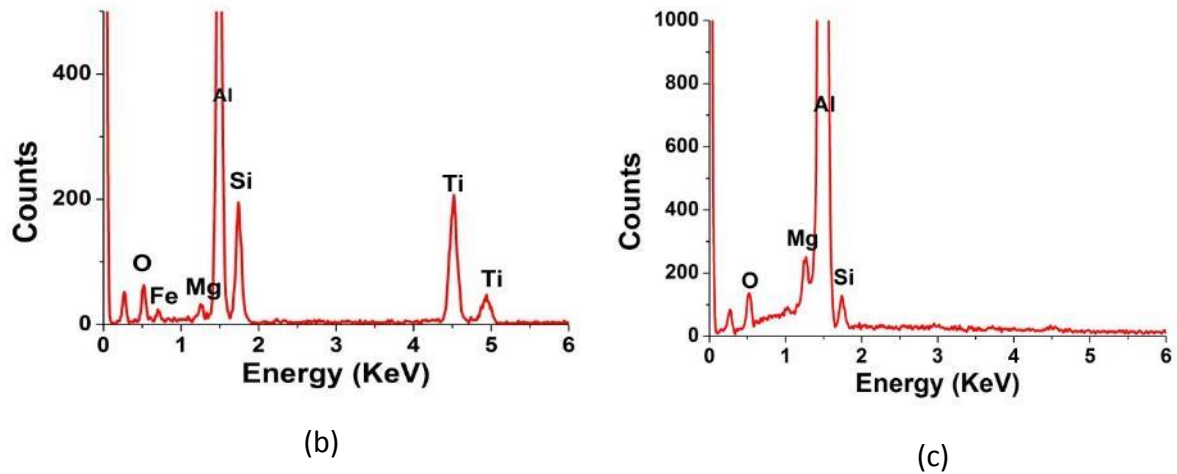
**Figure 4-16 (a) Ti containing oxide discovered on 2L99 + Ti sample; (b) EDX spectrum for X1; (c) EDX spectrum for X2.**

**Table 4-4 Quantity measurements for EDX spectrum from Figure 4-16.**

|  | spectrum 1 | spectrum 2 |
|---|---|---|
| Element | Concentration (at.%) | |
| O | 37.29% | 9.73 |
| Mg | 1.22 | 0.95 |
| Al | 35.24 | 87.14 |
| Si | 11.86 | 2.18 |
| Ti | 13.17 | |
| Fe | 1.22 | |



**Figure 4-17 Ti containing oxide growing discovered on the surface of 2L99 +Ti sample.**

(a)



(b)

(c)

**Figure 4-18 (a) High magnification of Ti containing oxide in Figure 4-17; (b) EDX spectrum for X1; (c) EDX spectrum for X2.**
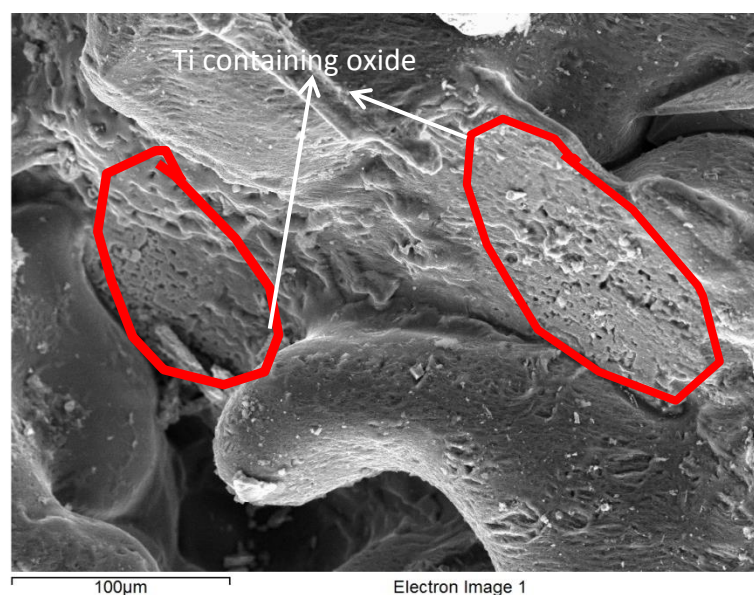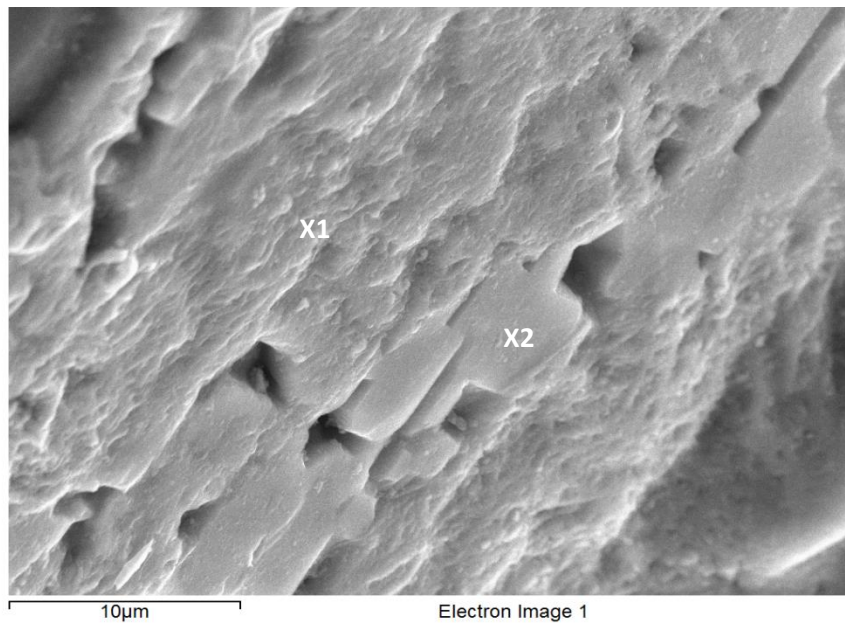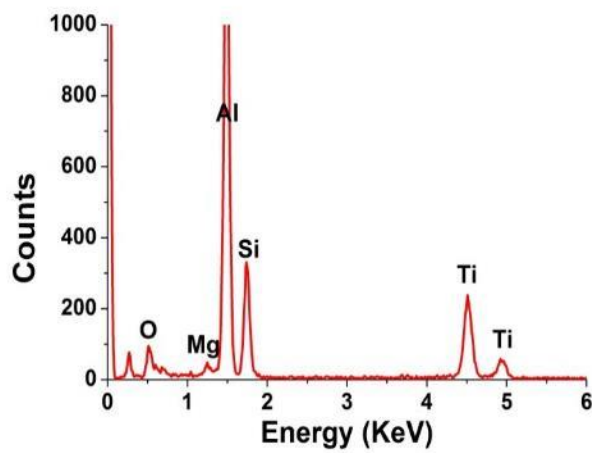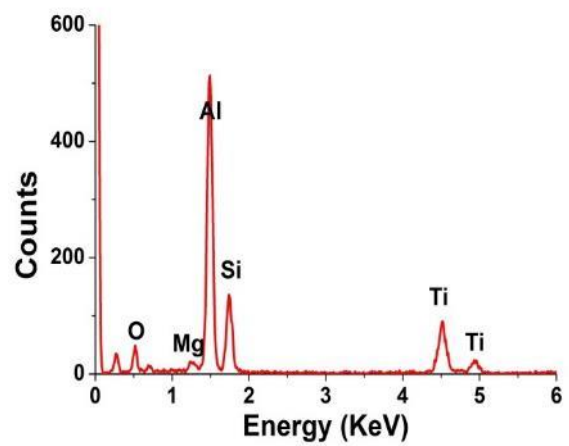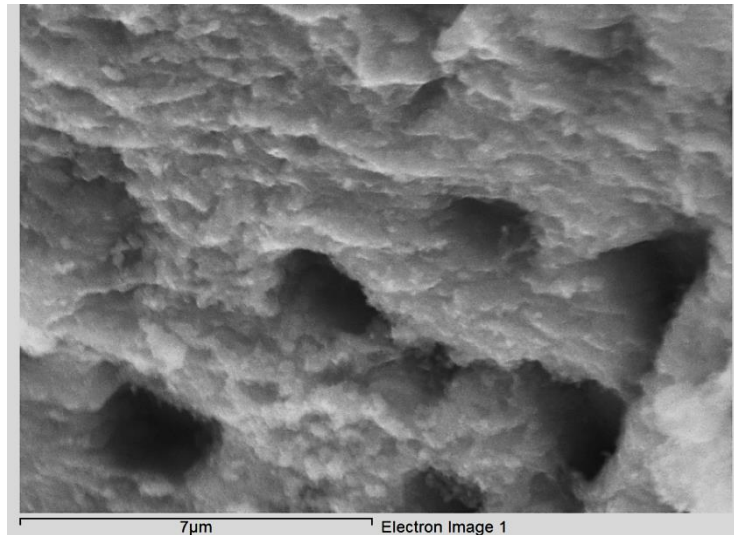
**Figure 4-19 High magnification of Ti containing oxide.**

**Table 4-5 Quantity measurements of the Ti containing oxide layer on Figure 4-18 X1 and X2.**

|  | Figure 4-18 X1 | Figure 4-18 X2 |
|---|---|---|
| Element | Atomic% | Atomic% |
| O | 33.09% | 31.47% |
| Mg | 1.09% | 0.89% |
| Al | 42.49% | 40.21% |
| Si | 7.82% | 15.4% |
| Ti | 14.81% | 10.84% |
| Fe | 0.70% | 1.19% |

### 4.1.2.3 The addition of Zr into 2L99 alloy

For the Zr addition to 2L99, the liquid metal rose 16 mm into the blind hole. SEM investigation of the sample surface failed to find nitride and EDX suggested that Zr was not seen participating in the reaction to form the oxide layer. The oxidised layer found on the sample surface is shown as Figure 4-20. The area of spectrum X2 showed a brighter band. Compositional analysis showed that these areas had a high Fe content, which suggested a Fe-rich intermetallic phase (possibly β-$Al_5FeSi$) in the nearby region.

Figure 4-20 (a) Oxide surface found on the sample surface with 2L99+Zr; (b) EDX spectrum for X1 and (c) EDX spectrum for X2.

Table 4-6 Quantity measurements for EDX spectrum in Figure 4-20.

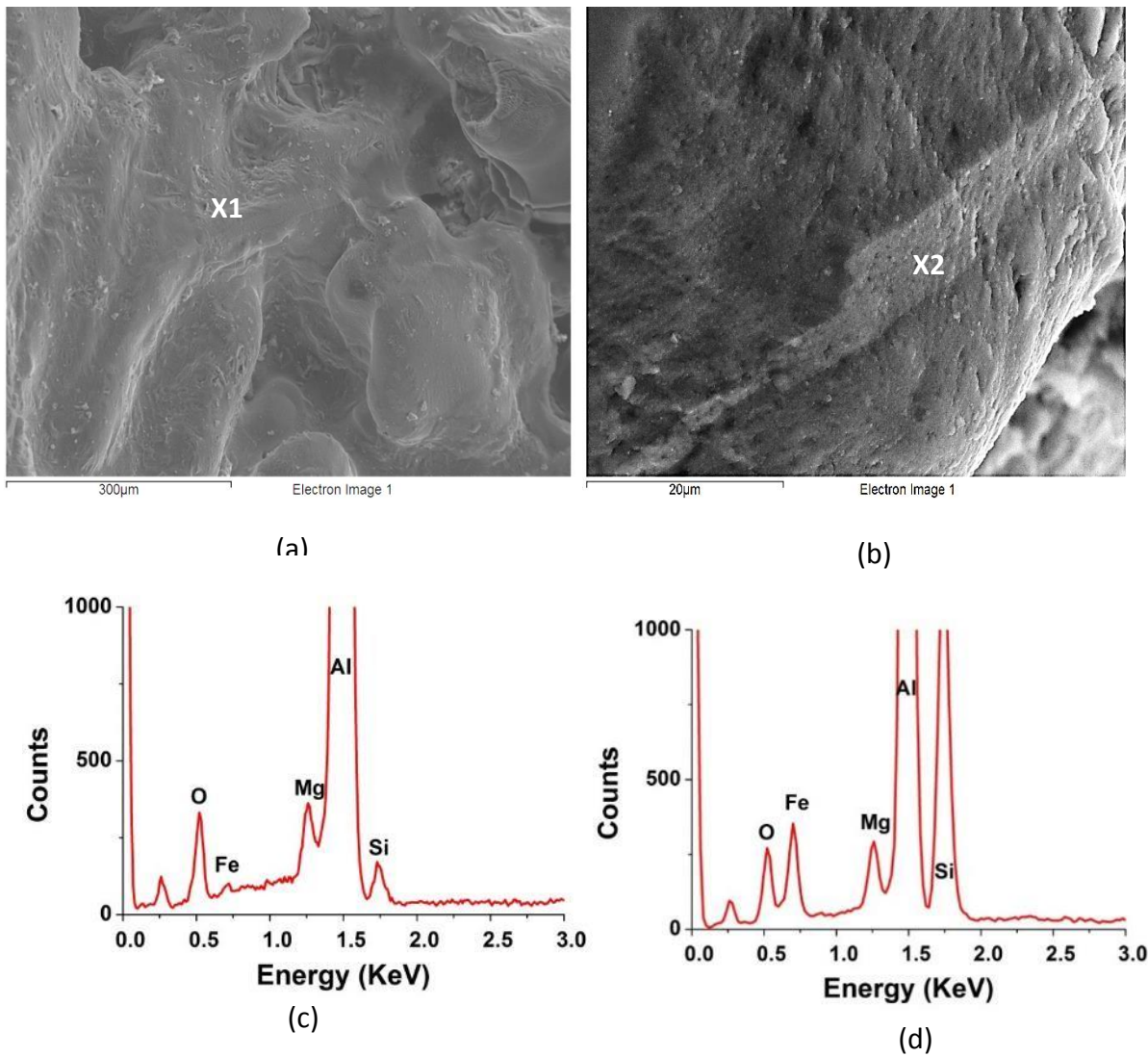|  | spectrum 1 | spectrum 2 |
|---|---|---|
| Element | Concentration (at.%) | |
| O | 10.27% | 20.50% |
| Mg | 1.06% | 2.45% |
| Al | 78.51% | 48% |
| Si | 6.60% | 20.70% |
| Fe | 0.34% | 8.25% |

### 4.1.2.4  The addition of Hf into 2L99 alloy

In this experiment, the liquid metal entered to a height of 14mm inside the blind hole. EDX analysis suggested that only oxide was found on the sample surface, and Hf did not participate in the oxide-forming reaction, as can be seen in Figure 4-21.



(a)                                              (b)
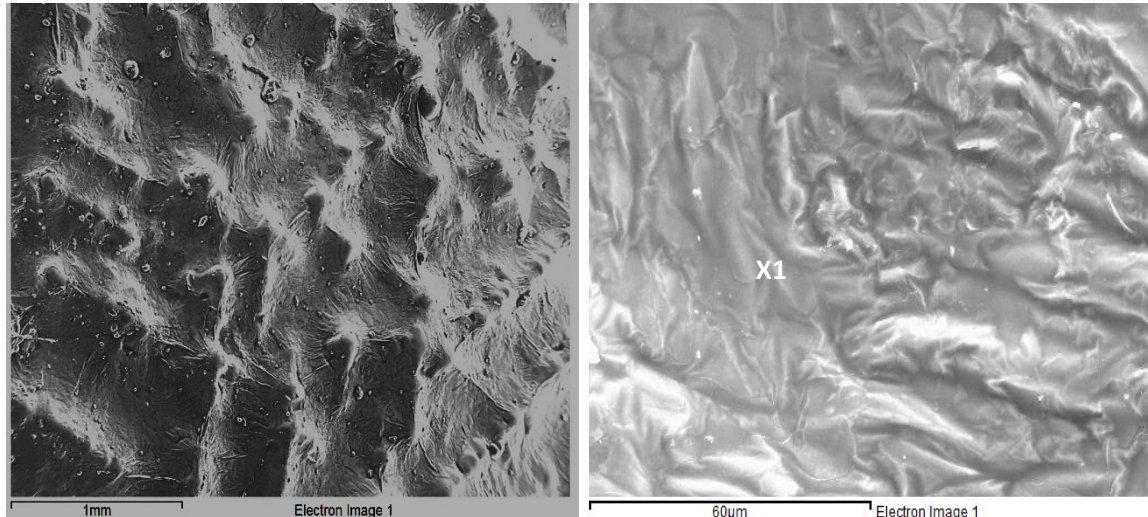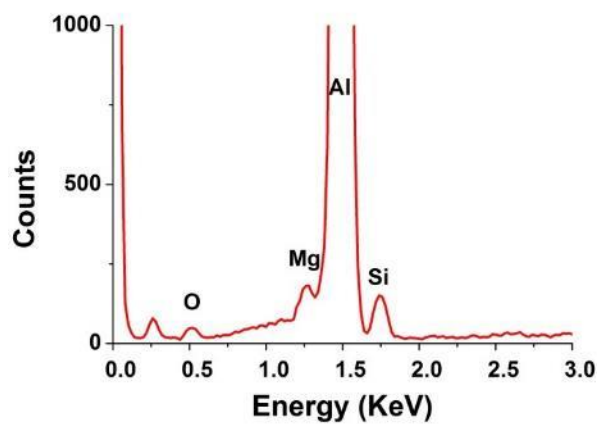


| Element | Concentration (at.%) |
|---------|----------------------|
| O       | 3.46                 |
| Mg      | 0.67                 |
| Al      | 92.42                |
| Si      | 3.45                 |

(c)                                              (d)

**Figure 4-21 (a)-(b) Sample surface of the experiment with 2L99+Hf; (c) EDX spectrum of X1 and (d) quantity measurements of spectrum x1.**

### 4.1.2.5   The addition of Sc into 2L99 alloy

With the Sc addition to 2L99, the liquid metal entered 35 mm inside the 40 mm blind hole, which suggested that the reaction between the liquid metal and the entrapped gas had reached a stage where the majority of the oxygen and nitrogen had been consumed. Both oxide and nitride were observed on the sample surface.

Figure 4-22 X1 showed a smooth oxide layer on the upper surface of the sample, with no N peak identified by EDX. In Figure 4-22 at X2 shows that the sample surface consisted of particles. EDX (see Figure 4-22(c)) suggested that this could be a nitride layer. Higher magnification images of the particles are shown in Figure 4-23 and Figure 4-24.

White spots, dispersed all over the sample surface, were shown to contain a high Mg and O content (Figure 4-22 X3, Figure 4-23 X2). They are, therefore, possibly to be spinel ($MgAl_2O_4$) or MgO particles.
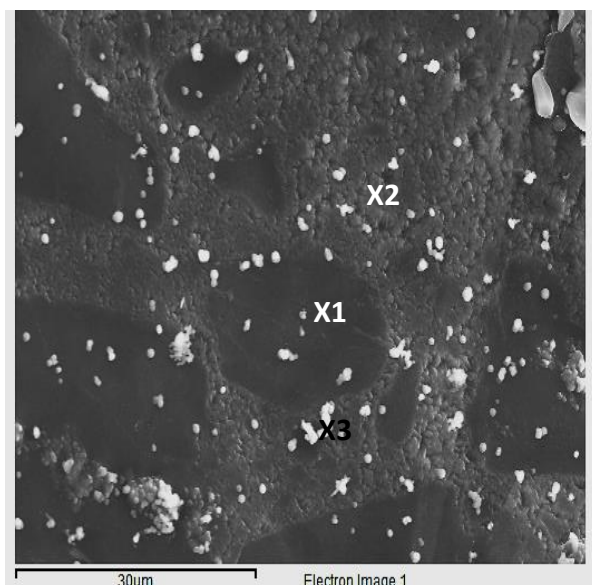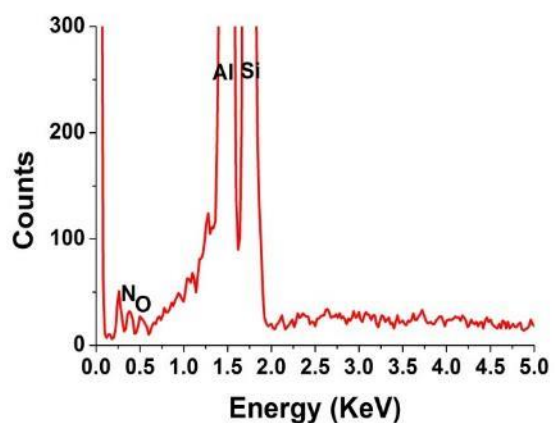


(a)                                                        (b)
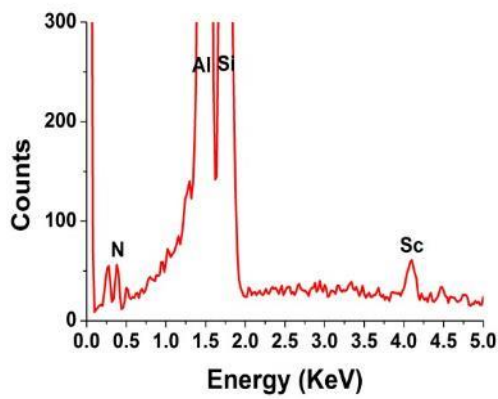
(c)
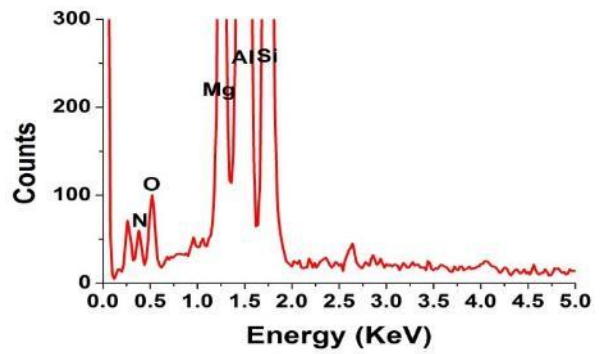


(d)

**Figure 4-22 (a) The surface morphology of the sample with 2L99+Sc; (b)-(d) EDX analysis of the area X1-X3.**
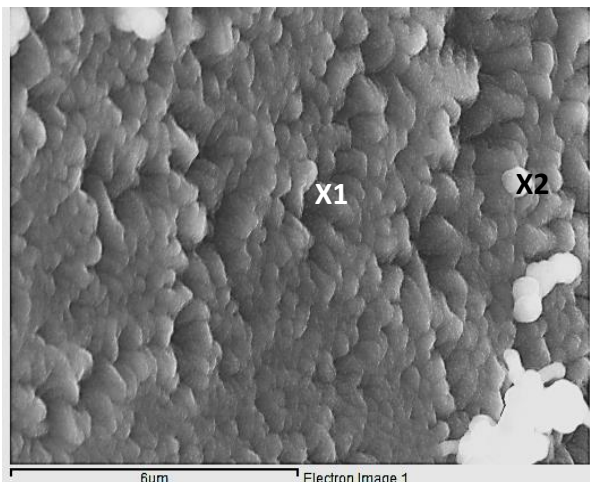


(a)
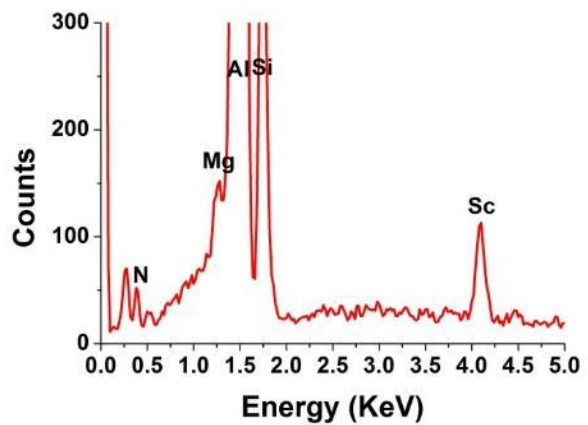


(b)

**Figure 4-23 (a) Sc containing nitride layer found on the surface of sample with 2L99 +Sc; (b)EDX of spectrum 1 showing the Sc containing nitride layer and (c) EDX of spectrum 2 showing the high Mg and O peak in the white spot in the area.**



(c)

(a)

(b)
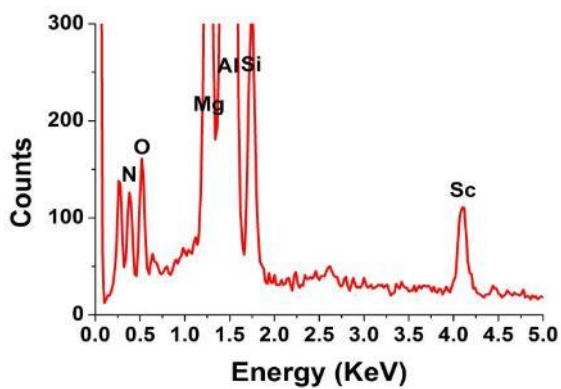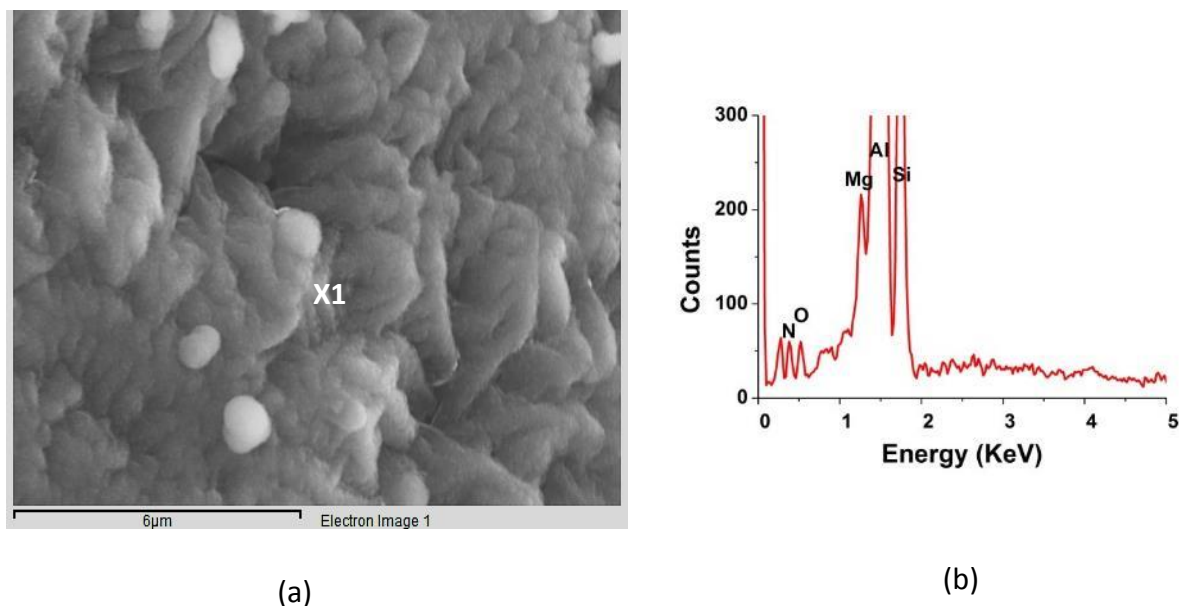
**Figure 4-24 (a) The high magnification image Figure 4-23 X1; (b)EDX spectrum of X1.**

In order to have a better understanding of the composition of the layer formed on the sample surface, Focused Ion Beam milling was used to extract a sample for the investigation of its cross-section.

Figure 4-25 (a) shows the area selected for FIB milling, while (b) shows the cross-section revealed after milling. A high magnification image of the red areas in Figure 4-25 (a) are shown in Figure 4-26 to Figure 4-28 respectively.

Figure 4-26 and Figure 4-28 are cross-sections of the smooth oxide layer, which are identical to the oxide in Fig.4-22 X1, observed from the top view.

Figure 4-26 X1 shows a dark coloured Si phase (see Figure 4-26 (b)). X2 shows the presence of Sc in the EDX (Figure 4-26(C)), which suggested that this could be an Al-Sc intermetallic compound. The Si phase and Al-Sc intermetallic phases are all located near the oxide layer (shown in Figure 4-26(c)). According to Campbell[1], they could be nucleated on the wetted side of the oxide layer.

109

Figure 4-28 showed a bright particle 1 μm in diameter. EDX (Figure 4-28 (b)) confirmed that this could be a spinel particle. X2 shows the oxide layer, which might be permeable and contain some microchannels (as labelled). EDX (shown in Figure 4-28 (c)) suggested the presence of Sc which indicated that Sc participated in the oxide-forming reaction.

Figure 4-27 showed the area identical to Figure 4-22 X2 but from the top. EDX for Figure 4-27 X1, shown in Figure 4-27 (c), suggested that N was involved in the formation of the surface layer.
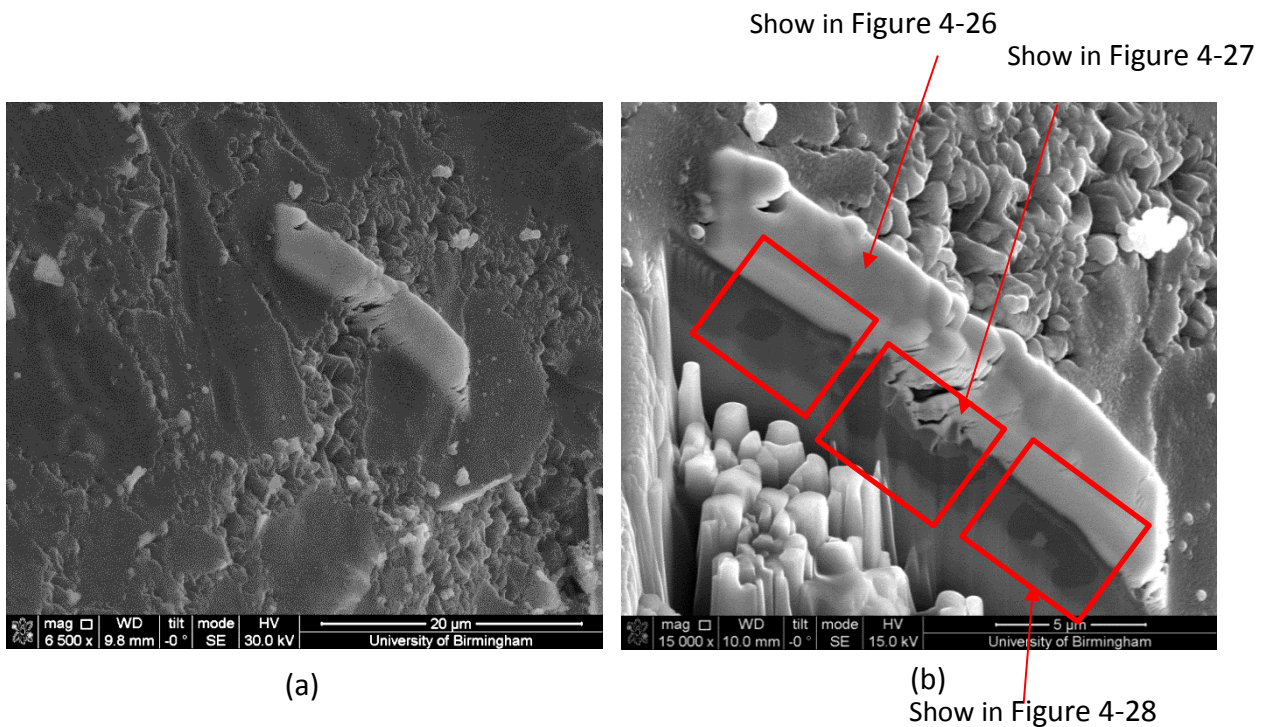


**Figure 4-25 The sample surface of 2L99+Sc used for cross-section examination.**
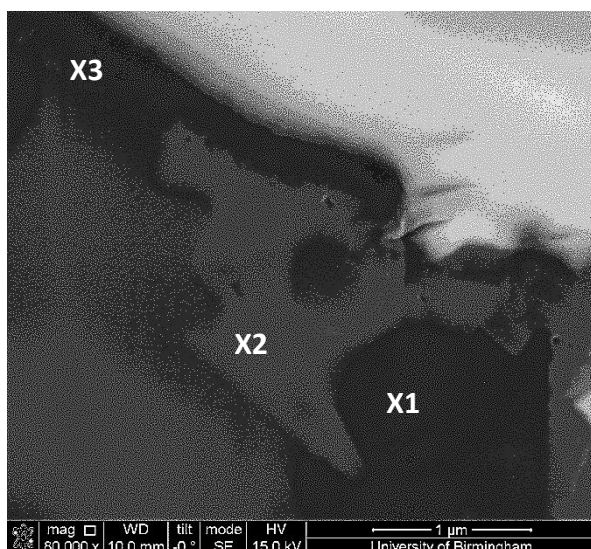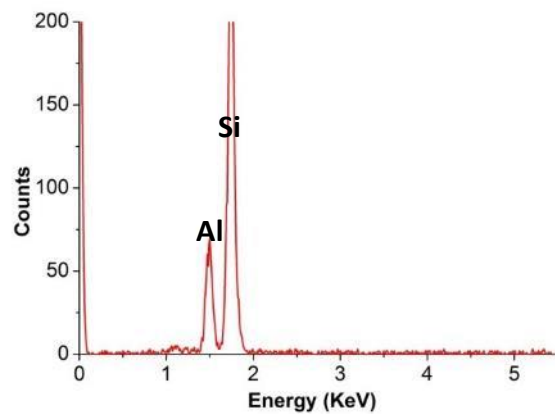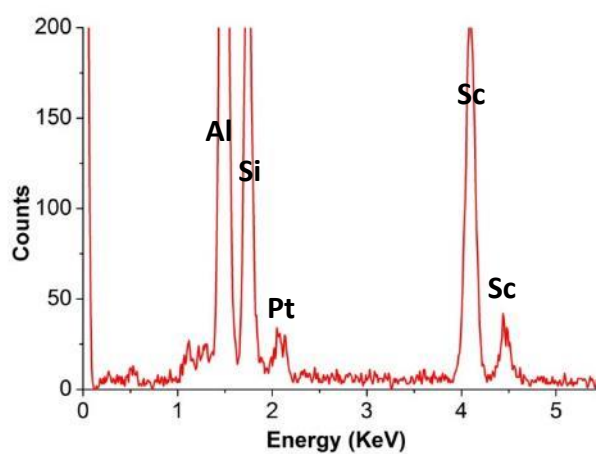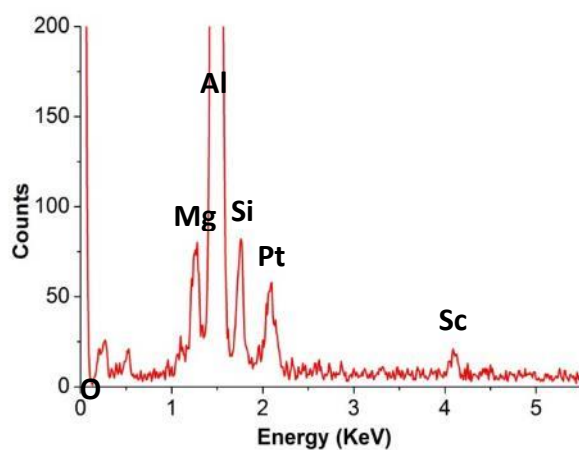
Figure 4-26 (a) The labelled area in Figure 4-25; (b)-(d) EDX spectrum of X1-X3 .
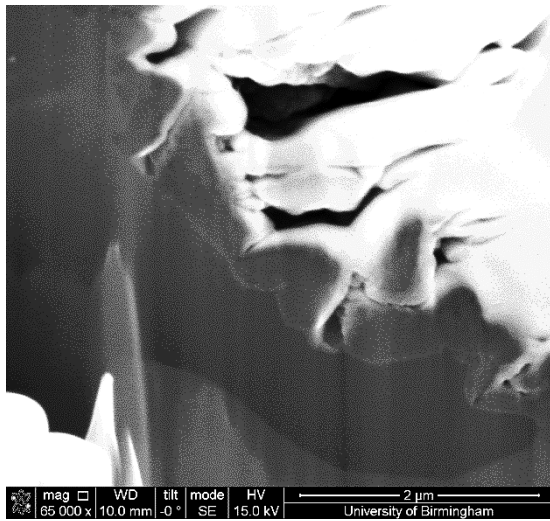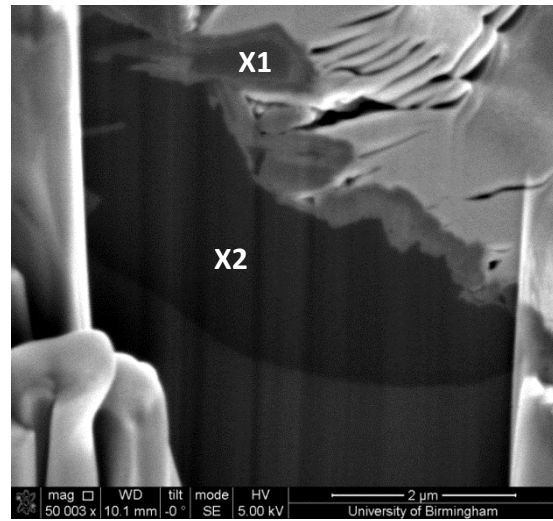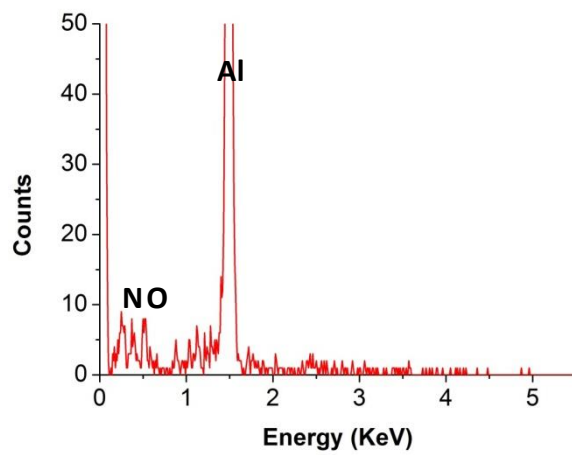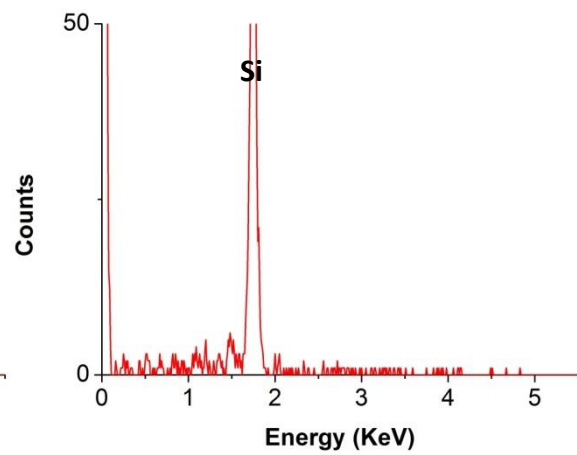
Figure 4-27 (a), (b) SEM image showing the labelled area in Figure 4-25; (c)-(d) EDX spectrum of X1 and X2 respectively.
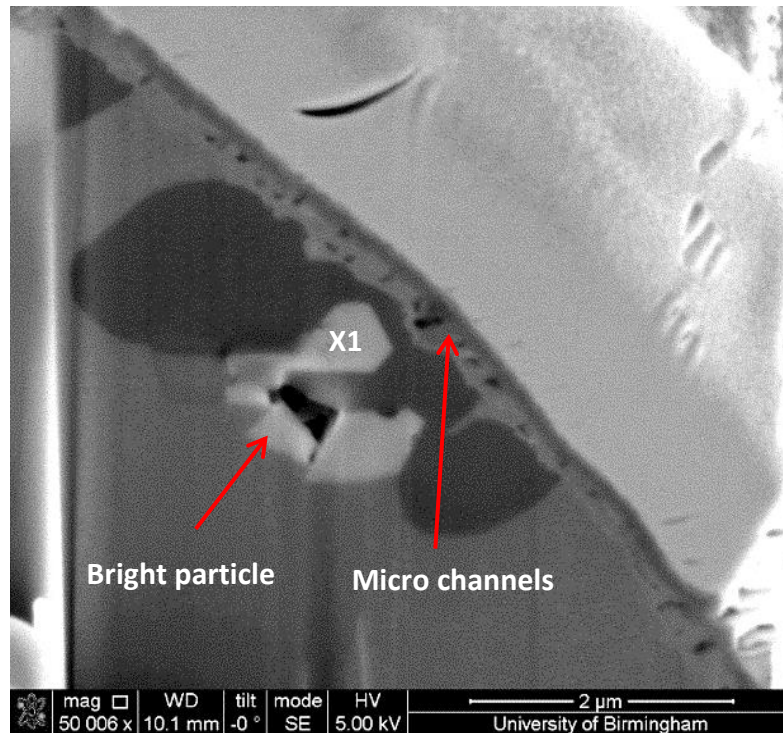
(a)
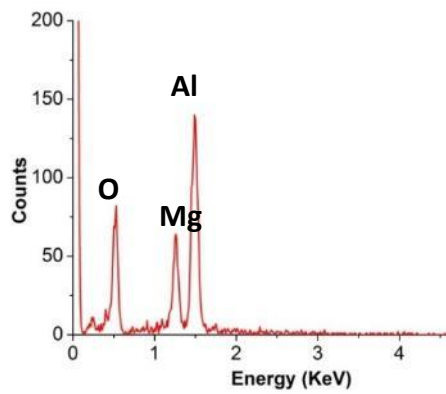


(b)
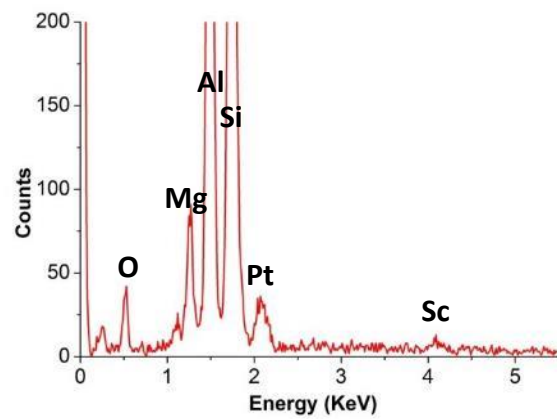


(c)

**Figure 4-28 (a) SEM showing the labelled area in Figure 4-25, (b)-(c) EDX spectrum of X1 and X2 respectively.**

### 4.1.2.6 The addition of Mo into 2L99 alloy

For the sample with Mo addition into 2L99, the liquid metal entered 23 mm into the blind hole (58% of its depth) and at this stage nitrogen would be expected to be consumed to form both oxide and nitride (Figure 4-29 to Figure 4-32), detected on the sample surface. Strong Mo peaks were also detected in those spectra. Figure 4-29 shows an area which contained both oxide and nitride. A high magnification image of Figure 4-29 is shown in Figure 4-30, which suggested that the layer consisted of 500 nm sized particles.
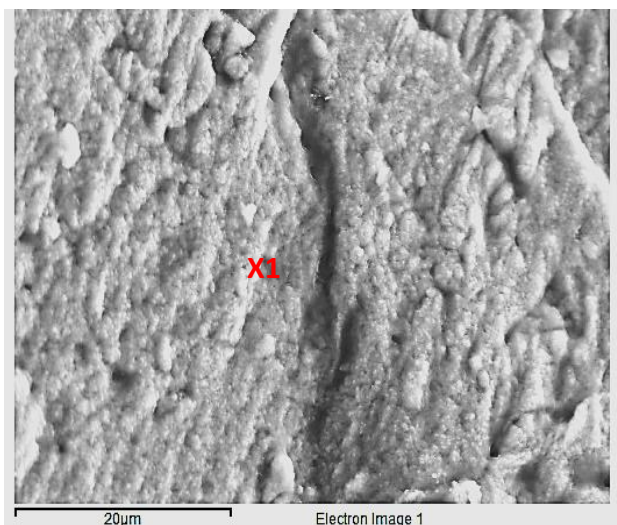


(a)
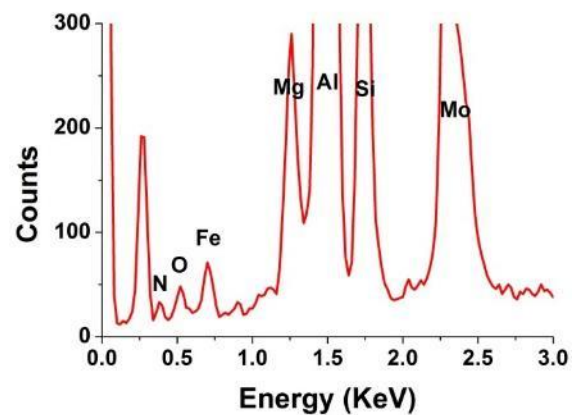
(b)

**Figure 4-29 Mo containing oxide layer on the sample with 2L99+Mo; (b) EDX spectrum of X1.**
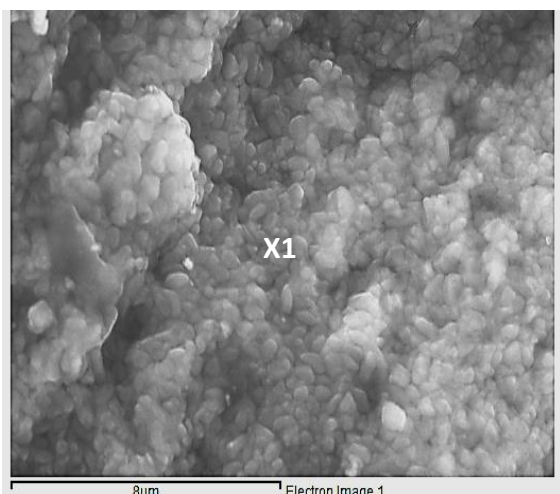
(a)
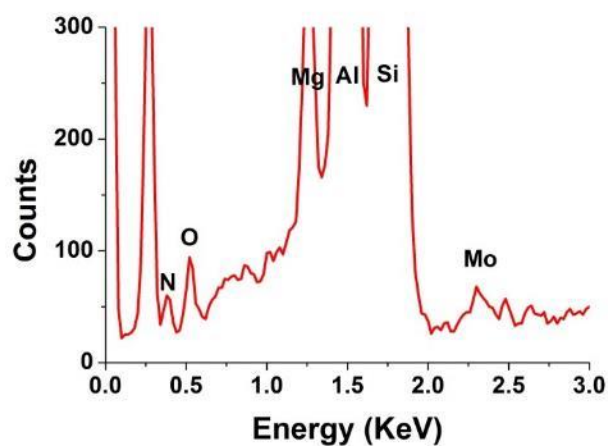
(b)

**Figure 4-30 (a) Higher magnification of the Mo containing oxide layer on Figure 4-29; (b) EDX spectrum for X1.**

A nitride layer was also observed, shown in Figure 4-31, (see Figure 4-32 for a high magnification image). The nitride had a granular appearance, and a Mo peak was detected in this area (see Figure 4-31 X1 and Figure 4-32 X1). As no oxygen peak was detected, it would seem that the nitride layer was growing directly on the aluminium alloy matrix.



(a)

(b)
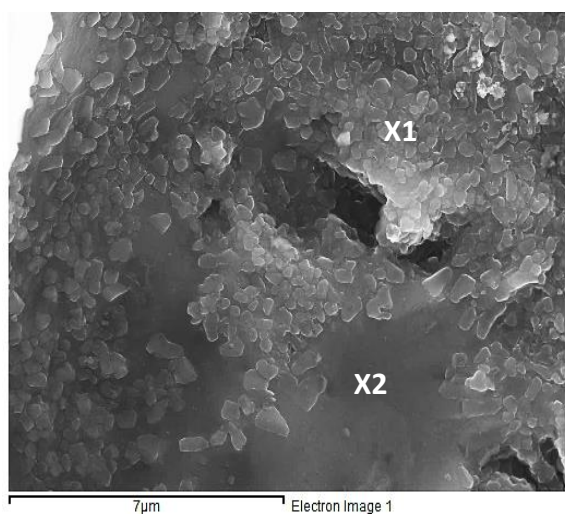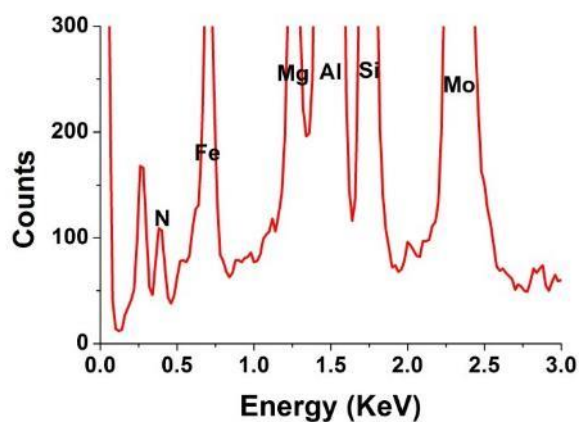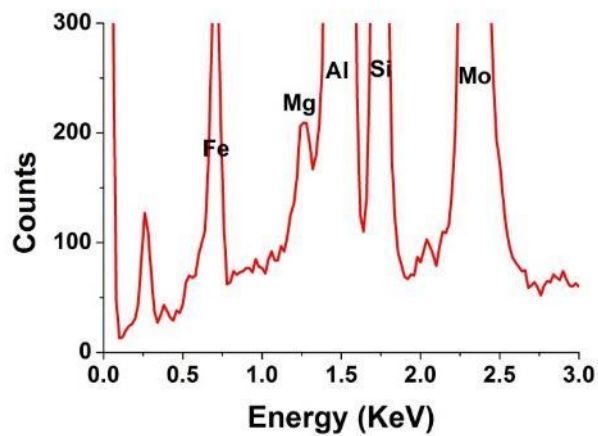
Figure 4-31 (a) Granular nitride found on the sample surface of 2L99+Mo; (b) EDX spectrum for X1 and (c) EDX spectrum for X2.

(c)
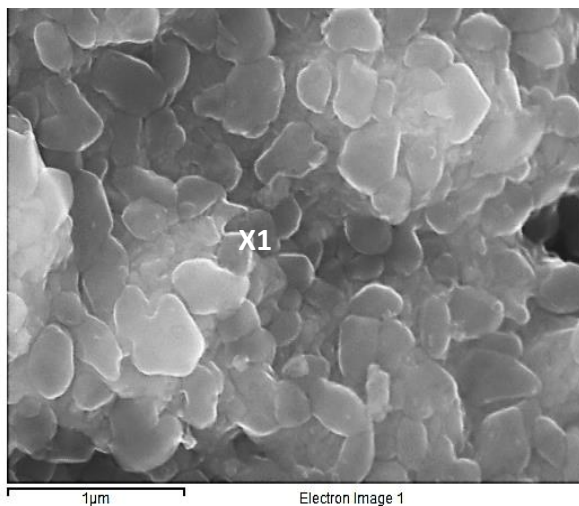
(a)
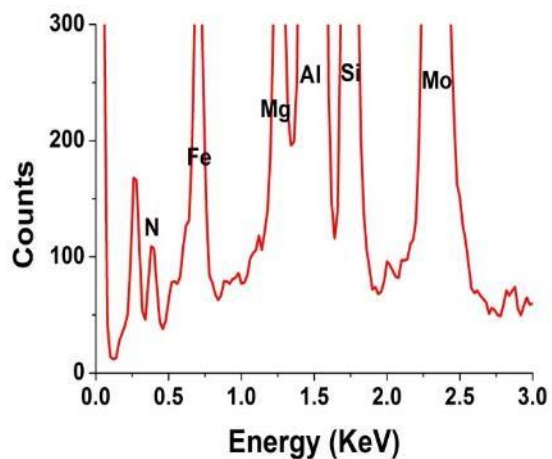
(b)

Figure 4-32 (a) High magnification image of nitride found on the sample surface of 2L99+Mo and (b) EDX spectrum for X1.

The quantification of the EDX spectra for Mo-containing oxide, Mo containing nitride and the aluminium matrix are shown in Table 4-7, which shows the Mo composition in all three areas was similar.

Figure 4-33 shows the Mo containing intermetallic phase growing on one side of a double oxide film. The intermetallic phase had a particle size of about 30μm.

(a)

(b)

(c)

(d)
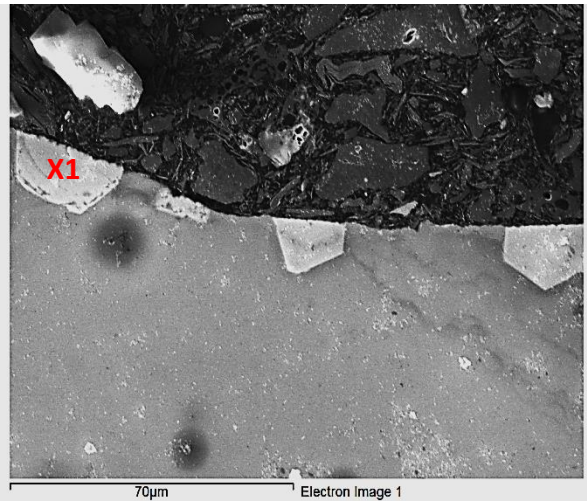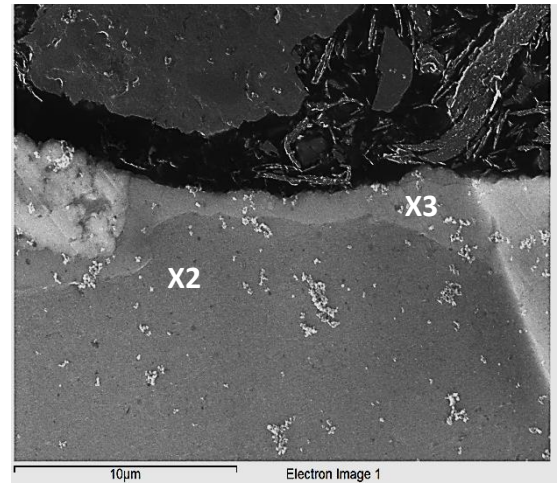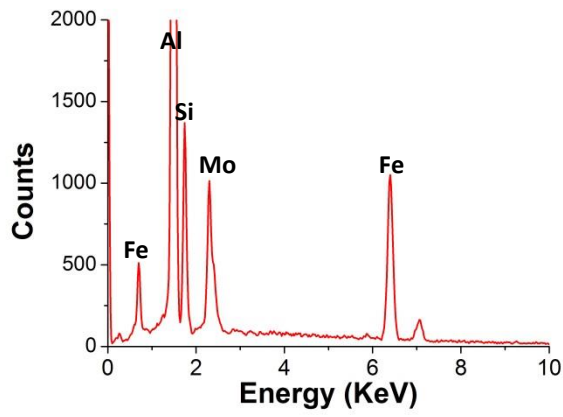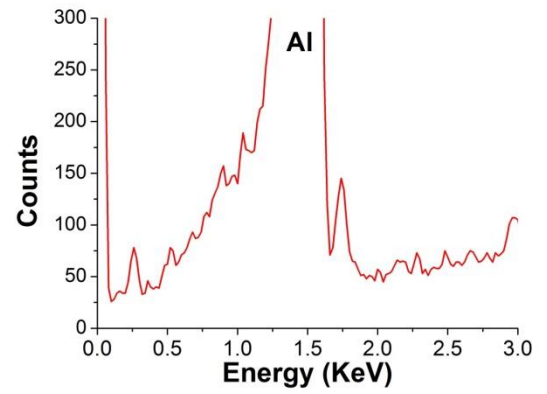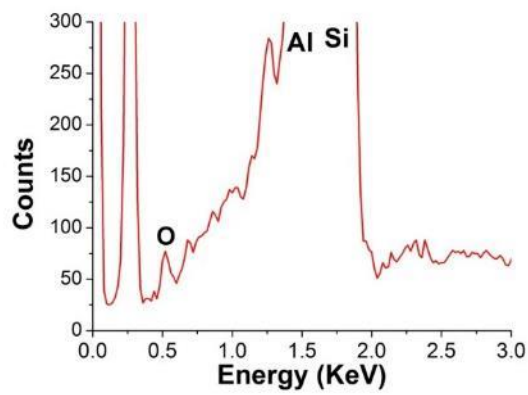
**Figure 4-33 (a) and (b) The cross-section of the sample with 2L99+Mo showing the intermetallic phase and the oxide layer; (c)-(e) EDX spectrum of X1-X3.**

(e)

**Table 4-7 Quantification of the EDX spectrum of the sample with 2L99+Mo.**

| Element | Figure 4-30 X1 | Figure 4-31 X1 | Figure 4-31 X2 |
|---------|---------|---------|---------|
|  | Concentration ( at.%) | | |
| N | 3.25 | 21.06 | 0 |
| O | 9.43 | 0 | 0 |
| Mg | 3.46 | 3.15 | 0.31 |
| Al | 58.79 | 52.56 | 40.46 |
| Si | 9.52 | 10.32 | 12.97 |
| Fe | 6.7 | 7.43 | 21.08 |
| Mo | 6.47 | 5.48 | 28.98 |

### 4.1.3 Entrapped air bubbles in Al-5Mg alloy

Three elements were added into Al-5Mg alloy, Ti, Zr and Mo. 0.5 wt.% of each element was added, and the actual recovery is shown in Table 4-8. The amount of liquid metal inside the blind hole is shown in Figure 4-34.

More liquid metal entered the blind hole in the experiment with Al-5Mg, compared with the experiments with CP-Al (i.e 30% more gas was consumed) or 2L99 (80% more gas consumed). Nitride was found on all of the samples, which confirmed that they were all at the stage where nitrogen was being consumed.

**Table 4-8 Element pickup for the experiment with additions added to Al-5Mg.**

| experiment | Element pickup | Fe pickup |
|---------|---------|---------|
| Al-5Mg | N/A | 1.55% |
| Mo addition | 0.37 wt.% | 1.35% |
| Ti addition | 0.32 wt.% | 1.46% |
| Zr addition | 0.40 wt.% | 1.89% |
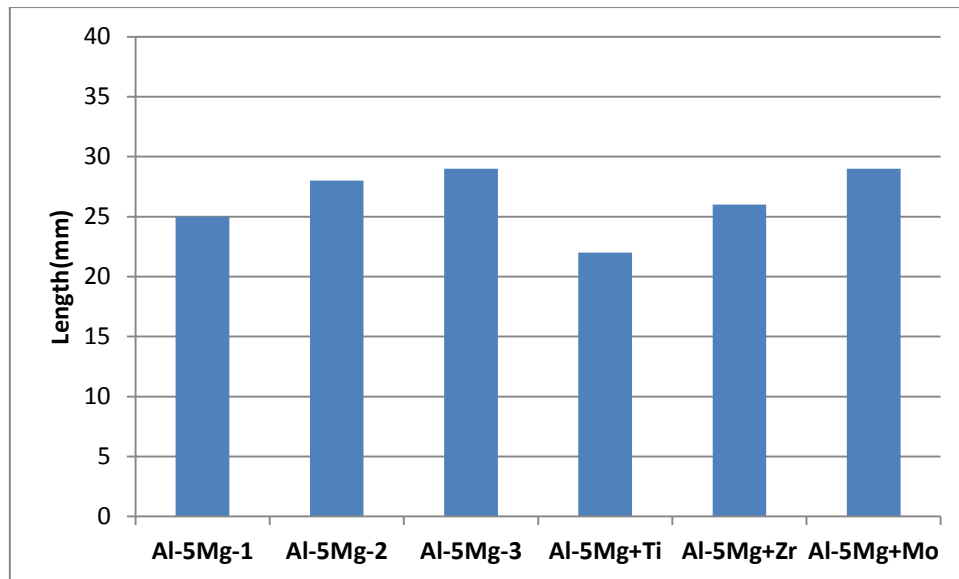
**Figure 4-34 Height of metal solidified in the blind hole for the experiment with elements addition into Al-5Mg alloy.**

### 4.1.3.1 The experiment with Al-5Mg alloy

For the experiment with Al-5wt.%Mg, the liquid metal entered 27 mm into the blind hole and Figure 4-35 was the sample surface. EDX showed a very small oxygen peak( 1.8 at.%) and nitride peak (5.6 at. %) which suggested that the area had a very thin oxide and nitride layer. Figure 4-36 showed a fracture of the surface layer (as labelled), which might be due to the stress generated during rising of the liquid metal.

A feather-like nitride layer was seen on the sample surface (see Figure 4-37 X2) surrounded by spots, their appearance assembling nitride found from the sample with CPAl. Figure 4-37 X3, with the EDX shown in (d), suggested that the smooth layer was an oxide layer. The compositions of the three spectra in Figure 4-37 are shown in Table 4-9.

Figure 4-38 (a) shows a higher magnification of the intersection between the oxide and nitride layers (as labelled). EDX analysis suggested that the smooth area shown in X1( Figure

4-38 (b)) was an oxide layer, which x3 and X4 (Figure 4-38 (d)-(e)) showed a nitrogen peak, which suggested that those areas might be nitride. X2 showed a similar composition as X1, which suggested that the area was an oxide island surrounded by nitride.

Figure 4-39 shows an intersection point between the feather-like nitride and oxide layer. Figure 4-40 shows a rupture of the nitride layer and the aluminium matrix underneath is revealed.



(a)

(b)
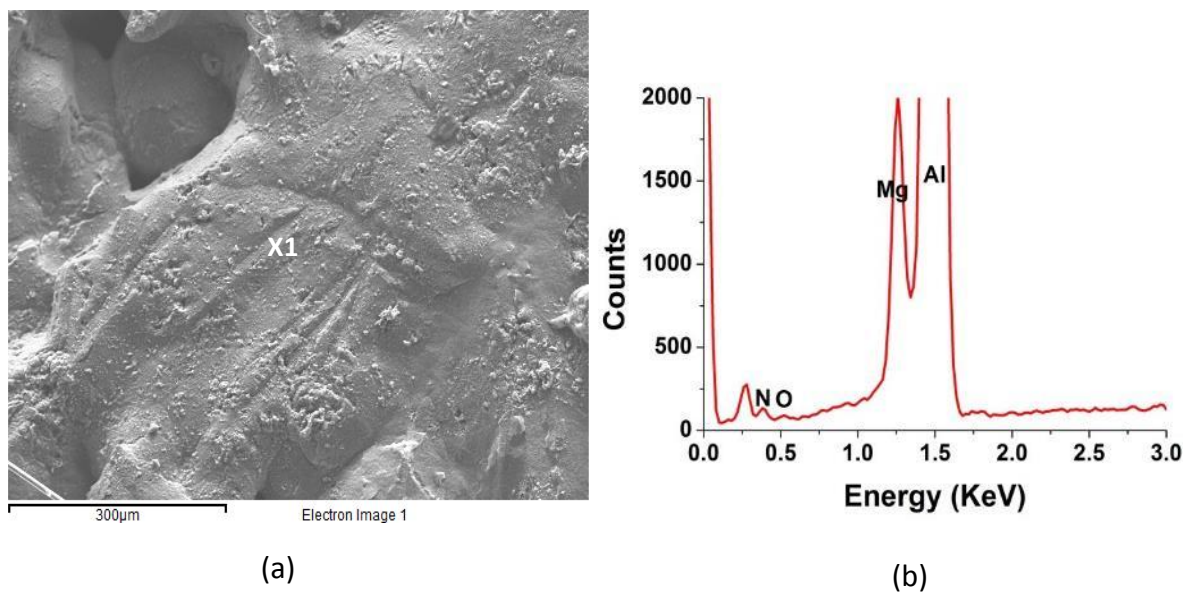
**Figure 4-35 (a) Morphology of the sample surface found on Al-5Mg alloy and (b) EDX spectrum of X1.**
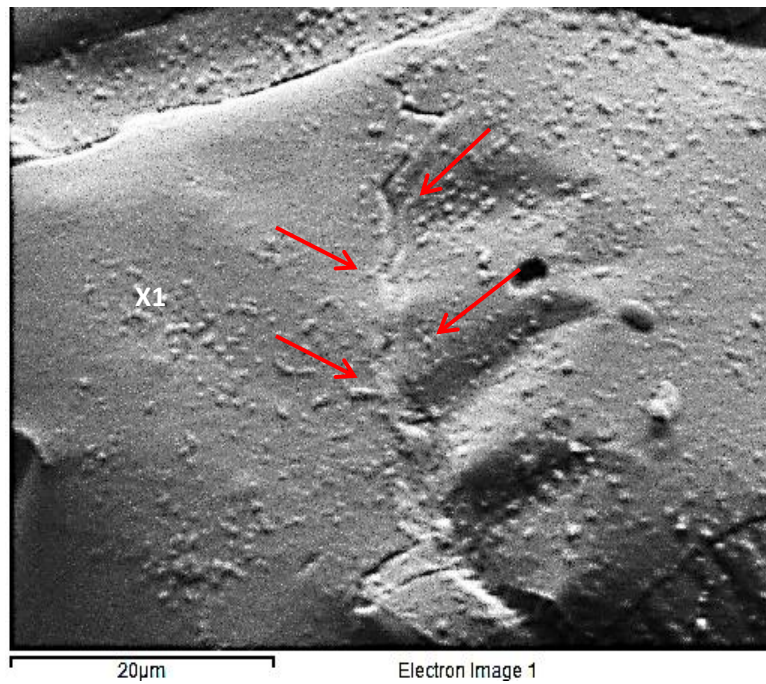
(a)
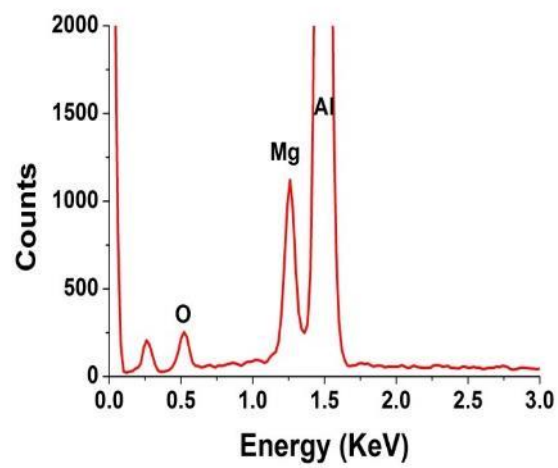


(b)

**Figure 4-36 (a) The rupture of the MgO layer and (b) EDX spectrum of X1.**
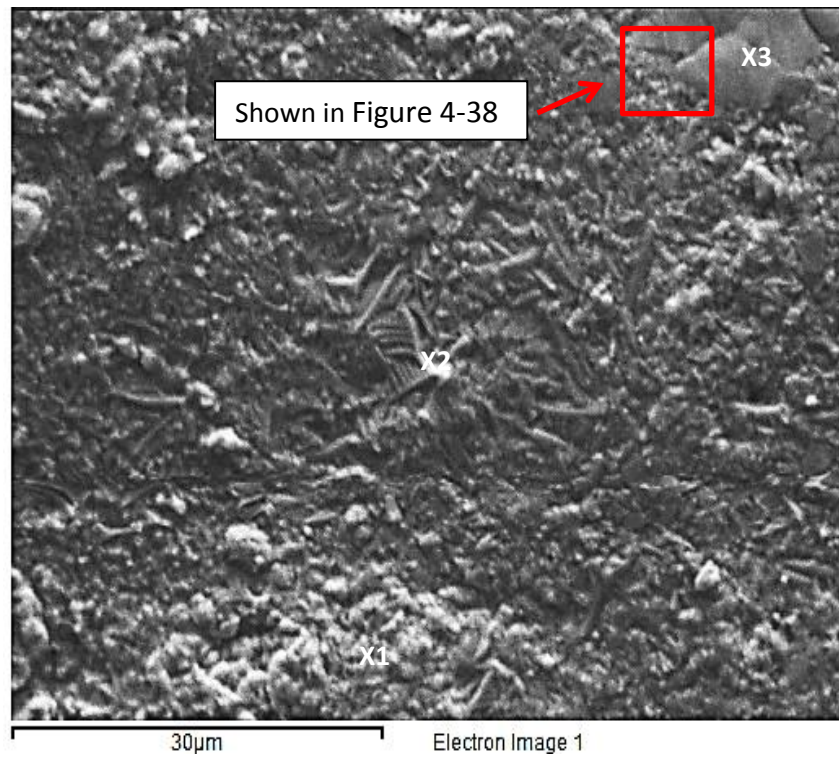
(a)
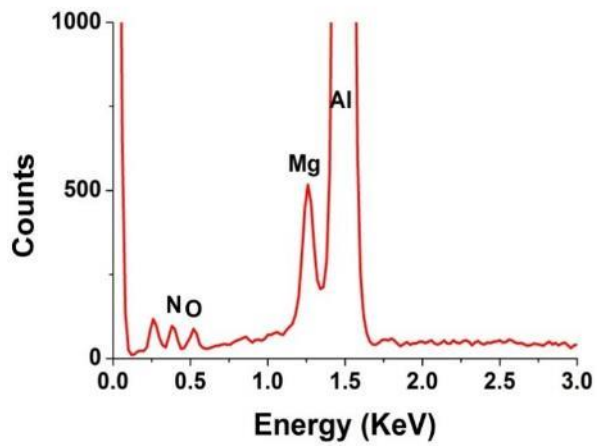


(b)
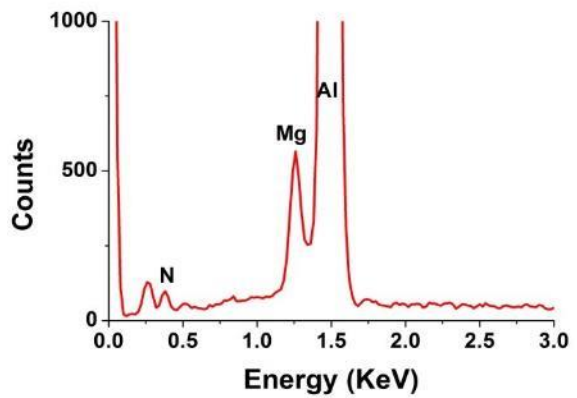


(c)
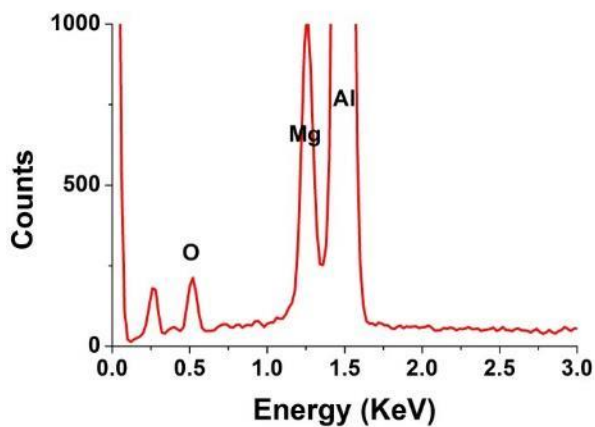


(d)

**Figure 4-37 (a) The nitride layer shown on the sample surface of Al-5Mg; (b) EDX spectrum for X1; (c) EDX spectrum for X2 and (d) EDX spectrum for X3.**

122
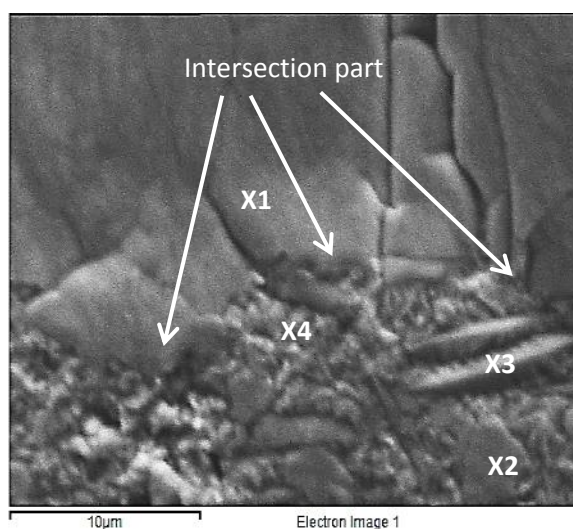
(a)
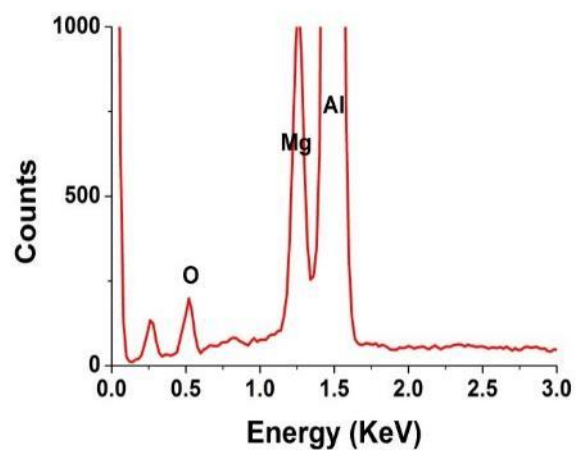
(b)
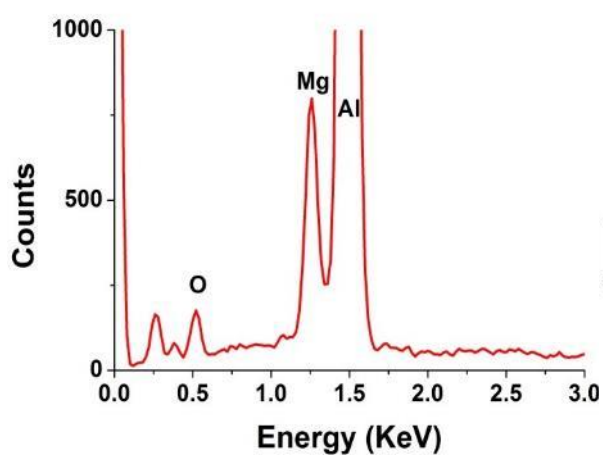
(c)
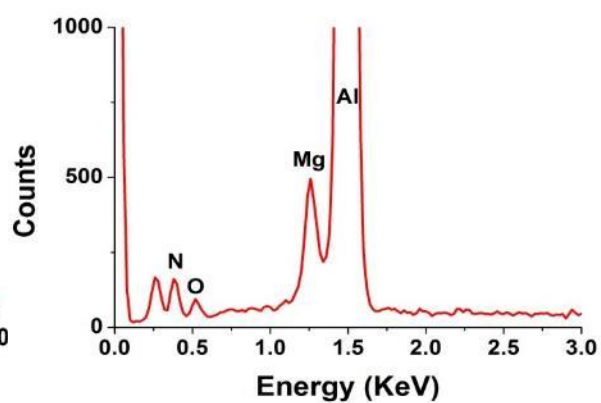
(d)
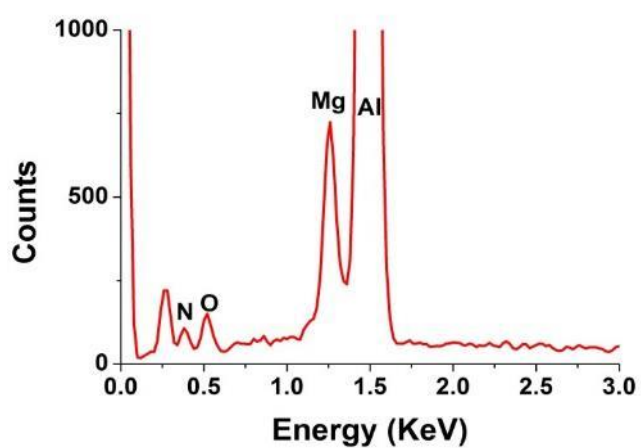
(e)

Figure 4-38 (a) High magnification image of the intersection area between the oxide an nitride as shown on Fig. 4-37; (b)-(e) EDX spectrum of X1-X4.

| | spectrum 1 | spectrum 2 | spectrum 3 |
|---|---|---|---|
| Element | Concentration (at.%) | | |
| N | 6.2 | 6.08 | 0 |
| Mg | 4.76 | 3.47 | 7.93 |
| Al | 83.05 | 90.45 | 86.43 |
| O | 2.02 | 0 | 5.64 |
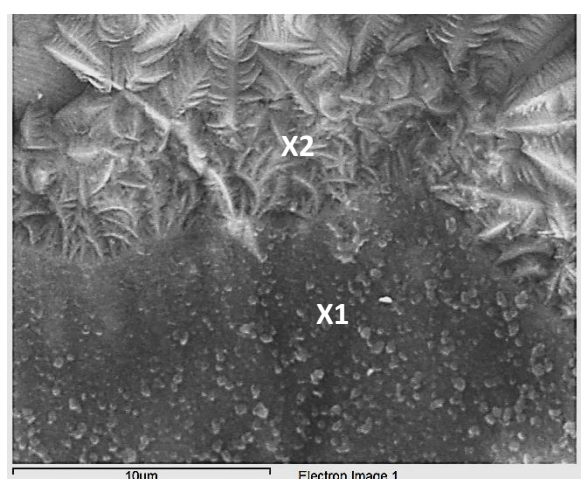


(a)
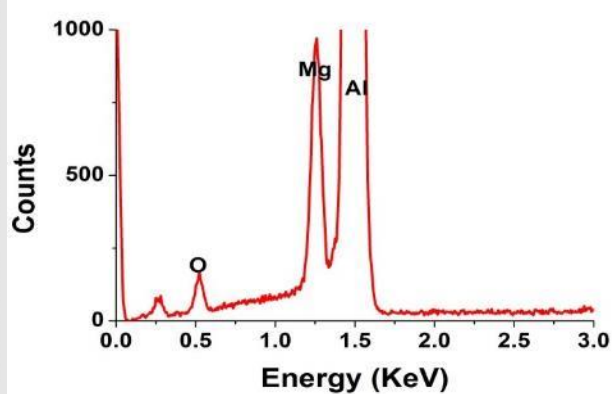


(b)
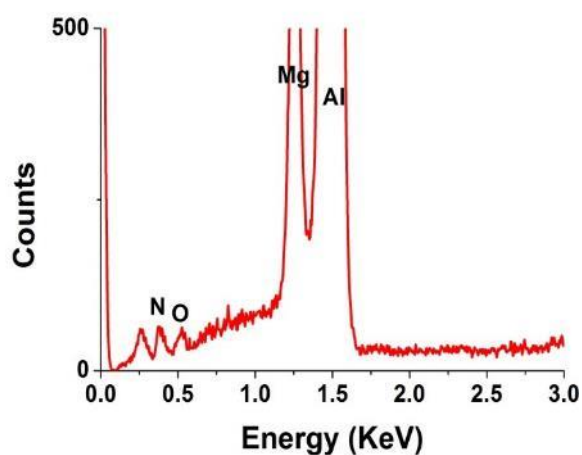


(b)

Figure 4-39. (a) The area showing the feather like nitride layer growing on the oxidised layer and (b) EDX spectrum for X1.
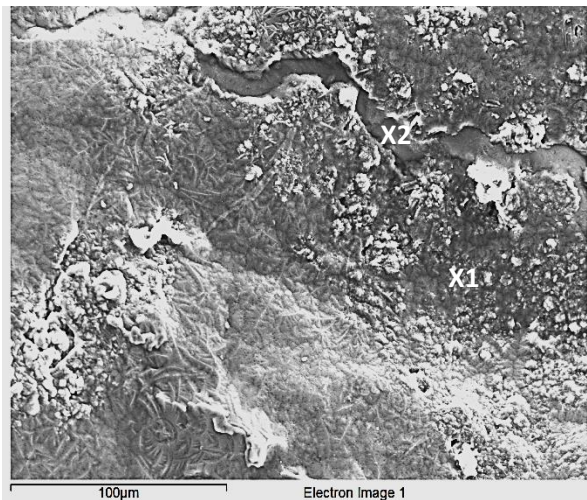
(a)
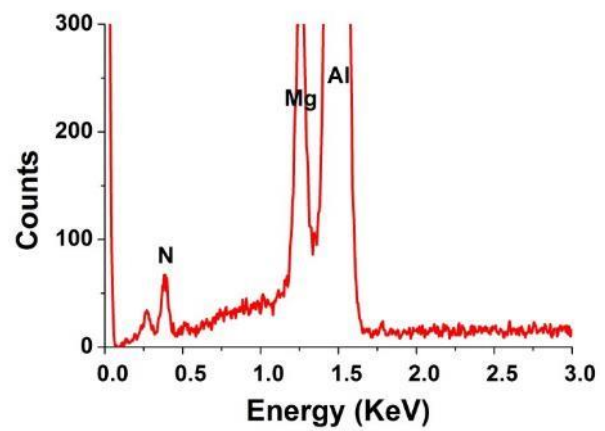
(b)
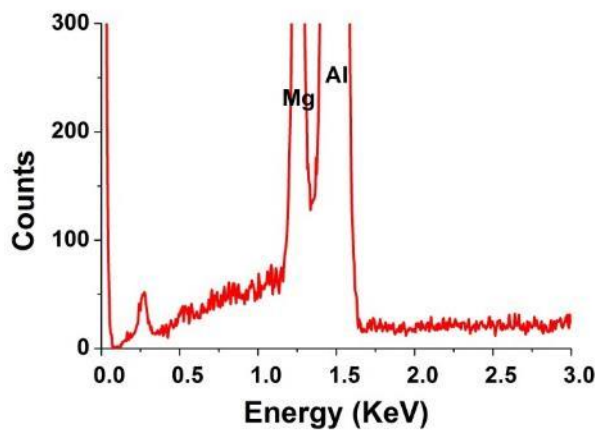
(c)

Figure 4-40. The rupture of nitride layer on the surface of Al-5Mg; (b)EDX for nitride layer shown as spectrum 1 and (c) EDX for spectrum 2 showing the breaking point of nitride layer.

### 4.1.3.2  The addition of Ti to Al-5Mg alloy

For the experiment with Ti addition into CPAl-5Mg, the liquid metal entered 23 mm inside the blind hole. Investigation of the sample surface indicated that feather-like nitride covered most of the sample surface (see Figure 4-41). There was no sign of Ti participating in the reaction with the nitride layer.
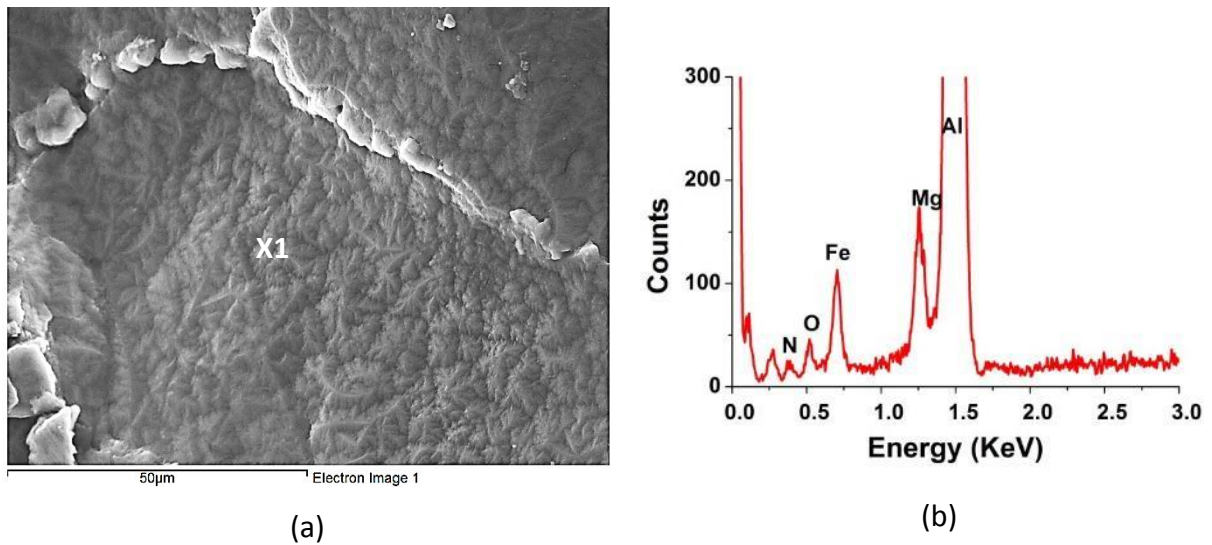
**Figure 4-41. (a) Surface morphology of the sample with Ti addition into Al-5Mg alloy and (b) EDX spectrum of X1.**

### 4.1.3.3 The addition of Zr to Al-5Mg alloy

In the experiment with 0.5 wt.% Zr addition to Al-5Mg alloy, the liquid metal entered 26mm into the blind hole. Feather-like nitride was again seen on the sample surface, see Figure 4-42. No evidence for Zr participating in the reaction was found.



(a)                              (b)

(c)                                              (d)
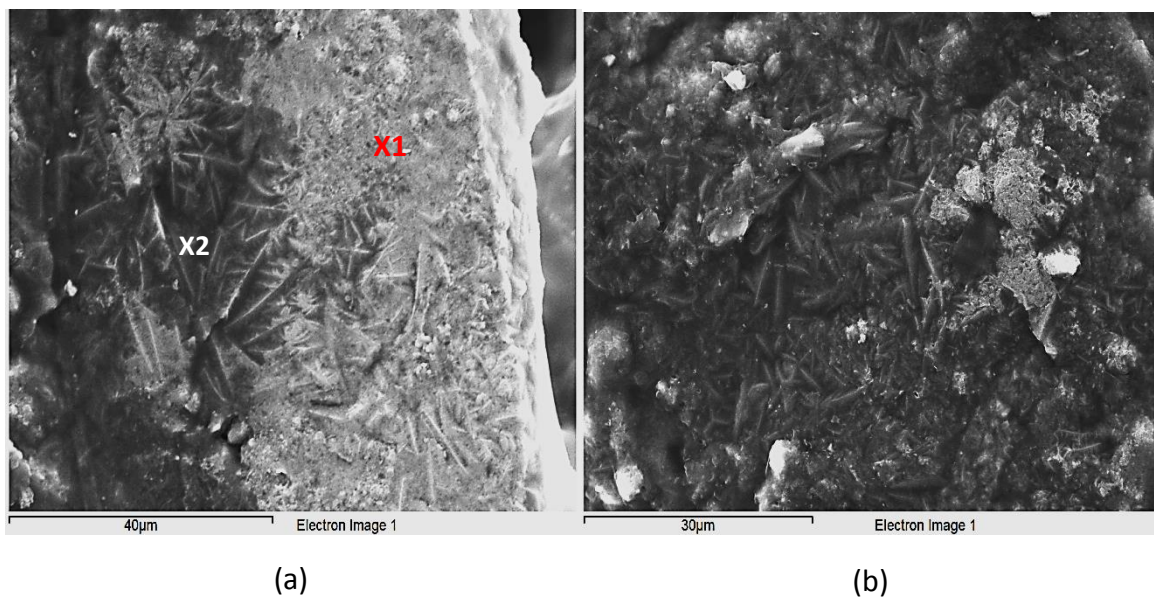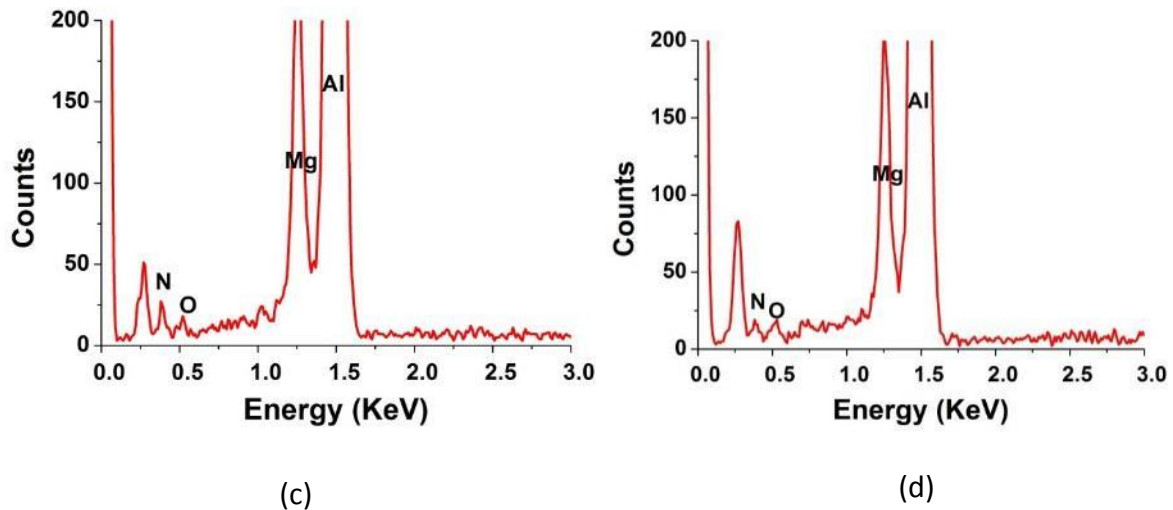
**Figure 4-42. Sample surface of Zr addition into Al-5Mg, showing surface layer which contain both oxide and nitride.**

Figure 4-42 (a) showed feather-like nitride with bright contrast present on the one end of the sample, where a high nitrogen content was detected by EDX (see Figure 4-42 X1). EDX (Figure 4-42 (b)) suggested that the N content was 15 at.%  while the N content in the nearby region ( Figure 4-42 X2) decreased to 8 at.%. This suggested a thicker nitride layer in the area in Figure 4-42 X1 and that the thickness of the nitride layer on the sample surface was irregular.

### 4.1.3.4   The addition of Mo into Al-5Mg alloy

With a Mo addition into Al-5Mg, the liquid metal entered 28 mm inside the blind hole. SEM examination showed feather-like nitride on the sample surface (shown in Figure 4-43) and EDX confirmed that it contained nitrogen. Mo containing oxide particles were seen on the sample surface (as shown in 4-44 X2, however a Si peak was seen in this spectrum, which could be due to contamination from the other previous castings done from the same crucible).

(a)

(b)



(c)
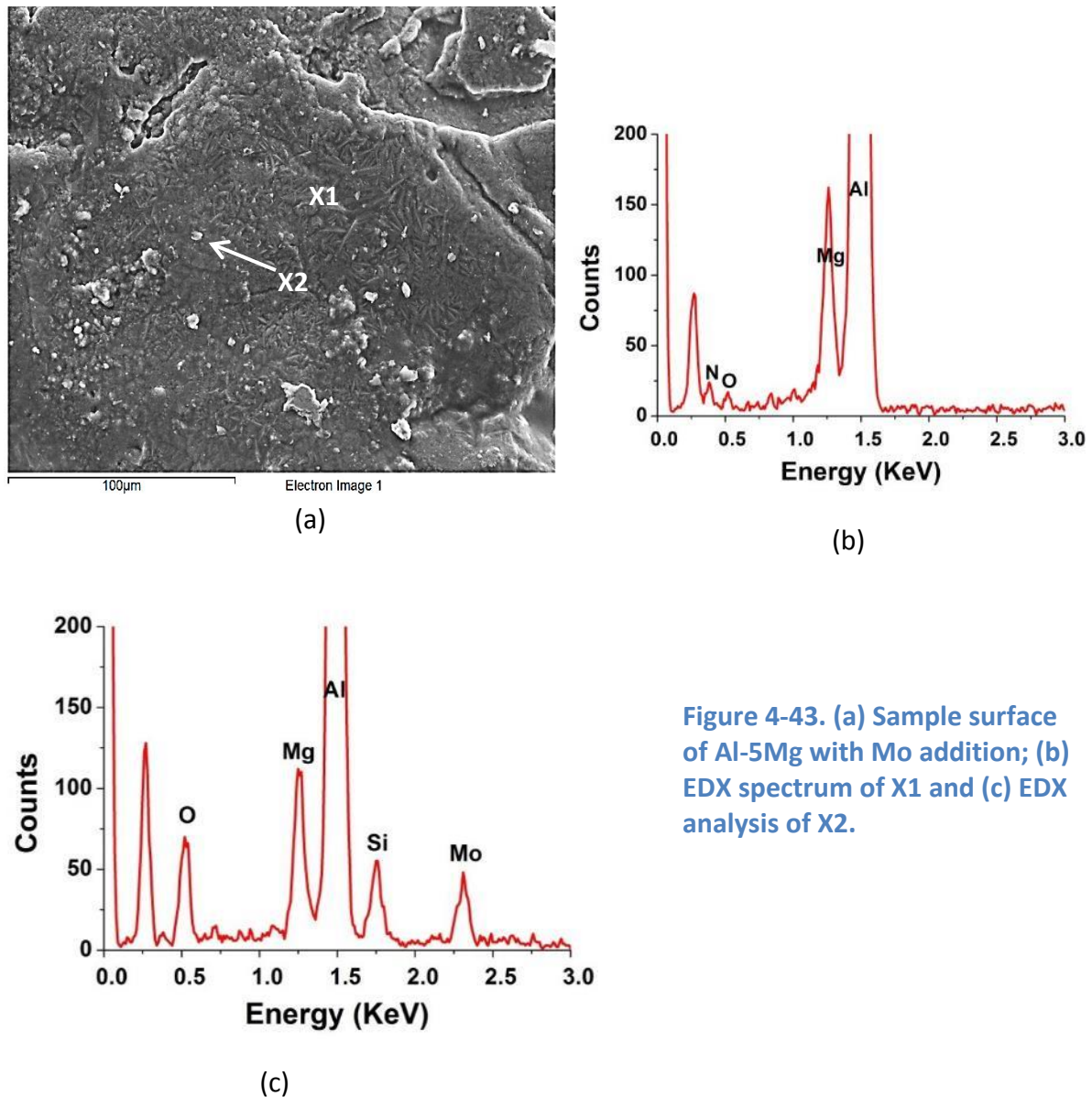
Figure 4-43. (a) Sample surface of Al-5Mg with Mo addition; (b) EDX spectrum of X1 and (c) EDX analysis of X2.

### 4.1.4  Summary

In the bubble trapping experiment, Al-Mg had the highest mean value of the sample height, which was followed by CP-Al. The experiment with 2L99 was least.  Ti addition tended to slow down the reaction between the liquid metal and entrapped gas in CP-Al while other elements had no effect. For the experiment with 2L99, the Ti addition showed some small areas of porous oxide on the sample surface, but the liquid metal-gas reaction was not accelerated, and no nitride was found on the sample surface. Both Mo and Sc addition showed an increase in the sample height, which suggested that the metal-gas reaction was

accelerated. EDX analysis suggested that both elements affected the oxide/nitride formation process. Large areas of nitride were found on the surface of all the samples with Al-5Mg. All the element additions tended to have no significant effect on the formation of the oxide/nitride.

## 4.2 An experiment to investigate the floatation of double oxide film defects

This experiment was carried out to investigate if double oxide film defects would float upwards to the upper surface in a casting.

In a four point bend test, the surface of the test bar placed downward experiences the maximum tensile strength and this side would be more sensitive to oxide film defects and is more likely to fail compared with other areas such as the upper surface.

2 moulds containing 60 rectangular test bars each were cast in the same condition and they are uniformly mixed before separating apart into two groups for the different tests. In one group, the top surface of the cast test bars was placed under the maximum tensile load, while in the other group the bottom surface of the cast test bar was placed under the maximum load.

The ultimate bend strengths (UBS) have been shown in Table 4-10 and Table 4-11, respectively. The UBS for the upper surface was more concentrated around 250-340 MPa while the UBS for the bottom surface was mostly concentrated around 400-420MPa. A Weibull Distribution was used here to fit the two groups of the population of UBS.

Figure 4-44 showed the Weibull plot for the UBS of the sample with top and bottom surface under maximum load respectively. The $R^2$ value for the bottom surface under maximum

load was 0.95 ( $R^2_{0.5}$=0.91), which showed a good fit for a Weibull plot. However, the $R^2$ value for the top surface under the maximum load was 0.88 which showed a poor fit for a Weibull distribution. Weibull plot was therefore divided into two groups to show two types of defect in the casting as shown in Fig. 4-133. The $R^2$ value then shifted to 0.91 and 0.93 respectively, and met the need for $R^2_{0.5}$.

Table 4-12 shows a summary of the results. The 2.5 and 97.5 percentile for $m_1$=30 and $m_2$=20 are 0.511 and 1.976. For $m_1$=30 and $m_2$=10, the values are 0.494 and 2.124 respectively. The m1/m2 values for the top and bottom surfaces under maximum load were 4.81 (bottom surface vs Group I of upper surface) and 1.53 (bottom surface vs Group II of upper surface).

The samples with the bottom surface under the maximum load had higher Weibull moduli for the UBS compared with the samples with the top surface under the maximum load (Group I). Also, the samples with the bottom surface under maximum load had higher mean value and lower standard deviation compared with the top surface under maximum load. The low Weibull moduli and mean value for the UBS of the sample with top surface under the maximum load could be attributed to the effect of double oxide film defects. It is Therefore the oxide film defect floated to the top of the cast test bar during the casting and solidification.

Fracture surface examination also suggested that, with the top surface under the maximum load, bi-film defects can be observed. However, such oxides were not seen in samples with bottom surface under the maximum load.

**Table 4-10. Ultimate Bend Strength of the sample with top surface under the maximum load.**

| No. | Ultimate Bend Strength (MPa) | No. | Ultimate Bend Strength (MPa) |
|---|---|---|---|
| 53 | 288.9 | 27 | 262.7 |
| 7 | 228.2 | 46 | 313.4 |
| 44 | 251.8 | 21 | 374.9 |
| 29 | 288.2 | 23 | 385.1 |
| 3 | 298.9 | 36 | 317.9 |
| 13 | 274 | 42 | 422.2 |
| 32 | 318.4 | 40 | 301.7 |
| 5 | 235.4 | 38 | 337.6 |
| 48 | 264.7 | 52 | 317.9 |
| 1 | 247.3 | 50 | 320.7 |
| 11 | 428.5 | 54 | 258.2 |
| 19 | 266.6 | 34 | 281.3 |
| 17 | 394 | 58 | 340.8 |
| 9 | 313.4 | 15 | 233.6 |
| 45 | 389.1 | 25 | 306.9 |
| Mean | 308.7 | | |

**Table 4-11 Ultimate Bend Strength of the sample with top surface under the maximum load.**

| No. | Ultimate Bend Strength (MPa) | No. | Ultimate Bend Strength (MPa) |
|---|---|---|---|
| 33 | 330.4 | 28 | 411.8 |
| 52 | 343.4 | 57 | 412.3 |
| 55 | 352.2 | 37 | 413.4 |
| 47 | 360.3 | 12 | 415.2 |
| 15 | 392.1 | 35 | 418 |
| 43 | 394.6 | 39 | 418.5 |
| 14 | 402 | 16 | 418.7 |
| 18 | 403.2 | 31 | 423.1 |
| 10 | 405 | 4 | 426.3 |
| 6 | 406.4 | 2 | 436.8 |
| 24 | 406.7 | 30 | 440.1 |
| 26 | 407.6 | 41 | 443.9 |
| 20 | 408.4 | 8 | 445.1 |
| 22 | 460.8 | 59 | 456.3 |
| mean | 409.0 | | |
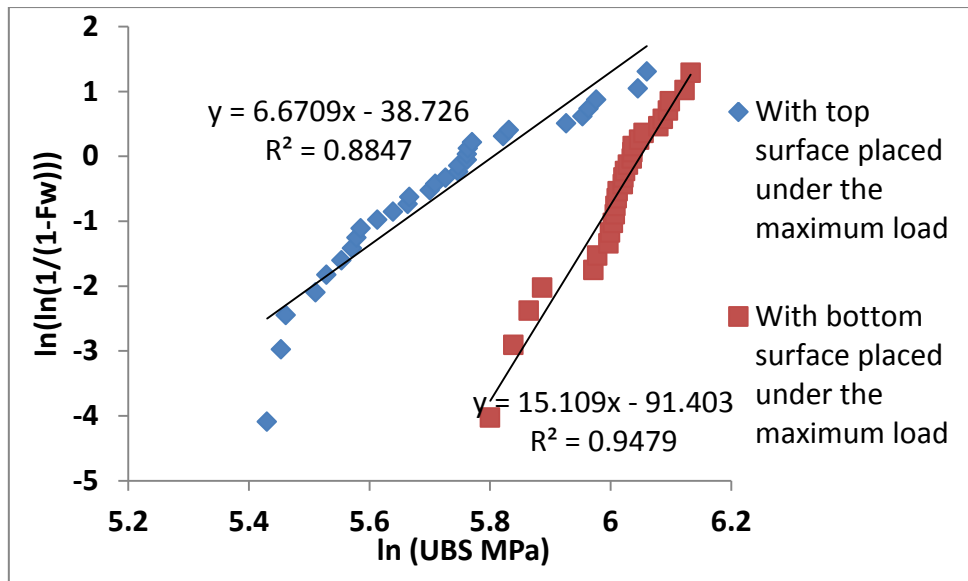
**Figure 4-44. Weibull moduli of Ultimate Bend Strength for the sample with (a) top surface under maximum load and (b) bottom surface under the maximum load.**
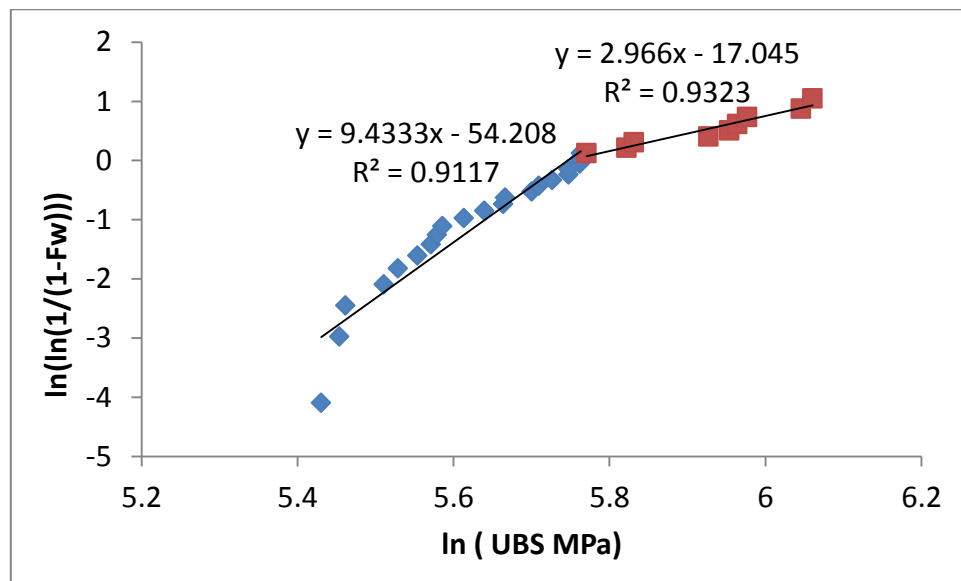


**Figure 4-45. Replotted Weibull Plot of UBS for sample with lower surface under the maximum load showing two different defects.**

**Table 4-12. Summary of the results between the upper surfaces and bottom surface of the test bar.**

|  | Upper surface (Group I) | Upper surface (group II) | Upper surface | Lower surface |
|---|---|---|---|---|
| Mean value | 371.1 MPa | 279.5 MPa | 308.7 MPa | 413.0 MPa |
| Standard deviation | 37.85 | 30.16 | 55.31 | 33.36 |
| Position parameter | 313.2MPa | 313.1MPa |  | 428.9MPa |
| Weibull Moduli | 2.97 | 9.43 |  | 14.3 |
| $R^2$ | 0.93 | 0.91 |  | 0.95 |

The side with maximum load



(a)

(b)

(c)

(d)

The side with maximum load
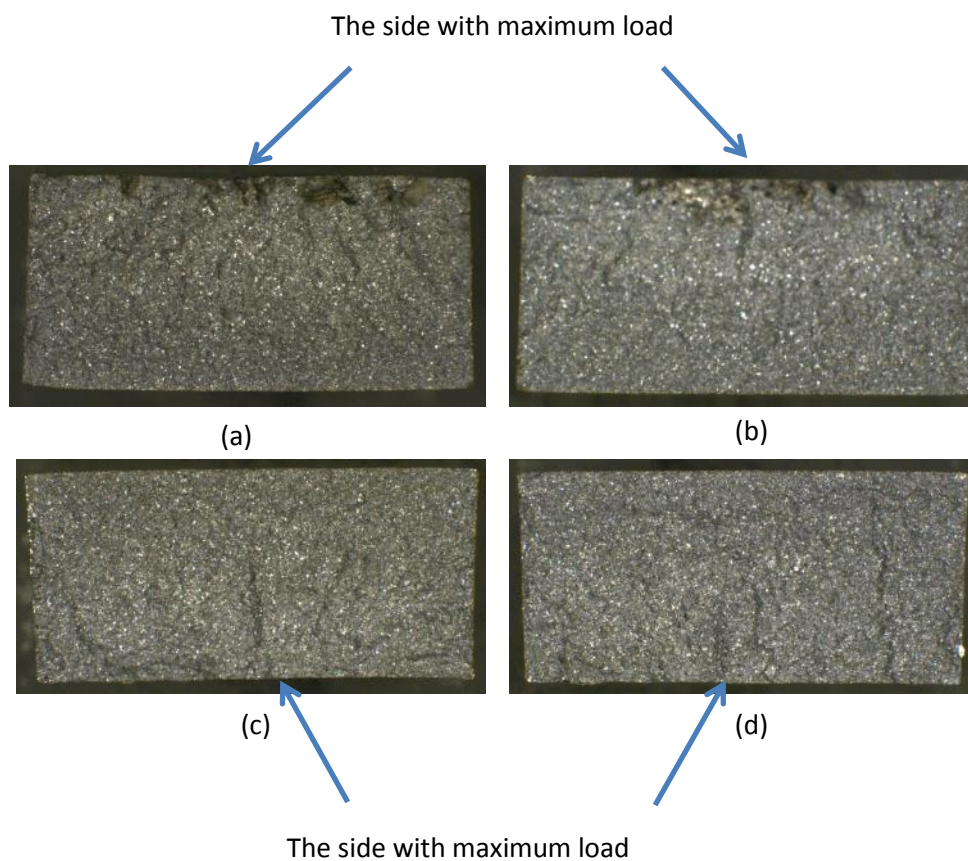
**Figure 4-46 (a) and (b) Fracture surface of 2L99 alloy with upper part under the maximum load; (c) and (d) fracture surface of 2L99 alloy with bottom part under the maximum load.**

## 4.3 The effect of different element additions into 2L99 on casting mechanical properties

### 4.3.1 Tensile test with no addition

#### 4.3.1.1 Mechanical test results

Three experiments were carried out with 2L99 alloy; as-cast, without subsequent heat-treatment, castings with a T6 heat-treatment, and casting with heat-treatment and roll-over (The roll-over device was used to reduce the formation of the shrinkage in the tensile test bar). The castings were then machined into tensile test bars and the UTS and %Elongation for each test bar from each casting recorded.

For castings without heat-treatment, 3 moulds were cast, to give 30 test bars. For casting with heat-treatment, 2 moulds were cast, to give 20 test bars. For the experiment with heat-treatment and roll over, 8 moulds were cast, which produced 77 test bars.

The hydrogen content in the castings was measured by LECO$^{TM}$, and is shown in Table 4-10. Three samples were measured for the casting with heat-treatment and roll over, while one sample each was measured for the castings with and without heat-treatment. XRF was used to measure the actual chemical composition of the castings, as shown in Table 4-11. The results for castings with and without heat-treatment are shown in Table 4-12. The result with heat-treatment and roll over is shown in Table 4-13.

**Table 4-10. LECO hydrogen content analysis results**

| Casting | ppm H |
|---|---|
| Casting without heat-treatment | 0.229 |
| Heat-treated | 0.197 |
| with heat treatment and roll over I | 0.181 |
| with heat-treatment and roll over II | 0.157 |
| with heat-treatment and roll over III | 0.225 |

**Table 4-11. Chemical composition of the castings for 2L99.**

| | unheat-treated | heat-treated | heat-treated and roll over |
|---|---|---|---|
| Element | Composition | Concentration | Concentration |
| Al | 92.40% | 90.61% | 90.42% |
| Si | 6.93% | 8.77% | 7.63% |
| Mg | 0.34% | 0.32% | 0.32% |
| Ti | 0.12% | 0.12% | 0.14% |
| Fe | 0.10% | 0.09% | 0.10% |

**Table 4-12. The results for UTS and %Elongation of 2L99 with and without heat-treatment.**

| Specimen | without heat-treatment | | with heat-treatment | |
| --- | --- | --- | --- | --- |
| | Elongation | UTS | Elongation | UTS |
| No. | % | MPa | % | MPa |
| 1 | 2.69 | 169.5 | 2.18 | 288 |
| 2 | 1.28 | 141.5 | 2.5 | 291 |
| 3 | 1.13 | 142.8 | 0.6 | 238 |
| 4 | 1.79 | 154.3 | 1.2 | 271 |
| 5 | 2.68 | 170.5 | 1.54 | 279 |
| 6 | 2.61 | 166.8 | 1.26 | 270 |
| 7 | 2.28 | 168.5 | 1.75 | 282 |
| 8 | 0.4 | 106.9 | 1.31 | 277 |
| 9 | 1.37 | 141.7 | 1.33 | 275 |
| 10 | 2.26 | 165.8 | 0.7 | 250 |
| 11 | 1.55 | 149.0 | 1.15 | 269 |
| 12 | 1.9 | 156.5 | 1.5 | 277 |
| 13 | 1.83 | 158.0 | 1.67 | 281 |
| 14 | 2.41 | 167.9 | 0.52 | 226 |
| 15 | 1.53 | 151.6 | 1.25 | 271 |
| 16 | 0.85 | 122.4 | 1.09 | 269 |
| 17 | 1.41 | 140.0 | 1.69 | 283 |
| 18 | 0.61 | 114.2 | 1.12 | 271 |
| 19 | 1.47 | 147.3 | 1.87 | 281 |
| 20 | 0.77 | 118.8 | 1.6 | 279 |
| 21 | 2.43 | 167.6 | | |
| 22 | 1.01 | 129.7 | | |
| 23 | 0.96 | 123.2 | | |
| 24 | 0.63 | 110.1 | | |
| 25 | 1.52 | 148.5 | | |
| 26 | 1.58 | 146.4 | | |
| 27 | 1.04 | 129.9 | | |
| 28 | 1.47 | 146.1 | | |
| 29 | 1.63 | 149.8 | | |
| 30 | | | | |
| Mean | 1.55 | 144.8 | 1.39 | 271.4 |

**Table 4-13. The results for UTS and %Elongation of 2L99 with heat-treatment and roll over.**

| Specimen No. | Elongation % | UTS MPa | Specimen No. | Elongation % | UTS MPa |
|---|---|---|---|---|---|
| 1 | 3.26 | 286.7 | 40 | 0.66 | 204.2 |
| 2 | 1.76 | 276 | 41 | 3.36 | 292.7 |
| 3 | 1.73 | 266.9 | 42 | 3.24 | 295.8 |
| 4 | 0.93 | 235.8 | 43 | 1.46 | 268.5 |
| 5 | 1.7 | 277.8 | 44 | 2.83 | 291.9 |
| 6 | 0.86 | 250.9 | 45 | 1.62 | 273 |
| 7 | 1.33 | 255.2 | 46 | 3.32 | 290.8 |
| 8 | 2.53 | 281.4 | 47 | 0.49 | 217.8 |
| 9 | 1.61 | 260 | 48 | 2.65 | 290 |
| 10 | 2.36 | 284.8 | 49 | 2.08 | 277 |
| 11 | 1.05 | 257.4 | 50 | 0.75 | 244.9 |
| 12 | 2.66 | 287.6 | 51 | 2.54 | 273.4 |
| 13 | 3.2 | 291.1 | 52 | 3.52 | 294.2 |
| 14 | 2.25 | 274.3 | 53 | 1.57 | 271.1 |
| 15 | 1.3 | 267.3 | 54 | 2.73 | 276.9 |
| 16 | 1.99 | 279.6 | 55 | 1.72 | 269.5 |
| 17 | 2.87 | 290 | 56 | 1.23 | 258.7 |
| 18 | 3.63 | 289.1 | 57 | 1.43 | 264.8 |
| 19 | 1.13 | 256.4 | 58 | 1.69 | 263.4 |
| 20 | 1.78 | 269 | 59 | 1.31 | 257 |
| 21 | 1.01 | 249.8 | 60 | 1.05 | 252.3 |
| 22 | 2.01 | 277.5 | 61 | 4.21 | 299.5 |
| 23 | 2.77 | 283.2 | 62 | 2.3 | 282.1 |
| 24 | 1.88 | 278.4 | 63 | 1.36 | 266.7 |
| 25 | 2.06 | 269.4 | 64 | 1.72 | 274.5 |
| 26 | 2.14 | 280.4 | 65 | 1.36 | 265.2 |
| 27 | 1.21 | 252.3 | 66 | 2.1 | 277.3 |
| 28 | 1.14 | 253.6 | 67 | 2.65 | 279.7 |
| 29 | 1.68 | 264.8 | 68 | 1.72 | 268.7 |
| 30 | 2.88 | 279 | 69 | 1.87 | 272.3 |
| 31 | 1.4 | 273 | 70 | 0.9 | 248.6 |
| 32 | 0.46 | 218.2 | 71 | 1.54 | 266.2 |
| 33 | 1.01 | 216.6 | 72 | 1.4 | 264.6 |
| 34 | 2.32 | 251.9 | 73 | 1.61 | 267.9 |
| 35 | 1.14 | 267.3 | 74 | 2.31 | 281.6 |
| 36 | 0.58 | 225.4 | 75 | 0.89 | 253.3 |
| 37 | 0.92 | 256.6 | 76 | 3.89 | 296.5 |
| 38 | 1.74 | 240.1 | 77 | 3.08 | 290.2 |
| 39 | 1.78 | 246.3 | | | |
| mean | 1.90 | 267.6 | | | |

For castings without heat-treatment (see Table 4-12), the mean value for the UTS was 144.8 MPa and 1.55% for %Elongation. The T6 heat-treatment doubled the mean value of the UTS to 271.4MPa but slightly decreased the %Elongation to 1.39%.

Table 4-13 showed that the roll over did not have an effect on the mean value of UTS. The mean UTS value for casting with and without the roll-over step was 271.4 and 267.6 MPa, respectively. However, the roll over increased the mean value of Elongation by 36% from (1.39% to 1.90%).

The Weibull plot for the UTS and %Elongation for each type of casting are shown in Figure 4-47 and Figure 4-48 and the relevant Weibull moduli and position parameters are summarised in Table 4-15.

Table 4-14 shows the comparison between $R^2_{0.05}$ and $R^2$ for castings of the 2L99 alloy. As can be seen, the $R^2$ values of the Weibull plots of all the UTS and %Elongation are higher than the corresponding $R^2_{0.5}$, which suggested that all the distributions can be accepted as Weibullian.

**Table 4-14 Statistical analysis showing if the distribution of UTS and %Elongation of2L99 castings follows the Weibull distribution.**

| Casting | sample size | $R^2_{0.05}$ | $R^2$ for UTS | Accepted as Weibull distribution? | $R^2$ for %Elongation | Accepted as Weibull distribution? |
|---|---|---|---|---|---|---|
| unheat-treated 2L99 | 29 | 91.17% | 96.20% | Yes | 98.60% | Yes |
| heat-treated 2L99 | 20 | 89.38% | 90.12% | Yes | 96% | Yes |
| heat-treated 3L99 with roll-over | 77 | 95.03% | 98.30% | Yes | 97.8% | Yes |
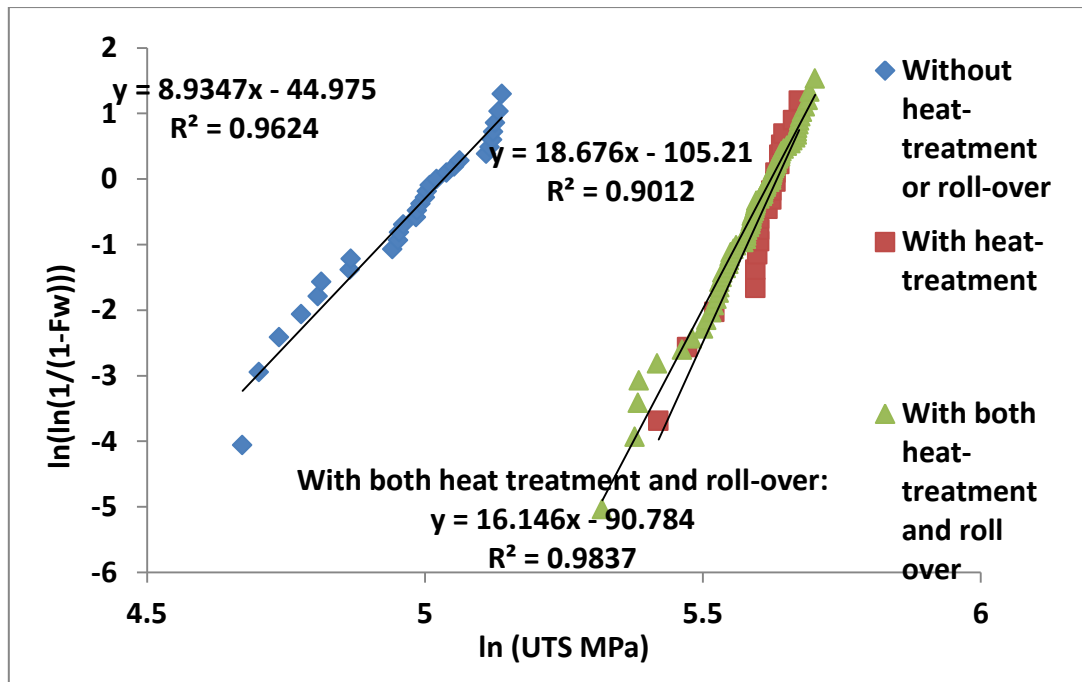
**Figure 4-47 Weibull plots of UTS of 2L99 castings.**
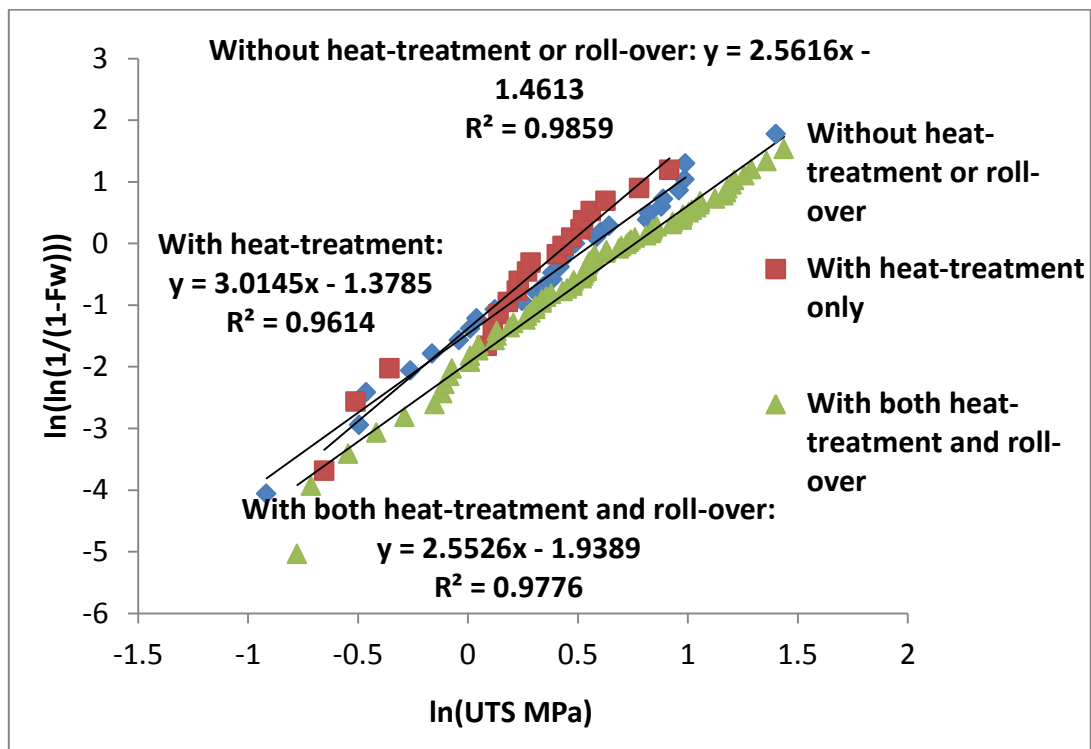


**Figure 4-48 Weibull plots of %Elongation of 2L99 alloys.**

140

**Table 4-15 Summary of the results for 2L99 alloy without addition.**

| Casting | Weibull moduli for UTS | Weibull moduli for %Elongation | Position parameter for UTS | Position parameter for %Elongation |
|---|---|---|---|---|
| 2L99 without heat treatment | 8.93 | 2.56 | 153.6 | 1.77 |
| 2L99 with heat-treatment | 18.68 | 3 | 279.6 | 1.57 |
| 2L99 with heat-treatment and roll over | 16.14 | 2.55 | 276.6 | 2.13 |

The comparisons between 2L99 with and without heat-treatment, and the comparison of the heat-treated 2L99 with and without rollover, are shown in Table 4-16. As can be seen, heat-treatment led to a statistically significant increase in Weibull moduli of the UTS, but its effect on %Elongation was unclear. Rollover did not statistically significantly alter the Weibull moduli of the heat-treated 2L99 casting.

**Table 4-16 Comparison of the Weibull moduli of 2L99 castings.**

| Comparison | 2.5 and 97.5 percentile | m1/m2 for UTS | Significant differences in UTS? | m1/m2 for %Elongation | Significant differences in %Elongation? |
|---|---|---|---|---|---|
| 2L99 with and without heat-treatment | 0.571, 1.799 | 0.477 | Yes | 0.853 | No |
| heat-treated 2L99 with and without roll over | 0.526,1.889 | 0.864 | No | 0.850 | No |

### 4.3.1.2 Fracture surfaces of 2L99 alloy

After the tensile test, the fracture surface of some of the tensile test bars were investigated using Scanning Electron Microscopy (SEM) equipped with Energy dispersive X-ray (EDX). Figure 4-49 shows representative images of two halves of the fracture surfaces of the tensile test bars for all three castings (i.e. 2L99 castings with and without heat-treatment, and 2L99 castings with heat-treatment and roll over). As can be seen, for each test bar selected, symmetrical areas with a dark colour were seen on the both sides of the fracture surfaces. These areas were halves of double oxide film defects and their symmetrical appearance revealed the doubled nature of this defect. SEM images of the defect area on the fracture surface are shown in Figure 4-50, EDX analysis suggested that it contained a small oxygen peak in addition to the main aluminium peak detected, showing it to be an oxide film.

Figure 4-51 showed a high magnification image of the oxide on the fracture surface. 100nm sized particles were seen on the surface layer, with some smaller sized particles ( ~10nm) growing between them. Those particles might be formed by the liquid metal penetrated through the existing oxide layer and reacting with the entrapped gas.

Figure 4-52 showed a high magnification image of another oxide layer, in which the oxide surface was fractured. An area of oxide, which appeared in different contrast, was seen covering the fracture. It seemed that the liquid metal penetrated the oxide layer through the fracture point to react with the entrapped atmosphere and formed a layer of new oxide which covered the fracture area.

Figure 4-53 showed gas porosity on the fracture surface of the tensile test bar (No. 16 of the heat-treated castings, and No. 15 of the unheat-treated castings, respectively). A higher

magnification image of Figure 4-53 (b) is shown in Figure 4-54, which suggested the presence of a smooth surface layer covering the internal wall of this porosity. EDX detected a very weak oxygen peak which suggested this to be a thin oxide layer. Figure 4-55 suggested that the internal wall of this oxide layer was ruptured.

More porosities are shown in Figure 4-56. EDX did not detect any oxygen inside these porosities. Those porosities are possibility therefore H porosity which came from the expanded oxide film defect. The thin oxide layer made it difficult to detect O in the EDX.
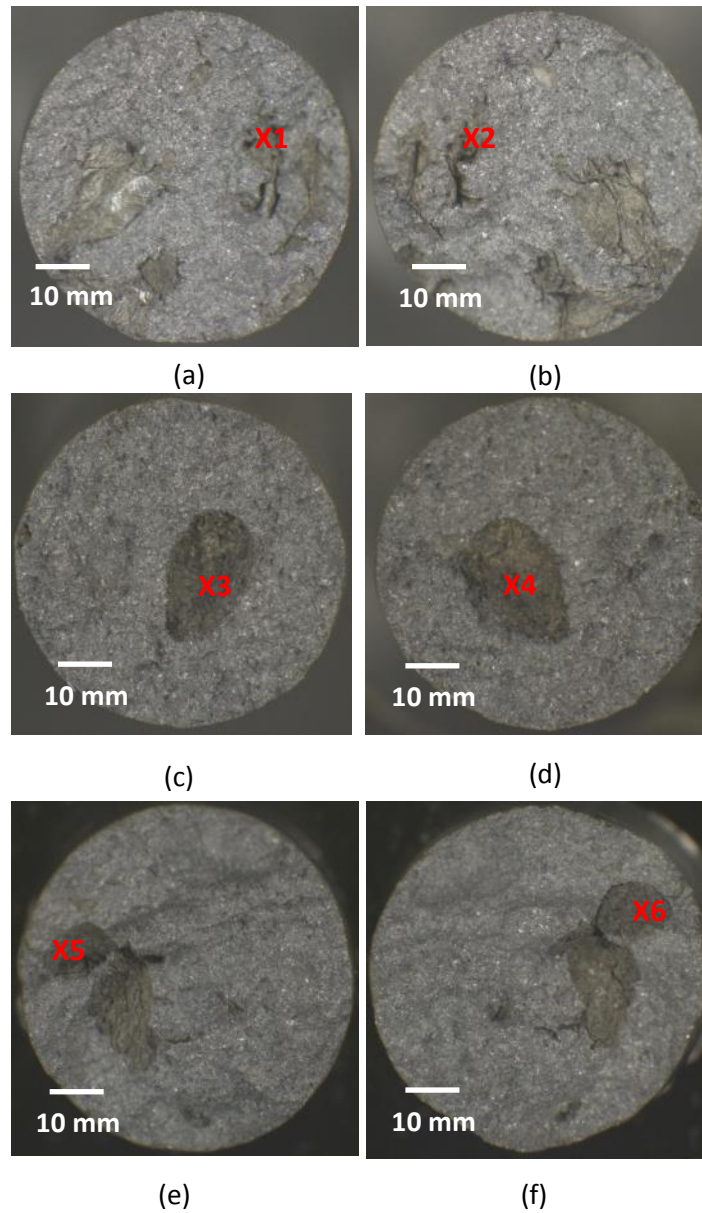
**Figure 4-49 Image of the fracture surface showimg the oxide film located symmetrically on both sides of the tensile test bar. (a) and (b) are from tensile test bar No. 18 of the batch without heat-treatment; (c) and (d) are from tensile test bar No. 10 of the batch with heat-treatment; (e) and (f) shows the tensile test bar No. 9 of heat-treatment and roll over.**
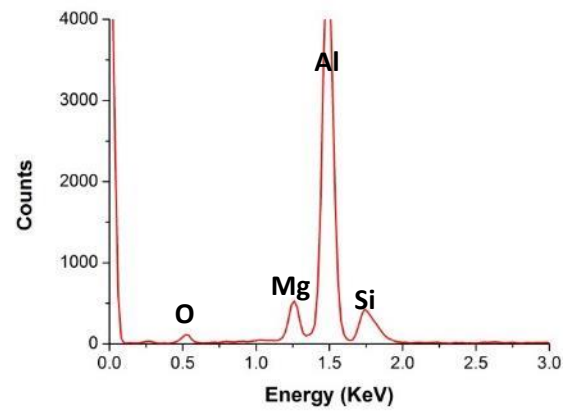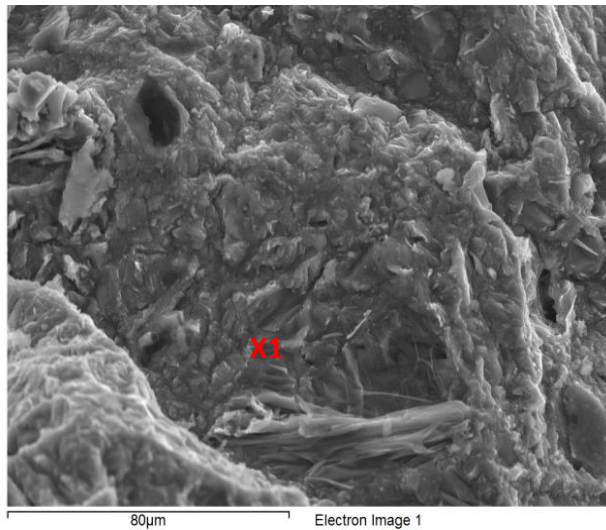
Figure 4-50 (a) SEM image of the oxide layer on Figure 4-49 X2; (b) EDX spectrum of X1.
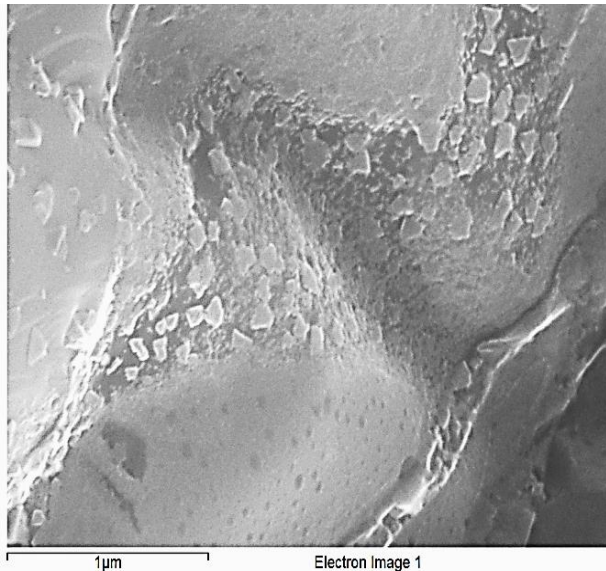


(a)
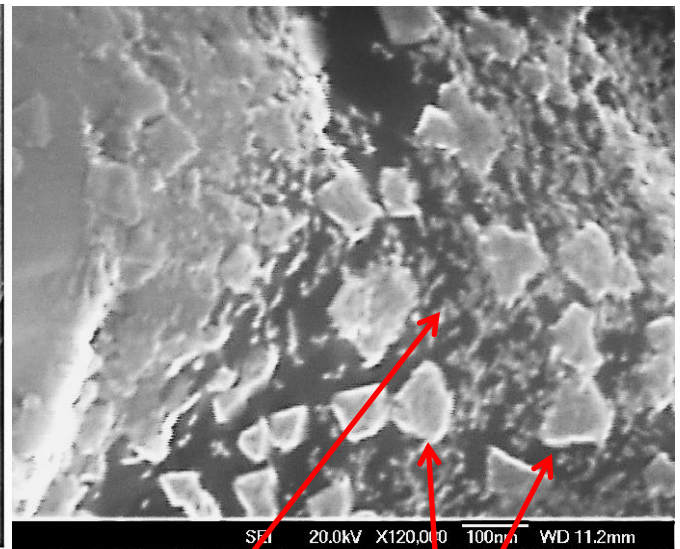


(b)

Smaller sized particles
between large particles

Oxide particles
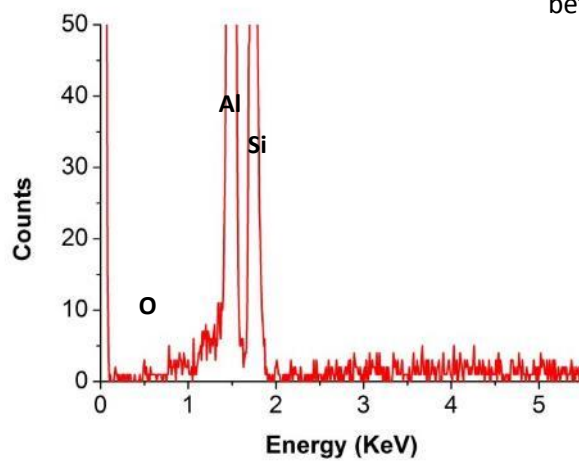


(c)

Figure 4-51 (a) and (b) High
magnification image of the
oxide layer on the fracture
surface of 2L99 alloy; (c) EDX
spectrum of X1.

145

(a)



Fracture of the oxide
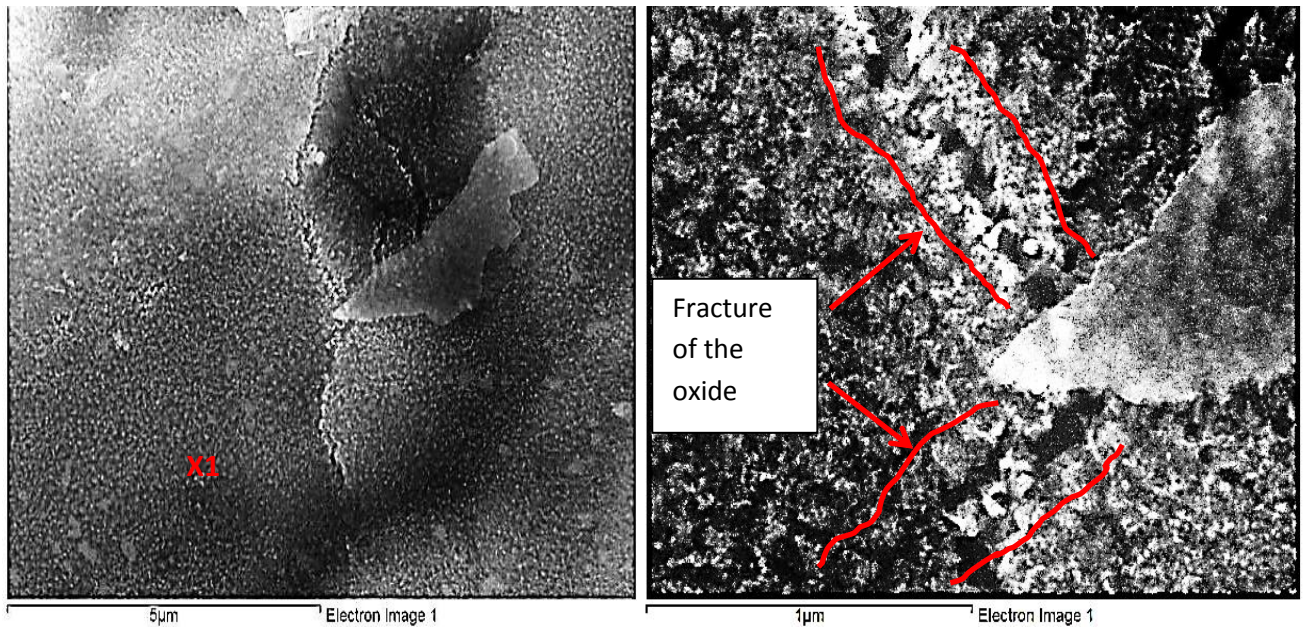
(b)
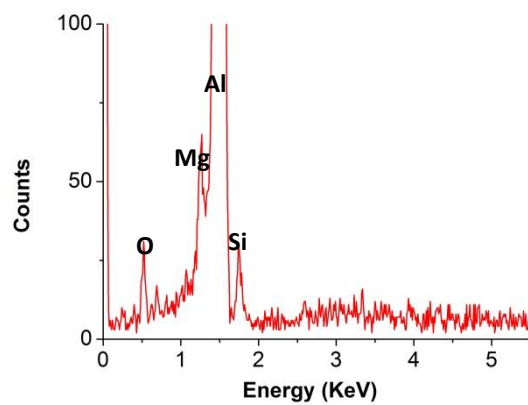


(c)

**Figure 4-52 (a) High magnification image of the oxide layer on the fracture surface of 2L99 alloy; (b)-(c) EDX spectrum of X1 and X2.**
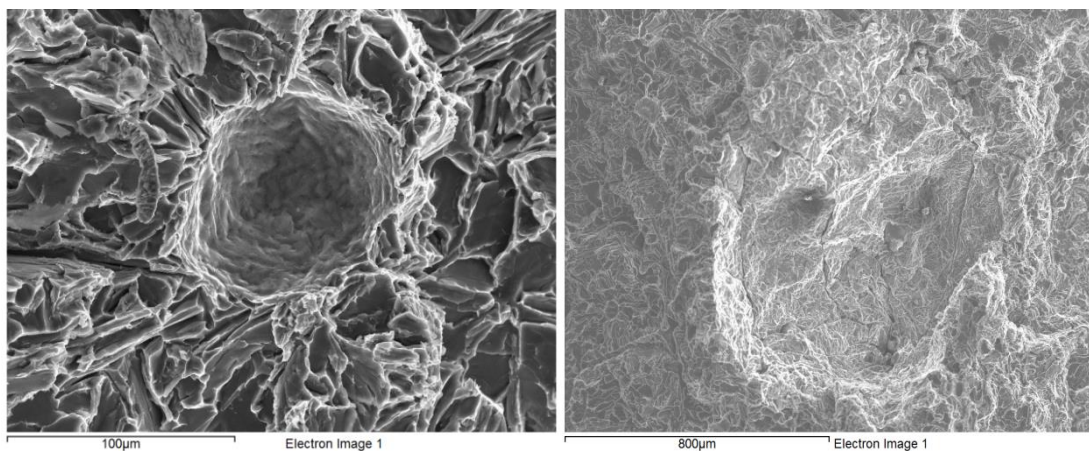


(a)



(b)

**Figure 4-53. Gas porosity found on the fracture surface of (a) test bar No. 16 of the heat-treated batches and (b) test bar No. 15 of the un-heat-treated batch.**

146
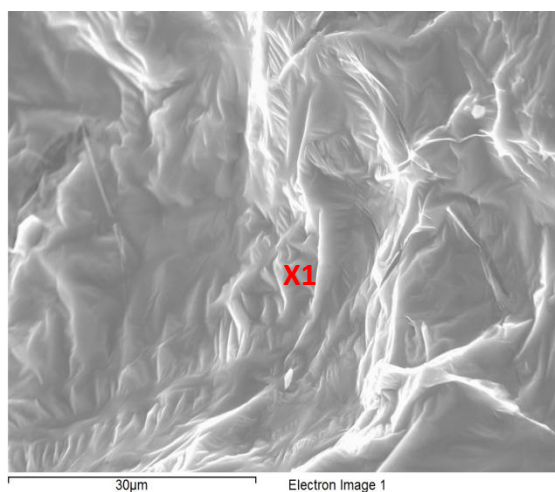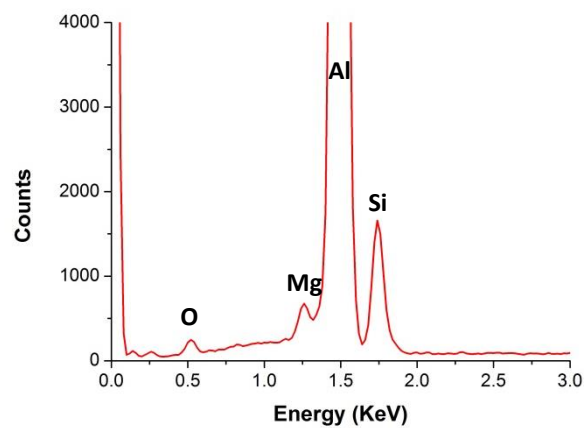
(a)                                                         (b)

**Figure 4-54 (a) Internal wall of the gas porosity of Figure 4-53 (b) shows the wrinkled surface.**
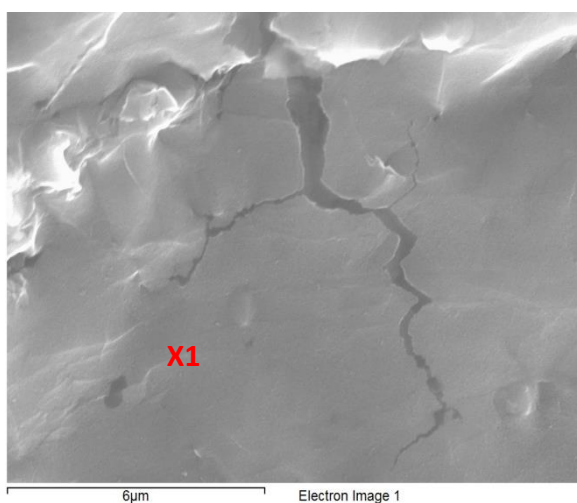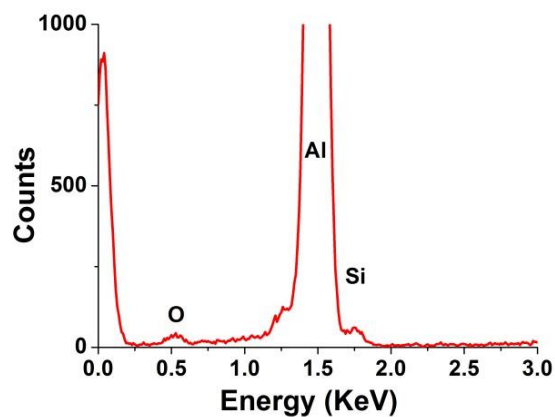


(a)                                                         (b)

**Figure 4-55. High magnification image of Figure 4-53 (b) shows the rupture of the internal wall of the air bubble.**
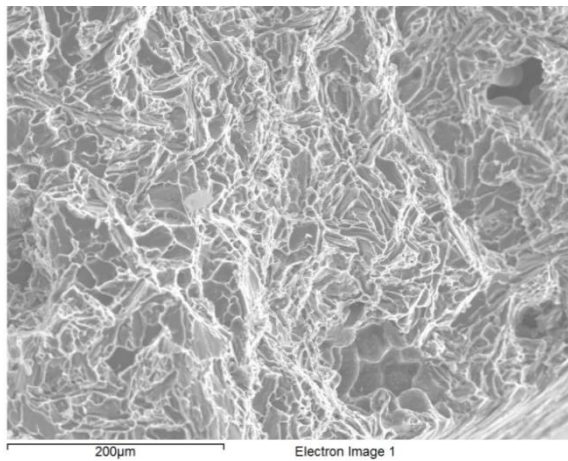
(a)
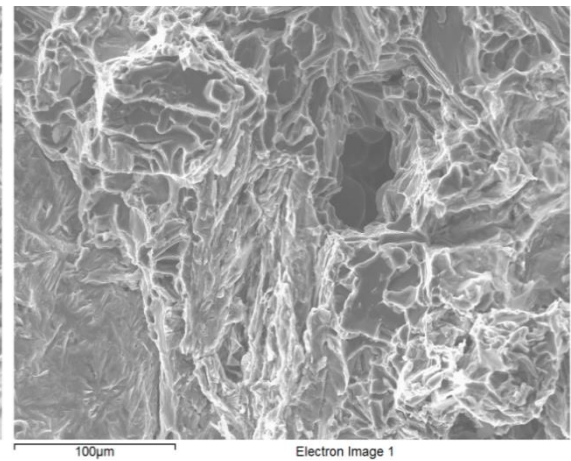
(b)
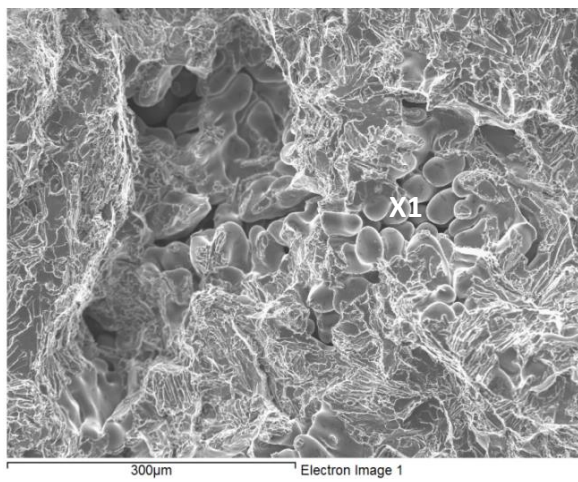
(c)
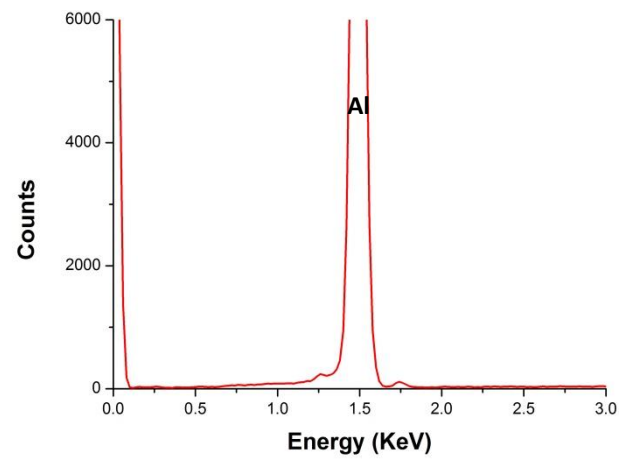
(d)

Figure 4-56. The porosity found on the sample surface of (a) Test bar No. 5 of the batch without heat-treatment and (b) Test bar No. 7 of the batch with heat-treatment and roll over.

The cross-section of the oxide layer in a 2L99 cast testbar was investigated with the aid of Focused Ion Beam (FIB) milling. As can be seen Figure 4-57, the cross-section of a tangled oxide film defect was revealed. The thickness of the oxide layer was non-uniform, and varied from about 50nm to about 300 nm, but the layer was continuous. Some oxide particles were seen in the internal wall of the oxide.



(a)



Oxide particles
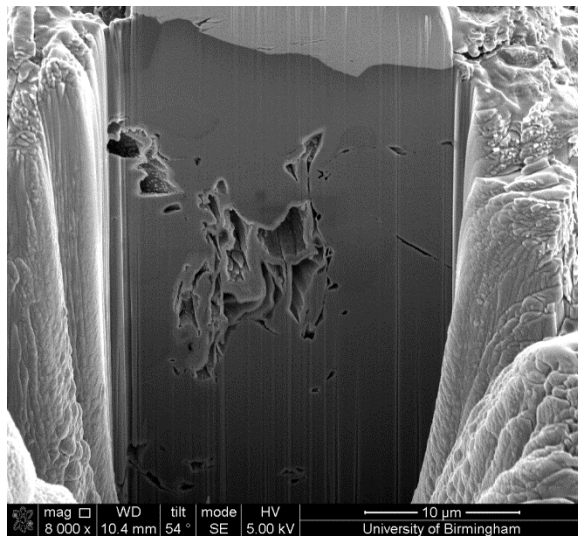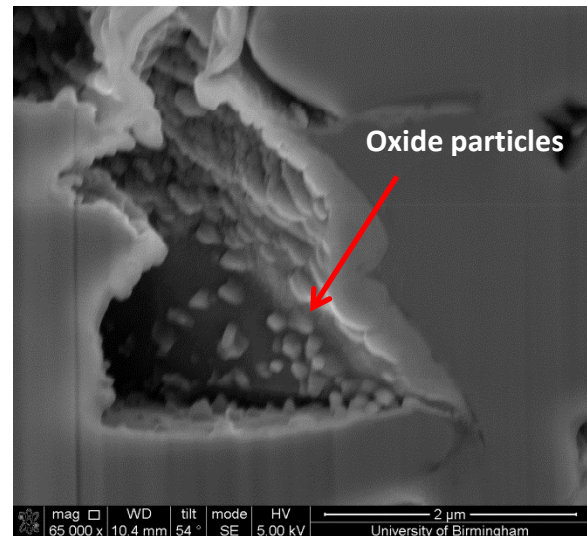
(b)
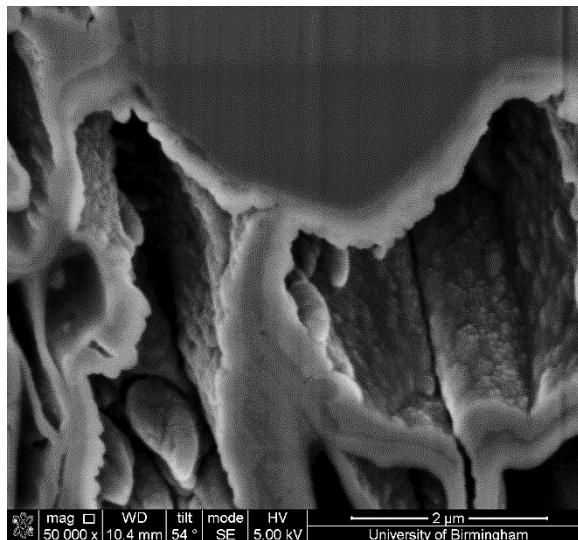


(c)

**Figure 4-57 Cross-section of the oxide film defects found near the fracture surface of 2L99 sample.**

### 4.3.1.3 Summary

The results showed that the T6 heat-treatment increased the mean value and position parameter of UTS for the 2L99 alloy, while the corresponding values for %Elongation showed a slight decrease. The Weibull moduli of UTS were also statistically improved as expected. Roll-over, which was supposed to reduce the possible shrinkage on the tensile test bar, showed no effect on the mean value, position parameter and Weibull moduli for the UTS, but was associated with a 20% increase in the mean value and position parameter of the %Elongation. SEM investigation showed that the morphology of the oxide layer was not affected with different casting approaches.

### 4.3.2 The effect of addition of modifiers (Sr, Na and Ba) to 2L99 alloy on Weibull moduli

### 4.3.2.1 Tensile test results

In this experiment, 3 moulds (30 test bars), were cast with modifier additions (Ba, Sr and Na), as shown in Table 4-17. All experiments were conducted with both T6 heat-treatment and roll over. The chemical composition was confirmed by XRF, as shown in Table 4-18. As the elements were added to a relatively small amount of alloy, the compositions of Ba, Na and Sr were further confirmed by Inductively Coupled Plasma Mass Spectrometry (ICP-MS), shown in Table 4-19. The result for Ba and Sr pickup was consistent with the result from XRF while for the Na pickup, which failed to show up on XRF, 140 ppm Na was obtained in ICP-MS.

**Table 4-17. The amount of modifiers added into 2L99 melt.**

| Modifier | Concentration (ppm) |
|----------|---------------------|
| Na | 250 |
| Sr | 300 |
| Ba | 990 |

**Table 4-18. The alloy composition with the addition of modifier (measured by XRF).**

| 2L99 +Na | | 2L99 +Ba | | 2L99 +Sr | |
|----------|---------------|----------|---------------|----------|---------------|
| Formula | Concentration % | Formula | Concentration % | Formula | Concentration % |
| Al | 92.75 | Al | 93.35 | Al | 92.15 |
| Si | 9.49 | Si | 9.3 | Si | 8.69 |
| Mg | 0.3 | Mg | 0.28 | Mg | 0.3 |
| Ti | 0.11 | Ti | 0.13 | Ti | 0.09 |
| Fe | 0.12 | Fe | 0.09 | Fe | 0.1 |
| | | Ba | 0.04 | Sr | 0.03 |

**Table 4-19. The composition of the modifier confirmed by ICP-MS.**

| No | Experiment | Element | Concentration (ppm) |
|----|-----------|---------|---------------------|
| 1 | 2L99 +Na | Na | 140 |
| 2 | 2L99 +Ba | Ba | 410 |
| 3 | 2L99 +Sr | Sr | 300 |

**Table 4-20. LECO Hydrogen content analysis results.**

| Experiment | ppm H |
|-----------|-------|
| 2L99 + Sr | 0.182 |
| 2L99 + Ba | 0.143 |
| 2L99 + Na | 0.202 |

This showed that Sr had 100% recovery while Ba and Na only had around 40%-50% recovery. The loss of the elements could be due to oxidation and vaporisation during the addition process. LECO$^{TM}$ measurement of H showed that the hydrogen content in the castings was around 0.15-0.2 ppm which was considered an acceptable range for casting.

Optical microscopy of the Si morphology is shown in Figure 4-58. Both Sr and Na addition showed the effective modification of the coarse Si phase while a weaker modification effect was seen with the Ba addition.



(a)          (b)

(c)          (d)
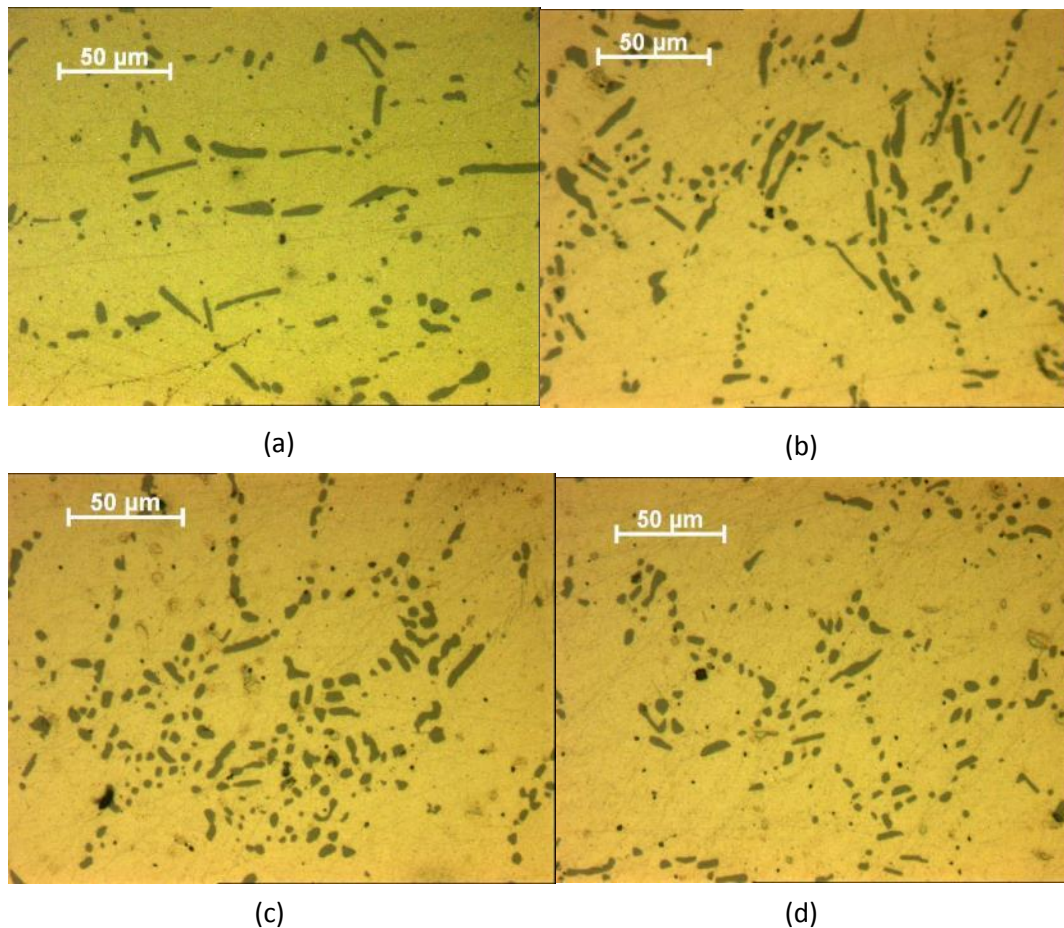
**Figure 4-58 The microstructure of the Si phase after the modification addition into 2L99. (a) 2L99; (b) 2L99+Ba; (c) 2L99+Sr and (d) 2L99+Na.**

The mechanical test results for the Ba, Sr and Na additions to 2L99 alloy have been shown in Table 4-21. Comparisons between the mean value of UTS and %Elongation of 2L99 and 2L99 with modifier additions are shown in Table 4-22. The addition of Sr and Na decreased the UTS by 7.1% and 6.5% respectively, while the addition of Ba caused no change in the UTS. For %Elongation, the addition of Ba and Sr caused an increase of 8.9% and 5.2% respectively, while the addition of Na decreased the mean value by 18%.

**Table 4-21. Tensile test results for modifiers additions into 2L99.**

| No | 2L99+Ba | | 2L99+Sr | | 2L99+Na | |
|---|---|---|---|---|---|---|
| | UTS | %Elongation | UTS | %Elongation | UTS | %Elongation |
| | MPa | % | MPa | % | MPa | % |
| 1 | 249 | 1.08 | 213 | 0.75 | 191 | 0.73 |
| 2 | 281 | 2.79 | 239 | 1.13 | 221 | 0.90 |
| 3 | 252 | 1.02 | 168 | 0.35 | 222 | 0.80 |
| 4 | 212 | 0.49 | 232 | 0.68 | 221 | 0.80 |
| 5 | 265 | 1.54 | 239 | 0.9 | 234 | 1.14 |
| 6 | 277 | 2.65 | 258 | 2.05 | 212 | 0.80 |
| 7 | 250 | 0.97 | 239 | 0.99 | 227 | 1.18 |
| 8 | 257 | 1.39 | 205 | 0.48 | 219 | 0.87 |
| 9 | 237 | 0.76 | 221 | 0.91 | 226 | 1.13 |
| 10 | 252 | 1.07 | 189 | 0.4 | 283 | 3.88 |
| 11 | 274 | 2.09 | 223 | 0.71 | 278 | 3.29 |
| 12 | 277 | 2.27 | 206 | 0.57 | 269 | 2.75 |
| 13 | 255 | 1.12 | 271 | 3.34 | 264 | 2.15 |
| 14 | 237 | 0.65 | 276 | 3.49 | 271 | 3.12 |
| 15 | 276 | 1.65 | 230 | 0.61 | 214 | 0.62 |
| 16 | 293 | 3.13 | 240 | 1.08 | 224 | 0.92 |
| 17 | 284 | 2.36 | 243 | 1.35 | 270 | 3.10 |
| 18 | 280 | 1.93 | 235 | 1.14 | 277 | 3.54 |
| 19 | 282 | 2.08 | 242 | 1.13 | 277 | 3.20 |
| 20 | 291 | 4.33 | 265 | 2.83 | 275 | 1.51 |
| 21 | 277 | 2.39 | 284 | 3.27 | 282 | 2.02 |
| 22 | 280 | 2.48 | 257 | 1.43 | 279 | 1.62 |
| 23 | 293 | 4.27 | 294 | 4.94 | 283 | 2.18 |
| 24 | 295 | 4.8 | 291 | 4.39 | 238 | 0.78 |
| 25 | 268 | 1.62 | 272 | 2.17 | 283 | 2.48 |
| 26 | 267 | 1.27 | 284 | 3.79 | 293 | 3.49 |
| 27 | 283 | 2.32 | 285 | 3.38 | 210 | 0.84 |
| 28 | 287 | 3.12 | 274 | 2.68 | 292 | 3.30 |
| 29 | 291 | 3.36 | 286 | 3.84 | 228 | 0.60 |
| 30 | 257 | 1.01 | 290 | 5.15 | | |
| mean | 269 | 2.07 | 248 | 2.00 | 250 | 1.85 |

**Table 4-22 Comparison of the mean value between 2L99 and modifiers additions (all the experiment were conducted with both heat-treatment and roll over).**

|  | 2L99 | 2L99+Ba | 2L99+Sr | 2L99+Na |
|---|---|---|---|---|
| mean value for UTS (MPa) | 267.6 | 269 | 248 | 250 |
| Mean value for %Elongation | 1.9 | 2.07 | 2 | 1.85 |

The Weibull plots for UTS and %Elongation for the 2L99+Ba, 2L99 +Sr and 2L99+Na are shown in Figure 4-59 and Figure 4-60, respectively.

The curve fitting for the Weibull plot is evaluated in Table 4-23. The casting with 2L99+Ba showed a good fit to a Weibull distribution, for both %Elongation and UTS. The Sr addition showed a good fit to a Weibull distribution for UTS, although the %Elongation suggested differently. For the 2L99+Na castings, neither UTS nor %Elongation showed a Weibull distribution. The Weibull plot of both the Sr and Na additions showed a tendency towards a bimodal. This might be due to more than one type of defect occurring, to cause the failure of the tensile test bar.
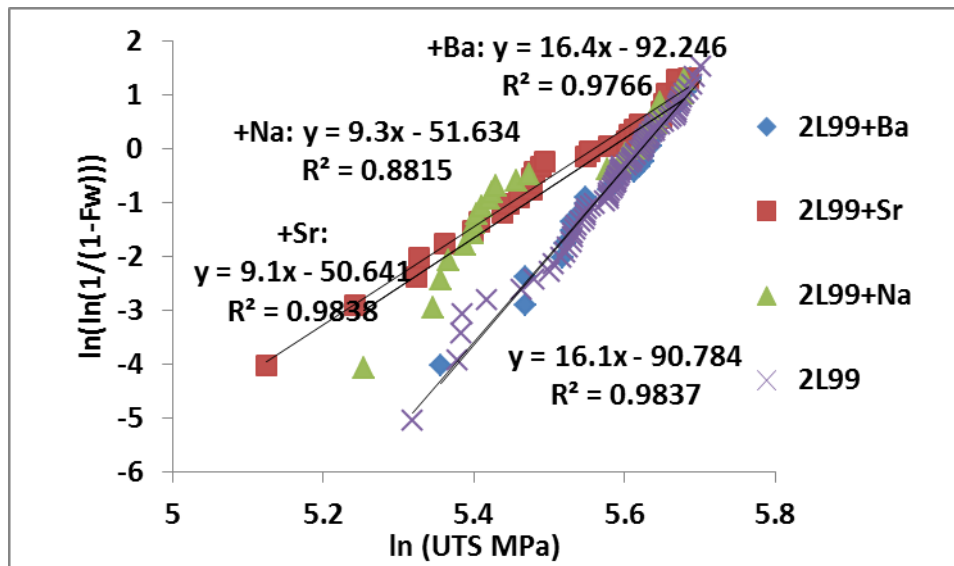
**Figure 4-59 Weibull plots of UTS of 2L99 with modifiers additions.**
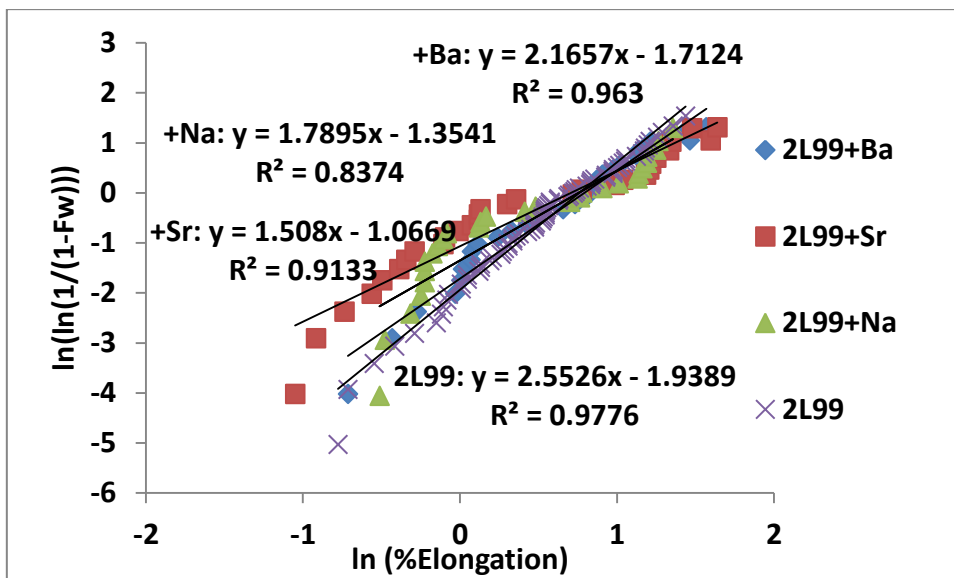


**Figure 4-60 Weibull plots of %Elongation of 2L99 with modifiers additions.**

**Table 4-23 Statistic analysis of R$^2$ value for the Weibull plots.**

| | $R^2_{0.05}$ | R$^2$ for %elongation | Weibull distribution for %Elongation? | R$^2$ for UTS | Weibull distribution for UTS? |
|---|---|---|---|---|---|
| 2L99+Ba | 91.30% | 96.30% | Yes | 97.70% | Yes |
| 2L99+Sr | 91.30% | 91.3% | Yes | 98.4% | Yes |
| 2L99+Na | 91.30% | 83.7% | No | 88.1% | No |

The Weibull plot of the %Elongation and UTS results for 2L99 +Na alloy was re-plotted to show two slopes in the casting. As shown in Figure 4-61, the UTS for 2L99 +Na castings with two defects, had a Weibull moduli of 18.5 and 16.8 respectively. However, for the Weibull moduli of %Elongation, even when the distribution was split into two, the R$^2$ value was still much lower than the requirement for fitting to a Weibull distribution.



(a)                     (b)
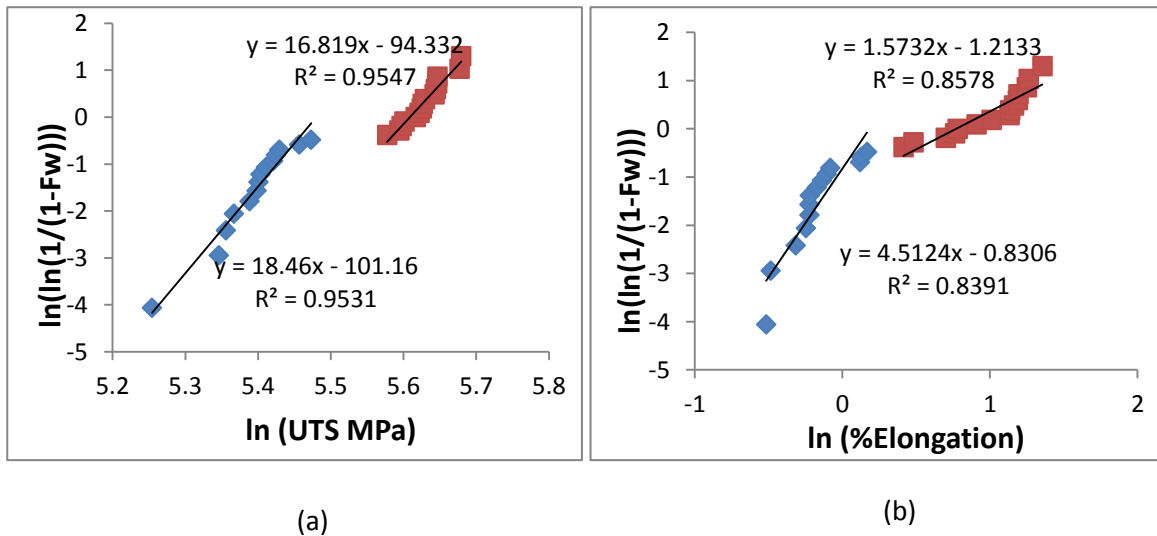
**Figure 4-61 Weibull plots of both UTS and Elongation, showing two types of defects in of 2L99 +Na casting.**

**Table 4-24 Summary of the results for modifiers addition into 2L99.**

| Casting | Weibull moduli for UTS | Weibull moduli for %Elongation | Position parameter for UTS | Position parameter for %Elongation |
|---|---|---|---|---|
| 2L99 +Ba | 16.4 | 2.2 | 278.6 | 2.35 |
| 2L99+Sr | 9.1 | 1.5 | 263 | 2.02 |
| 2L99+Na (Group 1) | 18.46 | N/A | 239.8 | N/A |
| 2L99+Na (Group 2) | 16.82 | N/A | 272.8 | N/A |

The Weibull moduli results are summarised in Table 4-24. The results of modifiers were compared to the 2L99 results with heat-treatment and roll over as the same experimental condition was used.

The method of Tiryakioğlu *et. al* for the comparison of two Weibull moduli was used here. The results are shown in Table 4-25. The Ba addition showed no effect on the Weibull moduli of both UTS and %Elongation. The Sr addition showed a statistically significient decrease of the Weibull moduli of UTS and %Elongation, while the two groups with the Na addition showed no effect of the Weibull moduli of the UTS.

**Table 4-25 Statistical comparison of the Weibull moduli for the modifiers addition into 2L99 compared with 2L99 without element addition.**

| Castings | 2.5 and 97.5 percentile for $m_1/m_2$ | m1/m2 (UTS) | Significant difference in the Weibull moduli of UTS | m1/m2(%Elongation) | Significant difference in the Weibull moduli of %Elongation? |
|---|---|---|---|---|---|
| 2L99 and 2L99 +Ba | 0.660,1.573 | 1.01 | No | 1.21 | No |
| 2L99 and 2L99+Sr | 0.660,1.573 | 1.82 | Yes | 1.7 | Yes |
| 2L99 and 2L99+Na (Group 1) | 0.574,1.823 | 1.14 | No | N/A | N/A |
| 2L99 and 2L99+Na (Group 2) | 0.594,1.823 | 1.04 | No | N/A | N/A |

### 4.3.2.2   Fracture surface analysis
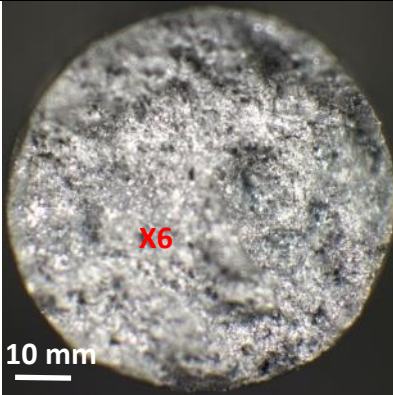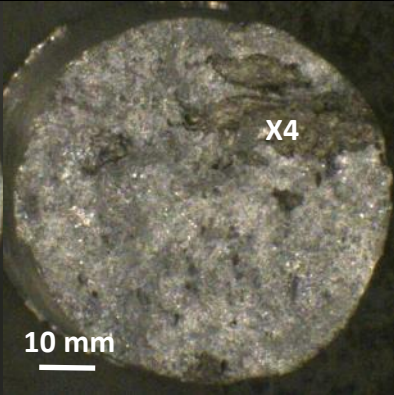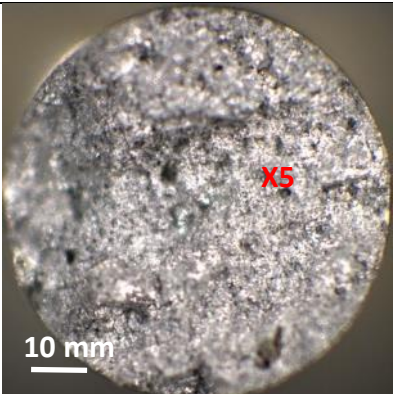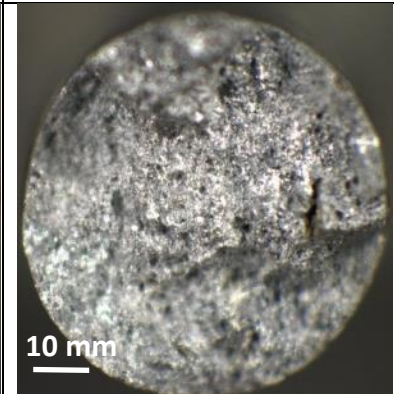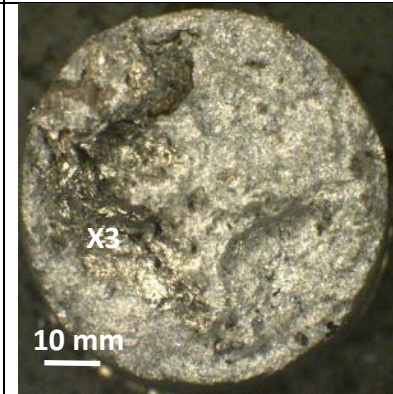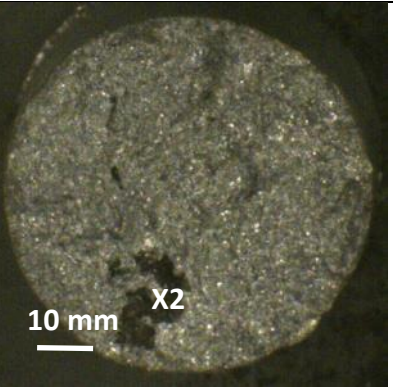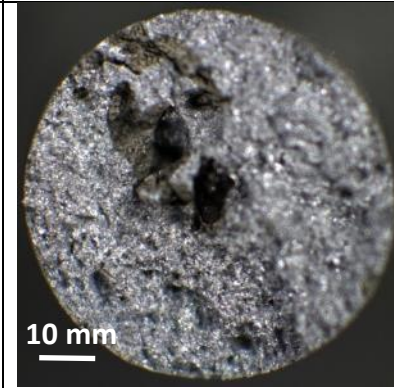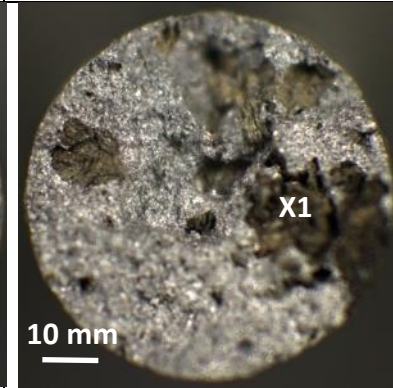
Table 4-26 showed a fracture surface of 2L99 with modifier additions. Three fracture surfaces were taken from each casting, to represent good, average and bad mechanical properties. As can be seen, for casting with a Sr addition, oxide film defects were the main defect in the test bar for both bad (No.10) and average(No.17) mechanical properties. While as for the test bar with good mechanical properties (No.23), porosity was the main defect.

For casting with a Na addition, oxide film defects were the main defect in the test bar with poor mechanical properties. Porosity was a commonly observed defect on the test bars with average and good mechanical properties. This observation is consistent with the Weibull distribution which suggested existence of a bi-model distribution in the Sr and Na modified castings.

For addition of Ba, oxide film defects were seen in all three fracture surfaces but the size of defect became smaller with the improvement of the mechanical properties.

Figure 4-62 shows a representative SEM image of the oxide film defects and gas porosity discovered on the fracture surfaces.

**Table 4-26 Fracture surfaces of 2L99 with modifiers addition.**

| Castings | With good mechanical properties | With average mechanical properties | With bad mechanical properties |
|---|---|---|---|
| 2L99+Sr |  |  |  |
| Main defect in the casting | porosity (No.23) | oxide film defect (No.17) | oxide film defect (No.10) |
| 2L99+Na |  |  |  |
| Main defect in the casting | Porosity (No.11) | Porosity (No.20) | oxide film defect (No.6) |
| 2L99+Ba |  |  |  |
| No. of test bar/main defect | oxide film defect (No.20) | oxide film defect (No.10) | oxide film defect (No.4) |

(a)

(b)

(c)

(d)
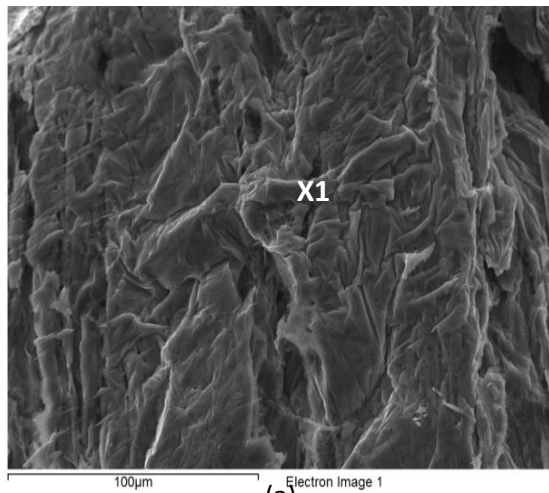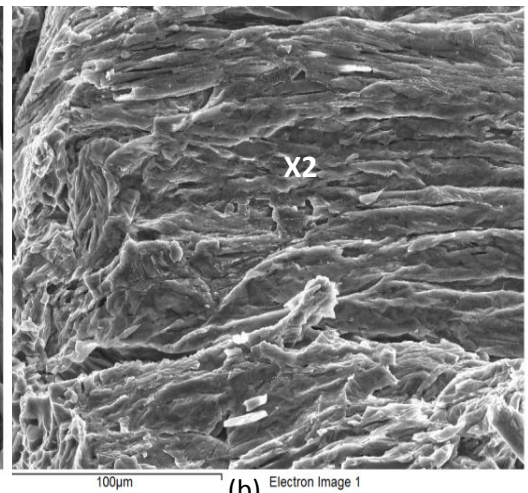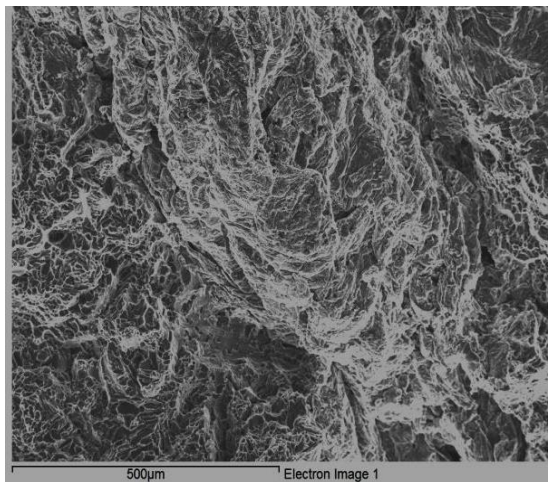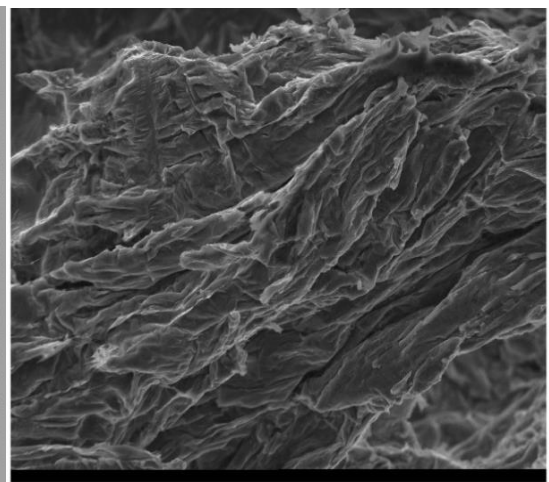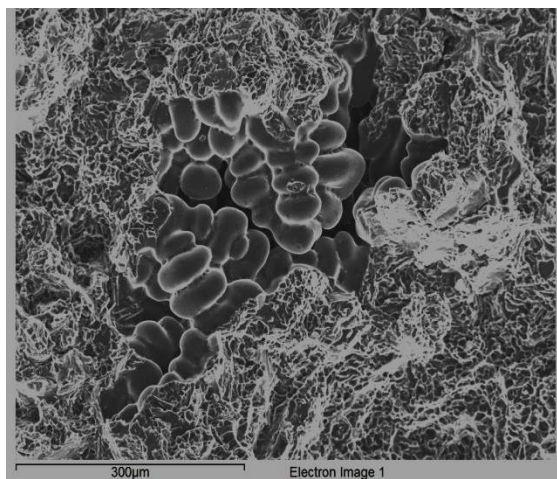
(e)
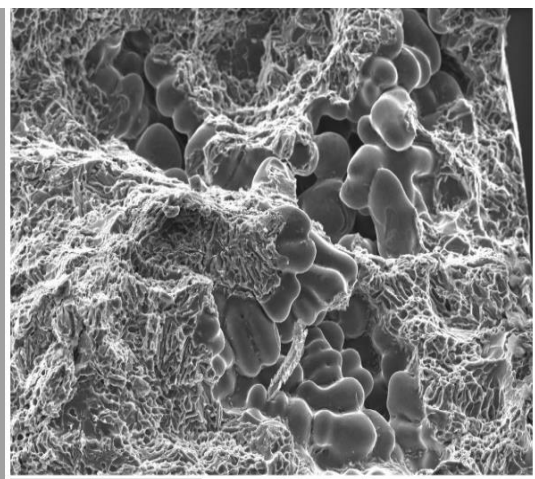
(f)
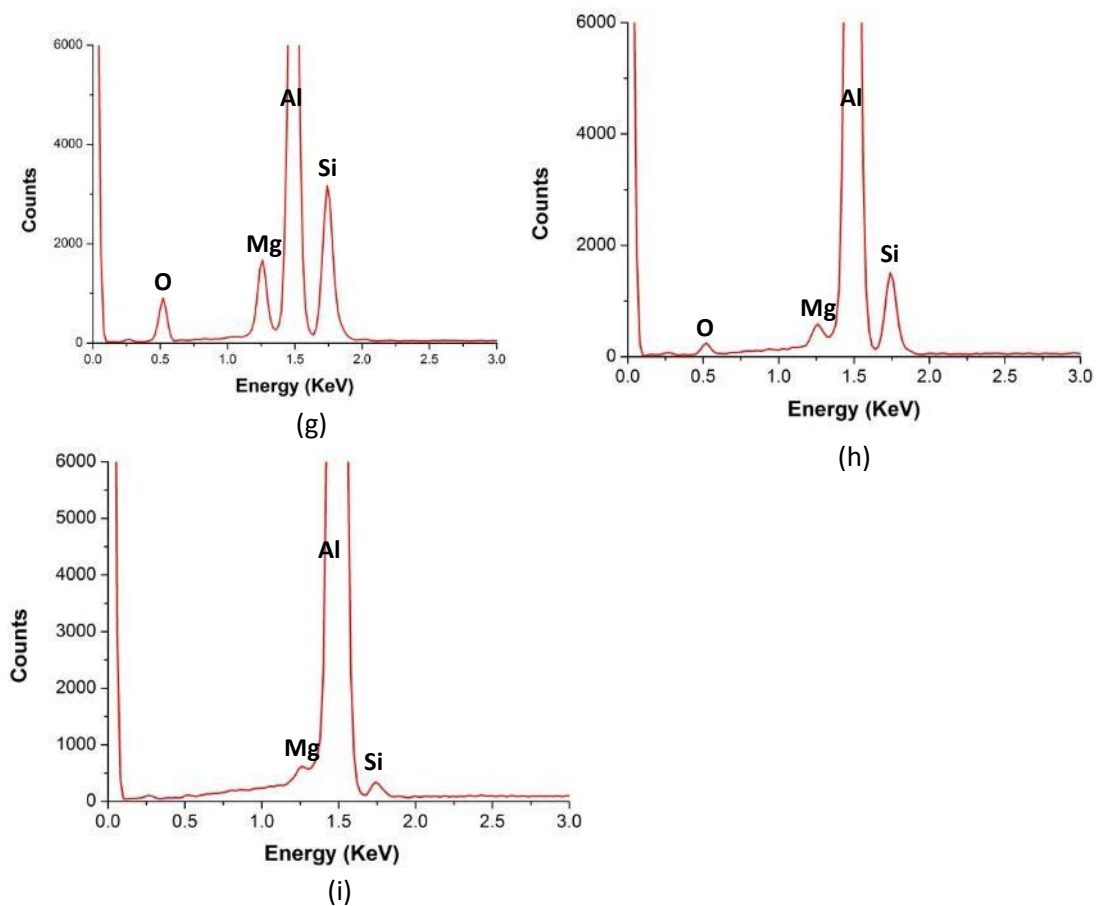
**Figure 4-62 (a)-(f) SEM images of Table 4-26 X1-X6; (g)-(h) EDX spectrum of X1-X3.**

Figure 4-63 and Figure 4-64 shows SEM images of the polished surface of the 2L99 casting with Ba and Sr modification which contained defects. EDX analysis showed that the defects contained oxygen which suggested that they could be double oxide film defect. Ba and Sr containing intermetallic phase was also observed possibly nucleated on the side of the oxide film.
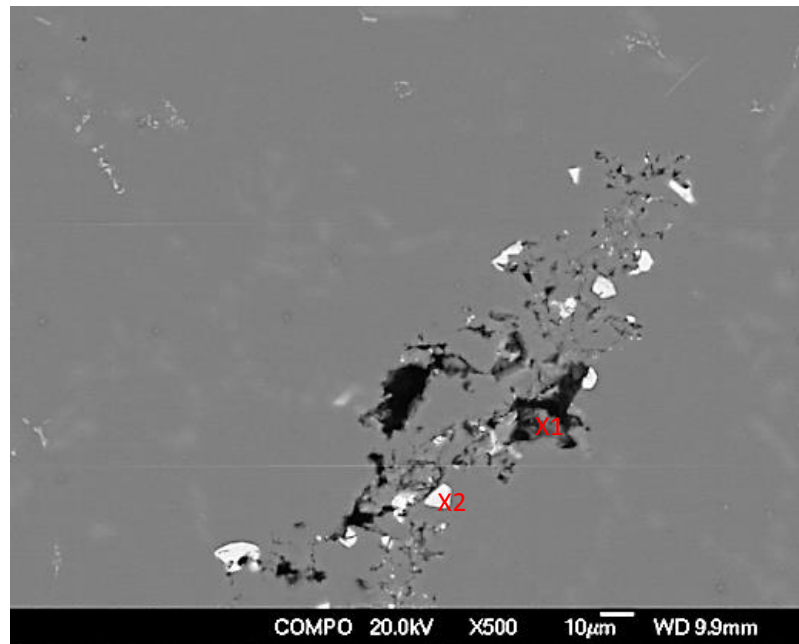
(a)
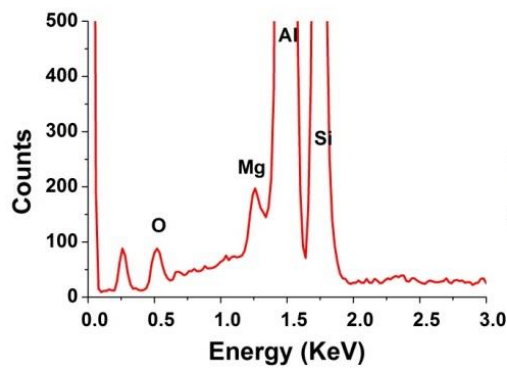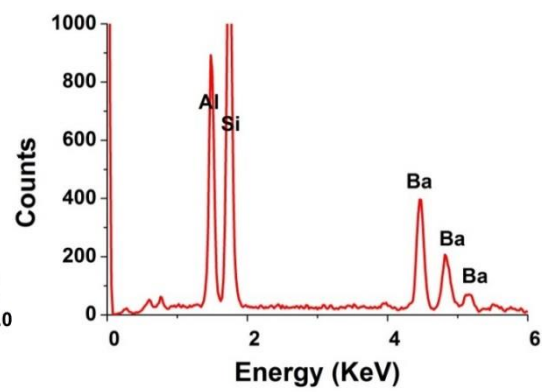
(b)                                        (c)

**Figure 4-63 (a)Polished surface of Ba added 2L99 casting showing the Ba containing intermetallic growing on the sides of double oxide film defect. (b) and (c) EDX spectrum for X1 and X2.**
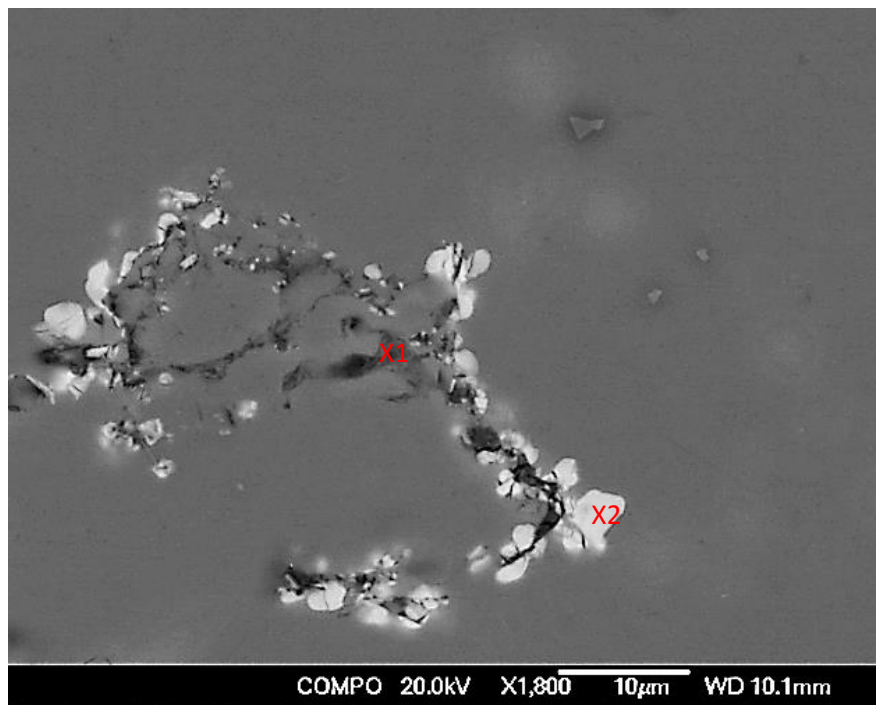
(a)
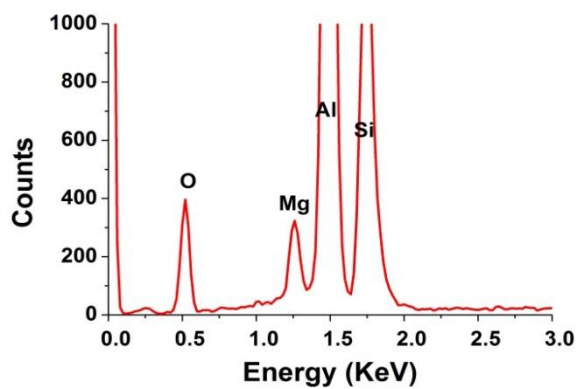


(b)
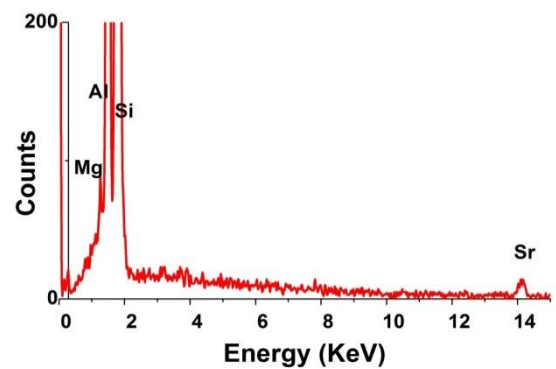
(c)

**Figure 4-64 (a)Polished surface of Sr added 2L99 casting showing the Sr containing intermetallic growing on the sides of double oxide film defect. (b) and (c) EDX spectrum for X1 and X2.**

### 4.3.2.3   Casting with reduced bi-film content

In order to further understand the effect of modifier additions on double oxide film defects in Al alloy castings, a comparison casting experiment was conducted with a filter placed in the running system of the mould, to reduce the amount of double oxide film defects

entering the casting testbars. 2 sets of castings were conducted; 2L99 alloy and 2L99 alloy modified with 300ppm Sr addition. 3 moulds were cast for each casting to give 30 testbars each. All of the testbars were T6 heat-treated before machining. The chemical composition of the cast testbars are shown in Table 4-27, which suggested that, for the 2L99 alloy with and without the Sr modification, the Fe, Mg content were all controlled within an acceptable range (with Fe<0.1% and Mg 0.32 +/- 10%). LECO hydrogen content analysis suggested that H content for 2L99 alloy and 2L99 modified with Sr, were 0.192 and 0.134 ppm respectively, which are all considered to be acceptable(<0.2 ppm). The effect of Sr modification was confirmed by optical microscopy, showing the modification of the plate-like Si to a coral shaped morphology (see Figure 4-65).

The tensile test results are shown in Table 4-28. As can be seen, when the Sr modifier was added, a 2% increase in the mean value of UTS was seen, and the mean value for %Elongation was dramatically increased, by 2.4 times. This result is consistent with the previous findings, which suggested an improvement in the mechanical properties, especially %Elongation, was achieved when the modifiers were added.

**Table 4-27 The composition of 2L99 and 2L99+Sr.**

|         | 2L99 casting | 2L99 +Sr casting |
|---------|--------------|------------------|
| Element | Composition (%) | Composition (%) |
| Al | 90.11 | 90.47 |
| Mg | 0.33 | 0.32 |
| Si | 9.32 | 8.95 |
| Fe | 0.09 | 0.1 |
| Ti | 0.15 | 0.13 |
| Sr | 0 | 0.03 |
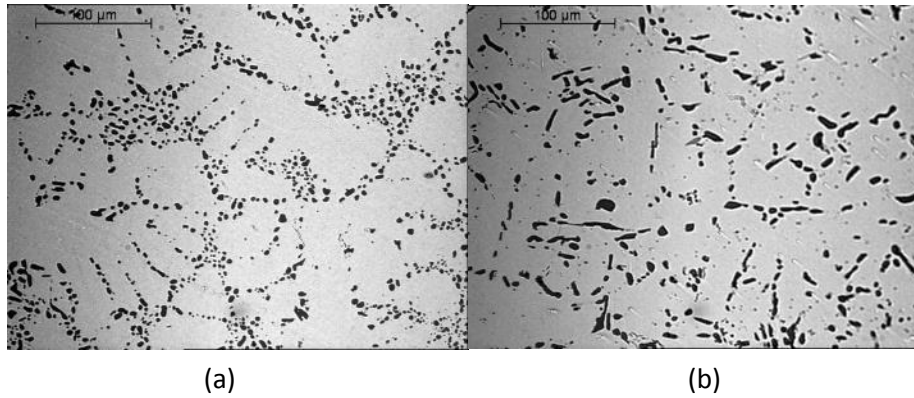
**Figure 4-65 The morphology of the Si phase in (a) 2L99 alloy modified with Sr and (b) 2L99 alloy.**

**Table 4-28 Tensile test results for 2L99 alloy and 2L99+Sr alloy.**

| | 2L99 alloy | | 2L99+Sr alloy | |
|---|---|---|---|---|
| No. | UTS (Mpa) | %Elongation | UTS (Mpa) | %Elongation |
| 1 | 266.2 | 1.73 | 283.6 | 4.46 |
| 2 | 264.3 | 1.48 | 284.2 | 5.07 |
| 3 | 269.7 | 1.94 | 281.8 | 4.63 |
| 4 | 261.8 | 1.46 | 286.5 | 4.60 |
| 5 | 270.8 | 1.34 | 288.2 | 5.46 |
| 6 | 277.6 | 2.14 | 279.2 | 3.75 |
| 7 | 279.8 | 1.95 | 287.7 | 5.83 |
| 8 | 269.2 | 1.57 | 284.0 | 4.52 |
| 9 | 274.7 | 1.93 | 261.2 | 2.45 |
| 10 | 272.3 | 1.74 | 300.5 | 3.45 |
| 11 | 259.9 | 0.90 | 287.0 | 5.06 |
| 12 | 259.6 | 0.87 | 277.7 | 4.17 |
| 13 | 253.6 | 0.91 | 284.8 | 4.51 |
| 14 | 282.5 | 1.73 | 275.2 | 3.89 |
| 15 | 289.6 | 2.60 | 263.7 | 2.54 |
| 16 | 288.1 | 1.79 | 273.0 | 4.06 |
| 17 | 296.3 | 1.51 | 281.9 | 4.71 |
| 18 | 252.3 | 0.83 | 285.4 | 5.03 |
| 19 | 258.7 | 0.85 | 282.8 | 4.50 |
| 20 | 280.5 | 1.71 | 286.3 | 5.74 |
| 21 | 276.6 | 1.60 | 288.6 | 4.87 |
| 22 | 296.0 | 2.71 | 285.6 | 4.58 |
| 23 | 292.8 | 2.33 | 283.5 | 4.32 |
| 24 | 295.9 | 3.21 | 276.6 | 2.93 |
| 25 | 295.9 | 3.41 | 283.7 | 4.00 |
| 26 | 291.3 | 2.44 | 296.5 | 6.18 |
| 27 | 297.5 | 2.79 | 289.1 | 5.49 |
| 28 | 286.5 | 2.06 | 291.6 | 6.26 |
| 29 | 284.7 | 1.99 | 287.1 | 4.64 |
| 30 | 297.4 | 2.99 | 290.7 | 6.00 |
| | | | | |
| Mean | 278.07 | 1.88 | 283.6 | 4.59 |

166

The Weibull moduli of UTS and %Elongation for 2L99 and 2L99+Sr have been shown in Figure 4-66. $R^2$ values for all plots were higher than $R^2_{0.5}$, which was 91.3%. This suggested that all the data can be accepted as following a Weibull distribution.

As can be seen, the addition of Sr has increased the Weibull moduli of the UTS of 2L99 from 23.9 to 42.7. However, the improvement in the mean value of %Elongation was not accompanied with the narrowing of the scatter of the results. The Weibull modulus of the %Elongation was increased from 3.1 to 5.4. A statistical comparison between the results is shown in Table 4-29, which suggested that both changes in the Weibull moduli were statistically significant.
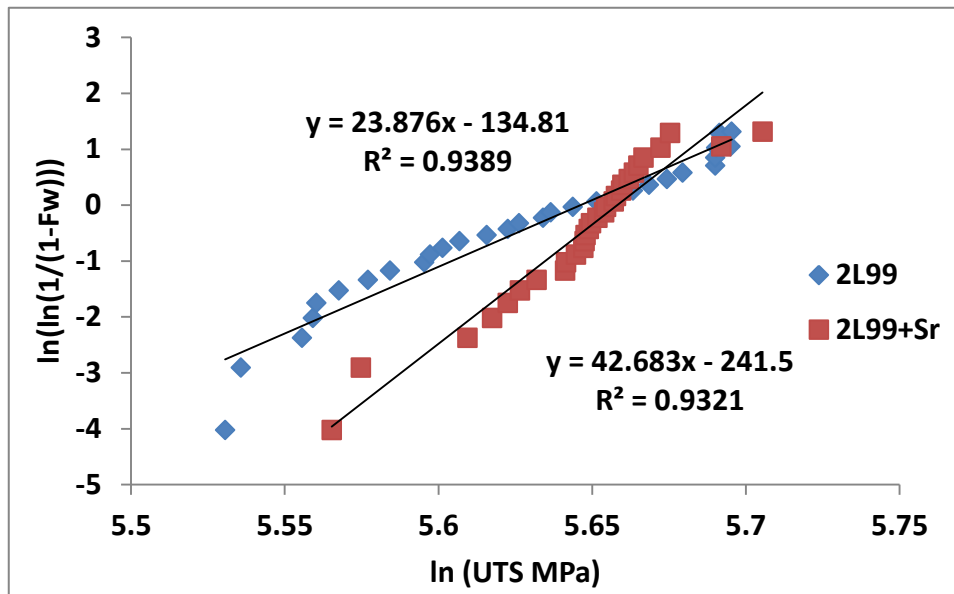
(a)
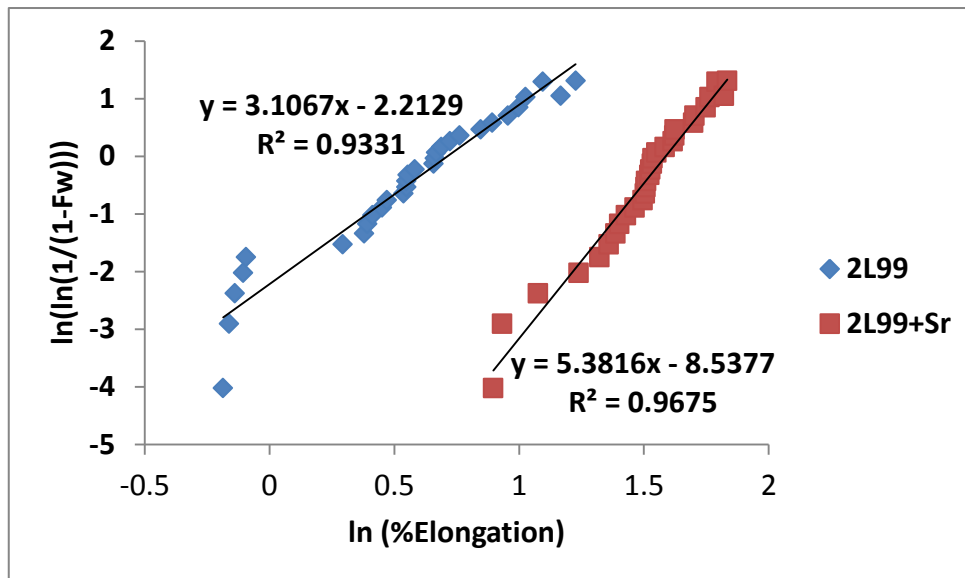


(b)
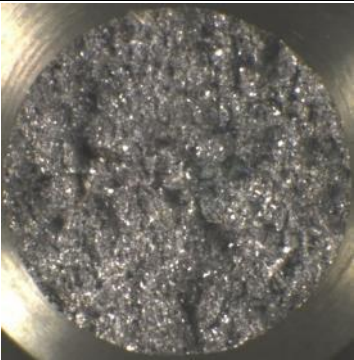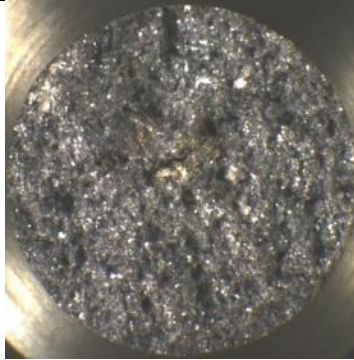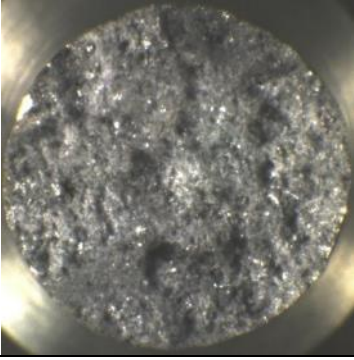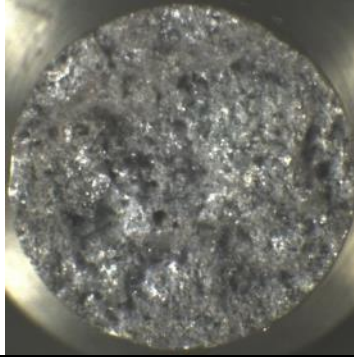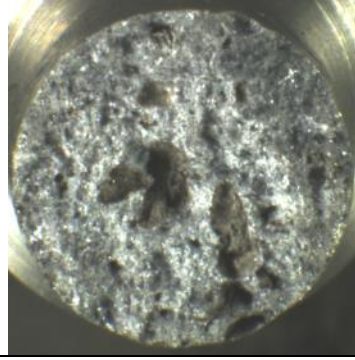
**Figure 4-66 The Weibull plots of (a) UTS and (b)%Elongation of 2L99 and 2L99+Sr castings.**

**Table 4-29 The Comparison between 2L99 alloy and 2L99 alloy modified with Sr.**

| comparison | 2.5 and 97.5 percentile point | m1/m2 (UTS) | Significant difference in the Weibull moduli of UTS? | m1/m2(%Elongation) | Significant difference in the Weibull moduli of %elongation? |
|---|---|---|---|---|---|
| 2L99, 2L99+Sr | 0.596, 1.677 | 1.78 | Yes | 1.73 | Yes |

The fracture surface examination of the testbars, which is shown in Table 4-30, suggested that the size of the bi-film became smaller for the castings with the use of a filter compared with the filter-free castings.

**Table 4-30 Fracture surface of tensile testbars of 2L99 alloy /2L99 alloy modified with Sr**

| Castings | With good mechanical properties | With average mechanical properties | With bad mechanical properties |
|---|---|---|---|
| 2L99 |  |  |  |
| Failure reason | (No.10) | Bi-film defect (No.15) | Bi-film defect (No.12) |
| 2L99+Sr |  |  |  |
| Failure reason | (No.30) | Porosity (No.18) | Bi-film defect/ porosity(No.39) |

### 4.3.2.4   Summary

These results suggest that for a casting with high bi-film defect content, the addition of modifiers worsen mechanical properties, (i.e. a decrease in the mean value of both UTS and %Elongation and a decrease in the Weibull moduli of UTS). However, with the bi-film content decreased, the addition of modifiers caused an improvement in the mean value of mechanical properties, especially %Elongation. The Weibull modulus of UTS was also significantly improved despite a decrease in %Elongation.

### 4.3.3   The effect of Mo addition to 2L99 alloy

This work was aimed at understanding the effect of the Mo additions on the reproducibility of mechanical properties of 2L99 alloy by potentially altering the nature of the double oxide film defect formed in the liquid metal.

Three types of castings were done to obtain tensile test bars; (a) 2L99 +0.4 wt. % Mo alloy, with no heat-treatment or roll-over involved, (b) 2L99 +0.4 wt. % Mo alloy with a T6 heat-treatment but no roll-over, and (c) 2L99 +0.4 wt. % Mo alloy with heat-treatment and roll-over. The results obtained were compared with corresponding results from 2L99 alloy with no addition, (see section 4.3.1).

A TP-1 test was also conducted to investigate the effect of Mo additions on the grain size of commercial purity aluminum and 2L99.

## 4.3.3.1　Tensile test results

For the experiment with unheat-treated 2L99+0.4 wt. % Mo alloy, three moulds were cast to give 29 test bars. For the 2L99 +0.4 wt. % Mo alloy with heat treatment (no roll-over), 2 moulds were cast to give 20 test bars. For the castings with heat-treatment and roll over (0.4 wt.% Mo), 3 moulds were cast to give 29 test bars. The hydrogen content in the castings was measured by LECO$^{TM}$ and was controlled within a relatively narrow range (0.2 ppm +/- 0.05ppm, see Table 4-27).

XRF was used to check the composition of the castings and the results are shown in Table 4-28. The Fe and Mg content, which might affect mechanical properties, were also controlled within an acceptable range (Fe<0.12 wt.%; Mg 0.3 wt.% +/- 0.03%).

The UTS and %Elongation of the tensile test results are shown in Table 4-29. The comparison of results shown in Table 4-30, showed that, without heat-treatment, the 0.4 wt.% Mo addition into 2L99 alloy showed a 20% increase in mean value of the UTS while the value for %Elongation was doubled compared with 2L99 alloy without addition. For the heat-treatment results however, there was no significant change in the mean value for both UTS and %Elongation (with and without addition of 0.4 wt. % Mo) compared with results from 2L99 alloy with heat-treatment but no roll-over. For the experiment with heat-treatment and roll over, the UTS increased by 12% and the %Elongation was increased by 80% compared to the 2L99 results with both heat-treatment and roll-over.

**Table 4-27 LECO hydrogen content analysis for different tensile test experiments with Mo addition into 2L99.**

| Casting | ppm H |
|---|---|
| 2L99+0.4wt.%Mo without heat-treatment | 0.221 |
| 2L99 +0.4wt.% Mo with heat-treatment | 0.204 |
| 2L99 +0.4 wt.% Mo with heat-treatment and roll over | 0.156 |

**Table 4-28 XRF result for the different tensile test experiment with Mo addition into 2L99.**

| | 2L99+0.4wt.%Mo without heat-treatment | 2L99 +0.4wt.% Mo with heat-treatment | 2L99 +0.4 wt.% Mo with heat-treatment and roll over |
|---|---|---|---|
| Formula | Concentration | Concentration | Concentration |
| Al | 85.15% | 89.92% | 90.55% |
| Si | 7.99% | 9.03% | 8.12% |
| Mo | 0.41% | 0.48% | 0.39% |
| Mg | 0.32% | 0.31% | 0.32% |
| Fe | 0.12% | 0.10% | 0.12% |
| Ti | 0.14% | 0.10% | 0.10% |

**Table 4-29 Tensile test results for Mo addition into 2L99 alloy.**

| No. | 2L99 +0.4 wt.% Mo without heat-treatment Elongation % | UTS MPa | 2L99+0.4 wt.% Mo with heat-treatment Elongation % | UTS MPa | 2L99+0.4wt.% Mo with heat-treatment and roll over Elongation % | UTS MPa |
|------|------|------|------|------|------|------|
| 1 | 2.58 | 171.3 | 1.48 | 279.1 | 1.62 | 281.7 |
| 2 | 3.84 | 179.7 | 0.71 | 258.4 | 2.86 | 289.9 |
| 3 | 3.54 | 178.3 | 1.00 | 272.9 | 1.75 | 283.1 |
| 4 | 4.56 | 182.5 | 1.00 | 274.4 | 1.56 | 280 |
| 5 | 2.92 | 172 | 0.86 | 264.9 | 1.58 | 274.1 |
| 6 | 4.2 | 181.4 | 0.59 | 247.0 | 2.18 | 288.7 |
| 7 | 2.5 | 166.6 | 1.43 | 276.4 | 2.2 | 284.8 |
| 8 | 2.24 | 164.7 | 0.70 | 255.3 | 1.34 | 272.4 |
| 9 | 3.31 | 178.4 | 1.21 | 274.2 | 0.68 | 255.4 |
| 10 | 2.65 | 173.9 | 1.00 | 272.0 | 1.96 | 278.8 |
| 11 | 3.69 | 183.5 | 1.51 | 278.0 | 1.78 | 279.1 |
| 12 | 3.4 | 179.8 | 1.45 | 279.3 | 0.85 | 258.4 |
| 13 | 2.12 | 163 | 1.06 | 273.5 | 1.2 | 272.9 |
| 14 | 2.11 | 163.6 | 0.76 | 262.5 | 1.2 | 274.4 |
| 15 | 2.77 | 173.6 | 1.19 | 274.2 | 1.03 | 264.9 |
| 16 | 4.09 | 184.6 | 0.72 | 264.0 | 0.71 | 247 |
| 17 | 2.07 | 165 | 0.97 | 267.3 | 1.72 | 276.4 |
| 18 | 2.53 | 169.7 | 1.16 | 270.2 | 0.84 | 255.3 |
| 19 | 3.51 | 180.2 | 1.47 | 277.2 | 1.45 | 274.2 |
| 20 | 3.43 | 181.6 | | | 1.2 | 272 |
| 21 | 3.95 | 182.5 | | | 1.81 | 278 |
| 22 | 3.68 | 180.9 | | | 1.74 | 279.3 |
| 23 | 4.47 | 185 | | | 1.27 | 273.5 |
| 24 | 4.96 | 190.6 | | | 0.91 | 262.5 |
| 25 | 3.57 | 181.4 | | | 1.43 | 274.2 |
| 26 | 3.76 | 182.4 | | | 0.86 | 264 |
| 27 | 3.23 | 178.5 | | | 1.16 | 267.3 |
| 28 | 1.47 | 148.5 | | | 1.39 | 270.2 |
| 29 | | | | | 1.76 | 277.2 |
| 30 | | | | | 1.45 | 272.8 |
| mean | 3.25 | 175.8 | 1.07 | 269.5 | 3.41 | 299.5 |

173

| | mean value (without-heat-treatment) | | mean value (with heat-treatment) | | mean value (with heat-treatment and Roll-over) | |
|---|---|---|---|---|---|---|
| | UTS (Mpa) | %Elongation | UTS (Mpa) | %Elongation | UTS (Mpa) | %Elongation |
| 2L99 | 144.5 | 1.55 | 271.4 | 1.16 | 267.6 | 1.9 |
| 2L99+0.4 wt.%Mo | 175.8 | 3.26 | 269.5 | 1.07 | 299.5 | 3.41 |

The Weibull plots for the UTS and %Elongation of the Mo addition castings are shown in Figure 4-67 and Figure 4-68. The $R^2$ value and the relative $R^2_{0.5}$ for each casting are shown in Table 4-31. The $R^2$ values for all of the castings were higher than $R^2_{0.5}$, therefore, all the castings can be treated as obeying a Weibull distribution.

**Table 4-31 $R^2$ value and the relative $R^2_{0.5}$ for each casting with Mo addition into 2L99.**

| | $R^2_{0.5}$ | $R^2$ for UTS | Distribution of UTS accepted as Weibull distribution? | $R^2$ for %Elongation | Distribution of %Elongation accepted as Weibull distribution |
|---|---|---|---|---|---|
| Unheat-treated results | 0.91 | 0.96 | Yes | 0.97 | Yes |
| Heat-treated results | 0.89 | 0.98 | Yes | 0.90 | Yes |
| heat-treated resuls with roll over 0.4 wt.% Mo addition | 0.91 | 0.98 | Yes | 0.95 | Yes |
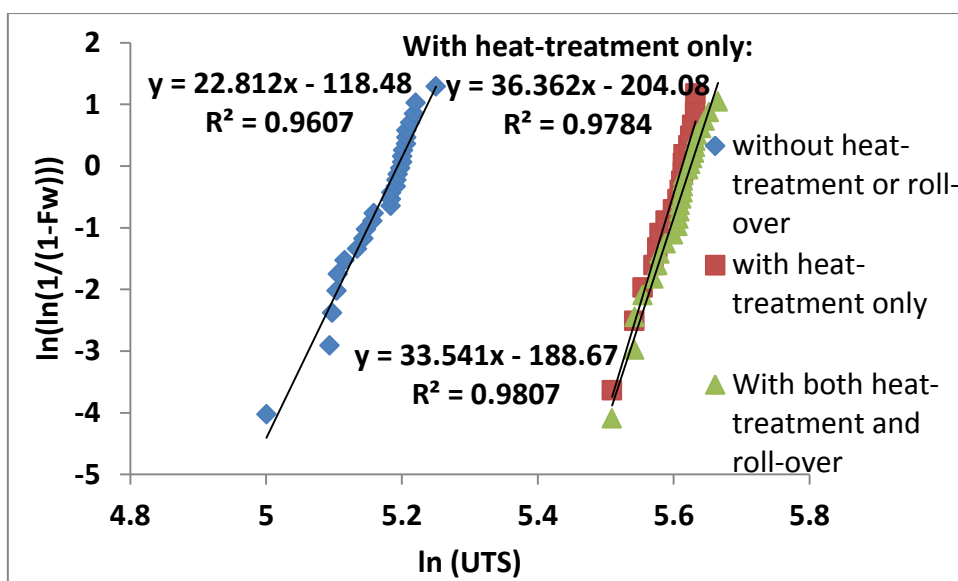
**Figure 4-67 Weibull plots of UTS of 2L99+Mo castings.**
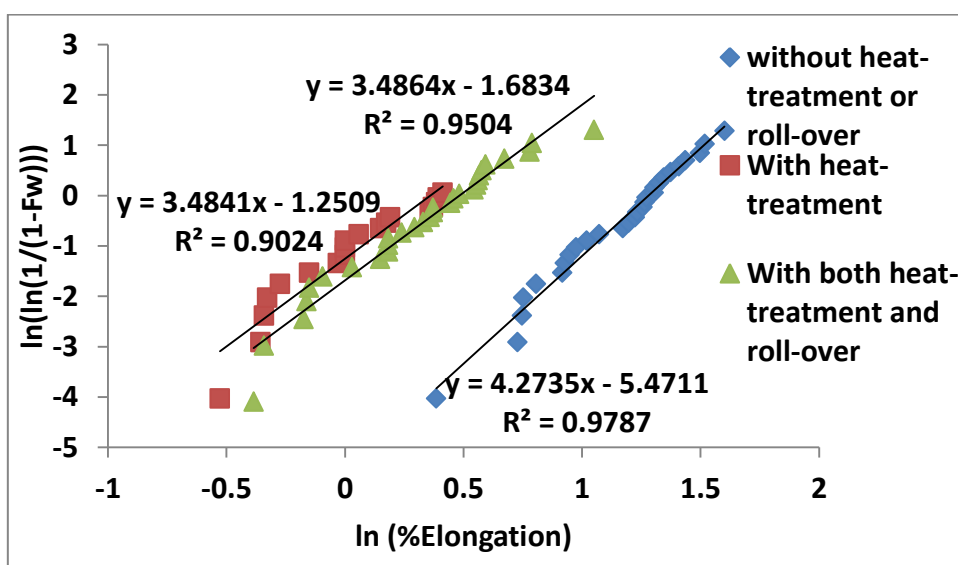


**Figure 4-68 Weibull plots of %Elongation of 2L99+Mo castings.**

**Table 4-32 The comparison of the Weibull moduli between 2L99 and 2L99+0.4 wt.% Mo**

|  | Weibull moduli (without-heat-treatment) | | Weibull moduli (with heat-treatment) | | Weibull moduli (with heat-treatment and Roll-over) | |
|---|---|---|---|---|---|---|
|  | UTS | %Elongation | UTS | %Elongation | UTS (Mpa) | %Elongation |
| 2L99 | 8.92 | 2.56 | 18.67 | 3 | 16.14 | 2.55 |
| 2L99+0.4 wt.%Mo | 22.8 | 4.3 | 36.4 | 3.5 | 33.5 | 3.5 |

**Table 4-33 The comparison of the Position Parameter between 2L99 and 2L99+0.4 wt.% Mo.**

| ` | Position Parameter (without-heat-treatment) | | Position parameter (with heat-treatment) | | Position parameter (with heat-treatment and Roll-over) | |
|---|---|---|---|---|---|---|
| | UTS | %Elongation | UTS | %Elongation | UTS (Mpa) | %Elongation |
| 2L99 | 153.6 | 1.77 | 279.6 | 1.57 | 276.6 | 2.13 |
| 2L99+0.4 wt.%Mo | 180.2 | 3.60 | 273.8 | 1.19 | 304 | 3.58 |

The comparison between 2L99 and 2L99+Mo of the Weibull moduli and position parameters are shown in Table 4-32 and Table 4-33, respectively. For the casting without heat-treatment, the Weibull modulus of the UTS was more than doubled with the addition of Mo. The Weibull modulus of the %Elongation was also increased, by 68%. For the experiment with T6 heat-treatment no roll-over, a similar trend was seen; the Weibull modulus of the UTS was almost doubled, while the %Elongation was increased by about 35% when 0.4 wt.% Mo was added. For the experiment with heat-treatment and roll over, the Weibull moduli for UTS was doubled and the Weibull moduli of %Elongation was increased by 30%, by the Mo addition.

The position parameters for the unheat-treated alloy showed an increase, with the addition of Mo, in both UTS and %Elongation, of about 17% and 100%, respectively. The results with heat-treatment showed little change in the position parameter for UTS (around 275 MPa) but the %Elongation was decreased by around 30%. For the results with heat-treatment and roll-over, the position parameter for the UTS and %Elongation was increased, with Mo addition, by 10% and 68% respectively, compared to 2L99.

The method of Tiryakioğlu et al. was used to compare the Weibull moduli for the two different alloys; 2L99 and 2L99 + Mo with different conditions (with no heat-treatment or

roll over, with heat-treatment but no roll-over, with both heat-treatment and roll-over). The result suggested that the addition of Mo significantly improved the Weibull moduli of UTS in all three castings. For the Weibull moduli of %Elongation, the unheat-treated casting and the casting with heat-treatment and roll over, both with 0.4 wt.% Mo addition, also showed a statistically significant improvement in the Weibull moduli. The results are shown in Table 4-34.

**Table 4-34 The comparison of the Weibull moduli for Mo addition into 2L99 castings.**

| comparison | 2.5 and 97.5 percentile point | m1/m2 (UTS) | Significant difference in the Weibull moduli of UTS? | m1/m2(%Elongation) | Significant difference in the Weibull moduli of %elongation? |
|---|---|---|---|---|---|
| unheat-treated (2L99, 2L99+0.4 wt.% Mo) | 0.596, 1.677 | 2.55 | Yes | 1.68 | Yes |
| heat-treated (2L99, 2L99+0.4 wt.% Mo) | 0.526, 1.899 | 1.95 | Yes | 1.16 | No |
| heat-treated with roll over (2L99, 2L99+0.4 wt.% Mo) | 0.674,1.523 | 0.47 | Yes | 0.72 | No |

*4.3.3.2    SEM investigation of the fracture surface*

4.3.3.2.1    Oxide found on the sample surface of 2L99 +0.4 wt.% Mo

In the casting with 2L99 + 0.4 wt.% Mo, some test bars (15%) were found associated with a feature that might have been a Mo-containing oxide, or a Mo-containing intermetallic compound. Figure 4-69 shows the fracture surface of No. 15 test bar of a unheat-treated 2L99+ 0.4 wt.% Mo casting. Figure 4-70 is the SEM image of the area at higher

magnification, which showed two different types of oxides (X1 and X2) growing near an Al-Si-Mo compound (X3):

The oxide shown in X1 of Figure 4-70 had a high oxygen content (55.2 at.%) which was much greater than the oxide usually found on the sample surface(10 at.%). This oxide layer , which consists of granular oxide particles, as shown in Figure 4-71 to Figure 4-72 at higher magnifications, had a different morphology compared with the oxide found in the 2L99 casting (as shown in Figure 4-51).

In Figure 4-70 X2, another type of oxide is shown. A higher magnification image is shown in Figure 4-73. EDX analysis showed that its oxygen content (22 at.%) was lower than the oxide layer shown in Figure 4-70 X1.

Near these oxide layers, a Mo-containing intermetallic compound was observed, as shown in X3 of Figure 4-70 and X1 of Figure 4-71. EDX analysis (shown in Table 4-35) showed that it contained Al, Si and Mo. The Mo:(Al,Si) ratio was roughly 1:2, which suggested $Mo(Al,Si)_2$. The composition of the oxide layer and the Mo-containing compound is shown in Table 4-35.



**Figure 4-69 Fracture surface of tensile test bar No. 15 of the heat-treated 2L99+ 0.4 wt.% Mo casting; X1 the area shows in Figure 4-70.**
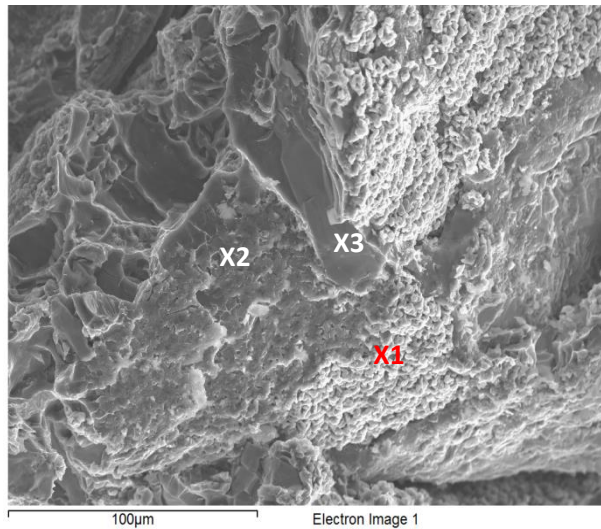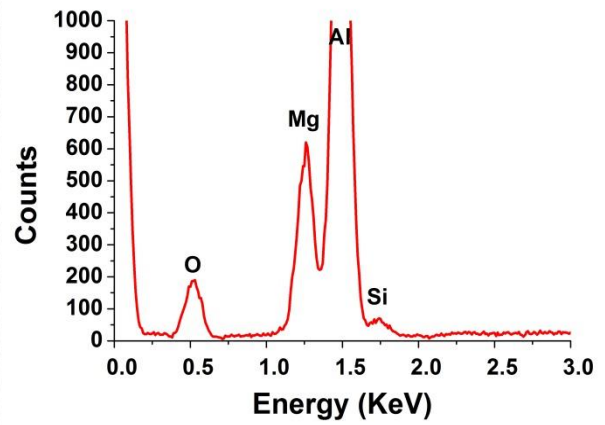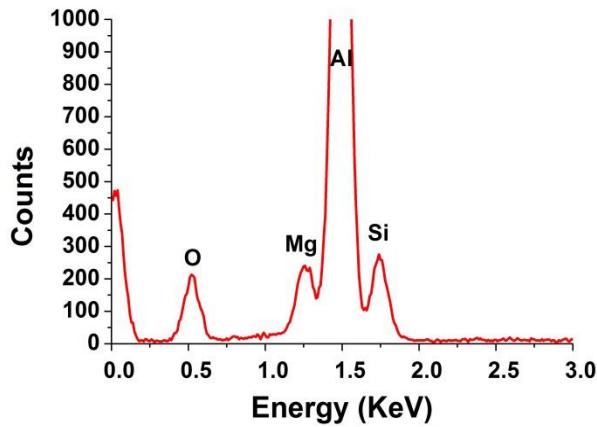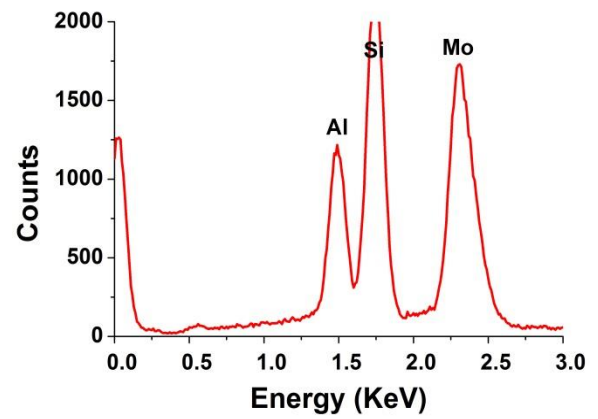
Figure 4-70. (a) The fracture surface of un-heat treated 2L99+Mo (Test bar No. 15); (b)EDX spectrum for X1;(c)EDX spectrum for X2 and (d) EDX spectrum for X3.

Table 4-35. Quantification of Figure 4-70 X1-X3.

|  | oxide layer(X1) | Oxide layer (X2) | Mo containing compound (X3) |
|---|---|---|---|
| O | 55.2 at.% | 22 at.% | 5.45 at.% |
| Mg | 13.59 at.% | 2.33 at.% | 0 |
| Al | 31.22 at.% | 57.4 at.% | 15.77 at.% |
| Mo | 0 | 0 | 31.13 at.% |
| Si | 0 | 18.06 at.% | 47.65 at.% |
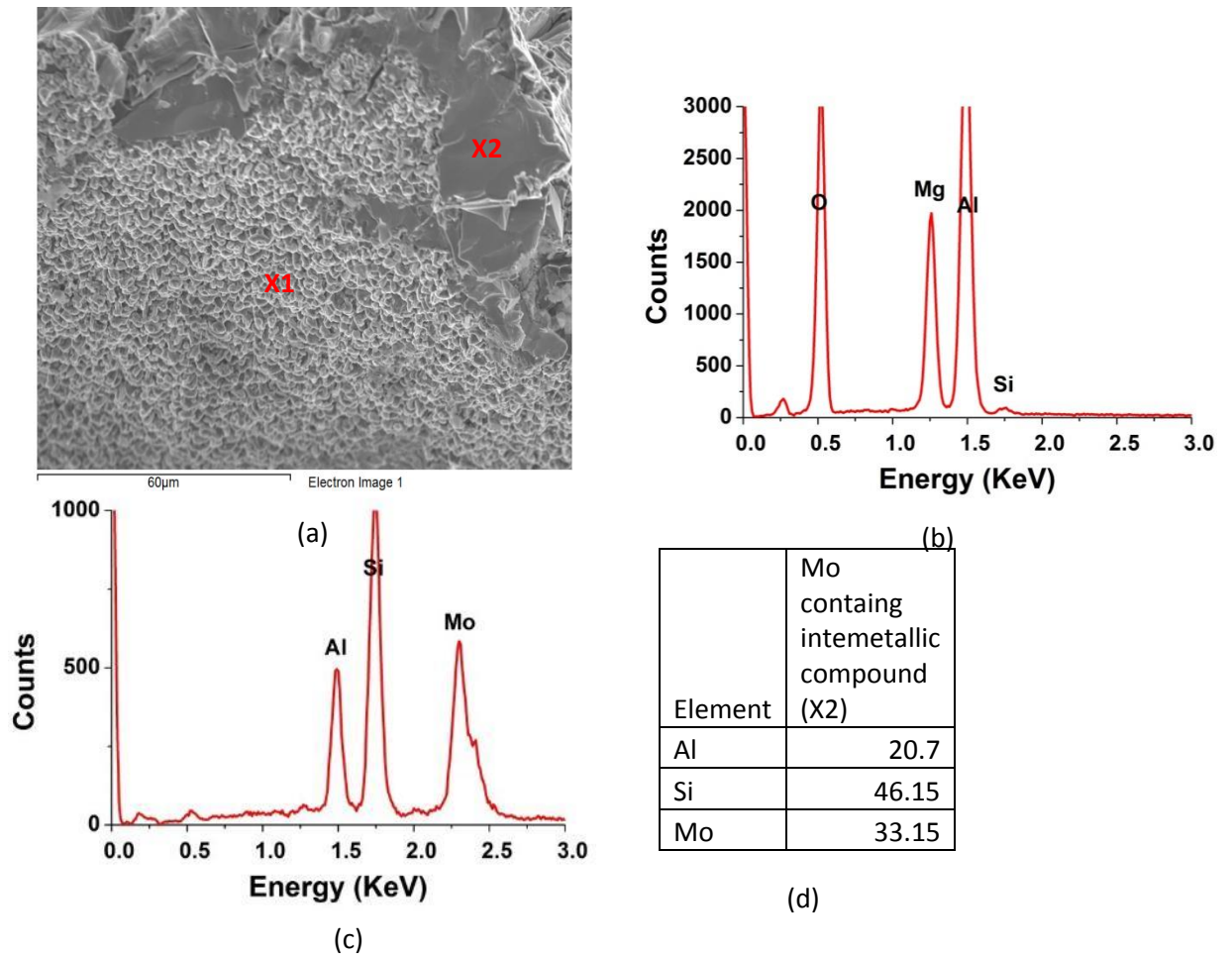
Figure 4-71 (a) Oxide layer found on the sample surface with 2L99+Mo; (b) EDX spectrum for X1 and (c) EDX spectrum for X2 and (d) Quantified EDX result for X2.

(a)



(b)
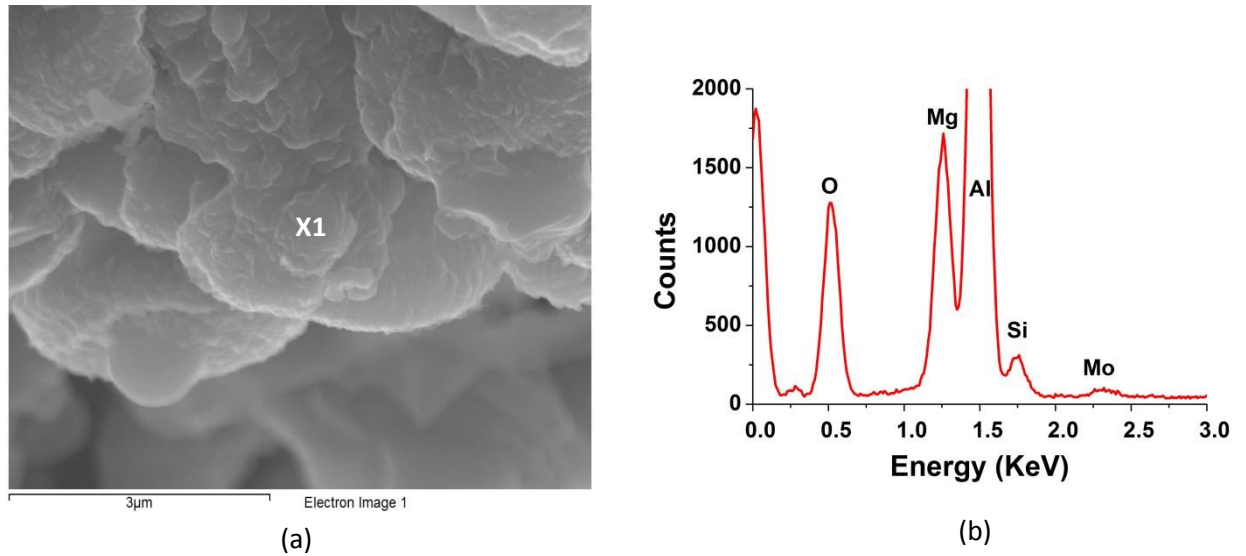
**Figure 4-72. (a) Higher magnification image of the oxide layer found on the sample surface with 2L99+Mo; (b) EDX spectrum for X1 and (c) EDX spectrum for X2.**



(a)



(b)
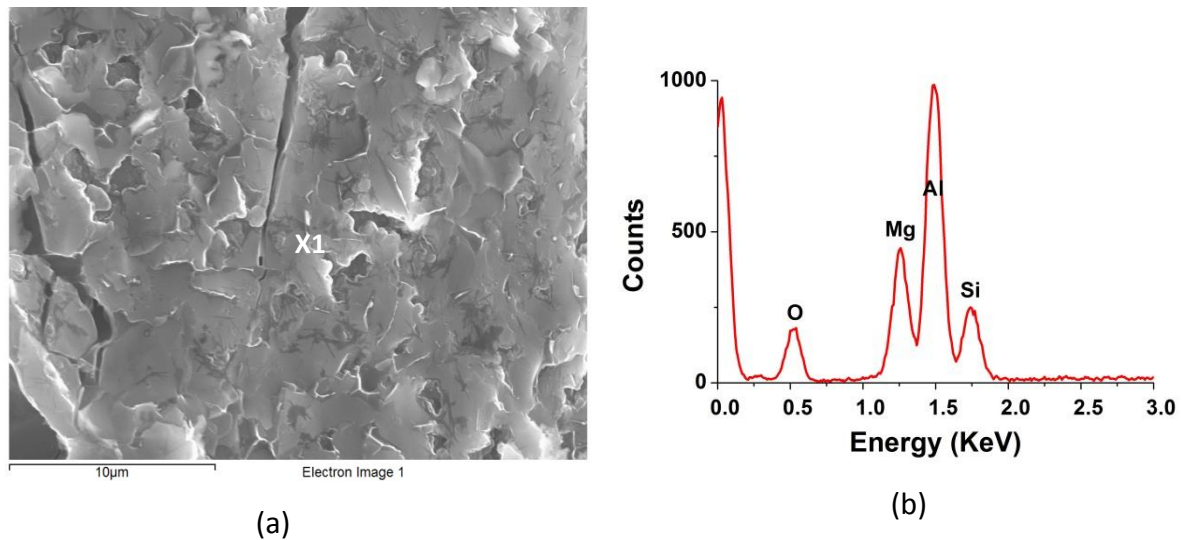
**Figure 4-73. (a) Higher magnification image of the X2 in Figure 4-92 ; (b) EDX spectrum for X1.**

Figure 4-74 and Figure 4-75 show an oxide found on the fracture surface of No. 18 testbar of the heat–treated castings, in which Mo was detected. The circled area in Figure 4-75 (X1) contained 4.15 at.% O and 1.16 at.% Mg, and no Mo peak was detected. EDX analysis of the area outside the circle (X2), however, suggested the presence of a Mo containing oxide layer. The high Mo, Si and O peaks detected in X3 suggested an oxidized Mo-containing

181

particle. X4 is another Mo-containing particle but with Fe detected. Quantification of the

EDX spectrum in Figure 4-75 is shown in Table 4-36.
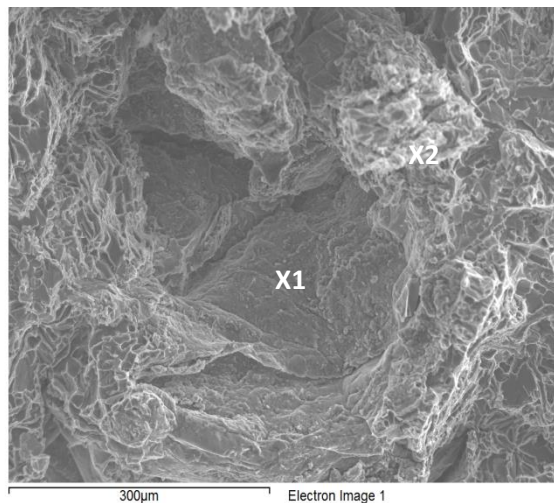


(a)
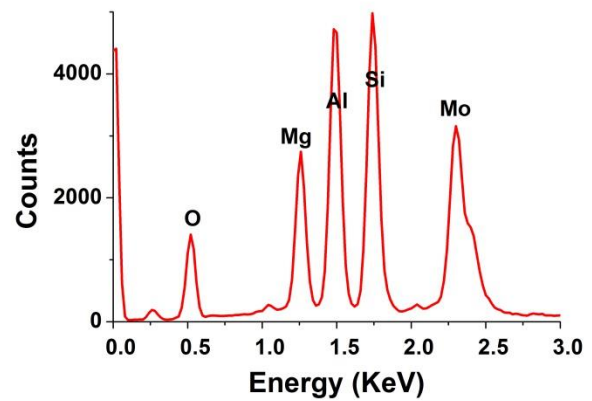


(b)
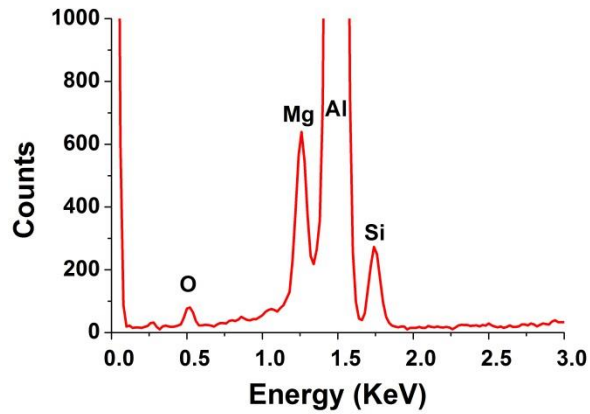


(c)

Figure 4-74. (a) Mo containing oxide shown on the sample surface of 2L99 + 0.4 wt.% Mo; (b) EDX spectrum for X1 and (c) EDX spectrum for X2.
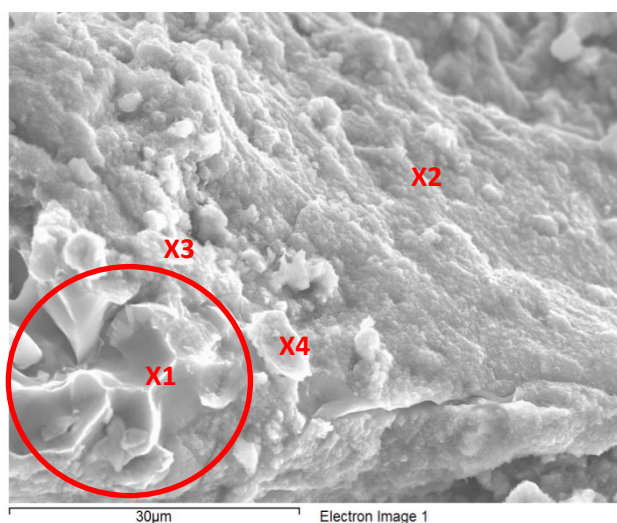
(a)
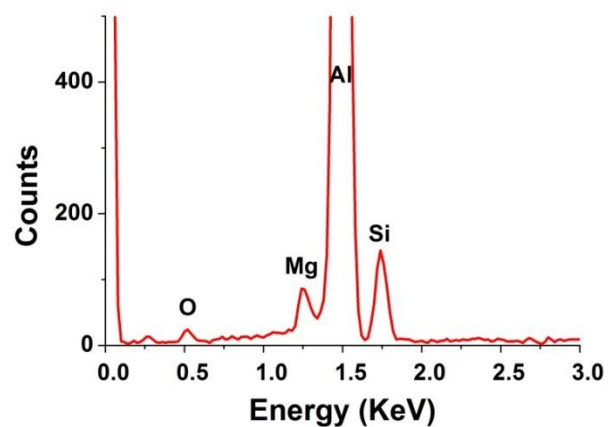
(b)
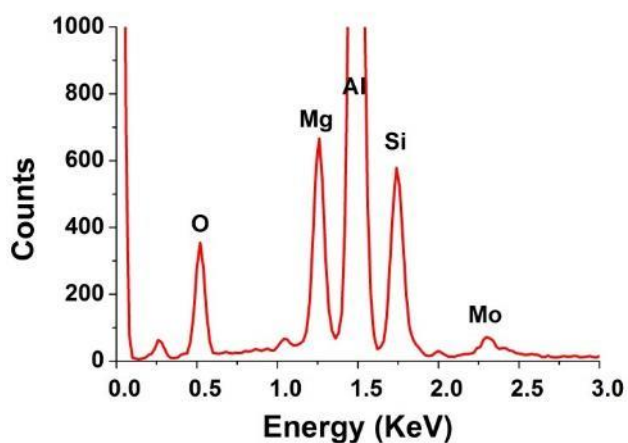
(c)
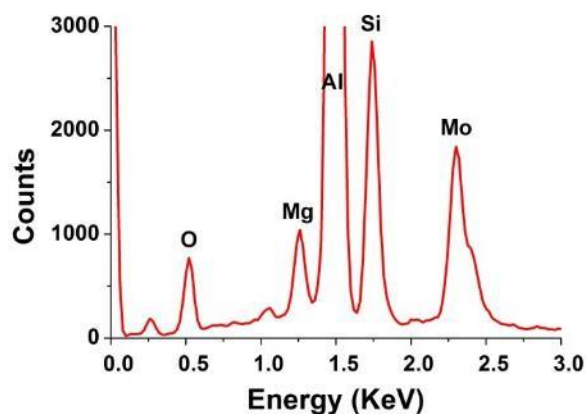
(d)
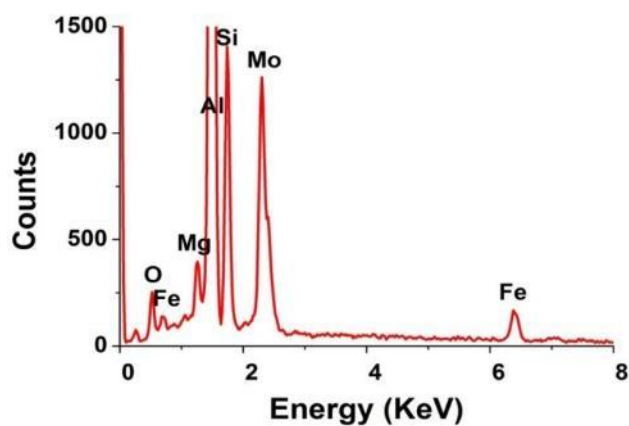
(e)

**Figure 4-75. (a) Higher magnification of the Figure 4-74 shows the Mo containing oxide layer growing on the alumina; (b) EDX spectrum for X1; (c) EDX spectrum for X2; (d)EDX spectrum for X3 and (e) EDX spectrum for X4.**

183

**Table 4-36. Quantification of the spectrum of Figure 4-75.**

|  | Spectrum 1 | Spectrum 2 | Spectrum 3 | Spectrum 4 |
|---|---|---|---|---|
| O | 4.15 at.% | 35.4 at.% | 27.14 at.% | 16.16 at.% |
| Mg | 1.16 at.% | 9.37 at.% | 3 at.% | 1.93 at.% |
| Al | 88.17 at.% | 40.98 at.% | 49.19 at.% | 57.43 at.% |
| Si | 6.51 at.% | 13. 34 at.% | 14.08 at.% | 13.84 at.% |
| Mo | 0 | 0.92 at.% | 6.58 at.% | 8.52 at.% |
| Fe | 0 | 0 | 0 | 2.12 at.% |

Figure 4-76 is another oxide (from the test bar No. 19 of the 2L99+ 0.4 wt.% Mo heat-treated casting with roll over) which showed the presence of Mo peaks in the EDX spectrum. In these cases, Mo might be participating in the oxide formation process.
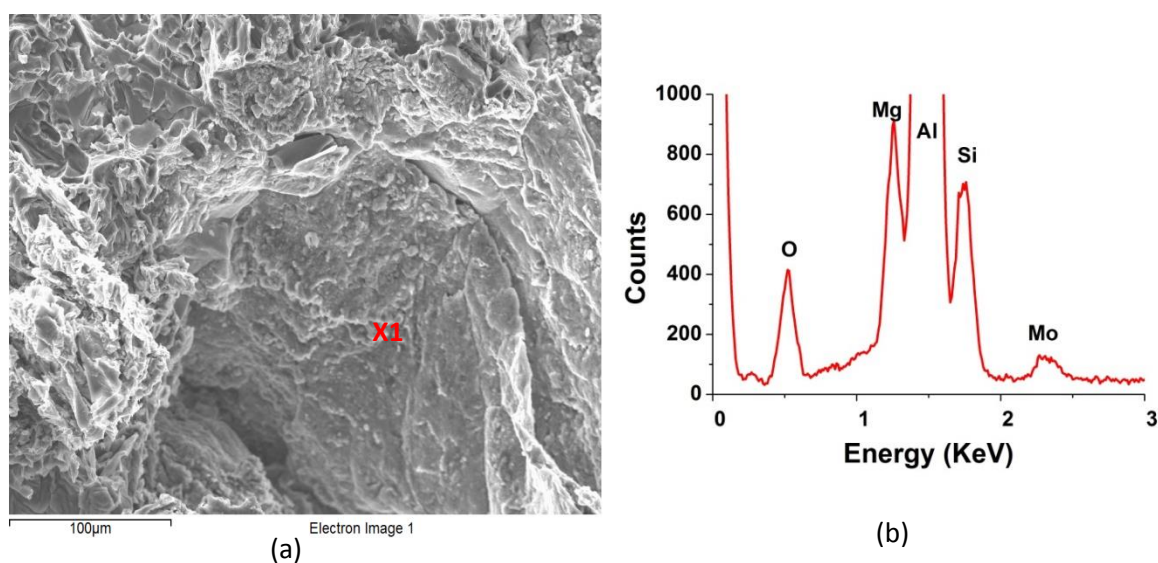


**Figure 4-76. (a) Sample surface of test bar No. 5 of the heat-treated 2L99+0.4 wt.% Mo casting with roll over suggest the Mo containing oxide and (b) EDX spectrum of X1.**

### 4.3.3.2.2　Nitride found on the sample surface of 2L99+ 0.4 wt.% Mo

In addition to the oxide found in the 2L99+0.4 wt.% Mo castings, a nitride layer was sometimes seen on the fracture surface . A nitride layer on a fracture surface has not been reported before, due to the difficulty of formation of nitride in the presence of oxygen in the entrapped gas. (Considering the lifetime of a double oxide film defect, which might be of the order of minutes, a typical double oxide film defect might not have enough time for complete consumption of its entrapped oxygen (or, at least the majority) to start the formation of nitride).

Figure 4-77 shows a nitride containing area from the tensile test bar No. 14 of the unheat-treated 2L99 +0.4 wt. % Mo casting. Figure 4-78 is the SEM image of this nitride layer. Mo was not detected in this N containing layer. However, some Mo containing intermetallic compounds (shown in Figure 4-79) were seen nucleated on the sides of the nitride layer which, confirmed by EDX, contained high Mo and Si content. Figure 4-79 showed that the intermetallic particles had different morphology. Some of the small pieces, (possibly fractured parts from a larger sized piece), were observed dispersed over the oxide layer.

Figure 4-80 shows an SEM image of the morphology of the nitride found on the fracture surface. Spectra 1, 3, 6, with tooth shaped morphology, could be a nitride phase(possibly AlN)  which contained a high N content (around 30 at.% to 40 at.%), a low Mg  content ( 0.5 at.% to 0.6 at.%) and moderate O content (10 at.% to 15 at.%). while spectra 2, 4, 5, having a particle shape, could be the spinel phase where lower N content (20 at.%) but higher Mg content(2 at.% to 4 at.%) and O content (15 at.% to 38 at.%) was detected. The presence of N peak on those spectrums could be due to AlN phase underneath. The quantification is shown in Table 4-37.



Show in Figure 4-78
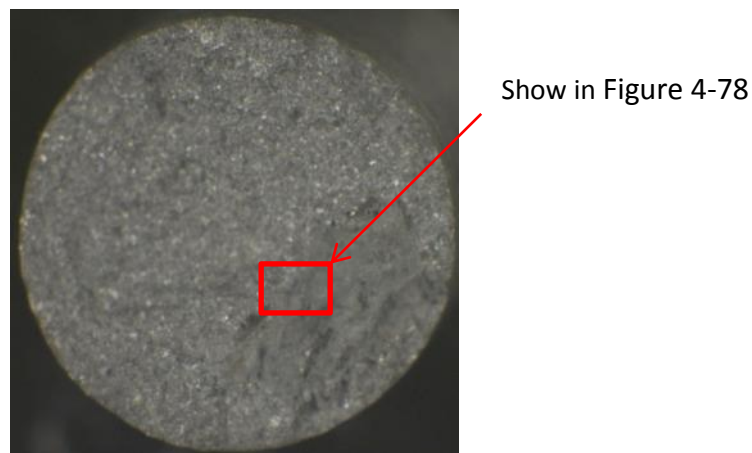
**Figure 4-77 Fracture surface of tensile test bar No. 14 of the casting with 2L99+0.4 wt.% Mo without heat-treatment.**
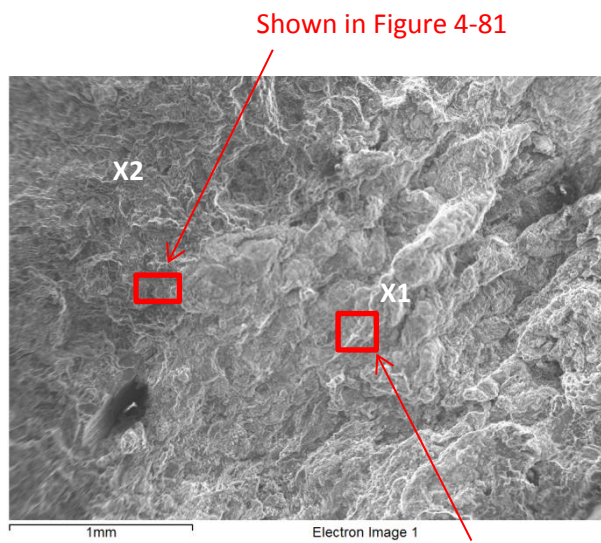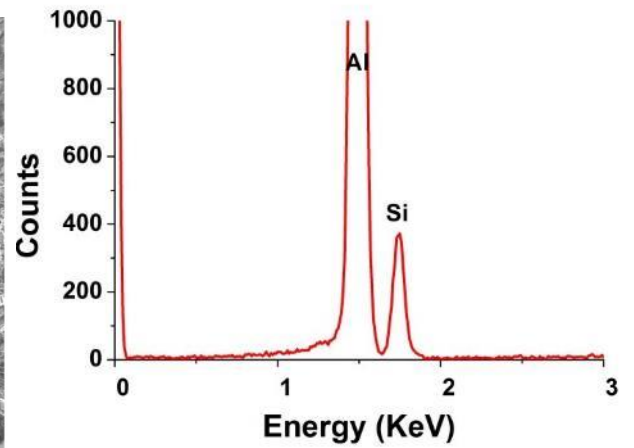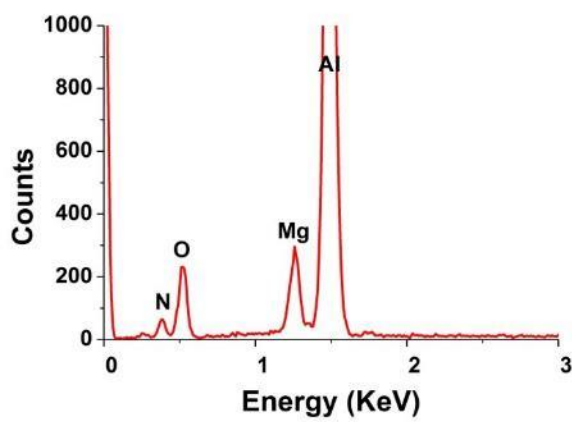
Figure 4-78. (a) Nitride found on the sample surface with unheat-treated 2L99+0.4 wt.% Mo; (b) EDX spectrum for X1 and (c) EDX spectrum for X2.
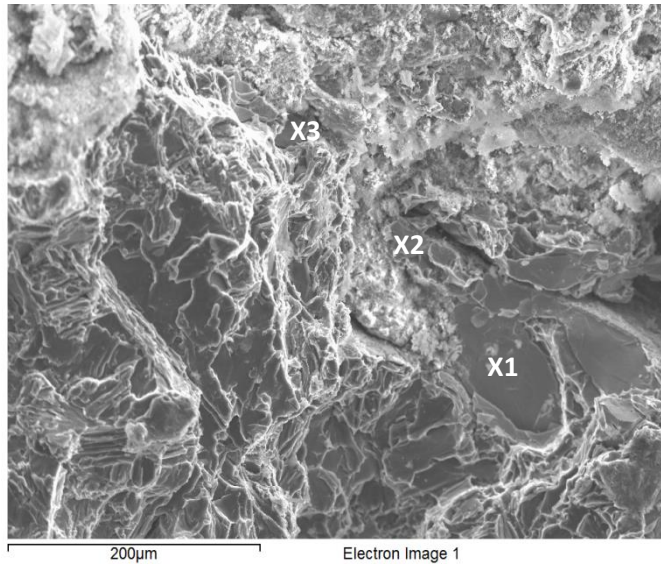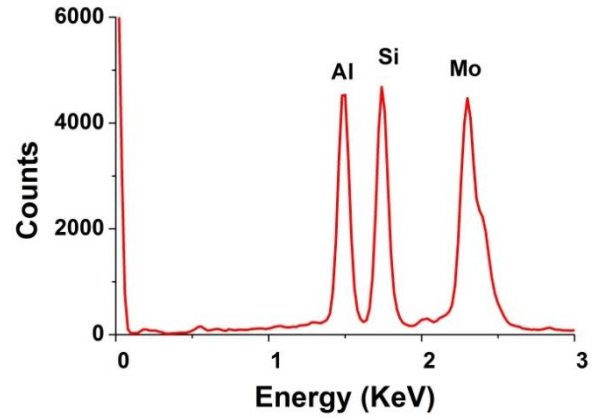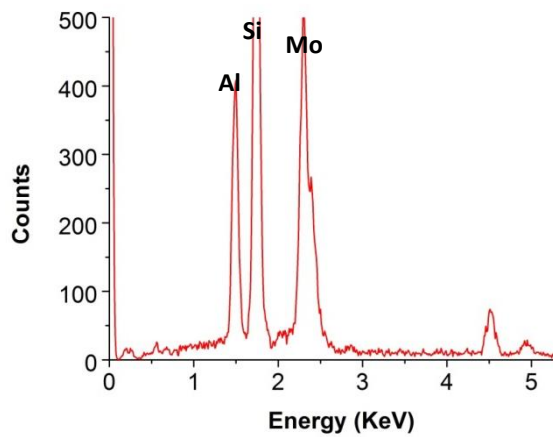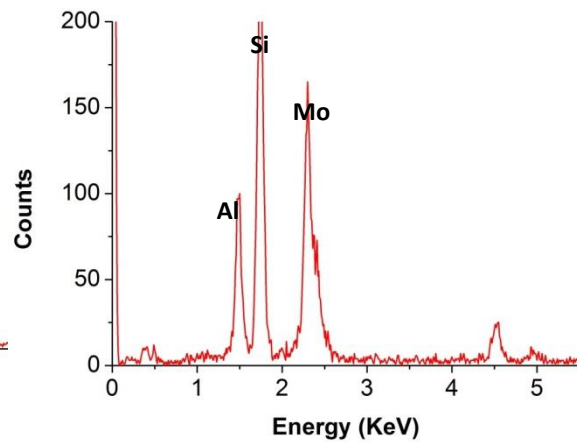
| Element | Mo containg intemetallic compound (X1) |
|---------|------------------------|
| Al      | 18.08                  |
| Si      | 48.94                  |
| Mo      | 32.98                  |

(e)

**Figure 4-79 (a) The intermetallic phase nucleated on the sides of double oxide film defect, (b)-(d) EDX spectrum of X1-X3 and (e) Quantified EDX spectrum of X1.**
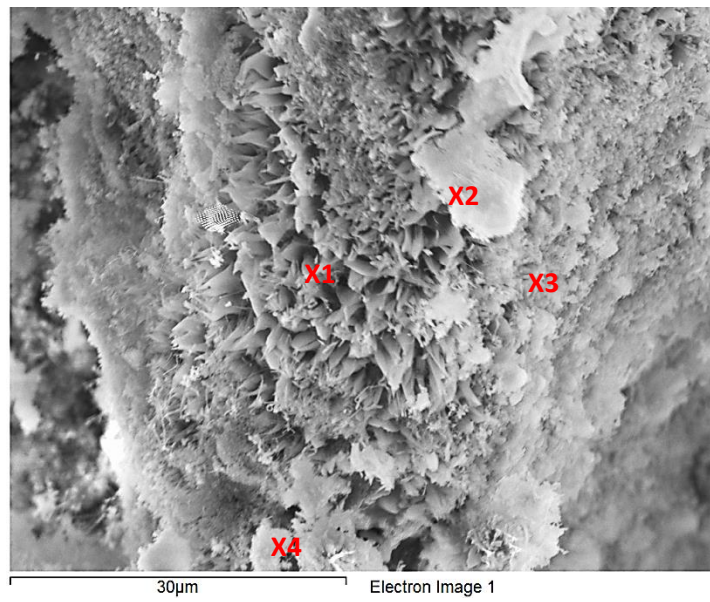
(a)
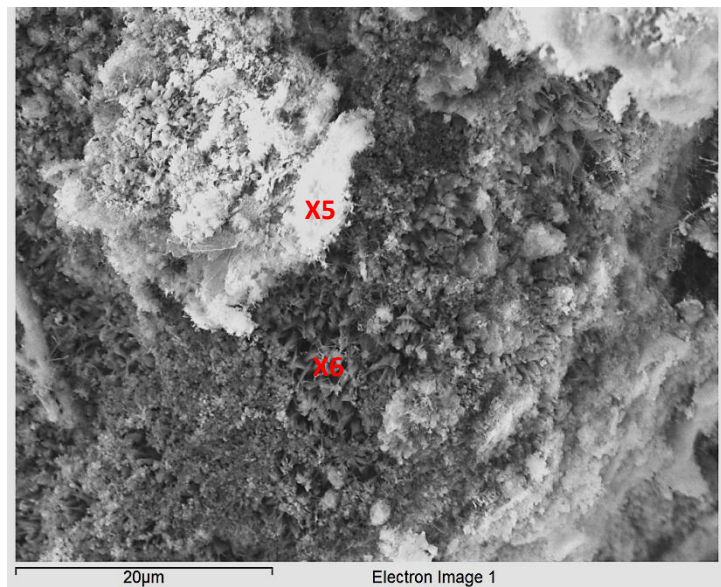


(b)
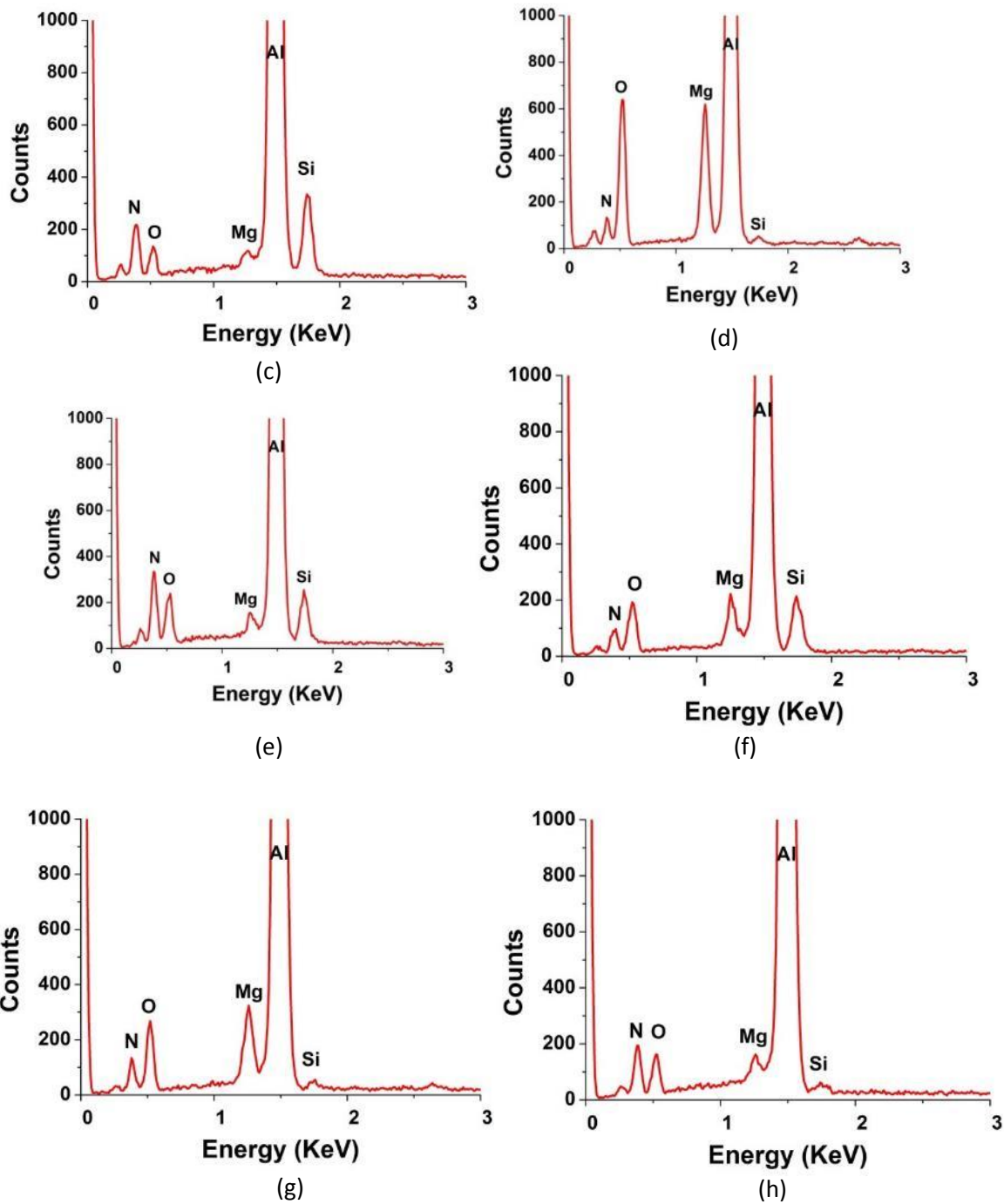
**Figure 4-80 (a)-(b) Surface morphology of the nitride found on the sample surface of unheat-treated 2L99+0.4 wt.% Mo; (c)-(h) EDX spectrum for X1 to X6.**

**Table 4-37. Quantification of spectrum in Figure 4-80.**

|    | Spectrum 1 | Spectrum 2 | Spectrum 3 | Spectrum 4 | Spectrum 5 | Spectrum 6 |
|----|-----------|-----------|-----------|-----------|-----------|-----------|
| N  | 36 at.%   | 17.68 at.% | 39.72 at.% | 21.52 at.% | 28.93 at.% | 22.61 at.% |
| O  | 9.19 at.% | 37.50 at.% | 14.51 at.% | 16.78 at.% | 9.96 at.% | 19.66 at.% |
| Mg | 0.44 at.% | 5.80 at.% | 0.63 at.% | 1.93 at.% | 0.57 at.% | 2.76 at.% |
| Al | 49.51 at.% | 38.19 at.% | 42.49 at.% | 55.41 at.% | 60.10 at.% | 54.43 at.% |
| Si | 4.86 at.% | 0.43 at.% | 2.66 at.% | 4.37 at.% | 0.44 at.% | 0.54 at.% |

Figure 4-81 shows a bifilm defect on the fracture surface of No. 18 of the heat-treated 2L99+ 0.4 wt.% Mo testbar. EDX analysis of Figure 4-82 (X1) suggested that a N peak was detectable in the area. Figure 4-83, which is the edge of this defect (higher magnification image of Figure 4-82 X2), suggested the presence of an Al-Si-Mo intermetallic phase. Figure 4-84, which is a high magnification image of Figure 4-83 X3, showed the morphology of the surface layer, which consisted of a whisker structure.



Defect which contains nitride
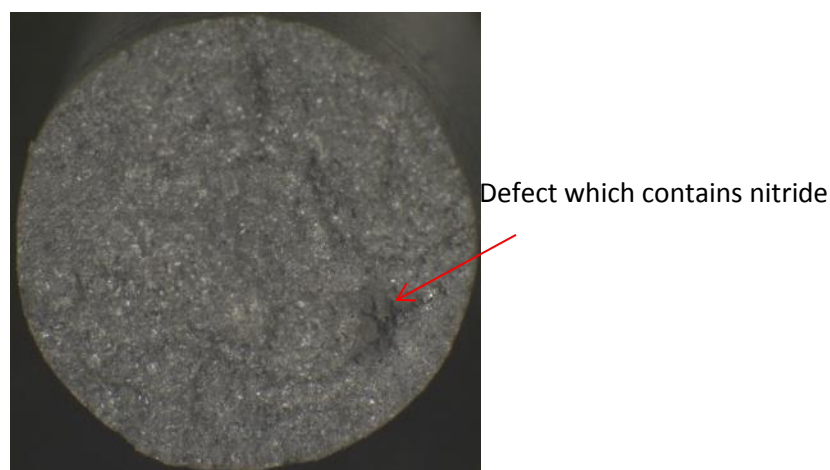
**Figure 4-81 Fracture surface of No. 18 of the heat-treated 2L99+0.4 wt.% Mo casting shows the presence of nitride on the double oxide film defect.**

(a)



Al
Si
N O
Mg

(b)

X2 Shown in Figure 4-83

X3 Shown in Figure 4-85
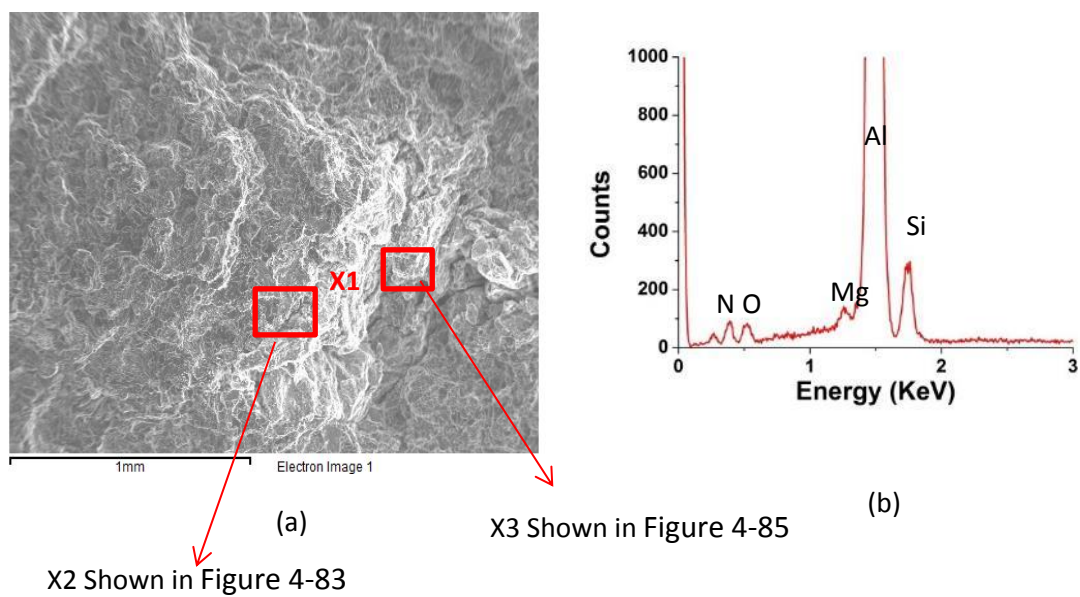
**Figure 4-82. SEM image of the defect showing in Figure 4-81.**



X3 Area showed in Figure 4-84

X2

X1

X

(a)



N
O
Mg
Al
Si

(b)



Al
Si
Mo

(c)

| Element | at.% Mo containg intemetallic compound (X2) |
|---------|------------------------------------------------|
| Al | 15.77 |
| Si | 50.3 |
| Mo | 33.84 |

(d)
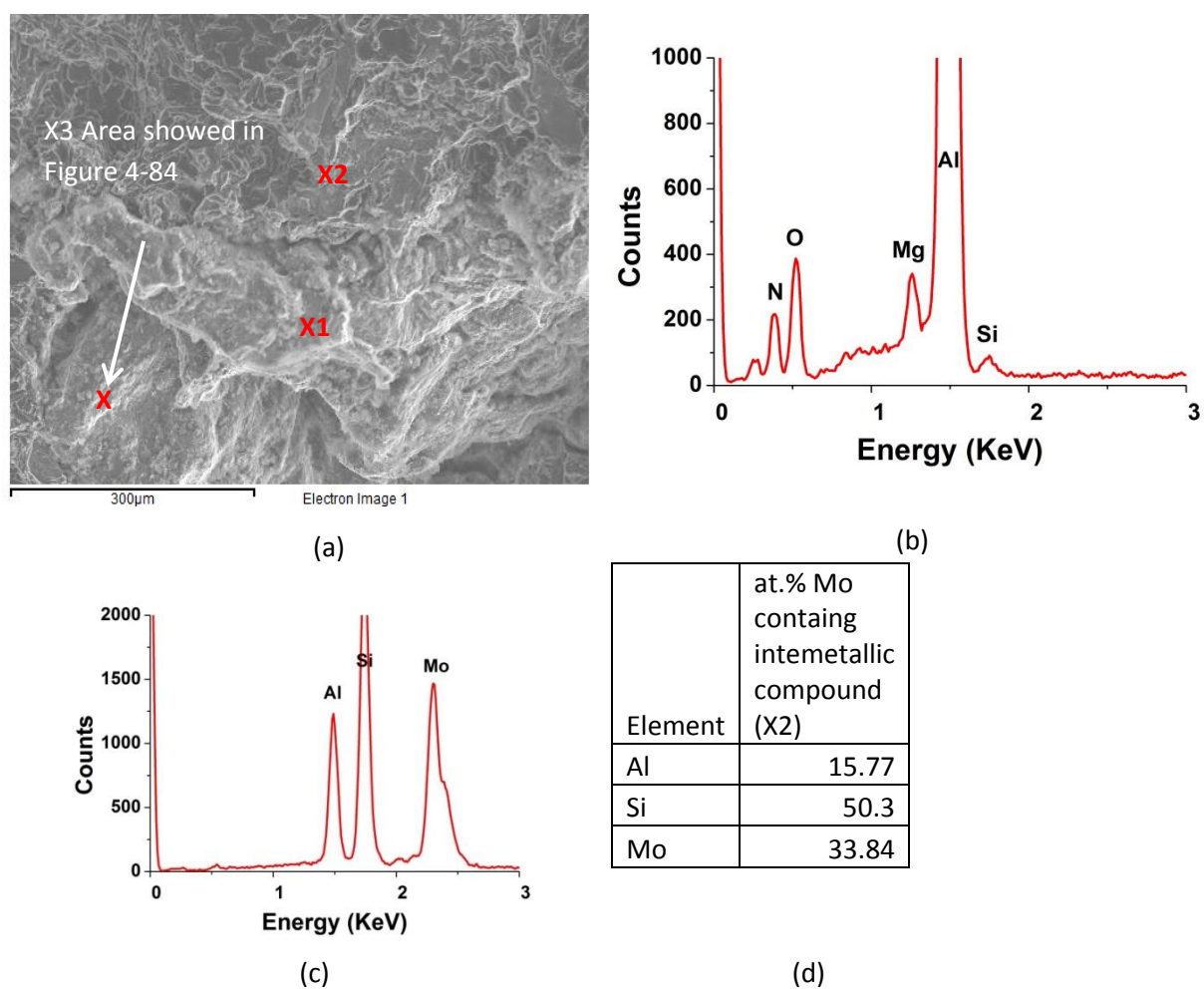
**Figure 4-83. Labelled area in Figure 4-82; (b) and (c) EDX spectrum of X1 and X2;(e) Quantified EDX result for X2**

192

(a)
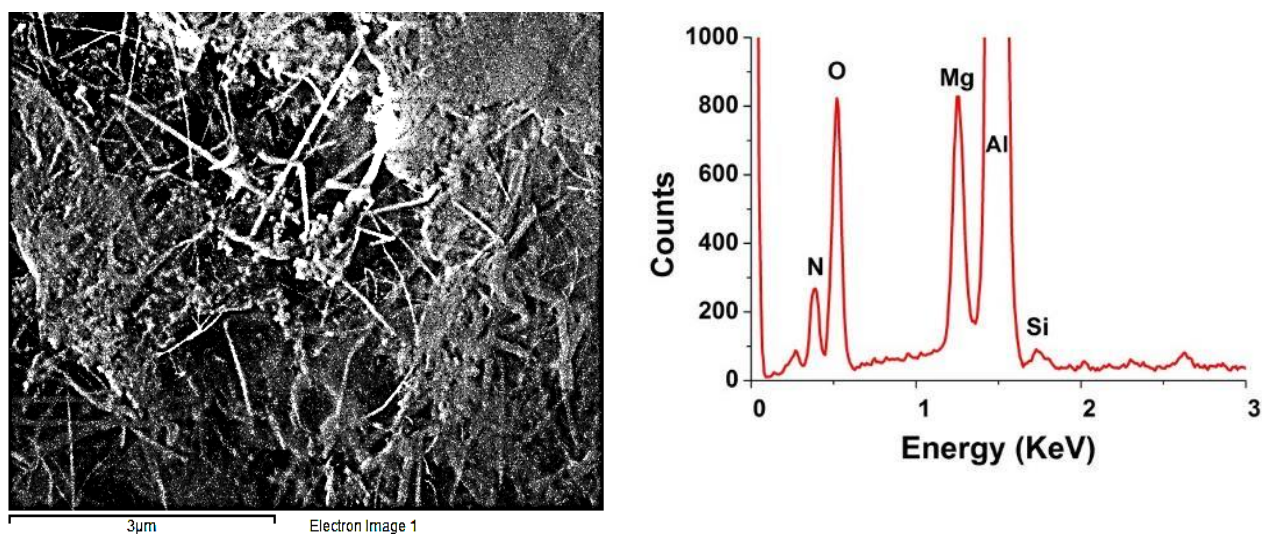
Figure 4-85 shows the area of Figure 4-82 X3. The high magnification image of the labelled areas in Figure 4-85 has been shown in Figure 4-86, Figure 4-87, Figure 4-88 and Figure 4-89 respectively.

Figure 4-86 showed tooth-shaped aluminum nitride (X1), growing on an Al-Si phase (X2, mostly Si). A similar structure was also found by TEM.

Figure 4-87 (a) and (b) shows layer of a whisker-structure phase on the fracture surface. EDX analysis of the whisker structure (Figure 4-87 (d)) suggested a high O and Mg peak, but a small N peak. Figure 4-87 (c), however, showed a nearby area where no whiskers appear. EDX analysis suggested that the area contained a nitride particle (X2) and aluminum particles (X3). It is possible that the surface layer here consisted of duplex layers: nitride

particles, mixing with aluminum particles, consisting of the bottom layer, permeable spinel whisker structurers loosely dispersed over the top.

Figure 4-88 showed an area of Al phase present on the fracture surface. EDX analysis suggested no oxygen/nitrogen was detected. This could be a place where liquid metal penetrate through one side of the oxide layer in the bi-film defect and connected to the other side before its solidification. Tensile force during the mechanical test breaks such bonding point, leaving an area which showed in Figure 4-88.

Figure 4-89 shows an area where only Al Mg and O was detected, suggesting a spinel layer.
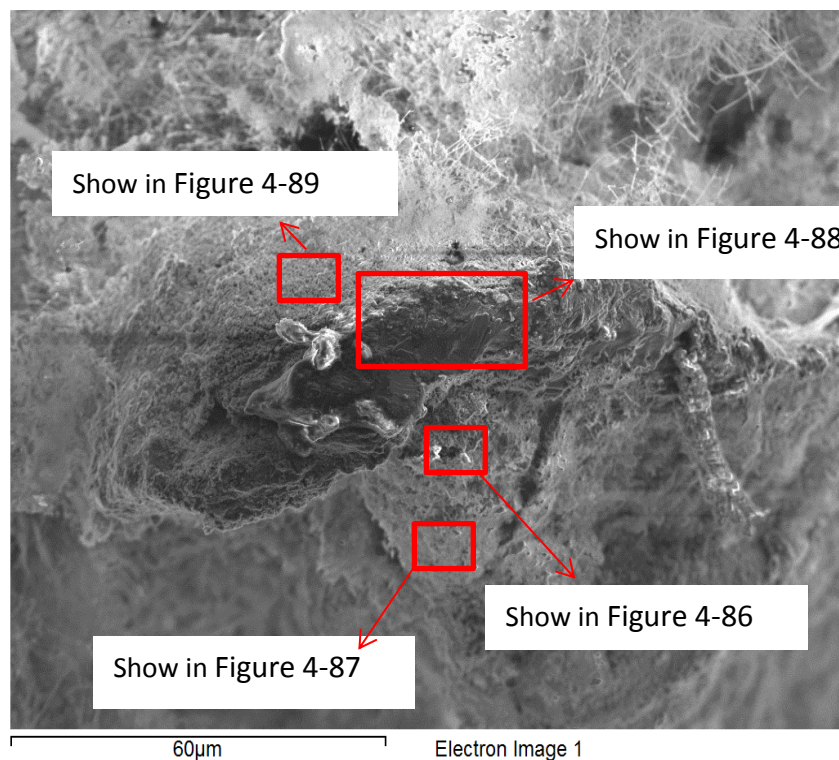


**Figure 4-85 High magnification image of the labelled area in Figure 4-82.**
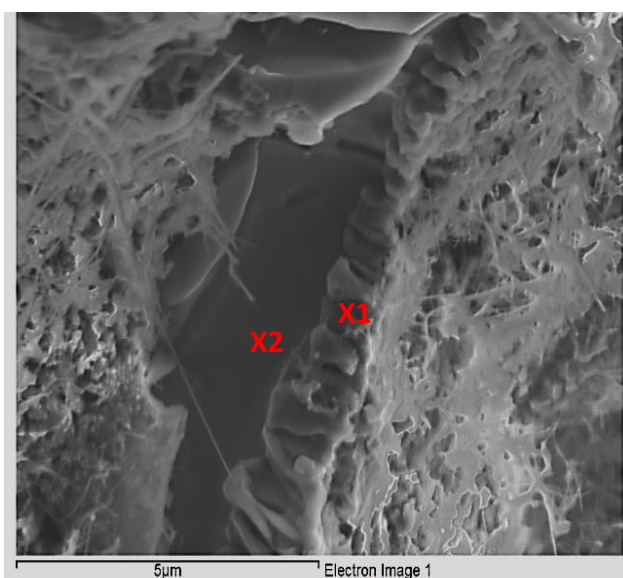
(a)
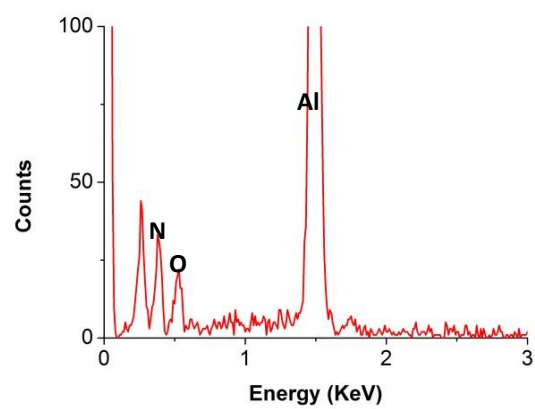


(b)
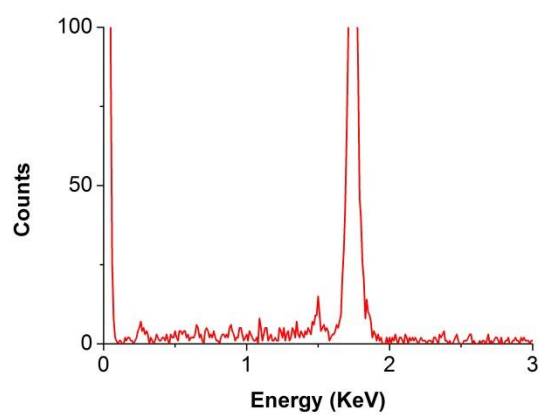


(c)

**Figure 4-86 (a) Labelled area show in Figure 4-85; (b) and (c) EDX spectrum for X1 and X2**
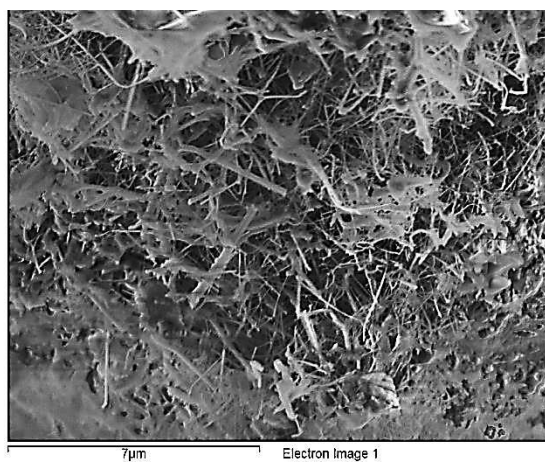


(a)
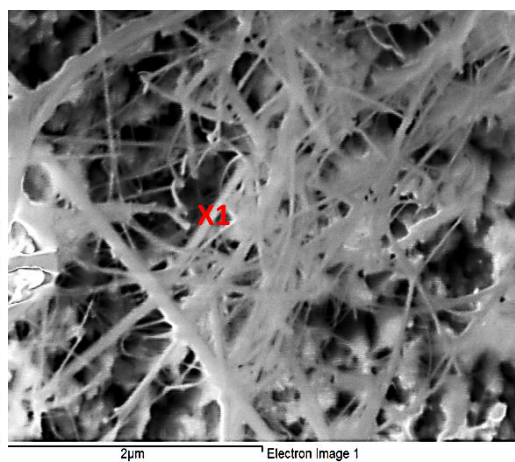


(b)
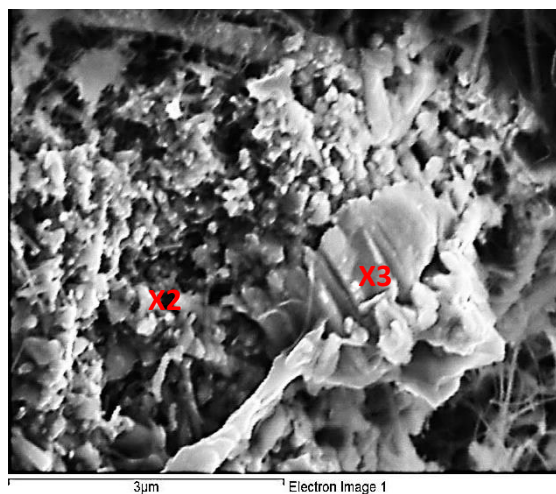
(c)
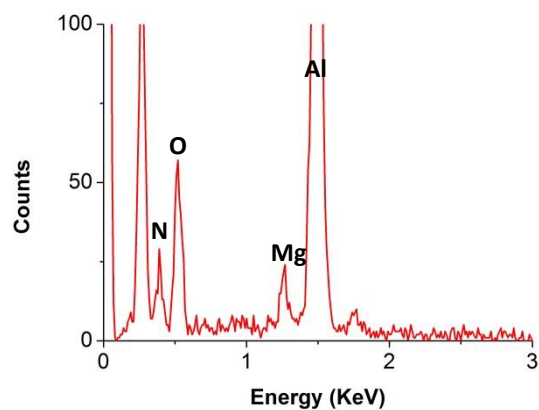
(d)
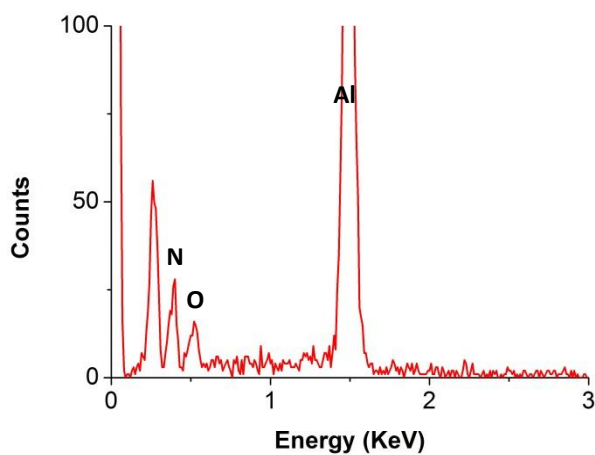


(e)
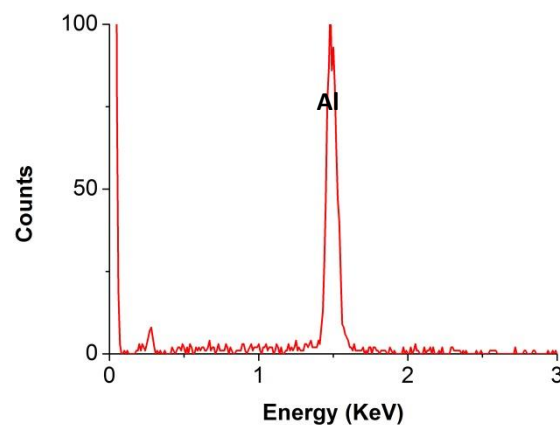
(d)

**Figure 4-87 (a) Labelled area showing in Figure 4-85; (b) and (c) EDX spectrum for X1 and**
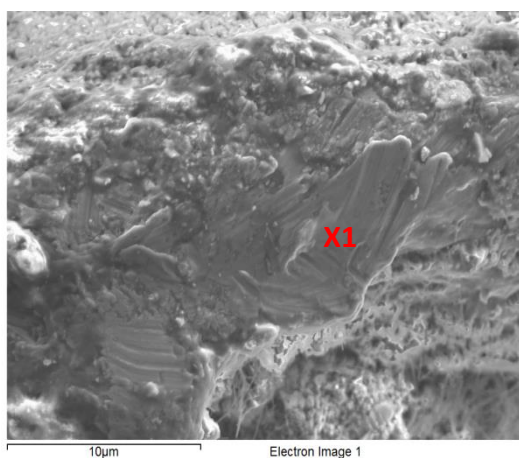


(a)
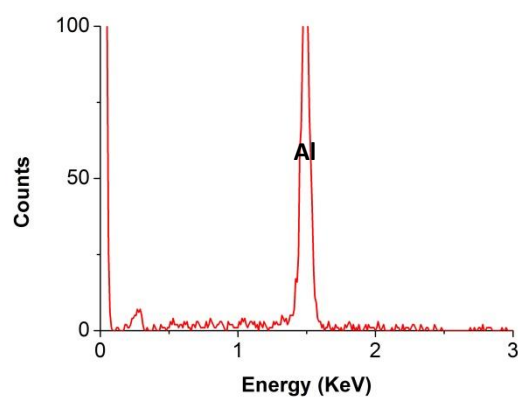
(b)

**Figure 4-88 (a) Labelled area showing in Figure 4-85; (b) EDX spectrum for X2.**

(a)                                                    (b)
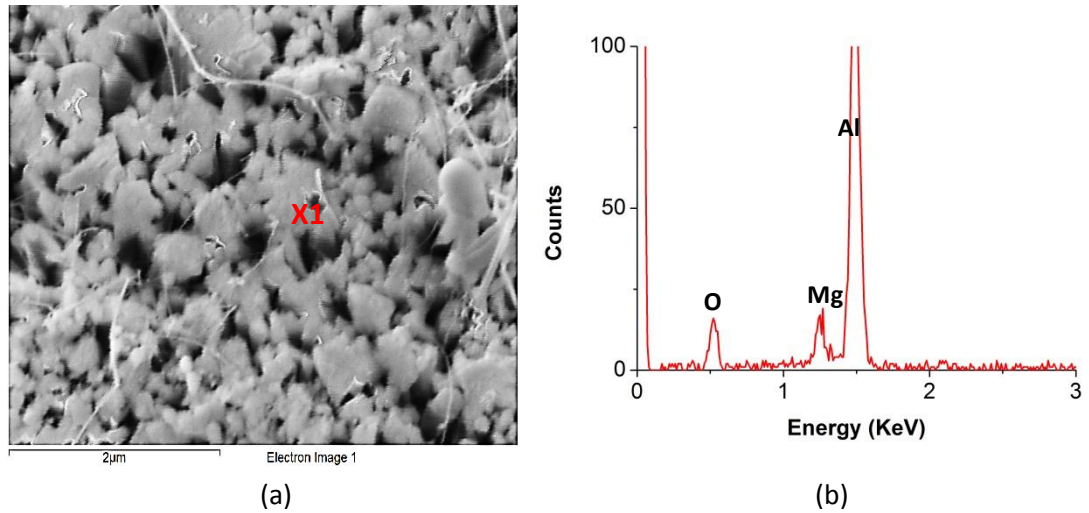
**Figure 4-89 (a) Labelled area show in Figure 4-85; (b) EDX spectrum for X2.**

Figure 4-90 to Figure 4-93 shows another nitride-containing layer on the fracture surface of tensile test bar No. 5 from the casting with heat-treatment and roll over. A duplex surface layer, with whisker structures (Figure 4-91, possibly mixed with some spinel particles), on the top and nitride particles (Figure 4-93) at bottom was observed, which is identical to the layer shown in Figure 4-87.



(a)                                                    (b)
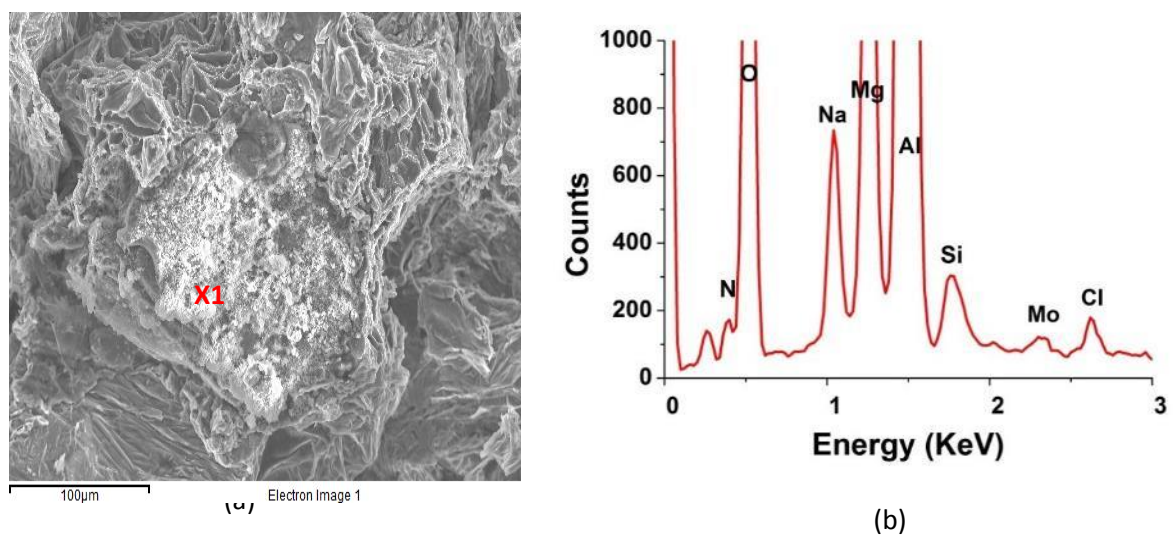
**Figure 4-90 . Nitride on the fracture surface of No. 5 of 2L99 +0.4 wt.% Mo casting with both heat treatment and roll over.**

whiskers

(b)

(a)
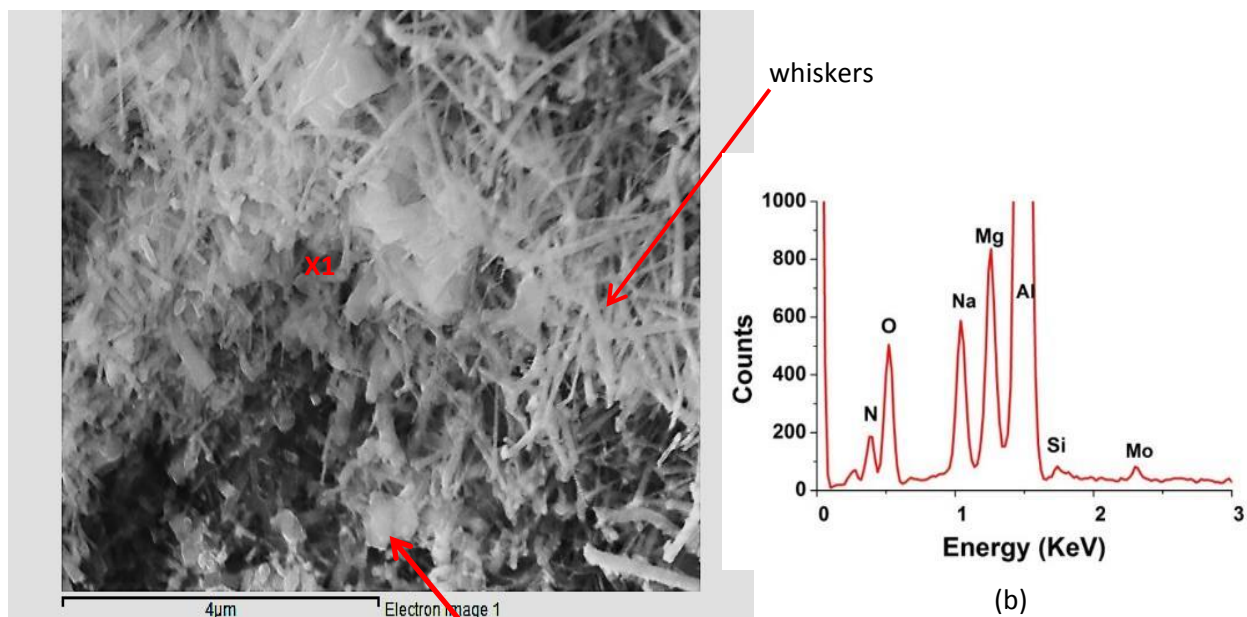
Figure 4-91. (a) Higher magnification image of Figure 4-90 showing the whisker like nitride layer; (b) Higher magnification of (a) and (c) EDX spectrum of X1.



(a)

(b)
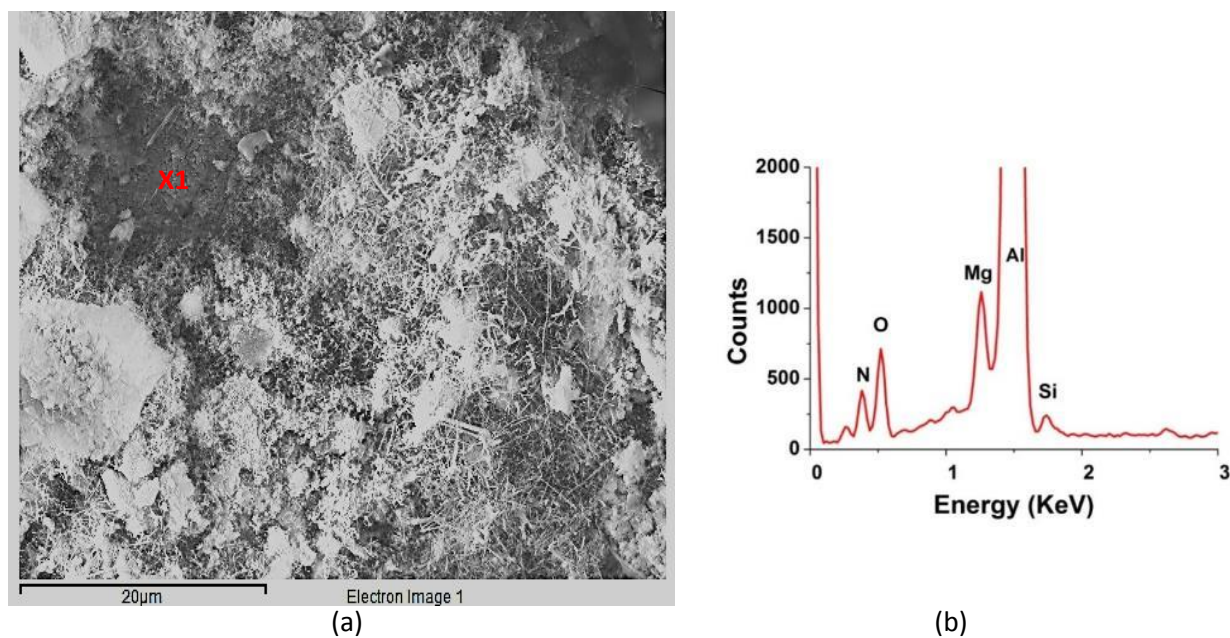
Figure 4-92. (a) Surface morphology of showing the nitride layer; (b) EDX spectrum of X1.
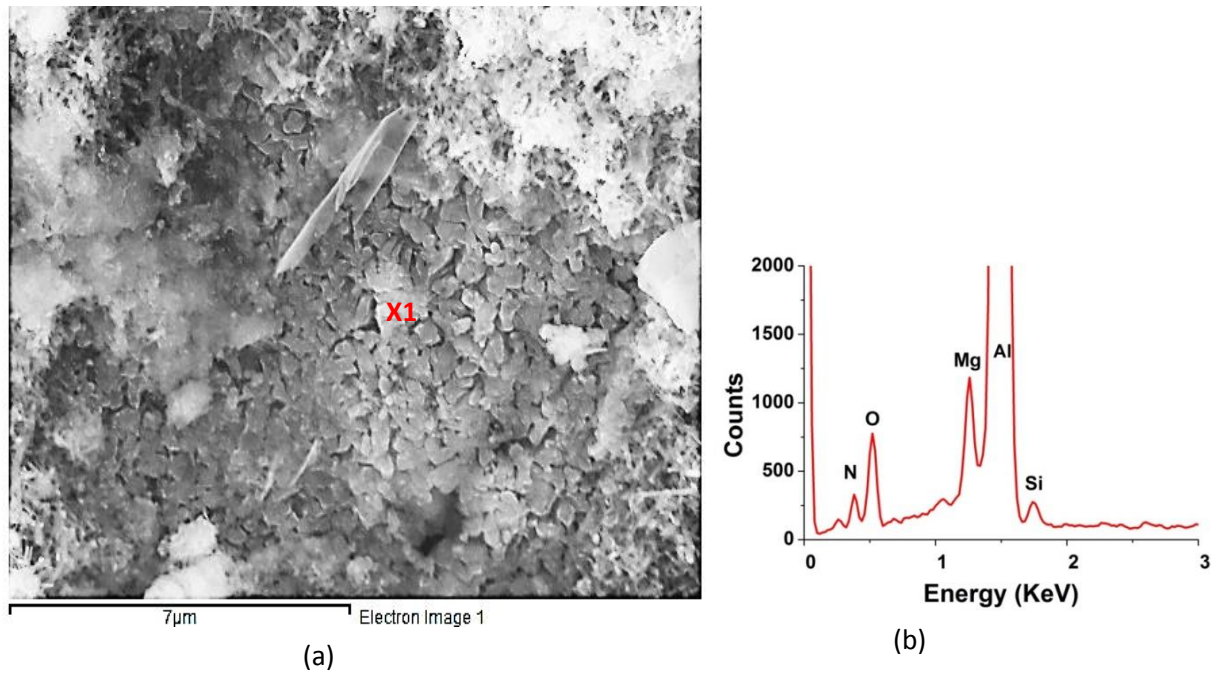
**Figure 4-93. Higher magnification of granular like nitride as shown in Figure 4-92.**

### 4.3.3.3 *Cross-section investigation of the nitride layer found in 2L99+Mo casting*

#### 4.3.3.3.1 Morphology of the cross-section of the nitride layer after FIB (Focused Ion Beam) milling.

Focused Ion Beam (FIB) milling was used to obtain a cross-section on the fracture surface of a tensile test bar No.14 (of the 2L99 castings without heat-treatment). SEM equipped with Energy Dispersive X-ray (EDX) was used for the cross-section area investigation. Figure 4-94 shows a cross section of the fracture surface with a nitride-containing surface layer at the top of the sample surface. Nitride containing particles (X1, X2) were seen directly growing on the aluminum matrix (X3).

(a)



(b)



(c)



(f)



(g)

200

(h)

**Figure 4-94. (a)-(c) Cross section of nitride containing fracture surface with 2L99+0.4 wt.% Mo; (f)-(i) EDX results for X1-X4.**
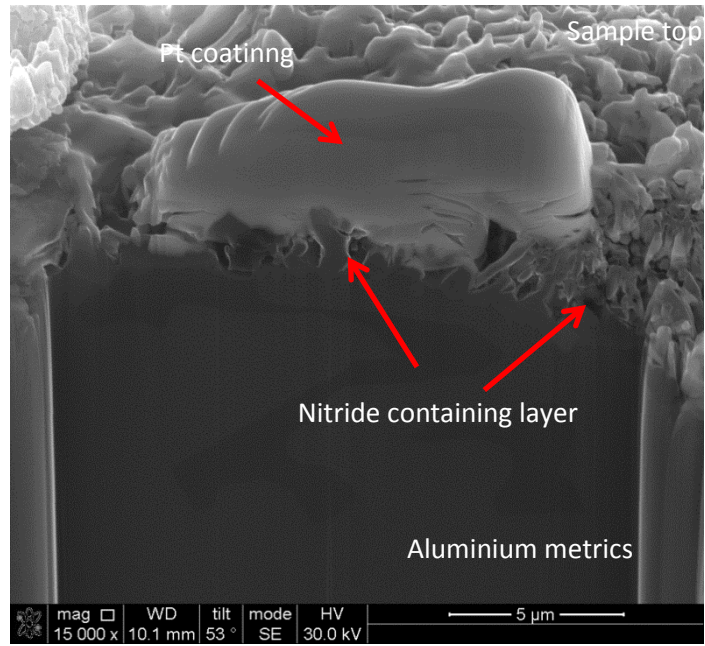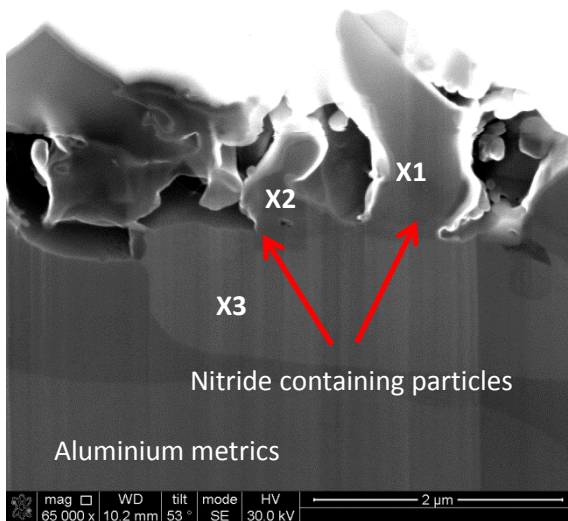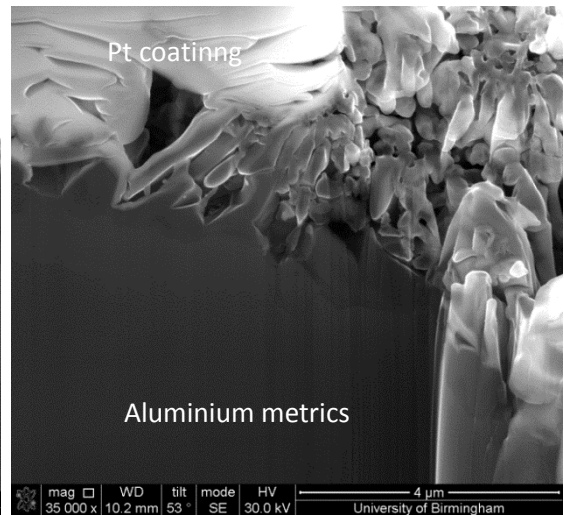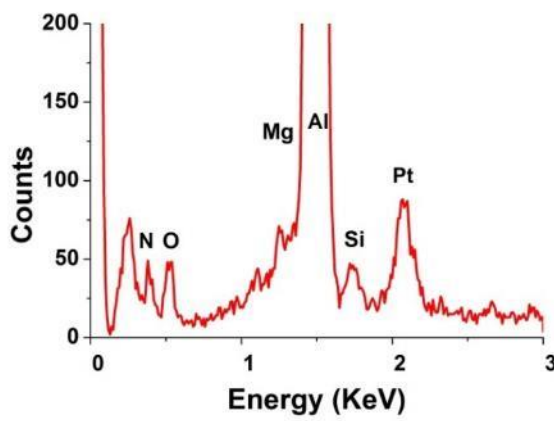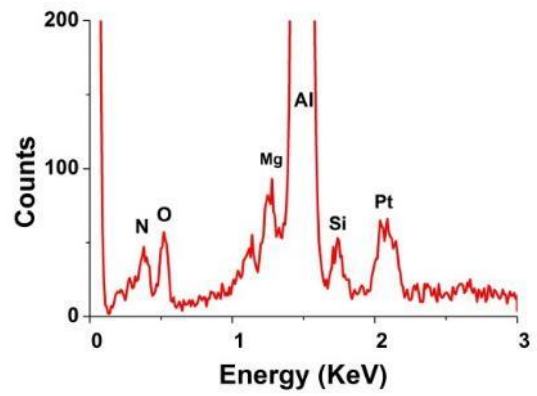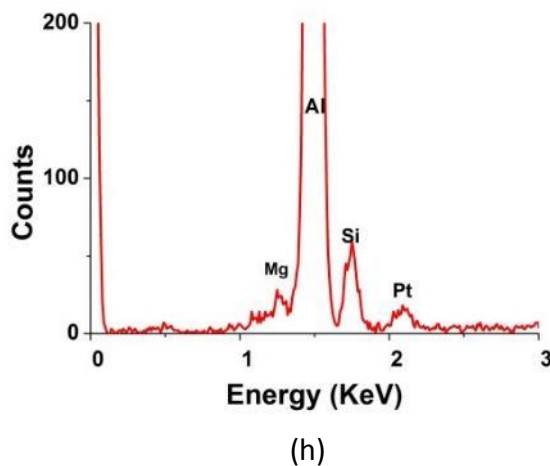
Figure 4-95 (a) shows the cross-section of another area of the nitride-containing fracture surface. Figure 4-95 (b) showed the higher magnification image of the permeable oxide layer, which have a thickness of 4.0 μm, (as labelled). Figure 4-95 (c) showed that the oxide layer could be as thick as 33 μm (labelled) and EDX analysis suggested that N peak was detected in the area. The permeable and thick oxide layer had different morphologies compared with the smooth oxide layer on 2L99 alloy without addition (as shown in Figure 4-57, having a thickness of around 500nm).



(a)
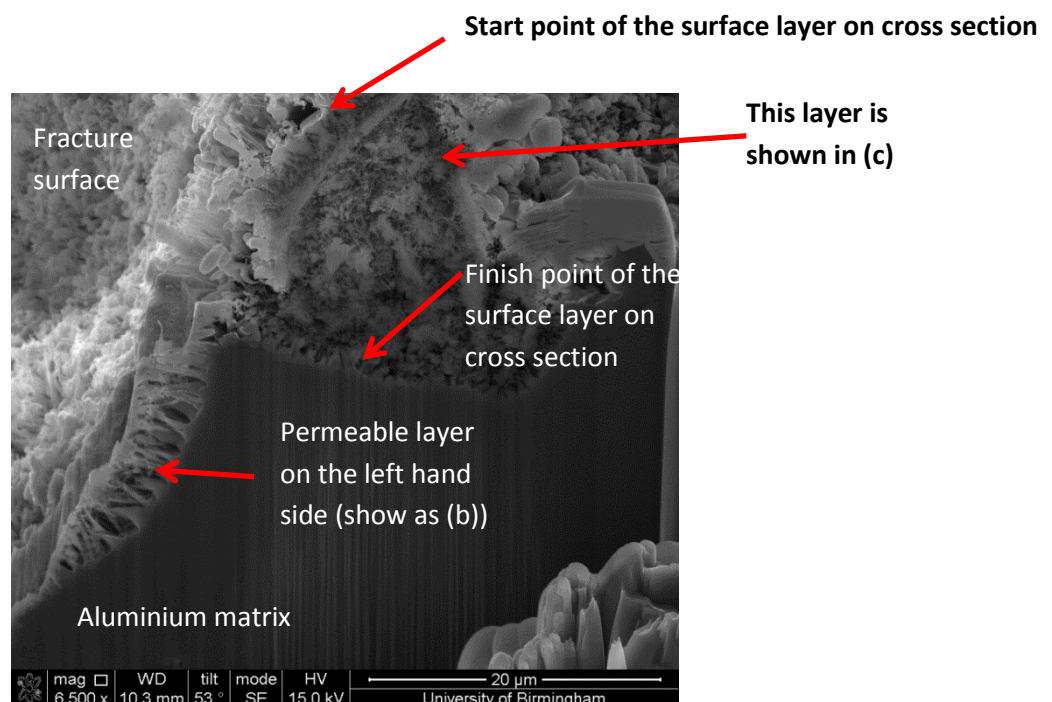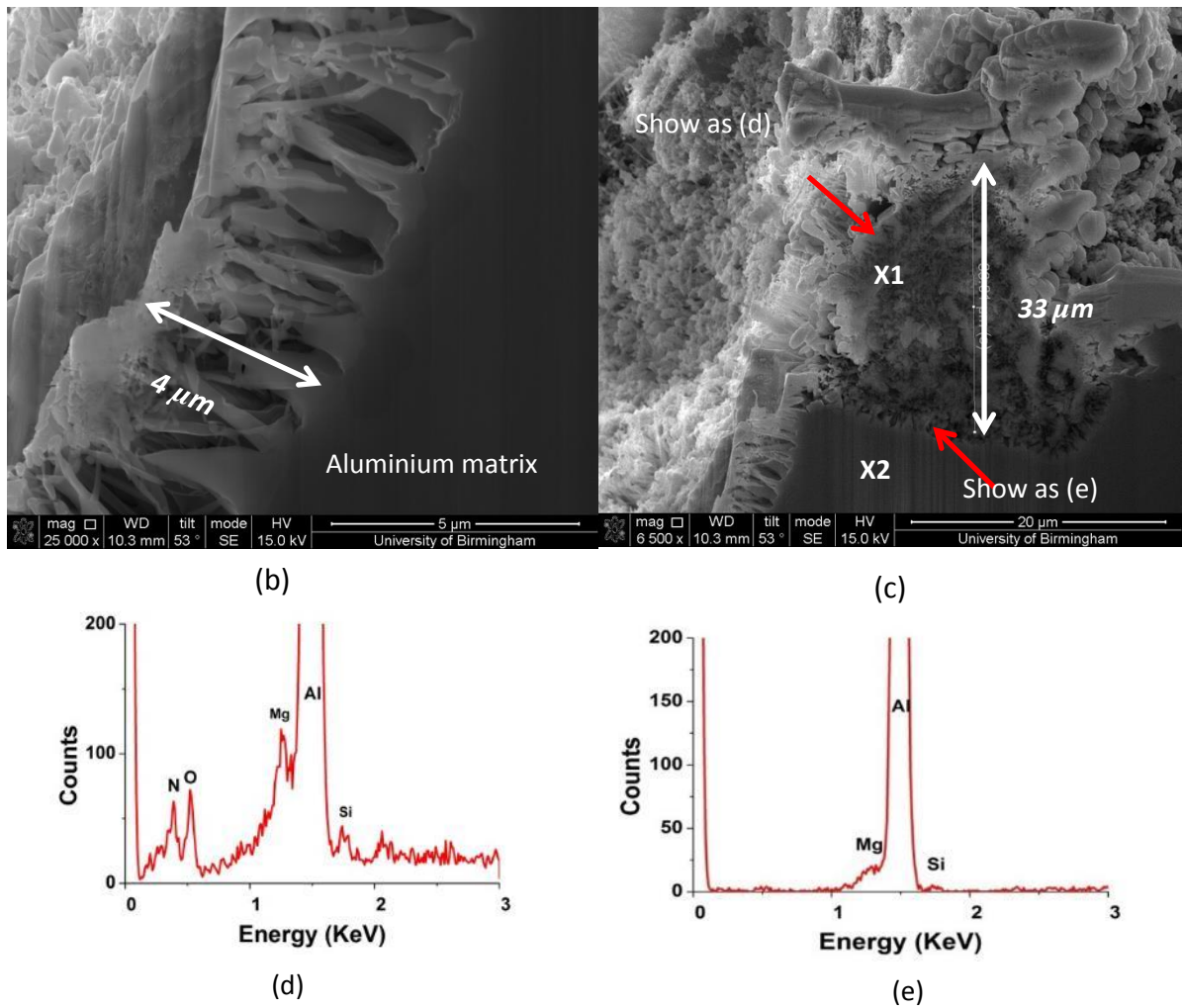
Figure 4-95. (a)-(i) EDX spectrum for X1-X9 in Fig. 4-119 respectively.

### 4.3.3.3.2    TEM analysis of the nitride layer

In order to further understand the phases involved in this cross-section, a TEM sample was prepared based on the arrowed area in the cross-section shown in Figure 4-96 (a). Figure 4-96 (b) is the actual TEM sample prepared. Three areas were analysised by TEM EDX mapping which are labelled as Areas 1, 2 and 3. Area 1 points to a rod like phase, and area 2 shows a band with bright contrast. Area 3 is the intersection between the surface layer and the aluminum matrix.

Area for TEM sampling

(a)



Area 1

Area 3

Area 2

(b)
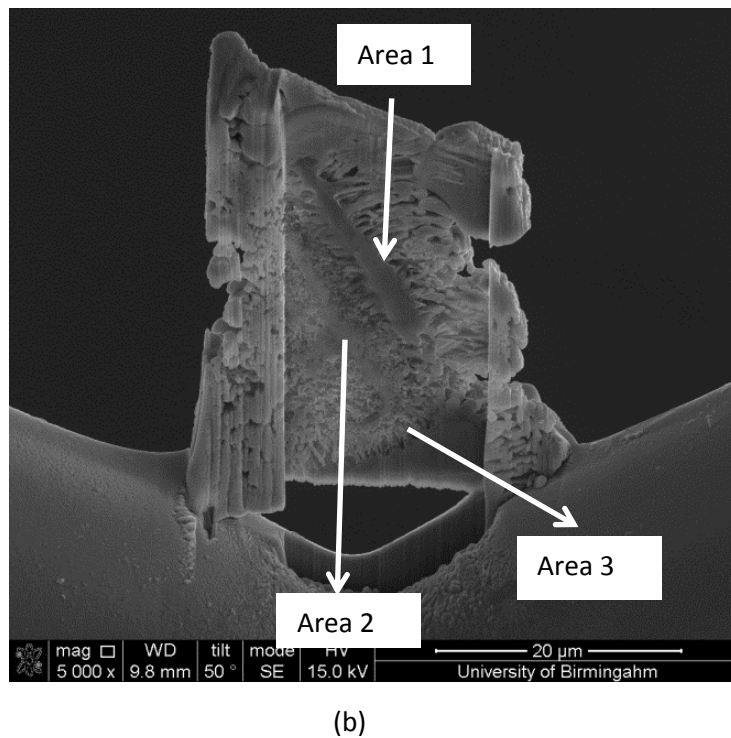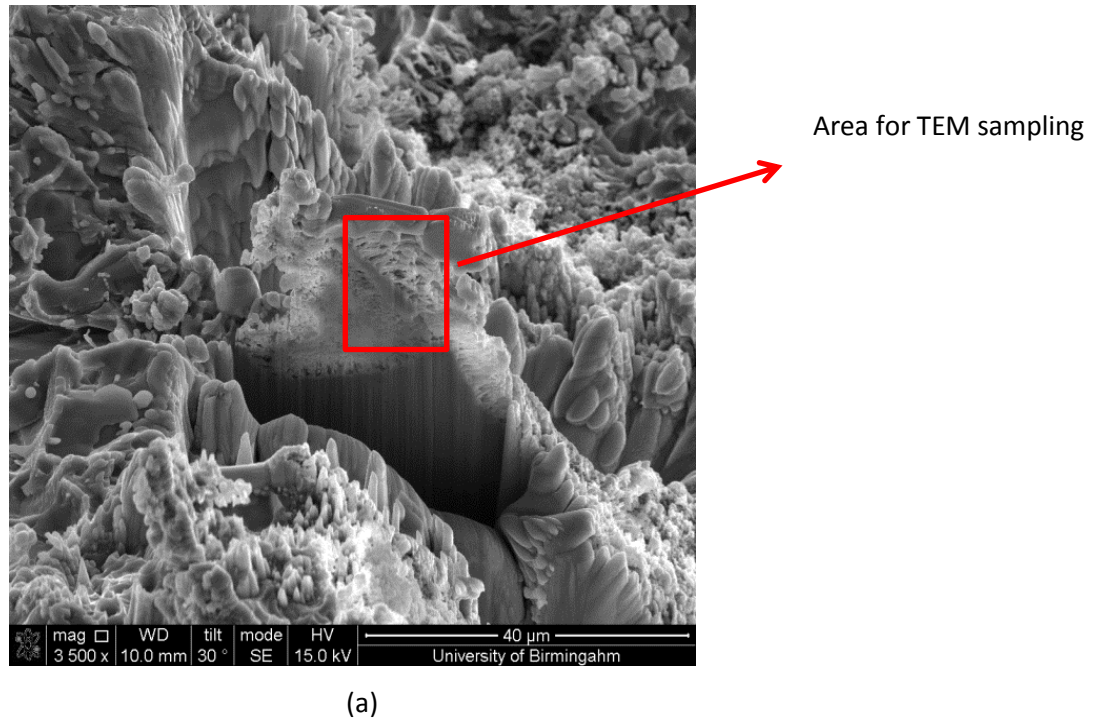
**Figure 4-96 (a) the cross-section area used for the preparation of a TEM sample; and (b) the TEM sample prepared.**

EDX mapping, shown in Figure 4-97 confirmed that the rod-shaped phase (Area 1) was an Al-Si phase, (with a Si phase in the middle and an Al phase surrounding it) and the tooth

structures grew near it were a nitride phase. Figure 4-99 is a high magnification image of the intersection between the tooth-shaped structure and the rod-shaped phase, which showed that the tooth shapes were growing on the aluminum phase. The EDX mapping suggested that the nitride might be AlN, but oxygen was also observed to present.

EDX mapping of area 2 in Figure 4-96 is shown in Figure 4-98, and Figure 4-100 shows a high magnification image. As can be seen, the area consisted of fine sized spinel particles (few hundred nm).

Figure 4-101 shows area 3 of Figure 4-96, in which aluminum nitride particles grow on the aluminum matrix. The Mg concentration was quite low in this area, which suggested that spinel was not present in this area.

TEM analysis confirmed the structure of the surface layer observed by SEM, which showed a duplex surface layer: a nitride layer (which consists of AlN particles) was seen directly growing on the aluminium matrix. Spinel, with the fine sized particles (few hundred nm in size) or whisker structures were seen growing over the top. The thickness of the spinel layer was quite variable, ranging from 0 to 30 μm. Rod shaped Al-Si phase was sometimes seen in the spinel layer, with some AlN growing on the sides.

**Table 4-38 The composition of the nitride by EDX on TEM.**

| Spectrum | Atomic % |
|----------|----------|
| N        | 33.86    |
| O        | 14.12    |
| Al       | 52.02    |
| Total    | 100      |
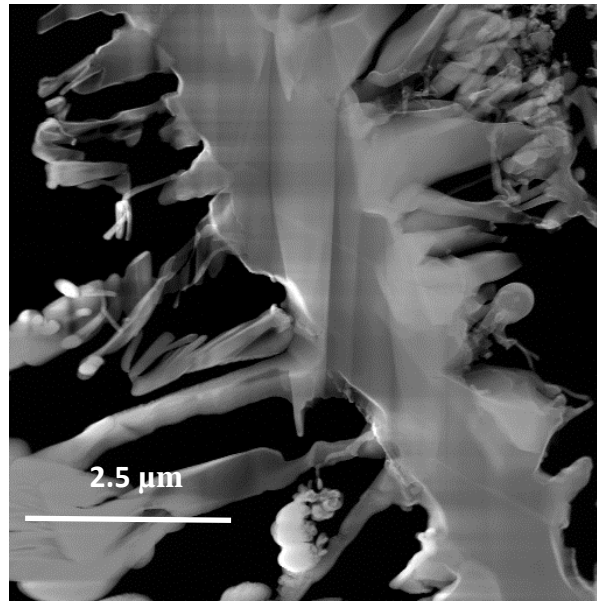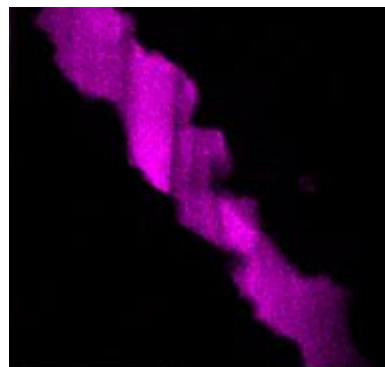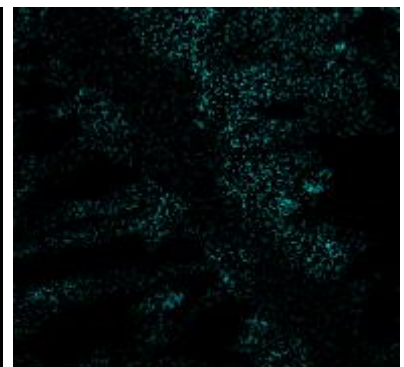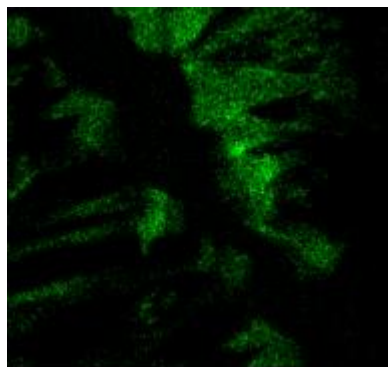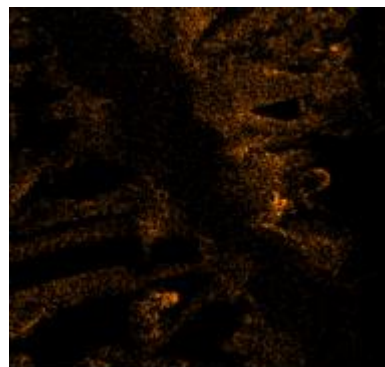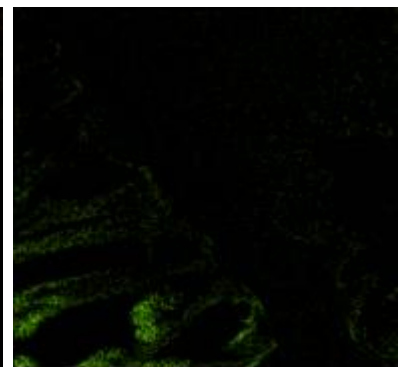
Figure 4-97 EDX mapping of the area 1 showing AlN phase growing on the stick-like Si phase.
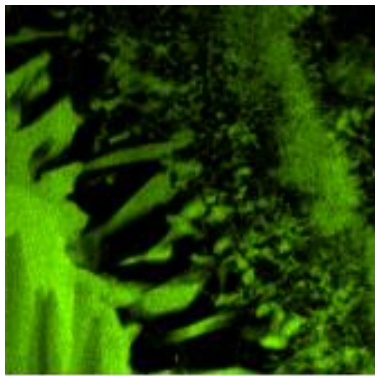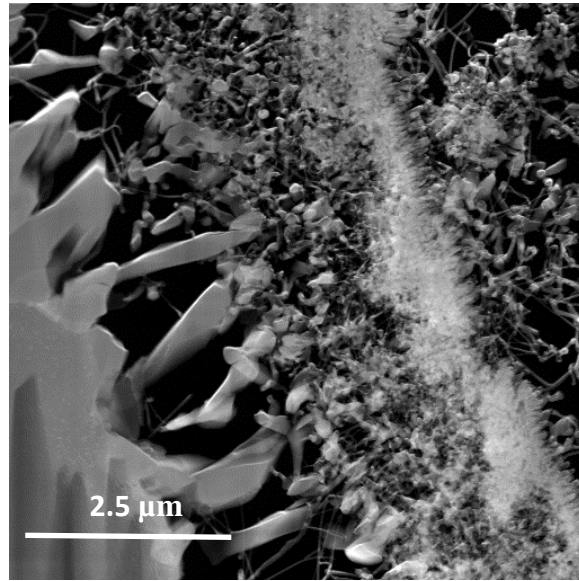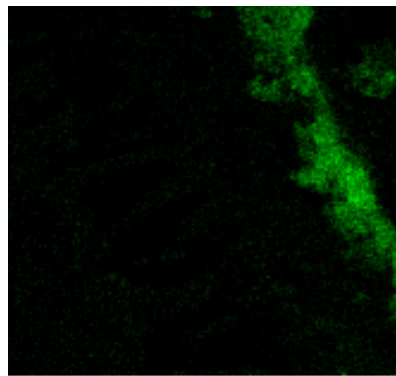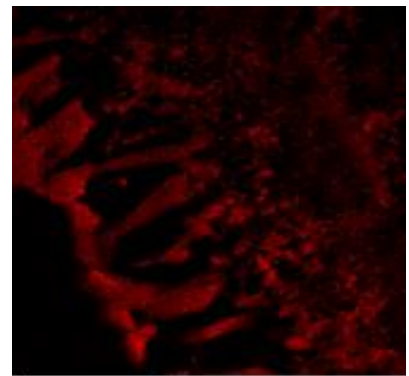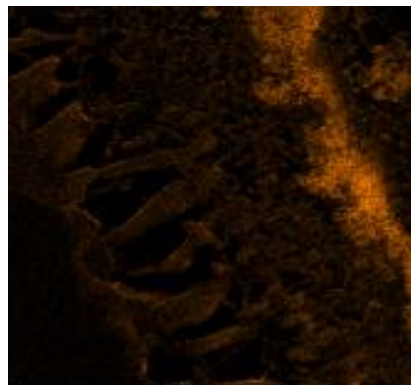
**Figure 4-98 EDX mapping showing the intersection area between the AlN layer and the bright contrast spinel layer.**
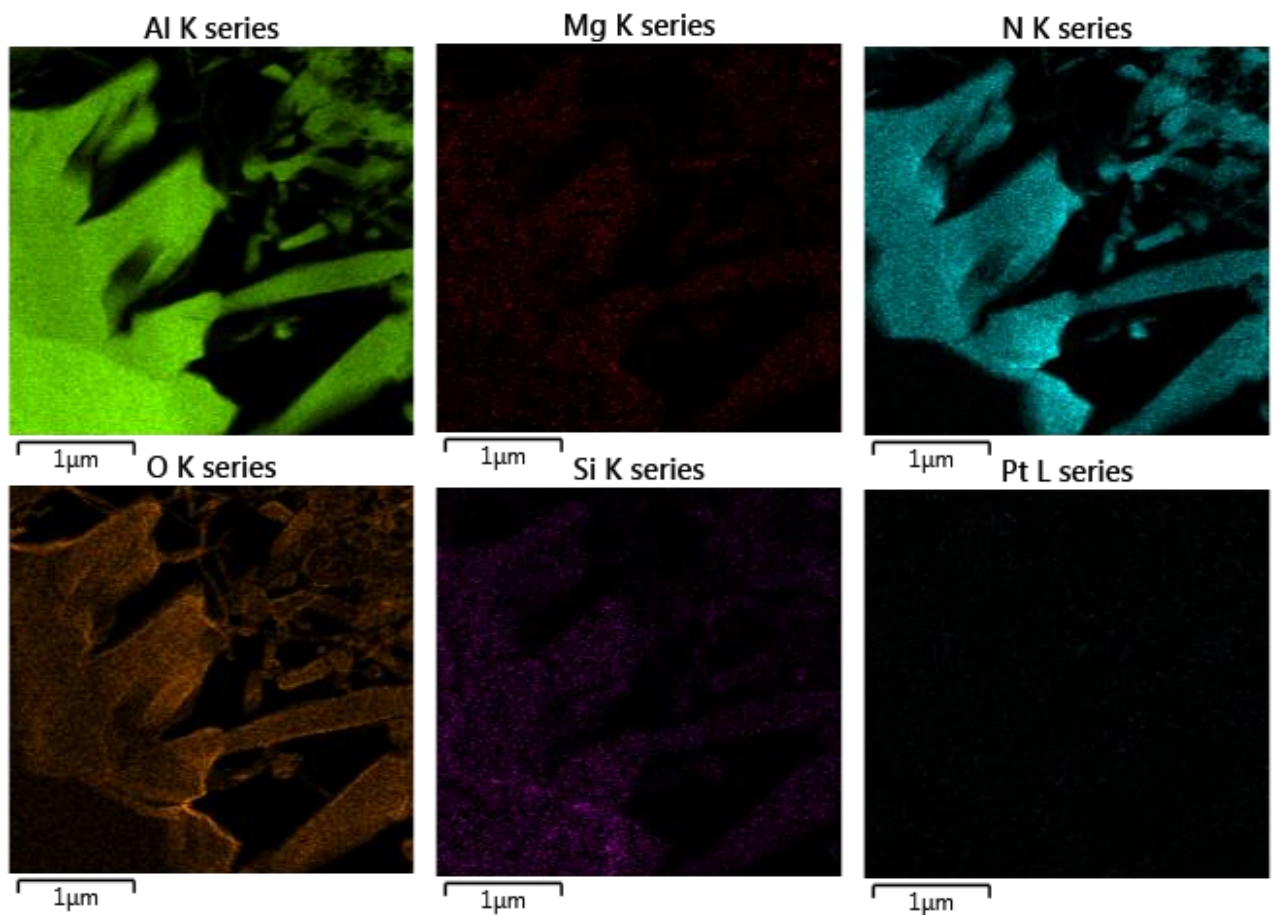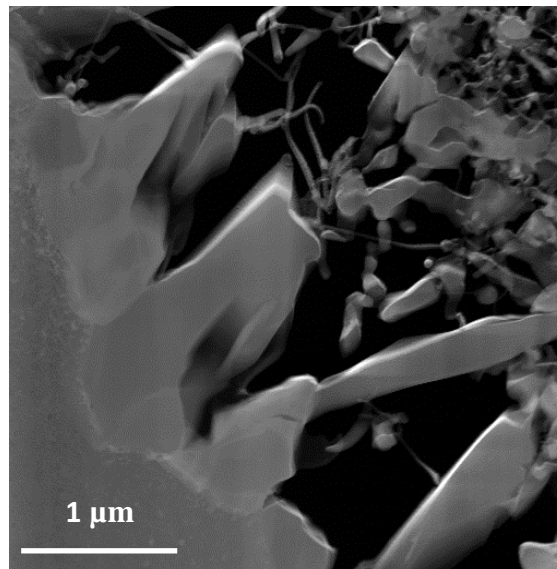
Figure 4-99. High magnification image of the area 1 showing the intersection between the tooth-like AlN phase and the aluminium matrix.
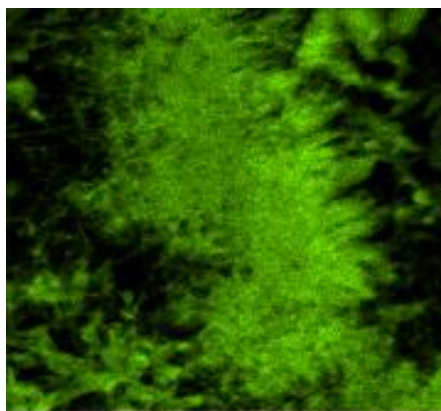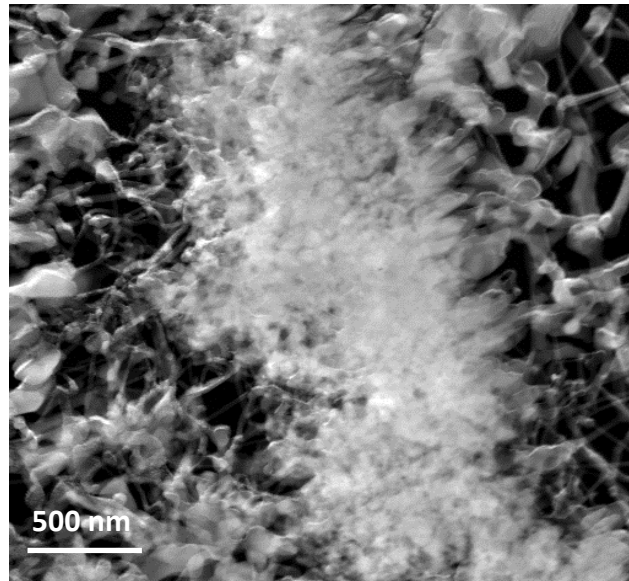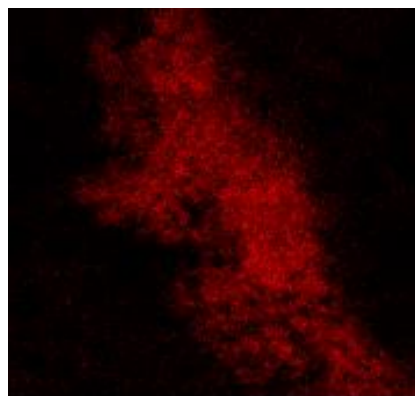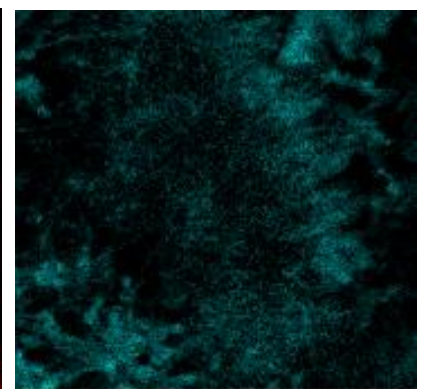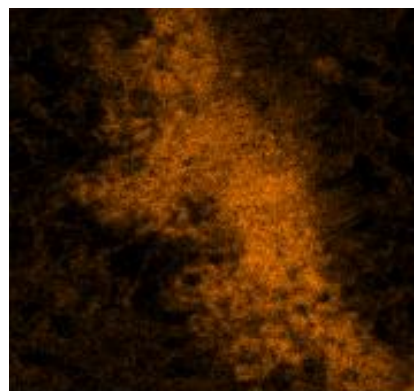
Figure 4-100 EDX mapping of the spinel layer in the area 2.
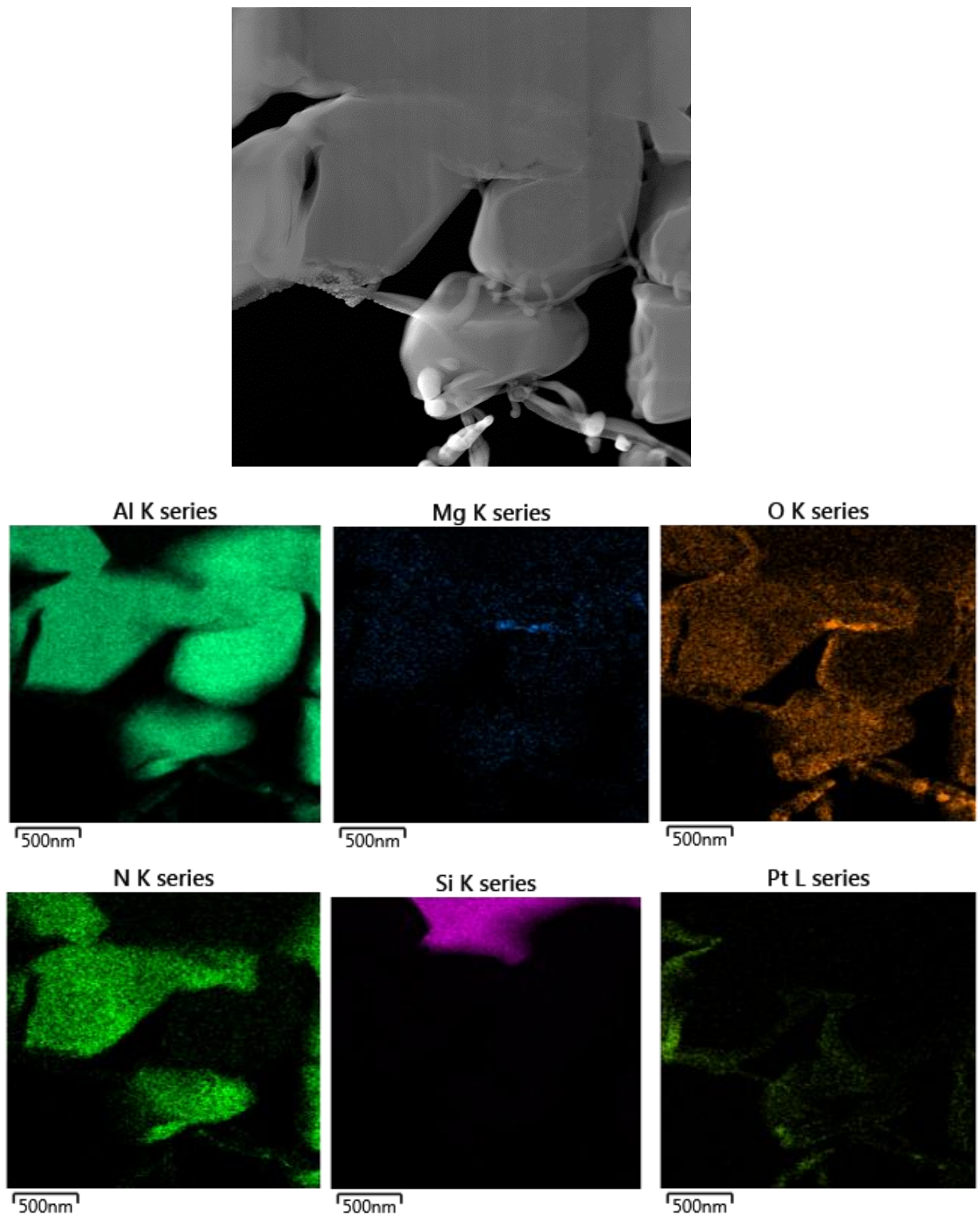
Figure 4-101. EDX mapping of the area 3, showing the AlN and $Al_2O_3$ growing on the aluminium/Silicon matrix.

### 4.3.3.4 *The effect of Mo addition on the grain size of Al alloy*

#### 4.3.3.4.1 The effect of Mo addition on the grain size of commercial purity aluminium

In this experiment, castings of commercial purity aluminium were made with the addition of a $TiB_2$ grain refiner, (5:1, Ti:B), and different amounts of Mo addition. For each experiment, about 300 grains were manually circled and measured using image J. The distribution of the grain size was obtained and the mean grain size recorded. The aim of this work was to investigate the effect of a Mo addition to commercial purity aluminium on the grain refining effect of $TiB_2$.

For commercial purity aluminium without addition, the grains were quite coarse with a size of 2014 μm. With the addition of 0.4 wt.% Mo alone, there was some grain refinement effects but the effect was not obvious. Some of the grains near the centre of the sample were slightly refined, (with a grain size of 565 μm), but the grains around the sides were still coarse (2100 μm). The addition of $TiB_2$ and $TiB_2$ and Mo greatly refined the grain size. For CPAl+$TiB_2$,the grain size was reduced to 163μm. The addition of 0.125%, 0.25%, and 0.5% Mo further reduced the grain size to 126 μm, 120 μm and 106 μm, respectively.
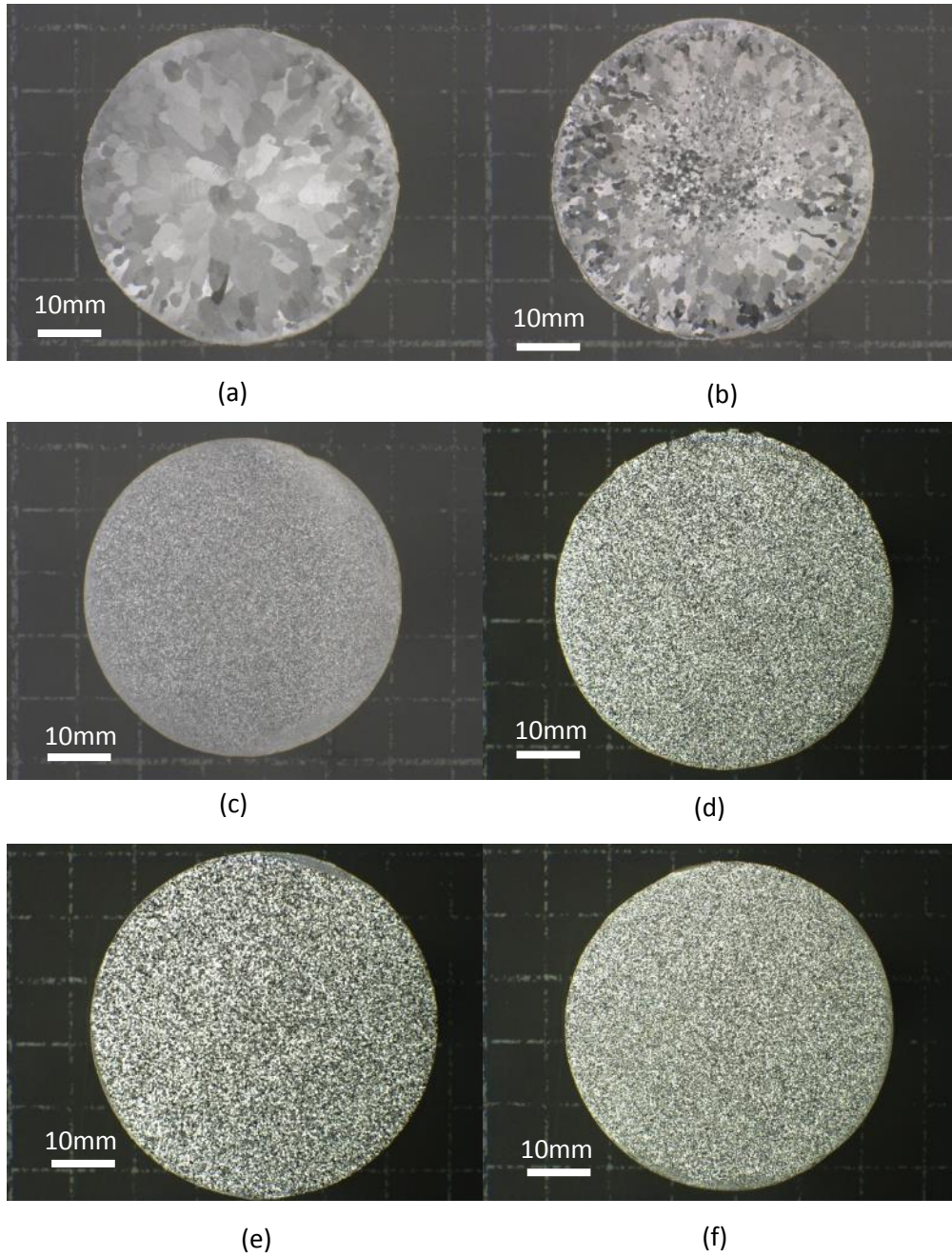
Figure 4-102 The etched surface of (a) CPAl; (b) CPAl+0.5 wt.% Mo, (c) CPAl+ 100 ppm $TiB_2$, (d) CPAl+100 ppm $TiB_2$+0.125 wt.% Mo, (e) CPAl+100 ppm $TiB_2$+0.25 wt.% Mo and (f) CPAl+100 ppm $TiB_2$+0.5 wt.% Mo.
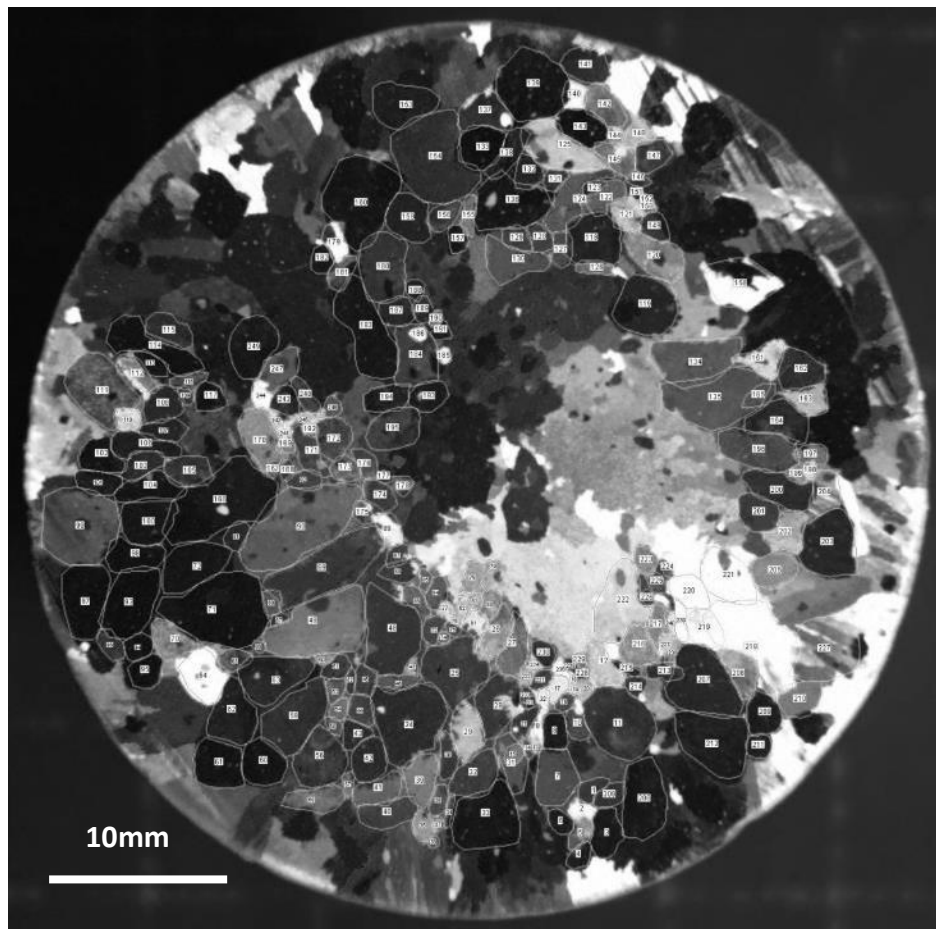
(a)
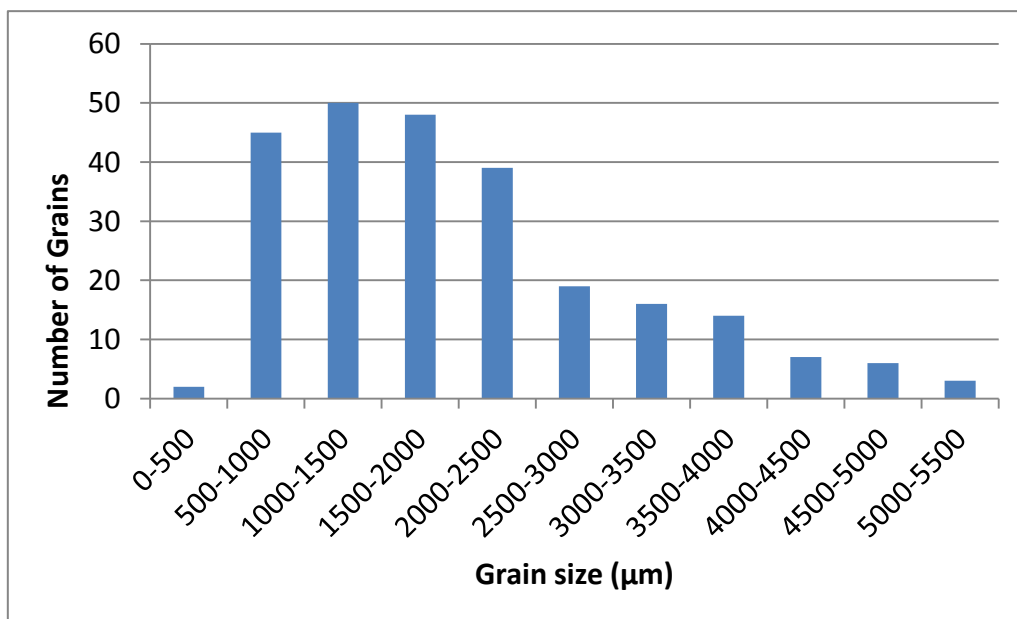


(b)

**Figure 4-103 Grain size distribution for commercial pure aluminium.**
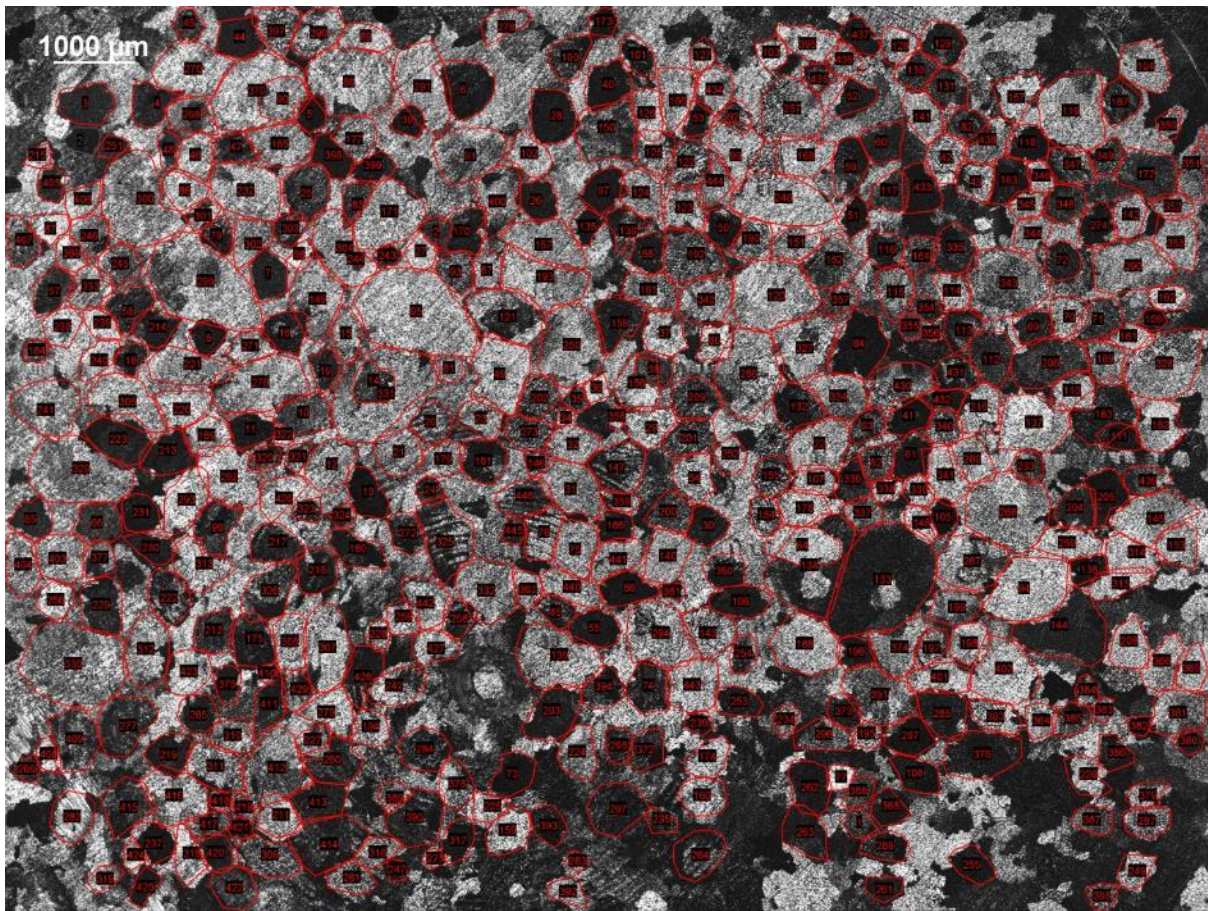
(a)
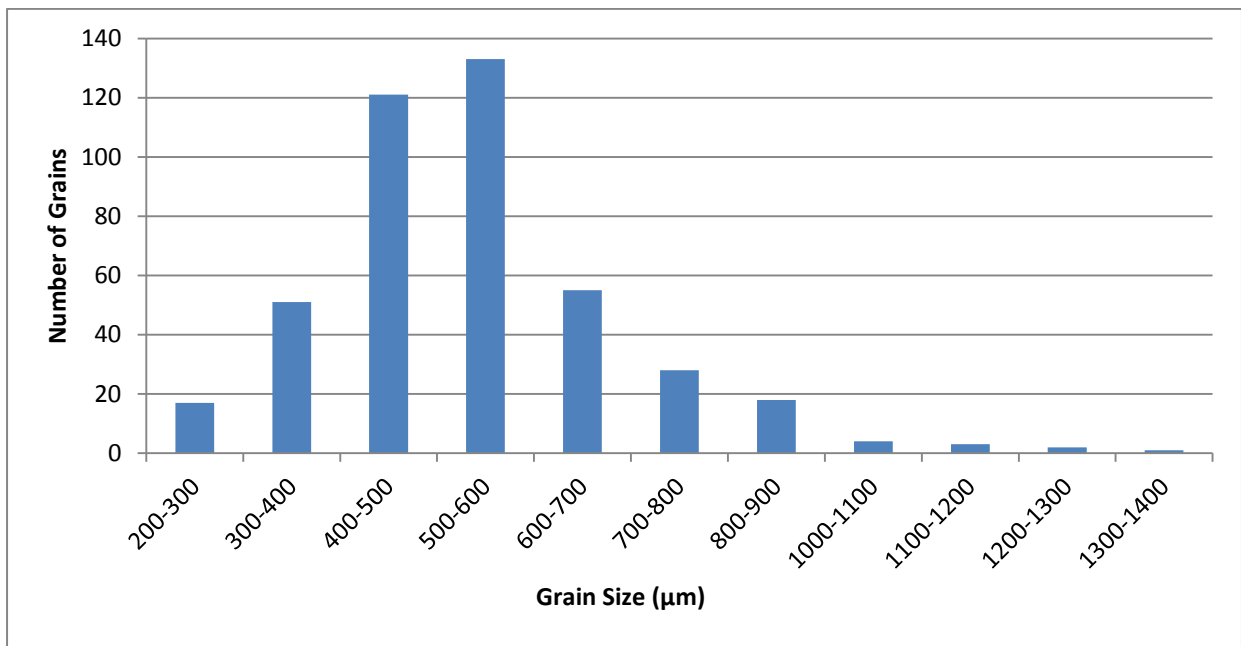


(b)

**Figure 4-104 Grain size distribution for the small grain area in commercial pure aluminium with 0.5 wt.% Mo addition.**
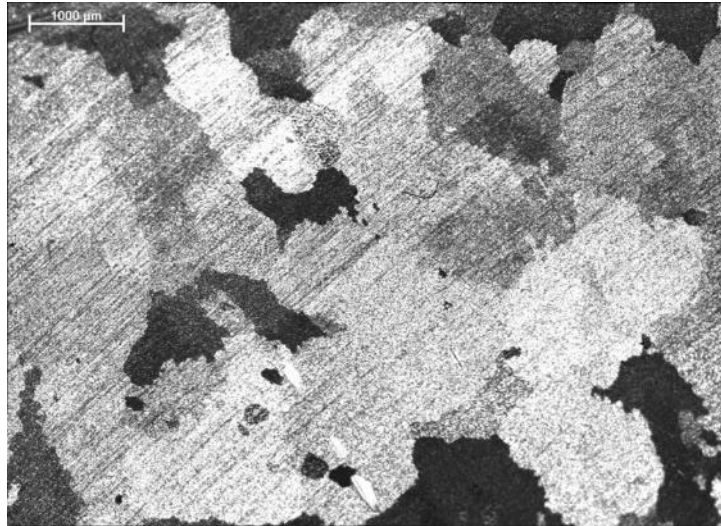
**Figure 4-105. Grain size of the edge of the TP-1 sample of CPAl+ 0.5 wt.% Mo showing large grains similar to those found on commercial pure aluminium.**
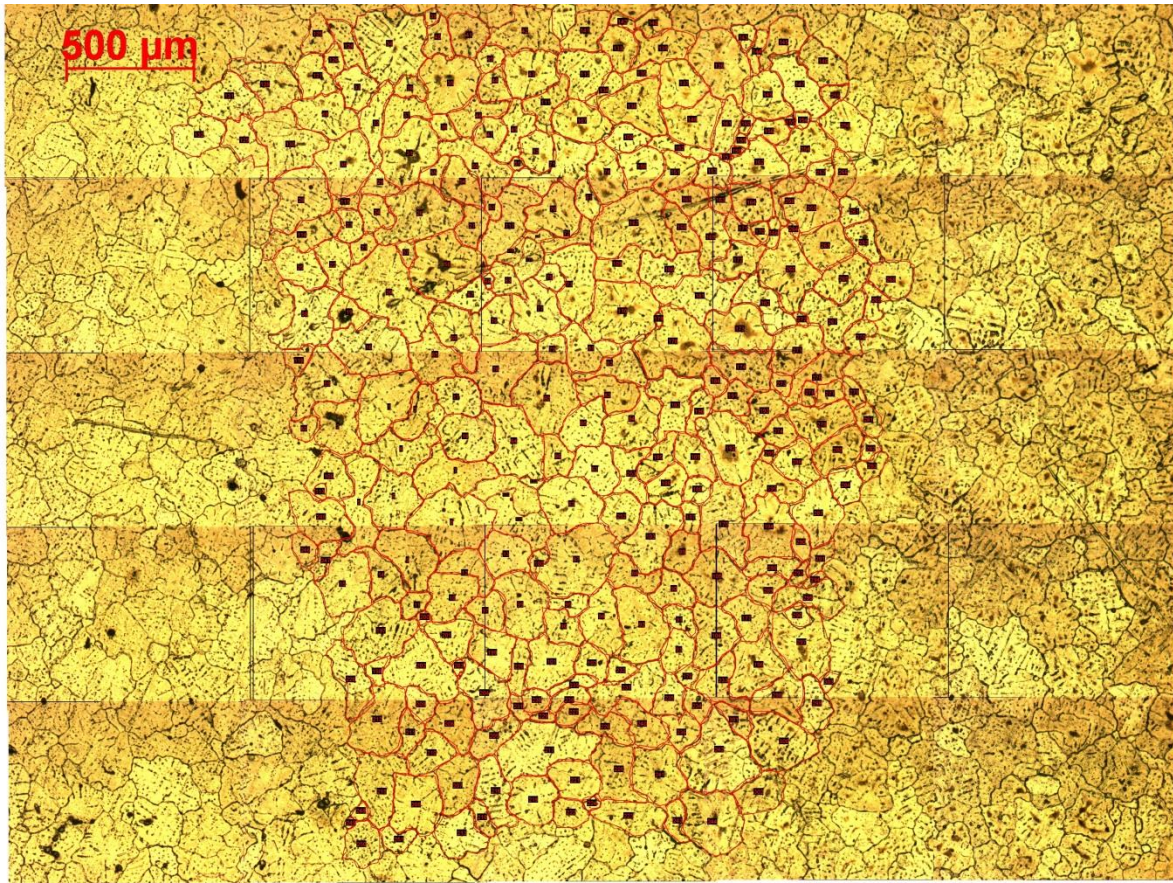
(a)
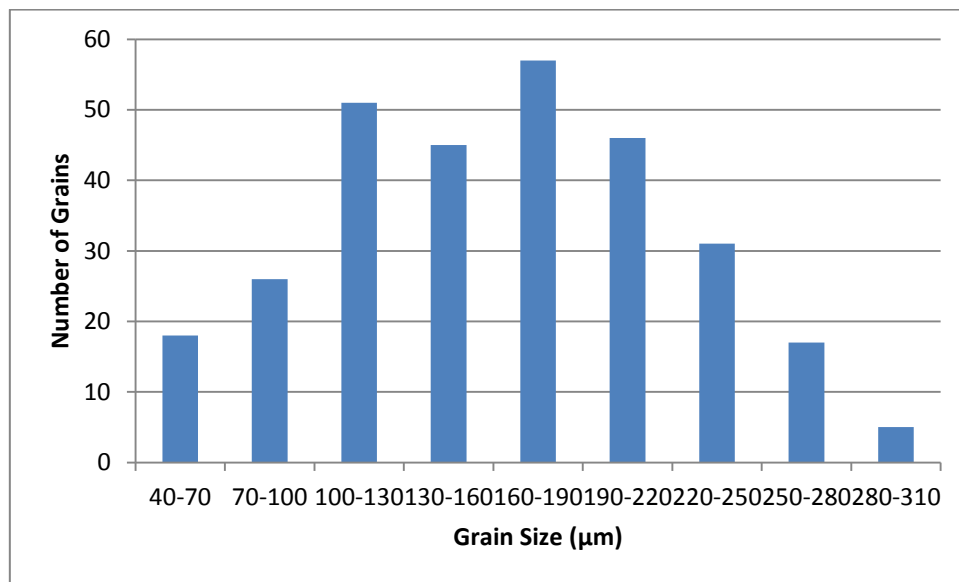


(b)

**Figure 4-106 Grain size distribution for commercial pure aluminium with 100ppm TiB$_2$ addition.**
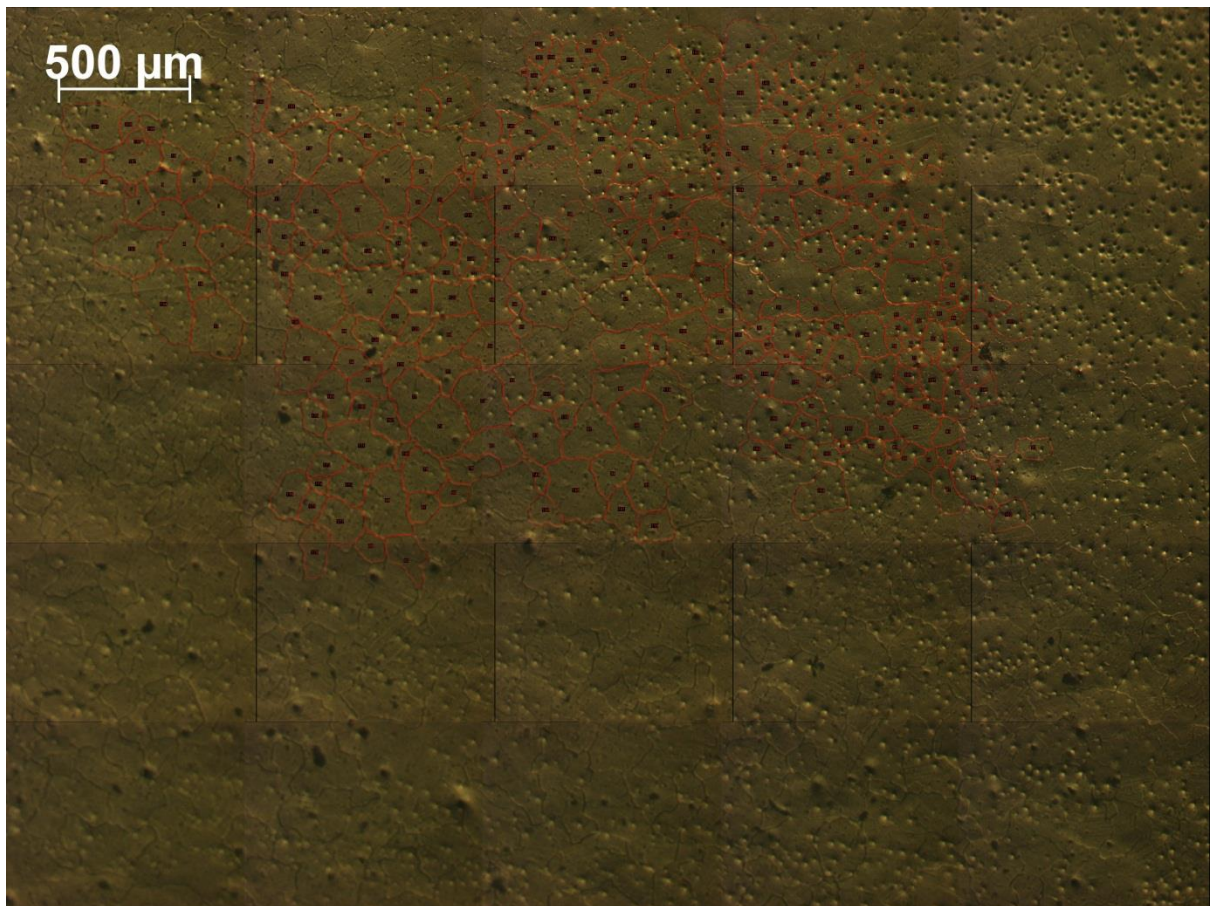
(a)
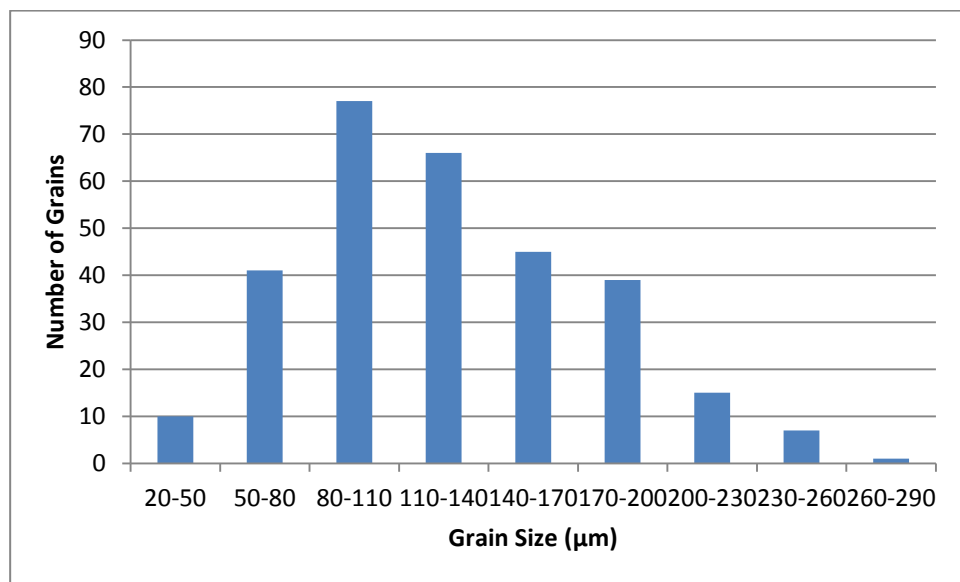


(b)

**Figure 4-107 Grain size distribution for CPAl+100 ppm TiB$_2$+0.125 wt.% Mo.**
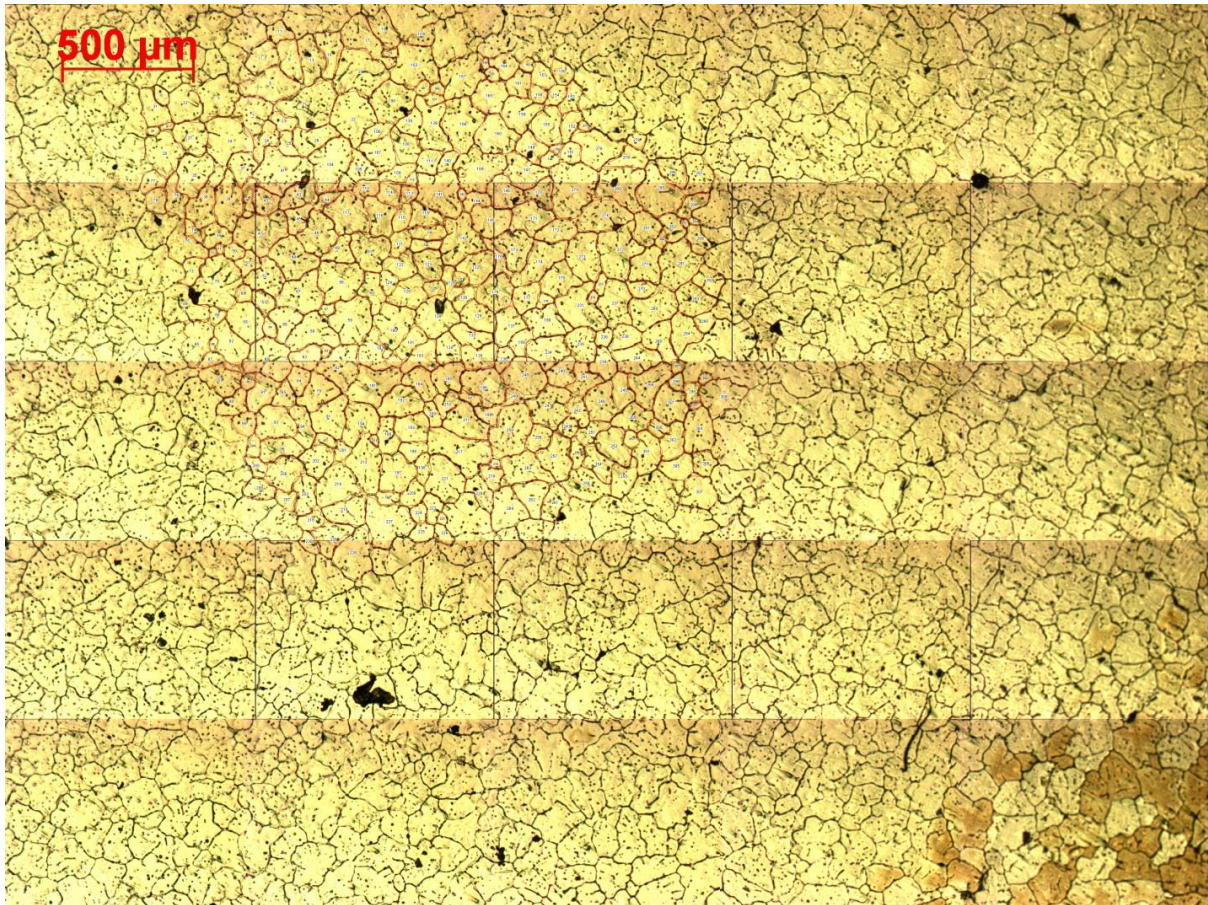
(a)
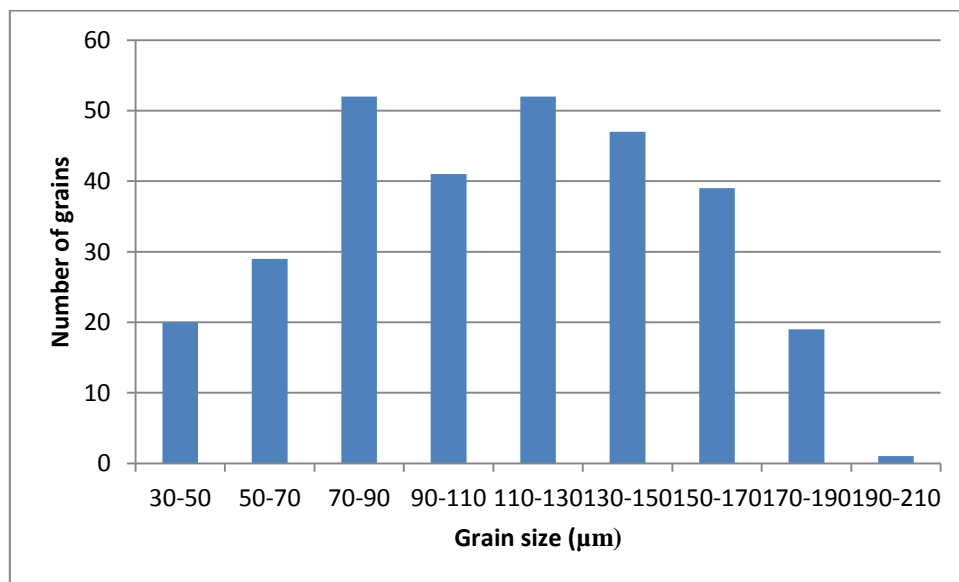


(b)

**Figure 4-108 Grain size distribution for CPAl+100 ppm TiB$_2$+0.25 wt.% Mo.**
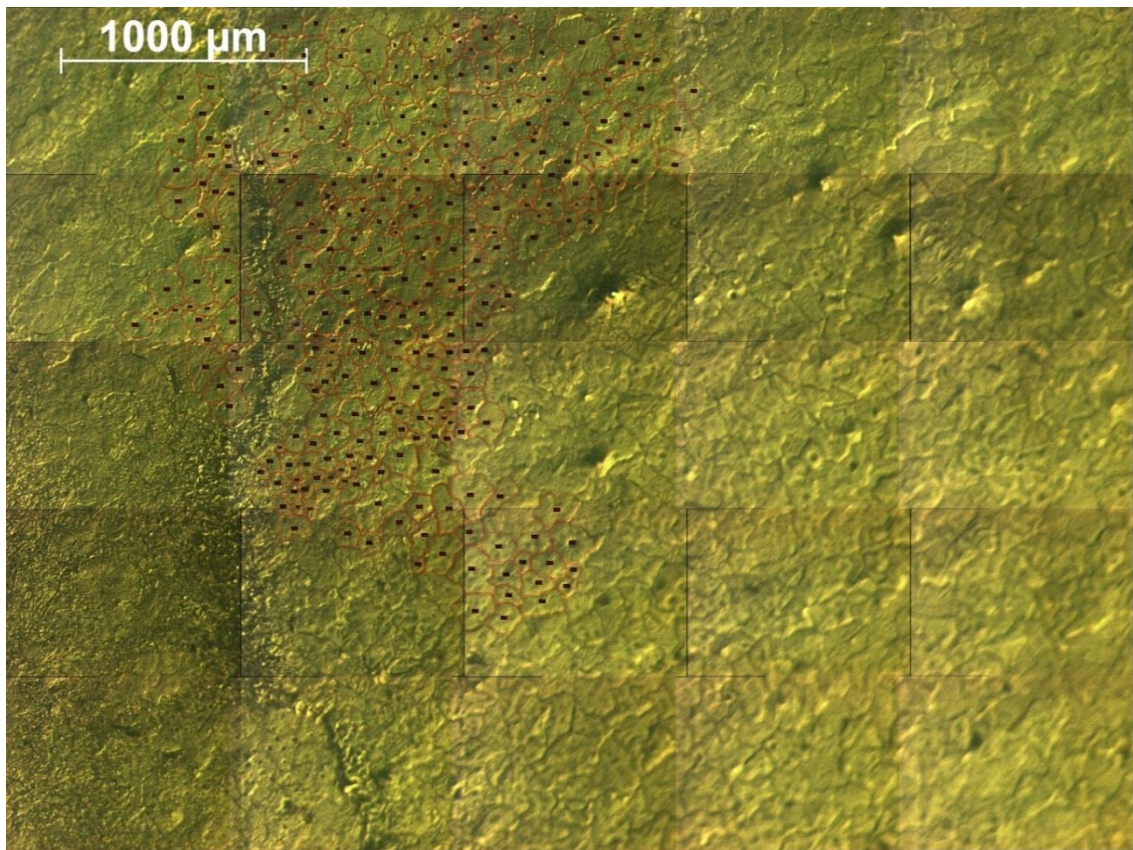
(a)
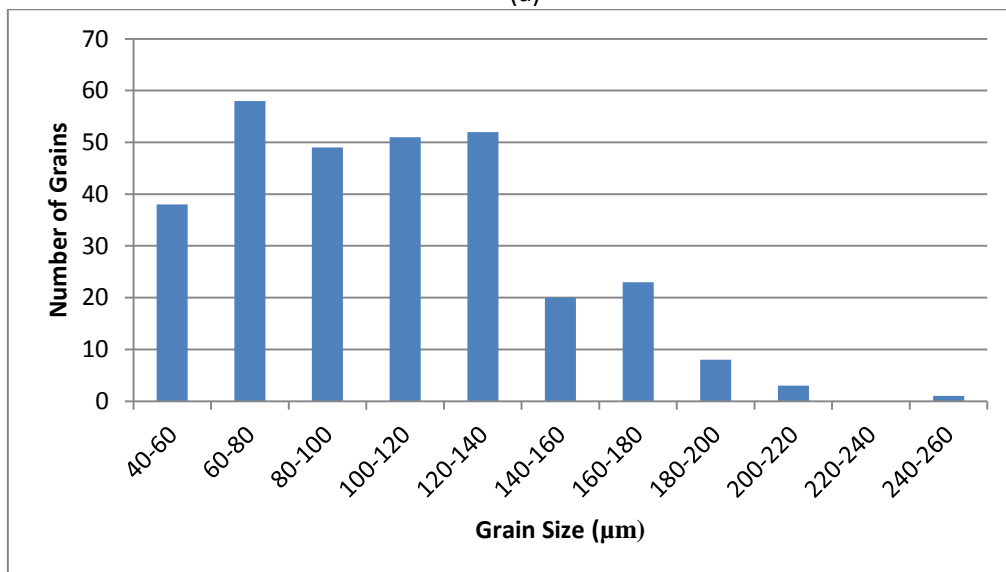


(b)

**Figure 4-109 Grain size distribution for CPAl+100 ppm TiB$_2$+0.5 wt.% Mo.**

**Table 4-39. Averge grain size for TP-1 Test.**

|  | Grain size ($\mu$m) |
|---|---|
| CPAl | 2014 |
| Al+ 0.5 wt.% Mo | 565 |
| Al+100 ppm TiB$_2$ | 163 |
| Al+100 ppm TiB$_2$+ 0.125 wt.% Mo | 126 |
| Al+100 ppm TiB$_2$+0.25 wt.% Mo | 120 |
| Al+100ppm TiB$_2$+0.5 wt.% Mo | 106 |

### 4.3.3.4.2   The effect of Mo addition on the grain size of 2L99 alloy

In this experiment, 0.5 wt.% Mo was added into 2L99 alloy and grain refined with TiB$_2$ ( with a B content of 50 ppm). The optical microscope image of the grain size and its distribution for 2L99 is shown in Figure 4-110 and the image and distribution for 2L99 +Mo is shown in Figure 4-111. The mean grain size for 2L99 was 543 $\mu$m and the mean grain size for 2L99+Mo was 560 $\mu$m which did not show significant difference. The distribution of the grain sizes for the two types of casting were also very similar.

(a)

(b)

(c)

(d)

(e)

(f)
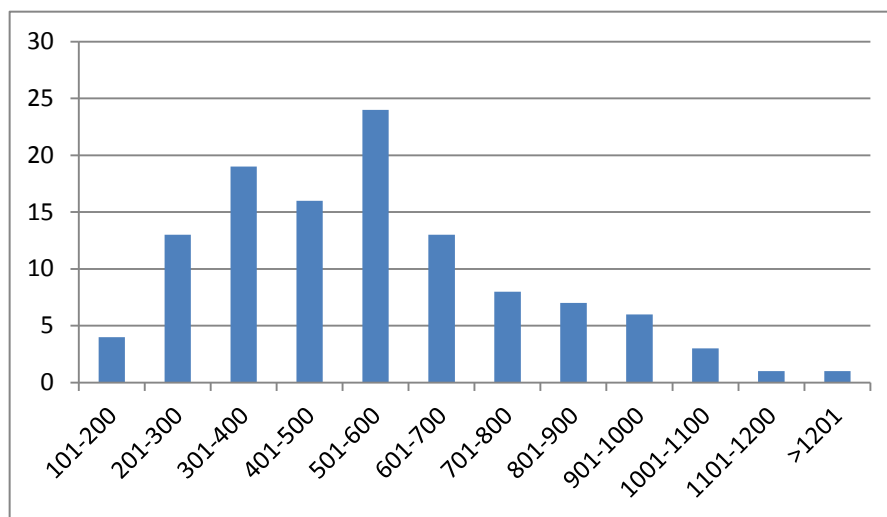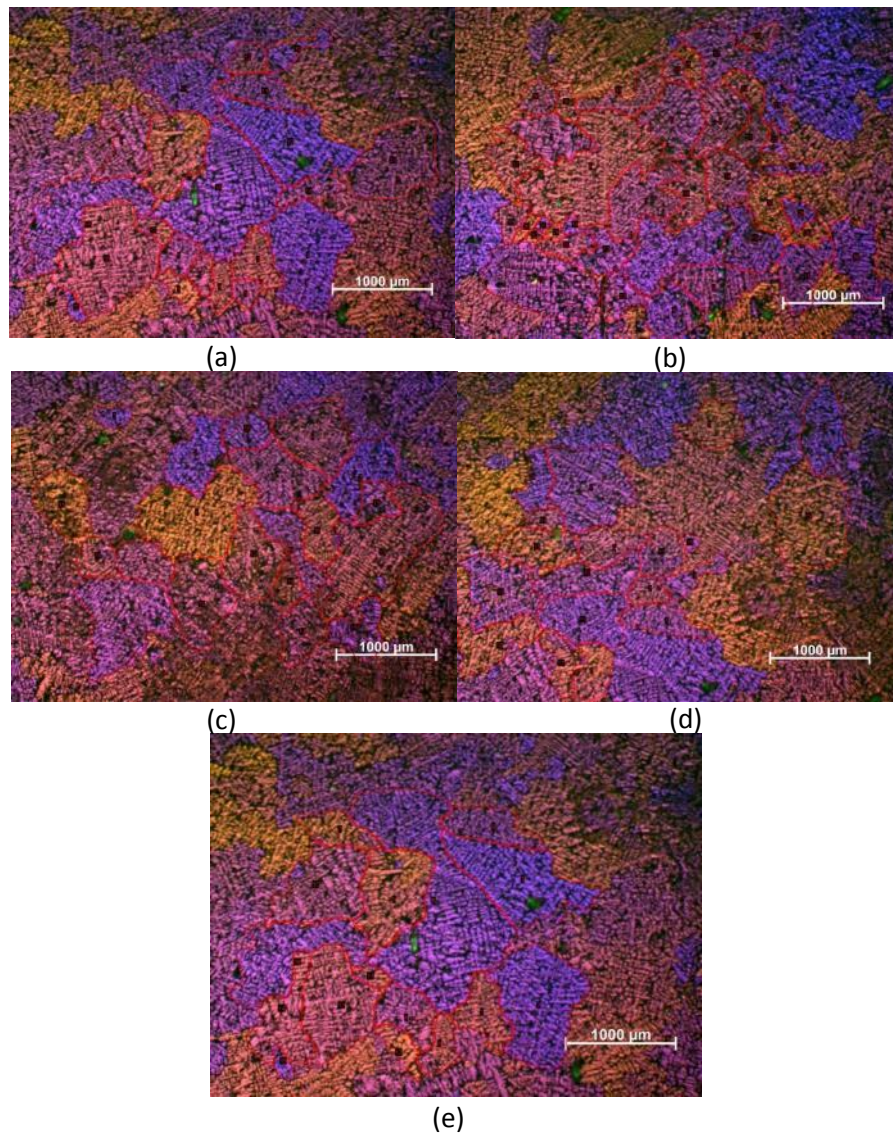
**Figure 4-110 (a)-(e) OM image of the 2L99 grains; (f) Distribution of grain size for 2L99.**
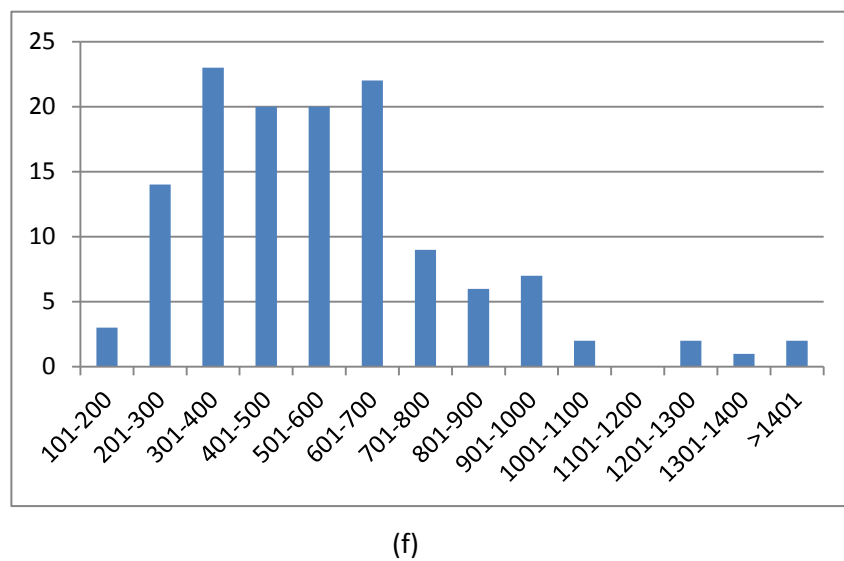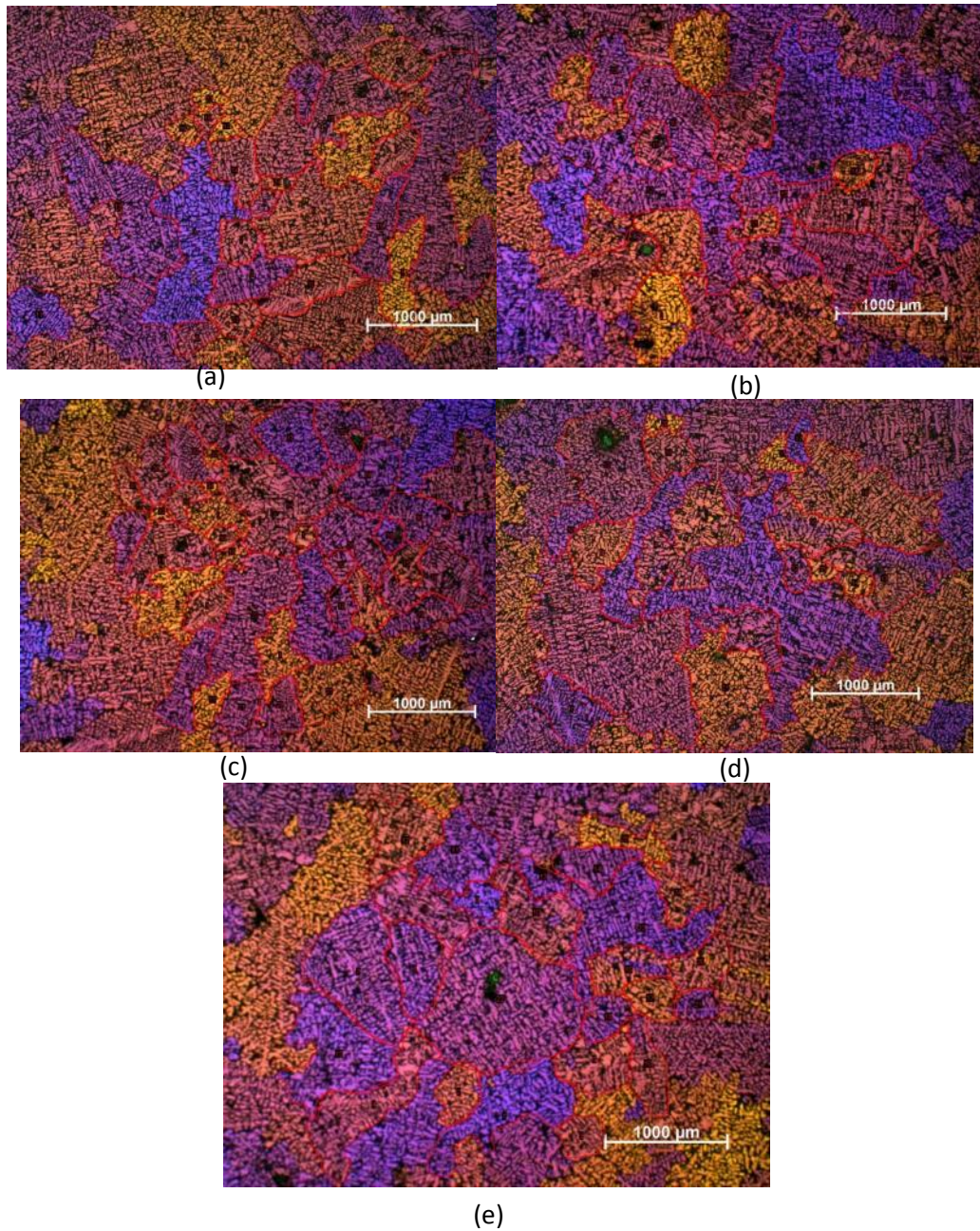
Figure 4-111 (a)-(e) OM image of the 2L99 +Mo grains; (f)Distribution of grain size for 2L99+Mo.

### 4.3.4 The effect of the addition of W into 2L99 alloy

#### 4.3.4.1 Mechanical property test results

The aim of this work was to understand the effect of a W addition on double oxide film defects and the reproducibility of mechanical properties of 2L99 castings.

3 sand moulds were cast, to give 30 test bars, which were cast with roll-over and heat-treatment. LECO[TM] measurements showed that the hydrogen content in the castings was 0.127 ppm and the chemical composition of the 2L99 castings with the W addition has been shown in Table 4-40. The Mg and Fe content were all controlled within an acceptable range (with Mg 0.3% +/-0.03% and Fe<0.1%).

**Table 4-40 Chemical composition of 2L99+W casting checked by XRF**

| 2L99+W | |
|---|---|
| Formula | Concentration |
| Al | 93.94% |
| Si | 9.93% |
| W | 0.44% |
| Mg | 0.33% |
| Ti | 0.14% |
| Fe | 0.09% |

The mechanical property results are shown in Table 4-41. The Weibull plot of the tensile test results are shown in Figure 4-112 and Figure 4-113. The $R^2$ values of the Weibull plot of UTS and %Elongation were 97.8% and 94.0% respectively, which are all higher than the

$R_{0.5}^2$ (91.1%). This suggested that both data sets (UTS and %Elongation) could be accepted as having a Weibull distribution.

The comparison of the tensile test results between 2L99 and 2L99+W are shown in Table 4-42. The addition of W increased the mean value of the UTS and %Elongation by 8% and 13% respectively. The position parameter for the UTS and %Elongation was also increased, by 6% and 20%, respectively.

The statistical analysis of the difference of the Weibull moduli between 2L99 and 2L99+W is shown in Table 4-43, which shows that the Weibull moduli of UTS was significantly improved with the W addition, while the difference in %Elongation was not clear.

**Table 4-41 tensile test results for 2L99+W.**

| 2L99+W | | | | | |
|---|---|---|---|---|---|
| | UTS | Elongation | | UTS | Elongation |
| No | MPa | % | No | MPa | % |
| 1 | 279 | 1.47 | 16 | 290 | 2.05 |
| 2 | 292 | 1.84 | 17 | 280 | 1.76 |
| 3 | 269 | 1.11 | 18 | 291 | 2.2 |
| 4 | 280 | 1.7 | 19 | 300 | 2.92 |
| 5 | 262 | 0.89 | 20 | 300 | 2.63 |
| 6 | 285 | 1.86 | 21 | 305 | 3.77 |
| 7 | 288 | 1.64 | 22 | 288 | 2.23 |
| 8 | 300 | 3.73 | 23 | 280 | 1.74 |
| 9 | 303 | 4.26 | 24 | 296 | 2.36 |
| 10 | 271 | 1.36 | 25 | 295 | 3.27 |
| 11 | 284 | 1.54 | 26 | 300 | 4.05 |
| 12 | 292 | 1.91 | 27 | 294 | 2.74 |
| 13 | 300 | 3.07 | 28 | 289 | 1.72 |
| 14 | 272 | 1.09 | 29 | 298 | 2.57 |
| 15 | 277 | 1.11 | 30 | 304 | 3.19 |
| average | 288.8 | 2.26 | | | |
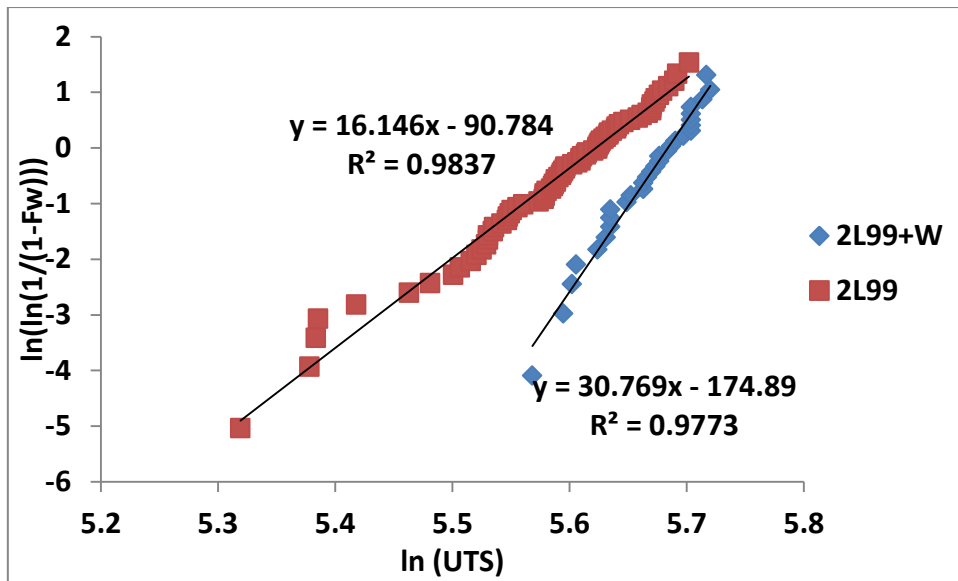
**Figure 4-112 Weibull plot of UTS of 2L99+W casting.**
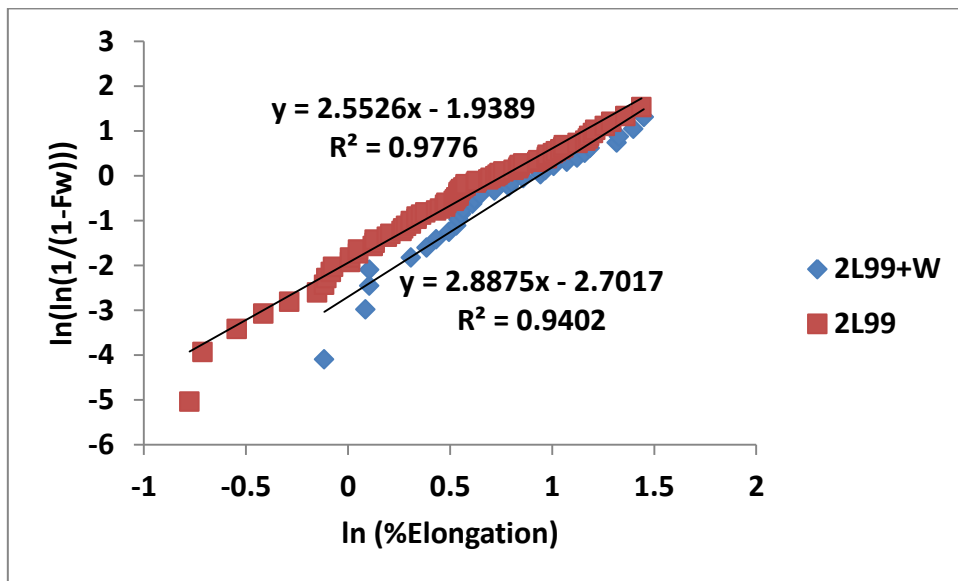


**Figure 4-113 Weibull plot of %Elongation of 2L99+W.**

224

**Table 4-42 the tensile test comparison between 2L99 and 2L99+W.**

|  | mean value for %Elongation | Mean value for UTS | Weibull moduli of %Elongation | Weibull moduli of UTS | position parameter of %Elongation | position parameter of UTS |
|---|---|---|---|---|---|---|
| 2L99 | 1.9 | 267.6MPa | 2.55 | 16.1 | 2.13 | 276.6 MPa |
| 2L99+W | 2.26 | 288.8 MPa | 2.89 | 30.8 | 2.55 | 294.1 MPa |

**Table 4-43 Statistic comparison of the Weibull moduli between 2L99 and 2L99+W.**

|  | 2.5 and 97.5 percentile | m1/m2(UTS) | Significant difference in UTS? | m1/m2(%Elongation) | Significant differences in %Elongation? |
|---|---|---|---|---|---|
| 2L99+W | 0.660,1.573 | 0.52 | Yes | 0.88 | No |

### *4.3.4.2 SEM investigation of the fracture surface*

Figure 4-114 shows the fracture surface of tensile test bars No. 20 and No.6 of the 2L99+W castings.

X1, X2 and X3 are shown in Figure 4-115 Figure 4-116 and Figure 4-117 respectively.

Figure 4-115 and Figure 4-116 showed the presence of spinel particles on the fracture

surface. Figure 4-116 showed that those spinel particles were inhomogeneous in size.

Figure 4-117 showed a W-containing intermetallic compound at the edge of the oxide film.

This intermetallic compound could nucleate on the wetted side of the bi-film defect. Figure

4-118 showed a W containing intermetallic compound underneath the oxide layer.

(a)                     (b)
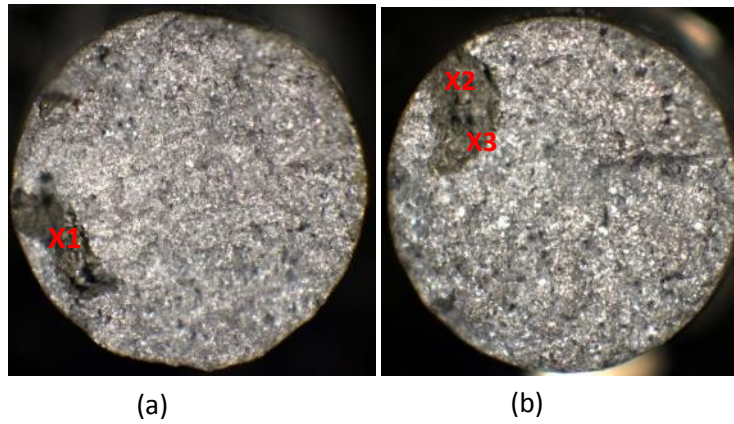
**Figure 4-114 Fracture surface of tensile test bar (a) No. 20 and (b) No. 6 of 2L99+W alloy.**



(a)



(b)
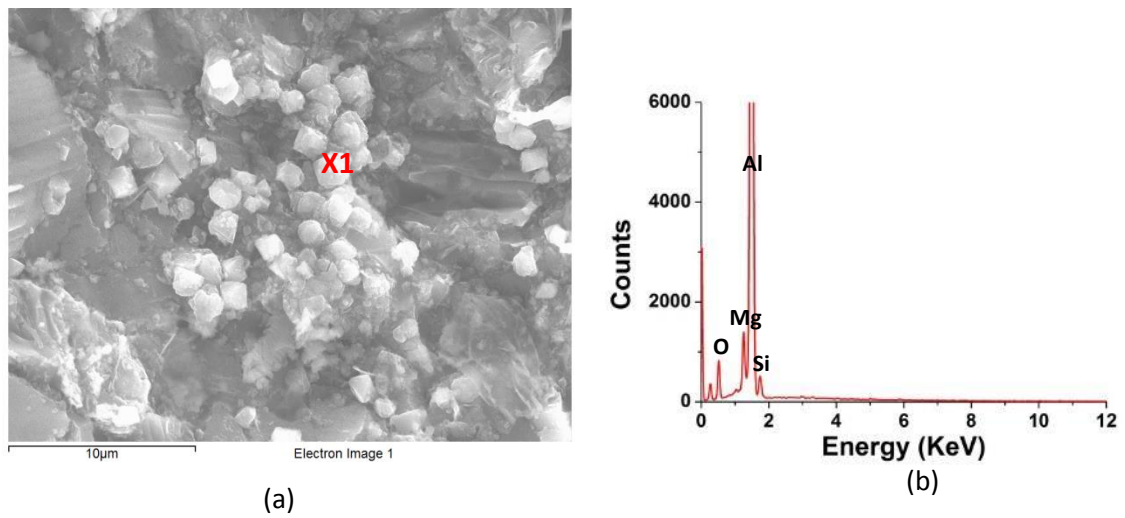
**Figure 4-115 (a) SEM image showing uniform sized oxide particles in Figure 4-114 X2; (b) EDX spectrums of X1.**
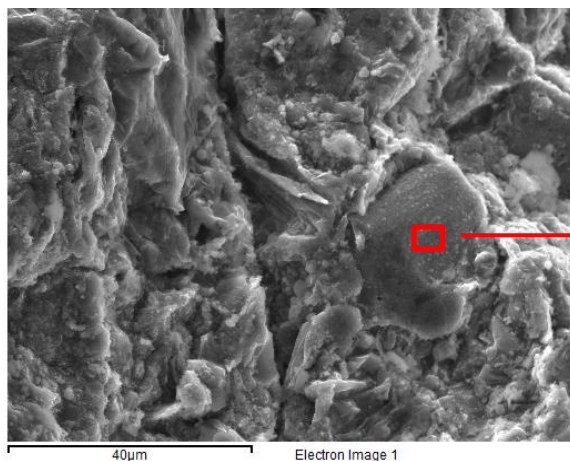
(a)
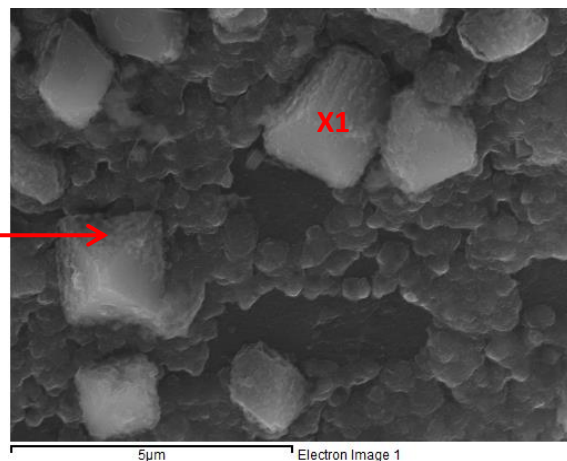
(b)
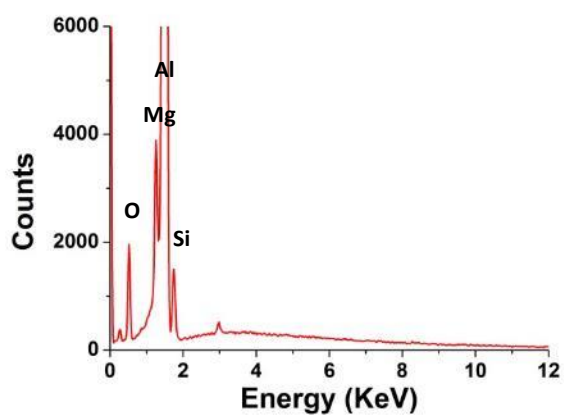


(c)

Figure 4-116. (a) (b) SEM image shows Figure 4-114 X3; (C) EDX spectrum of X1.
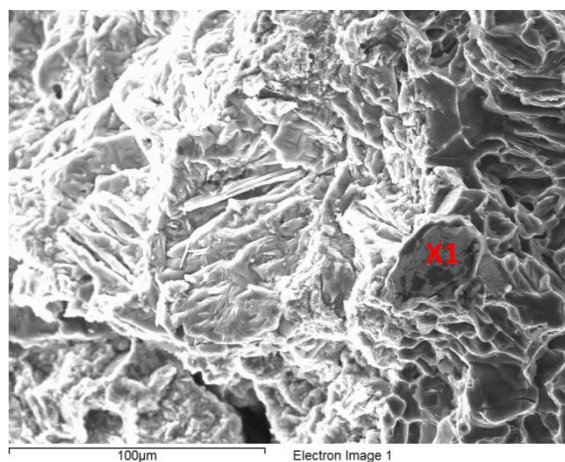


(a)
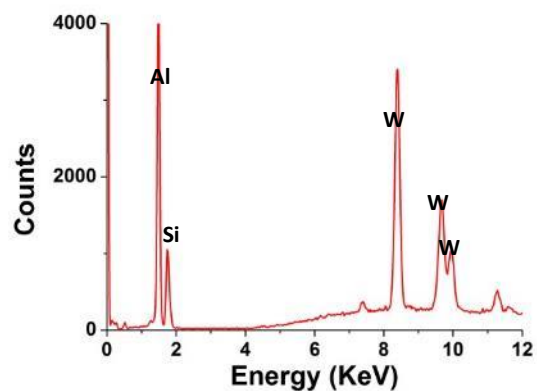


(b)

Figure 4-117 (a) SEM image shows the W containing intermetallic phase on the sides of the oxide film; (b) EDX spectrum of X1.
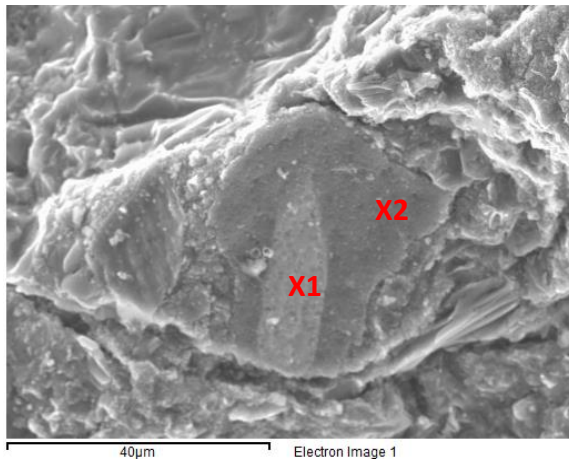
(a)
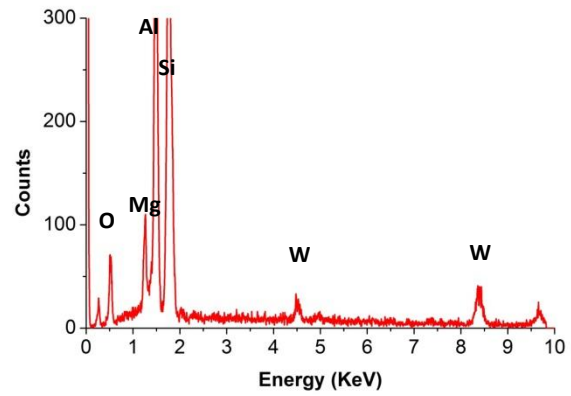


(b)
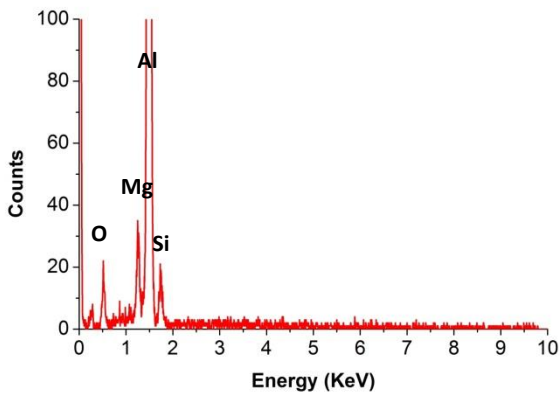


(c)

Figure 4-118 (a) SEM image showing the W containing intermetallic phase growing beneath the double oxide film; (b) EDX spectrum for X1 and (c) EDX spectrum for X2.

In order to understand the cross-section of the oxide layer, Focused ion beam milling was used to reveal the fracture surface.

Figure 4-119 shows the cross-section of the oxide from tensile test bar No.17. As can be seen, the oxide layer was about 200nm in thickness. Figure 4-119 (b) shows an oxide particle involved in the oxide layer, and EDX analysis confirms that this oxide particle contained W.
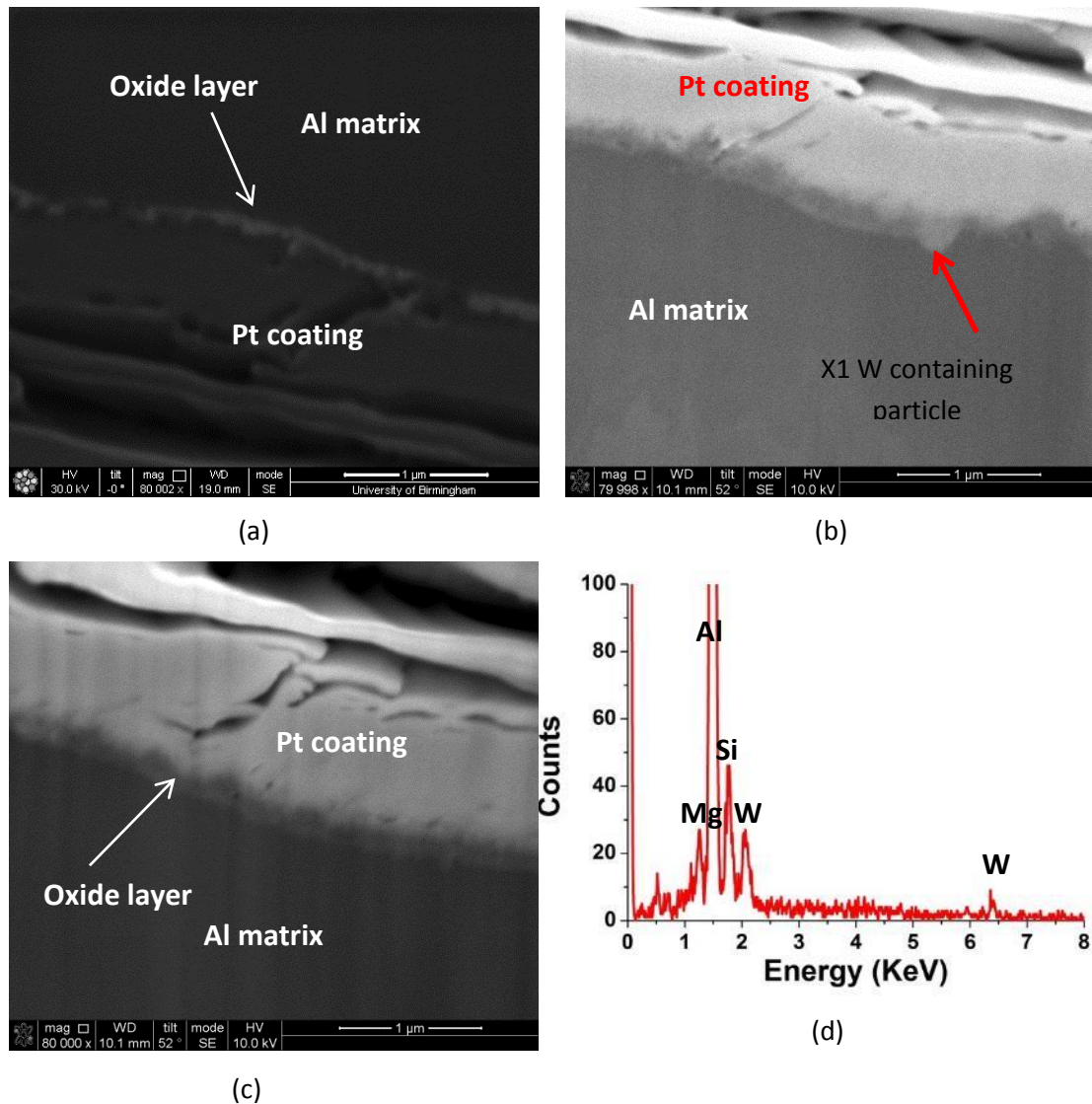
**Figure 4-119 (a)-(c) Cross-sections of the oxide layer from 2L99+W fracture surface; (d)EDX for X1.**

### 4.3.5  The effect of Ti addition into 2L99

#### 4.3.5.1  Mechanical property test

This work was aimed at investigating the effect of a Ti addition on double oxide film defects and the reproducibility of 2L99 casting.

3 moulds were cast which produced 30 test bars. A LECO^TM test suggested that the casting contained 0.146 ppm H (<0.2 ppm). The chemical composition of the casting was checked by

XRF and is shown in Table 4-44. Mg content and Fe content are all controlled within an acceptable range (0.32 wt.% +/- 0.02 wt.% for Mg content and 0.1 wt.% +/- 0.02 wt.% for Fe content).

The UTS and %Elongation value of 2L99+Ti are shown in Table 4-45. The Weibull plots of the UTS and %Elongation are shown in Figure 4-120 and Figure 4-121 respectively. The $R^2$ of the Weibull plot of UTS and %Elongation were 96.9% and 95.4% respectively, which suggested both distributions can be accepted as Weibull distribution.

The comparison of the tensile test results between 2L99 and 2L99+Ti are shown in Table 4-46 and Table 4-47. As can be seen, the addition of Ti had no effect on the mean value and position parameter of the UTS, however the relevant value for %Elongation was reduced by about 40%. Table 4-47 suggested that the Weibull moduli of both the UTS and %Elongation between 2L99 and 2L99+Ti were both statistically indifferent.

**Table 4-44 The chemical composition of 2L99+Ti casting.**

| 2L99+Ti | |
|---------|---------------|
| Formula | Concentration |
| Al | 92.95% |
| Si | 9.69% |
| Mg | 0.34% |
| Ti | 0.40% |
| Fe | 0.11% |

**Table 4-45 The tensile test results for 2L99+Ti.**

| | | 2L99+Ti | | | |
|---|---|---|---|---|---|
| | UTS | Elongation | | UTS | Elongation |
| No | MPa | % | No | MPa | % |
| 1 | 219 | 0.37 | 16 | 270 | 1.29 |
| 2 | 247 | 0.67 | 17 | 272 | 1.3 |
| 3 | 252 | 0.68 | 18 | 272 | 1.38 |
| 4 | 274 | 1.15 | 19 | 243 | 0.52 |
| 5 | 278 | 1.21 | 20 | 260 | 0.99 |
| 6 | 244 | 0.67 | 21 | 241 | 0.67 |
| 7 | 293 | 2.05 | 22 | 286 | 1.88 |
| 8 | 275 | 1.32 | 23 | 292 | 2.33 |
| 9 | 268 | 0.97 | 24 | 261 | 0.99 |
| 10 | 253 | 0.74 | 25 | 294 | 2.22 |
| 11 | 269 | 0.88 | 26 | 291 | 2.17 |
| 12 | 234 | 0.48 | 27 | 275 | 1.05 |
| 13 | 244 | 0.58 | 28 | 197 | 0.34 |
| 14 | 284 | 1.61 | 29 | 193 | 0.31 |
| 15 | 288 | 1.62 | | | |
| average | 261 | 1.12 | | | |
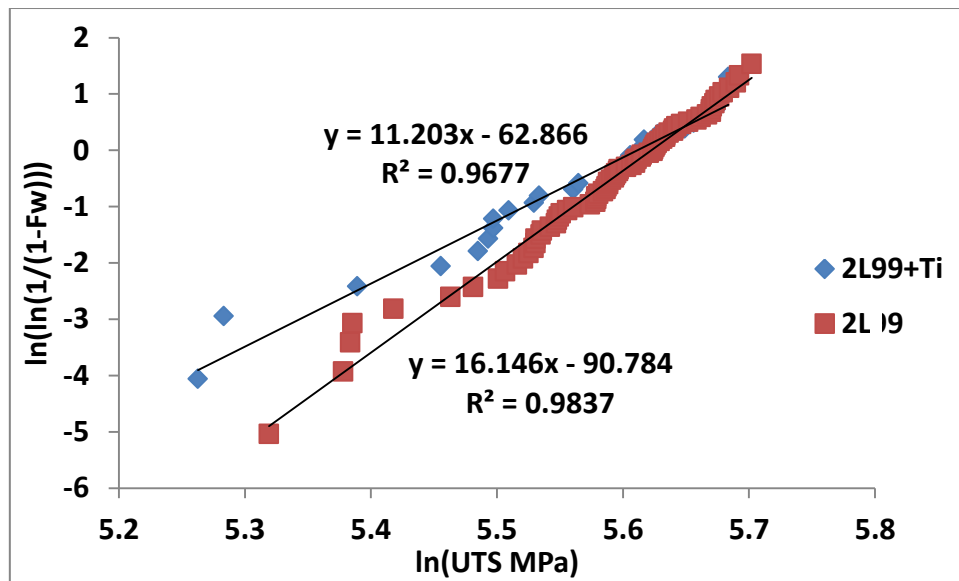


**Figure 4-120 Weibull plot of UTS of 2L99+Ti.**

y = 11.203x - 62.866
R² = 0.9677

y = 16.146x - 90.784
R² = 0.9837
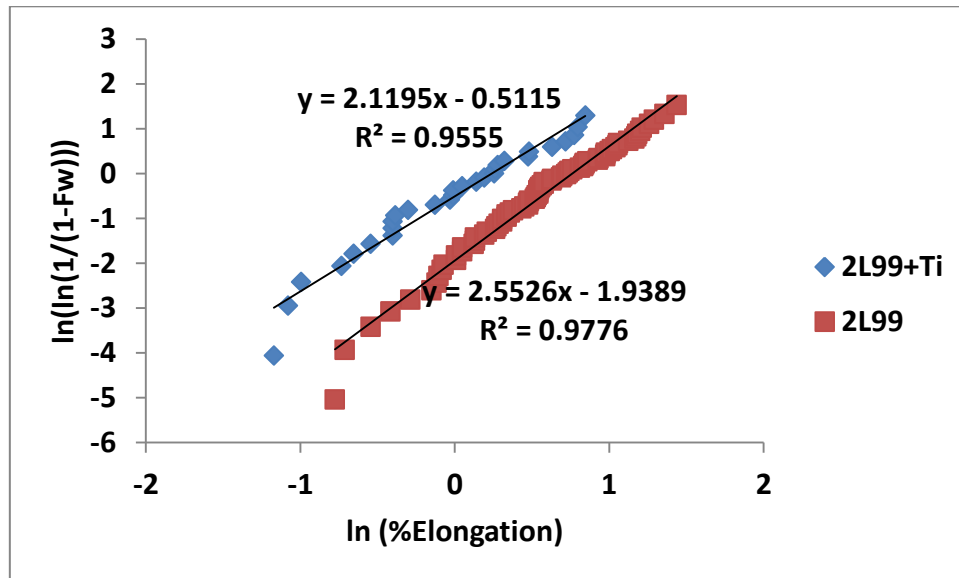
**Figure 4-121 Weibull plot of %Elongation of 2L99+Ti.**

**Table 4-46 The comparison of the mechanical test result between 2L99 and 2L99+Ti.**

|         | mean value |            | position parameter |            | Weibull moduli |            |
|---------|------------|------------|--------------------|------------|----------------|------------|
|         | UTS        | %Elongation| UTS                | %Elongation| UTS            | %Elongation|
| 2L99    | 267.6 MPa  | 1.9        | 276.6MPa           | 2.13       | 16.1           | 2.55       |
| 2L99+Ti | 261MPa     | 1.12       | 273.5MPa           | 1.27       | 11.2           | 2.12       |

**Table 4-47 The comparison of the Weibull moduli between 2L99 and 2L99+Ti.**

|         | 2.5 and 97.5 percentile | m1/m2(UTS) | Significant difference in UTS | m1/m2(%Elongation) | Significant difference in %Elongation |
|---------|-------------------------|------------|-------------------------------|--------------------|---------------------------------------|
| 2L99+Ti | 0.660,1.573             | 1.43       | no                            | 1.2                | No                                    |

232

### 4.3.5.2 SEM investigation of the fracture surface

For the Ti addition into 2L99 castings, Figure 4-122 (a) (b) and (c) shows the fracture surface of test bars No.12, No.24 and No.9 respectively.

SEM images of Figure 4-122 X1 are shown in Figure 4-123. EDX suggested that Ti was not participating in the formation of the oxide layer.

A SEM image of Figure 4-122 X2 has been shown in Figure 4-124; Ti-containing oxide particles (of size 2 μm) were seen on the surface oxide layer.



(a)



(b)



(c)
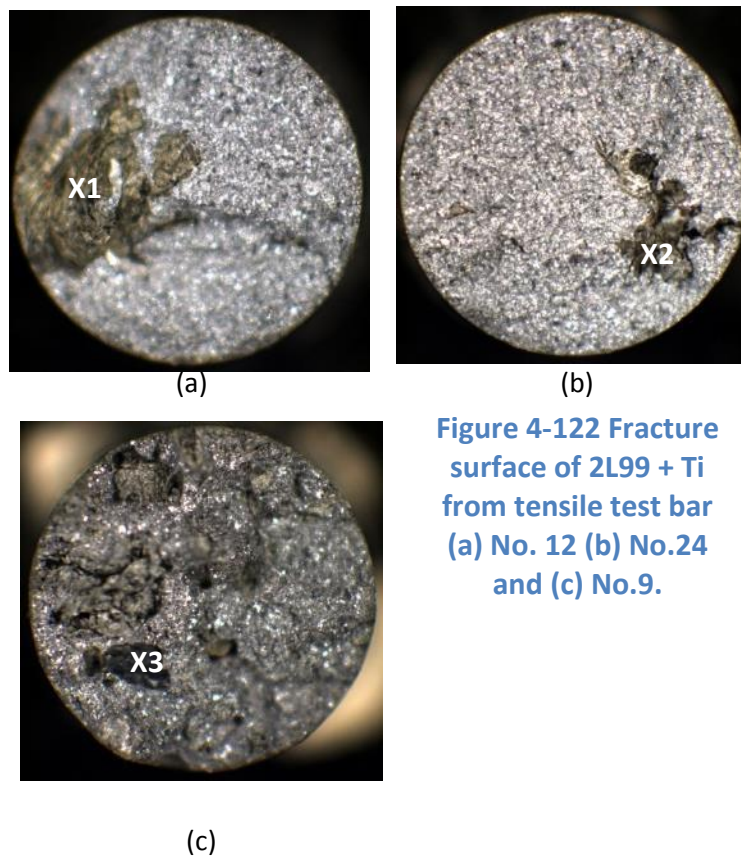
**Figure 4-122 Fracture surface of 2L99 + Ti from tensile test bar (a) No. 12 (b) No.24 and (c) No.9.**
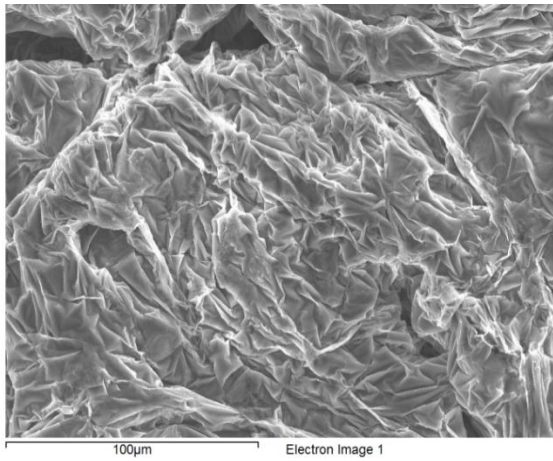
(a)
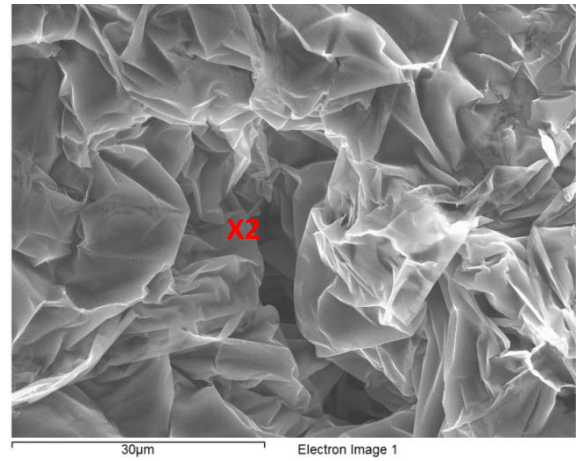


(b)
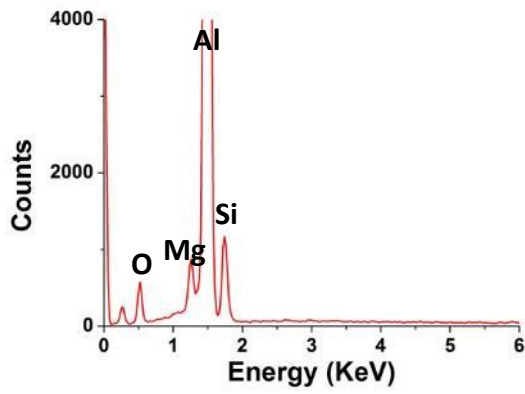


(c)

**Figure 4-123 SEM images show the area of Figure 4-122 X1.**
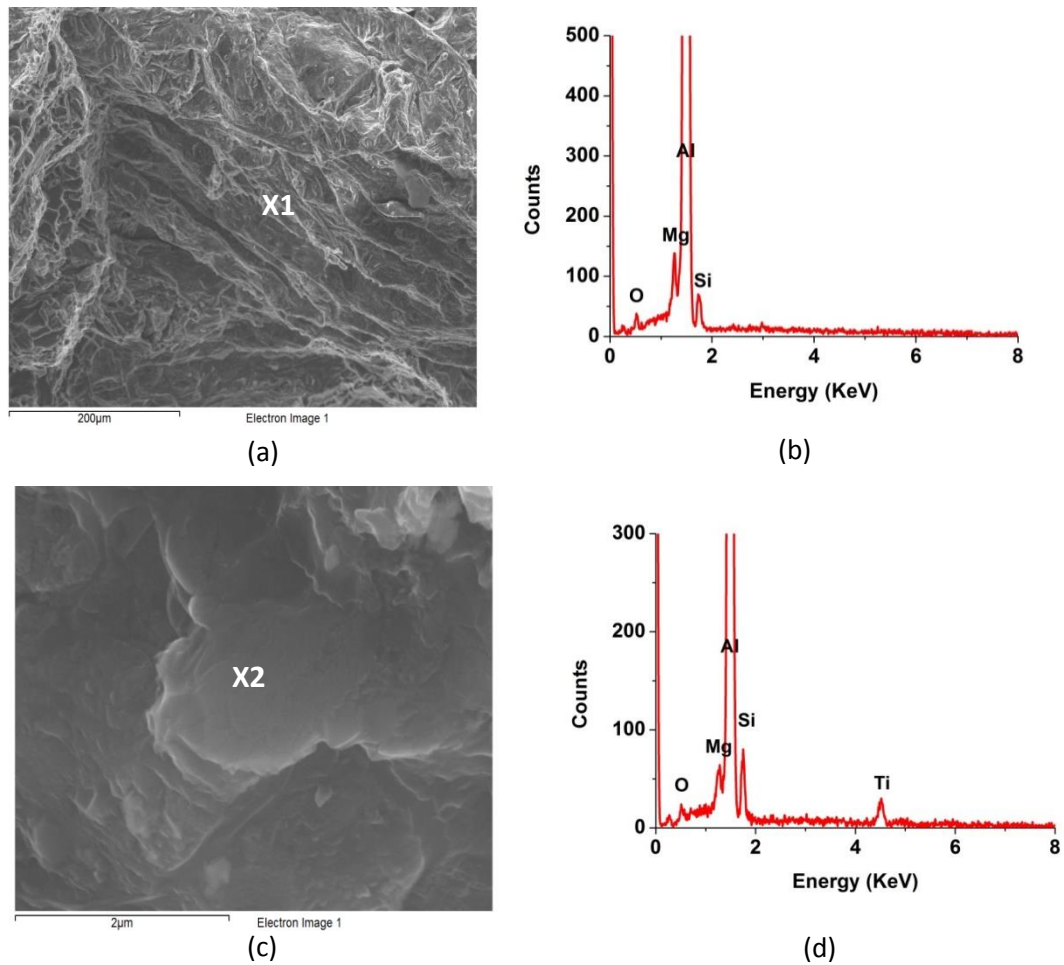
**Figure 4-124 (a), (c) SEM image showing Figure 4-122 X2; (b), (d) EDX spectrum of X1-X2.**

Figure 4-125 shows the oxide layer for which a Ti peak was detected by EDX, in large areas of the oxide. A high magnification image suggested that this oxide was permeable with a fibre-like structure. High Mg, O and Ti peaks were also observed by EDX.

In order to further understand the structure and the role of Ti in this oxide layer, Focused Ion Beam milling was used to reveal a cross-section of the area.

Figure 4-126 showed the top view of the oxide layer. Figure 4-127 showed the cross-section of the surface layer, which suggested that the oxide particles, of size 2-3 μm were growing

on the aluminium matrix. X1 and X3 was shown by EDX to be Ti containing oxide particles, while X2 was shown to be aluminium oxide.

Figure 4-128 and Figure 4-129 are another area of the cross-section of the surface layer which suggested that the fibre shaped oxide, with the height of 3-4µm, was observed growing on the aluminium matrix. A Ti-containing intermetallic was seen near the surface layer. EDX spectrum in Figure 4-129 X1 suggested that no Ti was observed on the surface layer. It is therefore the Ti detected from the top surface came from the Ti containing oxide particles and Ti containing intermetallic phase.
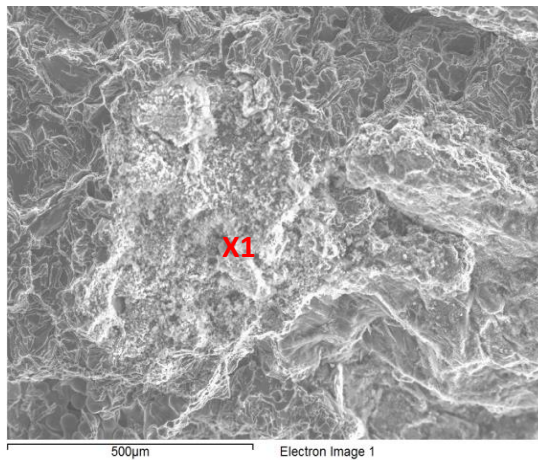
(a)
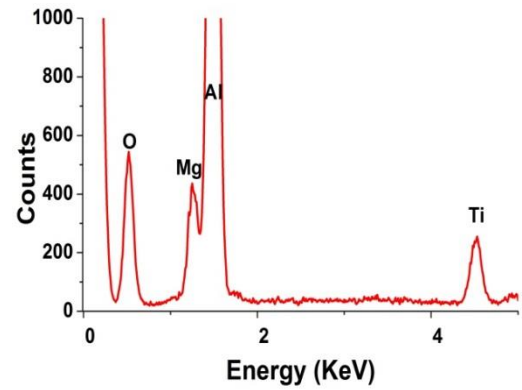
(b)
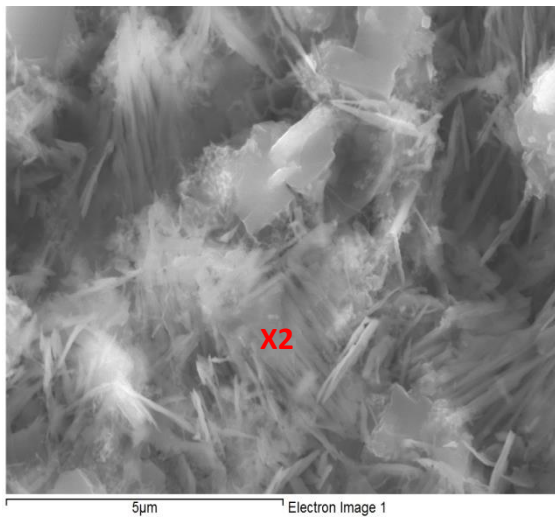
(c)
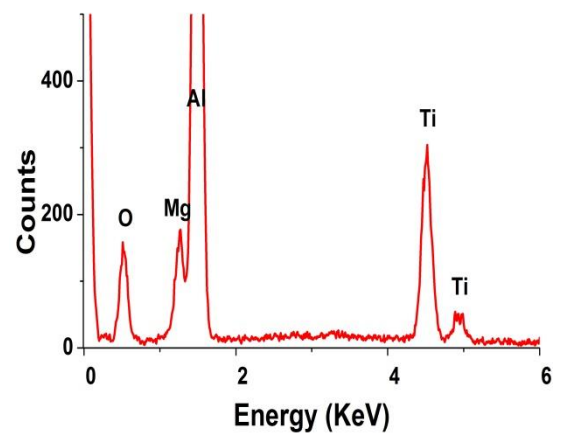
(d)

**Figure 4-125 (a) and (c) SEM image shows Figure 4-122 X3; (b) and (d) EDX spectrum of X1 and X2 respectively.**
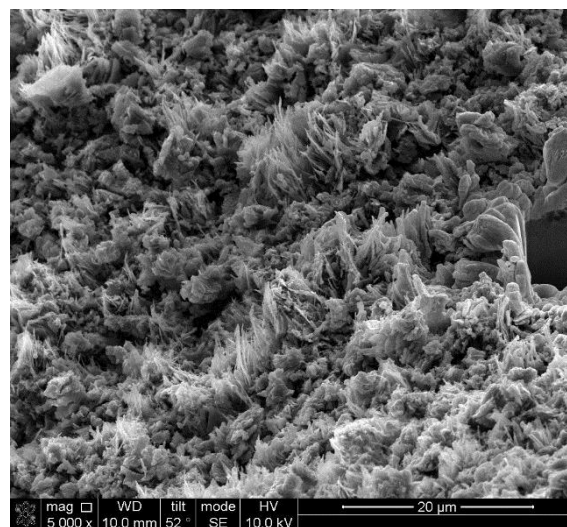


**Figure 4-126 Top view of the oxide layer in Figure 4-122 X3 used for cross-section milling.**

237
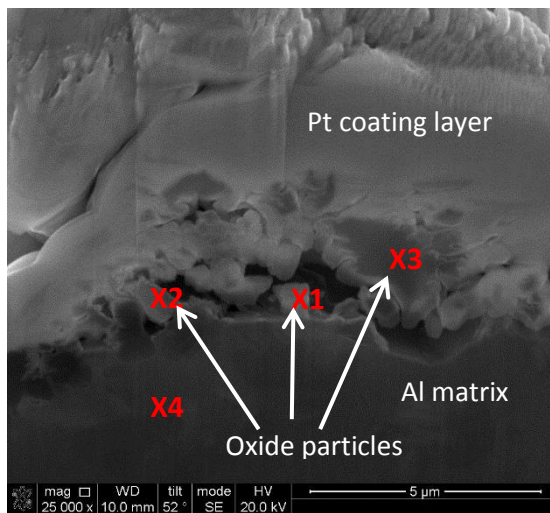
(a)
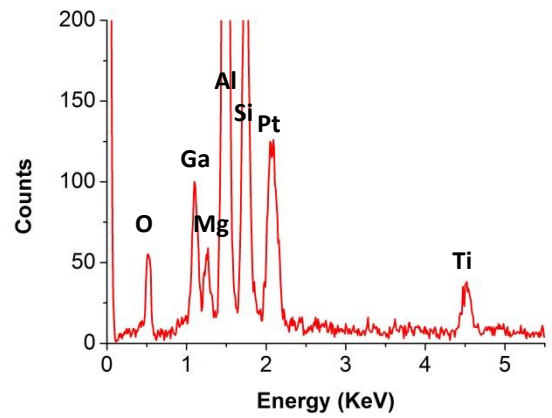
(b)
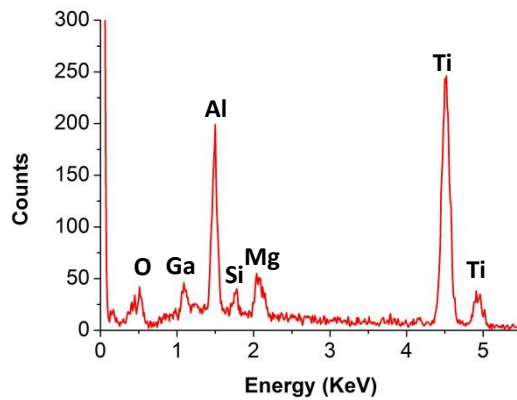
(c)
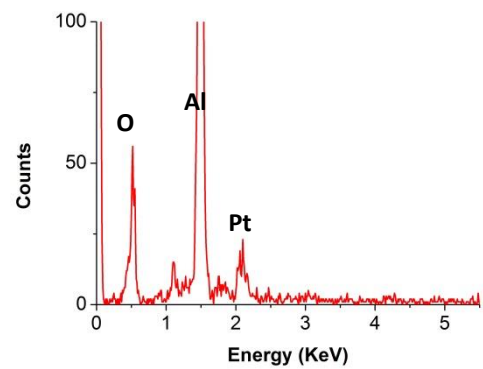
(d)
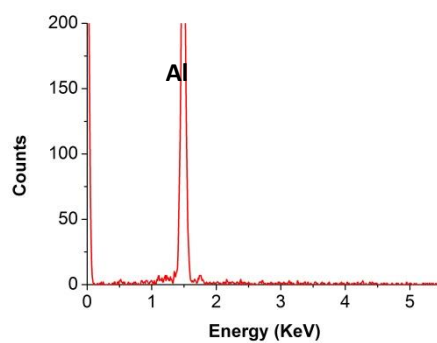
(e)

**Figure 4-127 (a) cross-section of the surface layer showing the Ti containing particle. (b)-(e) EDX spectrum of X1-X4.**
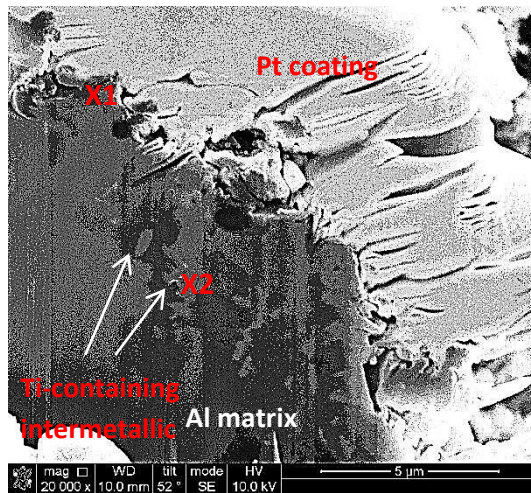
(a)
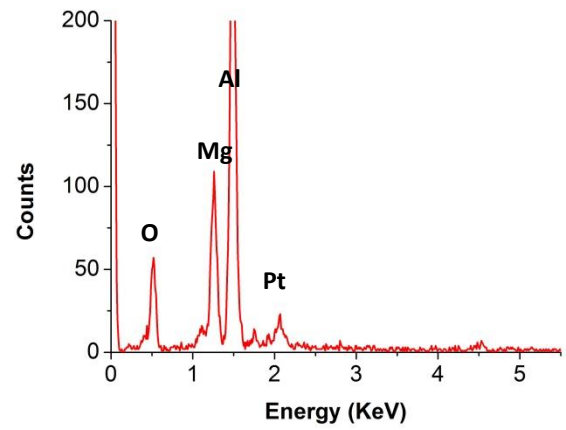


(b)
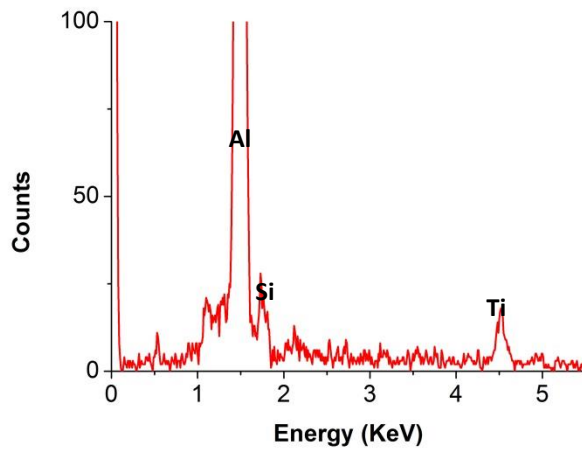


(c)

**Figure 4-128 (a)Cross-section of the surface layer showing the Ti containing intermetallic compound; (b)-(c) EDX spectrum X1 –X2.**
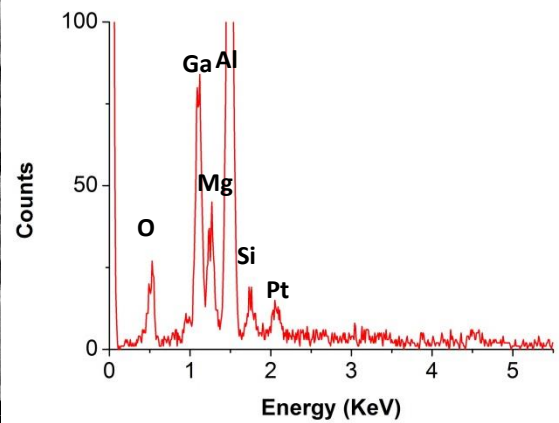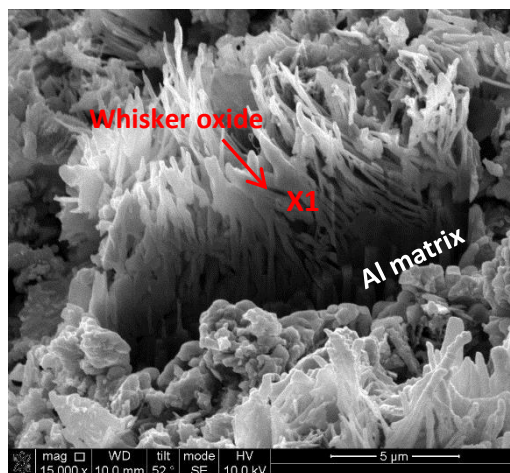




**Figure 4-129 EDX showing the cross-section of the whisker structured spinel.**

239

### 4.3.6 The effect of Mn addition into 2L99 casting

#### 4.3.6.1 Mechanical properties test

The aim of this work was to understand the effect of a Mn addition on double oxide film defects and the reproducibility of 2L99 castings.

3 moulds were cast to give 30 test bars. LECO$^{TM}$ Hydrogen content analysis suggested that the hydrogen content in the Mn containing castings was 0.106 ppm. The chemical composition of the 2L99+Mn casting was shown in Table 4-49. As can be seen, the H, Mg and Fe contents were all controlled within an acceptable range (H$\leq$0.2 ppm, Mg 0.3%$\pm$ 0.03%, Fe$\leq$0.1%).

The UTS and %Elongation of the test bars for the Mn addition into 2L99 are shown in Table 4-50. The Weibull plot of the UTS and %Elongation are shown in Figure 4-130 and Figure 4-131, respectively. The R$^2$ value for UTS and %Elongation were 97.2% and 92.6%, which suggested that both data sets can be accepted as Weibull distribution.

The comparison of the tensile test results between 2L99 and 2L99+Mn are shown in Table 4-51 and Table 4-52. As can be seen, the addition of Mn decreased the mean value and position parameter of the UTS by about 7%. The mean value and position parameter of the %Elongation was decreased by 58% and 47%, respectively. Statistically the effect of the addition of Mn did not significantly change the Weibull moduli of the 2L99 alloy, for both UTS and %Elongation.

**Table 4-48.  LECO hydrogen content analysis for Mn addition into 2L99.**

| casting | ppm H |
|---------|-------|
| 2L99+Mn | 0.106 |

**Table 4-49. XRF results for casting with 2L99 + Mn.**

| 2L99+Mn | |
|---------|---------------|
| Formula | Concentration |
| Al | 93.14% |
| Si | 11.08% |
| Mn | 0.59% |
| Mg | 0.32% |
| Ti | 0.13% |
| Fe | 0.07% |

**Table 4-50. Tensile test results for Mn addition into 2L99 casting.**

| 2L99+Mn | | | | | |
|---------|------|------------|-----|------|------------|
| | UTS | Elongation | | UTS | Elongation |
| No | MPa | % | No | MPa | % |
| 1 | 250 | 0.66 | 16 | 244 | 0.59 |
| 2 | 196 | 0.4 | 17 | 266 | 0.94 |
| 3 | 237 | 0.56 | 18 | 269 | 1.09 |
| 4 | 202 | 0.36 | 19 | 217 | 0.42 |
| 5 | 257 | 0.87 | 20 | 257 | 0.74 |
| 6 | 227 | 0.51 | 21 | 271 | 0.97 |
| 7 | 233 | 0.56 | 22 | 292 | 1.79 |
| 8 | 248 | 0.7 | 23 | 264 | 0.84 |
| 9 | 237 | 0.57 | 24 | 259 | 1.09 |
| 10 | 268 | 1.13 | 25 | 275 | 1.3 |
| 11 | 194 | 0.32 | 26 | 272 | 1.33 |
| 12 | 246 | 0.63 | 27 | 228 | 0.45 |
| 13 | 266 | 0.92 | 28 | 270 | 1.03 |
| 14 | 242 | 0.6 | 29 | 221 | 0.42 |
| 15 | 267 | 0.91 | 30 | | |
| average | 247.4 | 0.78 | | | |
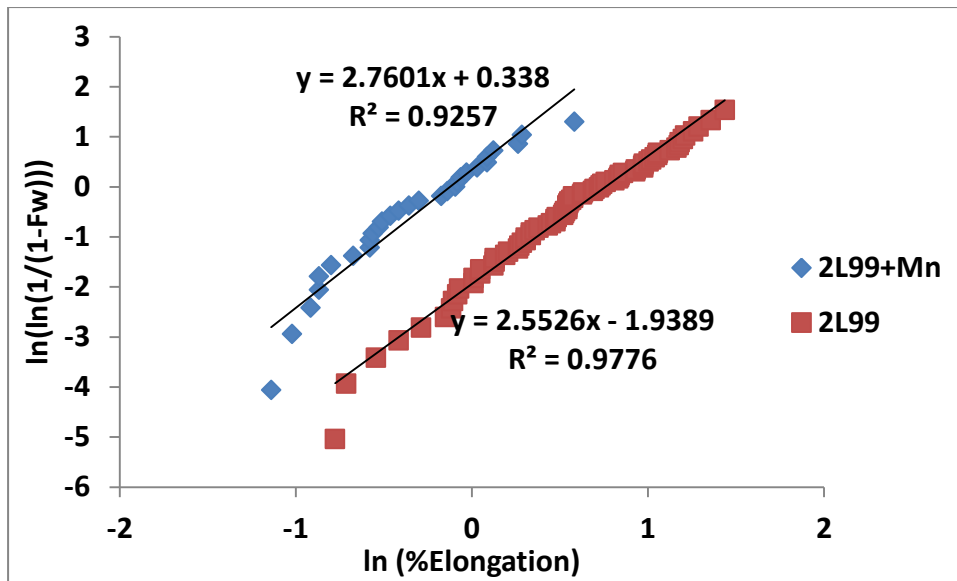
**Figure 4-130 Weibull plot of %Elongation of 2L99+Mn casting.**
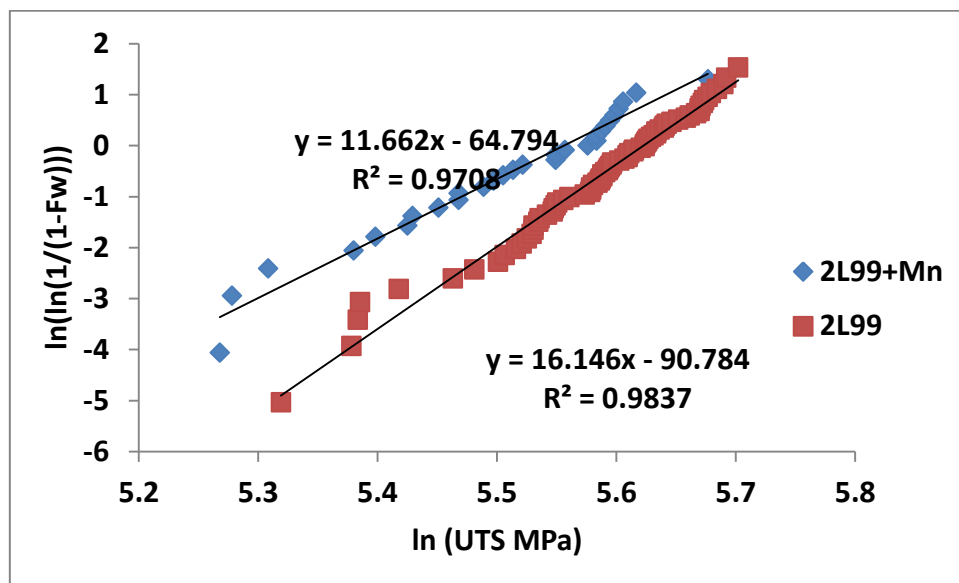


**Figure 4-131 Weibull plot of UTS of 2L99+Mn casting.**

**Table 4-51 The comparison of the tensile test results between 2L99 and 2L99+Mn.**

|  | mean value | | position parameter | | Weibull moduli | |
|---|---|---|---|---|---|---|
|  | UTS | %Elongation | UTS | %Elongation | UTS | %Elongation |
| 2L99 | 267.6 MPa | 1.9 | 276.6MPa | 2.13 | 16.1 | 2.55 |
| 2L99+Mn | 247.4MPa | 0.78 | 258.8MPa | 1.13 | 11.67 | 2.76 |

**Table 4-52 The comparison of the Weibull moduli between 2L99 and 2L99+Mn.**

|  | 2.5 and 97.5 percentile | m1/m2(UTS) | Significant difference in UTS? | m1/m2(%Elongation) | Significant difference in %Elongation |
|---|---|---|---|---|---|
| 2L99+Mn | 0.660,1.573 | 1.38 | No | 0.92 | No |

### 4.3.6.2 *SEM investigation of the fracture surface*

Figure 4-132 shows the fracture surface and an oxide layer in tensile test bar No. 18 which showed no sign of a Mn affected oxide film. A Mn-containing intermetallic phase was seen on the fracture surface (as seen in Figure 4-133). As can be seen, the intermetallic phase was present in a relatively large size (about 300 μm).
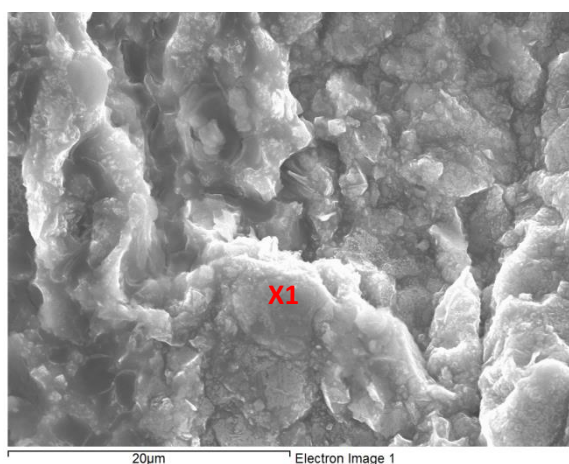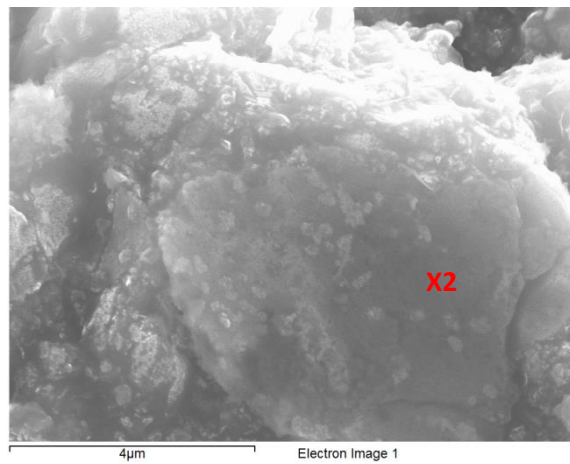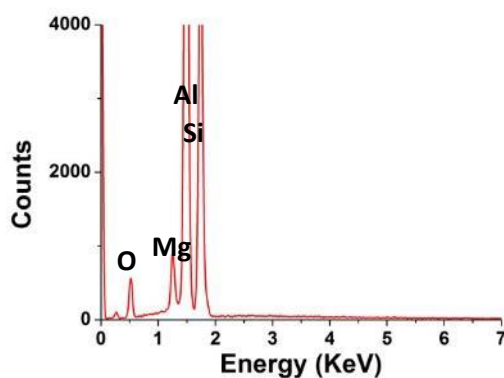
Figure 4-132. (a)-(b)Granular like oxide with different shapes were found on the sample surface with 2L99+Mn; (c) EDX spectrum of X1.
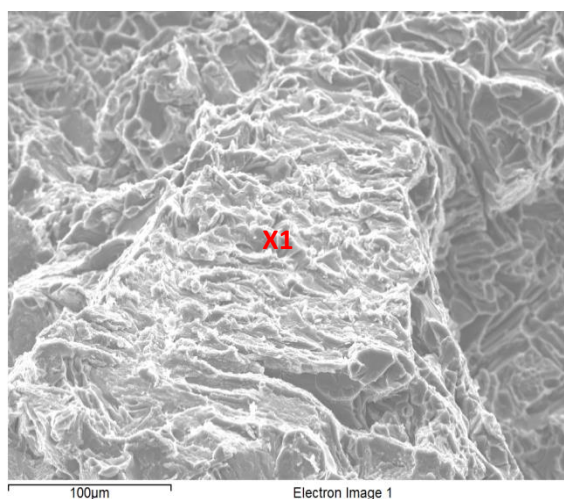




(a)
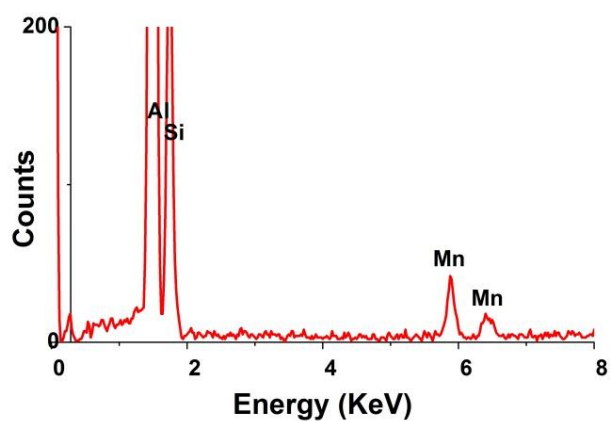
(b)

Figure 4-133. (a)Mn containing Intermetallic compound on the fracture surface of 2L99+Mn casting; (b) EDX spectrum of X1.

# Chapter 5   Discussion

## 5.1   The bubble trap experiment

### 5.1.1   The calculation of the change of the liquid metal enter the blind hole with different experimental condition

This work was aimed at understanding the change in size of an entrapped bubble, and predicting when nitride will occur on the sample surface of the experiments, (in the three different alloys).

The experiment involved three stages: In the first stage, the steel rod was inserted into the aluminium melt to a depth of 85mm. Before the insertion, the steel rod with a blind hole at one end was placed above the liquid aluminium to heat up the gas inside the blind hole, as well as heating up the steel rod. The gas inside the blind hole was heated up to around 400 °C (measured by a K-type thermocouple). After insertion, the entrapped gas increased its temperature to 730 °C, which resulted in an expansion. However, the entrapped bubble at a depth of 85 mm in the aluminium melt also experienced metallostatic pressure, which tended to reduce the bubble size. The pressure and volume of the gas trapped inside the blind hole satisfied the following equation:

$$p_0 v_0 / T_1 = p_1' v_1' / T \tag{43}$$

$$\frac{p_0 h_0 S}{T_1} = (p_0 + \rho g (H_1 - \Delta h)) * (h_0 - \Delta h) * S / T \tag{44}$$

$P_0$: the pressure of the air

$V_0$: the volume of the blind hole

$T_1$: the temperature of the air in the blind hole before insertion into the aluminium melt

$P_1'$: the pressure of the entrapped gas after the steel rod had been inserted into the aluminium melt

$V_1'$: the volume of the entrapped gas remaining after the initial expansion

T: the temperature of the aluminium melt

$h_0$: the height of the blind hole

S: the cross-section area of the blind hole

ρ: the density of the aluminium melt

g: the acceleration due to gravity

$H_1$: the depth in the aluminium melt to which the rod was entered

Δh: the change in height in the blind hole


We have:

$P_0$= 1*10$^5$ Pa

$h_0$=0.040m

h=0.085m

ρ=2.4 g/cm$^3$[154]

g=9.8 m/s$^2$

$T_1$=673K

T=1003K

Therefore, the equation (2) can be transformed into:

$$\frac{10^5 Pa * 40mm}{673K} = \frac{(10^5 Pa + (\frac{2400kg}{m^3}) * (9.8m/s^2) * (85mm - \Delta h)) * (40mm - \Delta h)}{1003K}$$


$$\Delta h = -0.018m$$

This means that, at this stage, the bubble trapped inside the aluminium melt expanded 18mm (45%) due to the increase in temperature from 400 °C to 730 °C. The excess gas in the entrapped bubble likely escaped from the blind hole and the height of the bubble inside the blind hole would be maintained at 40mm.

In the second stage, the liquid metal reacted with molten metal and formed an oxide. If 95% of the oxygen inside the blind hole was consumed before nitrogen reacted with the aluminium melt[155], then the size of the bubble would be:

$$\left(p_0 + \rho g H_1\right) * V_0 / \left(\left((P_0 + \rho g(H_1 - \Delta h)) * (V_0 - \Delta V)\right)\right) = nRT / 0.8005 nRT \quad （45）$$

Since:

$h_1$=40mm

n: mole number

R: gas constant 0.082 atm*L/mole*K

The equation (3) can be transformed into:

$$\frac{10^5 Pa + \left((2400 kg/m^3) * 85mm\right) * 40mm}{(10^5 Pa + (2400 kg/m^3) * (85mm - \Delta h) * (40mm - \Delta h)} = \frac{1}{0.8005}$$

Therefore :

$$\Delta h = 0.00792 m$$

This means that liquid metal entered 7.92 mm into the blind hole before the start of consumption of the nitrogen in the entrapped atmosphere.

In the third stage, the liquid metal solidified inside the crucible, which led to the shrinkage of the entrapped gas.

Suppose the temperature for complete solidification of the liquid metal for pure aluminium, 2L99 and Al-5Mg alloys were 660°C, 580°C and 580°C, respectively. The pressure and volume of the entrapped atmosphere caused by the shrinkage of the entrapped gas satisfies the following equation:

$$(P_0 + \rho g H_2) * \frac{h_2 * S}{T} = \left(P_0 + \rho g(H_2 - \Delta h)\right) * (h_2 - \Delta h) * S/(T_2, T_3) \quad （46）$$

$H_2$: the depth of the liquid metal in the blind hole before solidification

$h_2$: the depth of the entrapped air in the blind hole before solidification

$T_2$: the temperature of the liquid aluminium when commercial purity aluminium completely solidified

$T_3$: the temperature at which 2L99 and Al-5Mg solidified

Since:

$H_2$=0.07708 m

$h_3$=0.03208 m

Equation (4) can be transformed into:

$$\left(10^5\ Pa + \left(\frac{2400Kg}{m^3}\right) * \left(\frac{9.8m}{s^2}\right) * 77.08\ mm\right) * \frac{32.08\ mm}{1003K} = \left(10^5 Pa + \left(\frac{2400Kg}{m^3}\right) * \left(\frac{9.8m}{s^2}\right) * \right.$$

$$\left. (77.08\ mm - \Delta h)\right) * (32.08\ mm - \Delta h)/(T_2, T_3).$$

$$\Delta h_{CPAl} = 0.0025\ m$$

$$\Delta h_{2L99,CPAl-5Mg} = 0.0055 \, m$$

This suggested that the shrinkage of the entrapped gas during solidification caused a rise in height of 2.5 mm and 5.5 mm of the liquid metal entrapped inside the blind hole.

Therefore, for the commercial purity aluminium, the volume reductions of the entrapped atmosphere occurred in three stages of 0 mm, 7.9 mm and 2.5 mm respectively, which added up to a total of 10.5mm. This suggested that any nitride formed would not appear on the sample surface until the trapped metal inside the blind hole reached a height of 10.5 mm.

For 2L99 and Al-5Mg alloys, the volume reduction of the entrapped atmosphere during the three different stages was 0mm, 7.9 mm and 5.5 mm respectively, which added up to a total of 13.4 mm which suggested that any nitride should appear on the sample surface after this height was reduced.

The actual experimental data suggested that, for commercial purity aluminium and 2L99 alloy, nitride appeared on the sample surface with a sample height greater than 14 mm and 17 mm respectively, which suggested 33 % and 26.8 % more gas consumed, respectively, compared with the calculated values. This might be due to a leak path, which formed during the steel rod insertion into the aluminium melt, (i.e. a layer of oxide attaching to the side of the steel rod which connect the entrapped atmosphere to the outside environment).

Despite the fact that the leak path was interrupted mechanically by the rotation of the steel rod and the use of a separate steel rod to touch the side of the spinning rod, there was roughly a 40s delay between the steel rod insertion and the breaking of any leak path.

During this time, part of the entrapped atmosphere might escape through this leak path, reducing the volume of the entrapped atmosphere and causing the rise of the liquid metal.

Another possible reason is that the nitride formed at an early stage of the reaction and moved to the sides of the sample and was not seen on the sample top surface. The oxide which formed at the early stage, however, was raised to the top of the sample. Therefore, for those apparently nitride free sample surfaces, a small amount of nitride might already have formed but was not apparent on the sample surface.

## 5.1.2 The effect of different alloys on the formation of the oxide layer on the sample surface

In this experiment, three alloys were used, commercial purity aluminium, 2L99 (Al-7Si-0.35Mg) and Al-5Mg. Different types and structures of oxide are supposed to be formed with different alloying composition, which resulted in different consumption rates of the entrapped atmosphere.

### 5.1.2.1 The oxide layer on commercial pure aluminium

For commercial purity aluminium the oxide layer formed, which is the reactant between the pure aluminium melt and the entrapped atmosphere (mainly air), is likely to be $Al_2O_3$[3]. The PBR of $Al_2O_3$//Al is 1.26 which suggests a homogeneous and protective oxide layer[156]. Figure 5-1 suggested that the consumption of the entrapped gas for commercial purity aluminium is 20 % faster than that for 2L99 but 54 % slower than Al-5Mg alloy during the experiment.
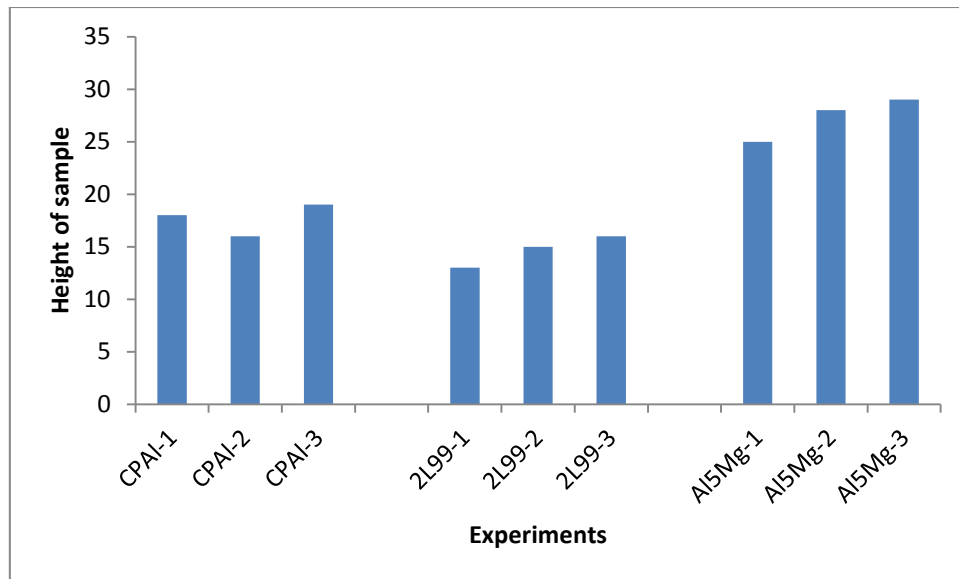
**Figure 5-1 The comparison of the sample height in the bubble trapping experiment in three different alloys**

Two forms of aluminium nitride were found on the sample surface with commercial purity aluminium (see Figure 4-3 and 4-4).This suggested that the partial pressure of oxygen was reduced and the reaction between the nitrogen and aluminium melt became possible, to form AlN. However, the complete consumption of the oxygen was not necessary for the nitride to begin to appear. Although Zheng et al.[87], suggested that a trace amount of oxygen (with partial pressure >$10^{-7}$ Pa) in the gas system might affect the formation of aluminium nitride (see section 2.3.1). Both Raeiszadeh[153] and El-sayed [92] observed nitride to have formed before the complete consumption of oxygen in the entrapped gas. In this work, oxygen peaks were detected by EDX on the nitride phase which suggested multiple surface layers which contained both oxide and nitride.

The feather like aluminium nitride, shown in Figure 4-3, was also observed by Raeiszadeh [153], which formed a permeable nitride layer. The permeability of the nitride layer offers an ideal pathway for the continuous reaction between liquid aluminium and the entrapped

atmosphere. It might also allow hydrogen to diffuse into and cause expansion of the entrapped atmosphere.

The other type of aluminium nitride observed, shown in Figure 4-4, produced a much smaller nitrogen peak, detected by EDX, which possibly formed at the early stage of nitride formation and did not have enough time to grow thicker before the solidification.

In the experiment with element additions into CP-Al, the presence of Ti tended to slow down the consumption rate of the entrapped atmosphere. Thermodynamic calculations in Appendix I suggested that of the Ti containing oxides, $Ti_3O_5$ and $Ti_4O_7$ could form preferentially compared with $Al_2O_3$. Those oxides could be formed at the initial stage of the experiment while the Ti content in the melt is still high (0.4%). The Pilling-Bedworth ratios of TiO, $TiO_2$, $Ti_3O_5$ and $Ti_4O_7$ are 1.04, 1.63/1.86, 1.24 and 1.44 respectively, which are all protective oxides. Impey [68] suggested that $Al_2O_3$, once formed, will transform from γ state to α state, which would introduce stress into the oxide layer and caused its rupture. This rupture will allow the liquid metal to react with the entrapped atmosphere so the reaction could be continuous. The Ti-containing oxides might not be able to experience the phase transformation as $Al_2O_3$, so there would be less rupturing of the oxide layer and the gas consumption rate would be reduced. However, at a later stage of the experiment, the negative pressure caused by the shrinkage of the entrapped atmosphere during solidification would draw the liquid metal upward, which may cause ruptures of the oxide. At this stage, the Ti concentration in the melt was reduced due to the formation and settling of Al-Ti intermetallic phase. Figure 5-2 is the ThermoCalc$^{TM}$ prediction of the Ti consumption for the formation of $Al_3Ti$ in Al-0.4 wt.%Ti. As can be seen, 32% Ti in the solution was consumed at 730 °C. However, as the temperature reduced to 664.9 °C, 70% of the Ti in the

solution was consumed. Those intermetallic phases formed might settled to the bottom of the liquid metal and concentration for Ti in the solution was reduced. The Ti-related oxide formed at a earlier stage might also contribute to the reduction of the Ti content. The oxide formed more preferentially is $Al_2O_3$ again.
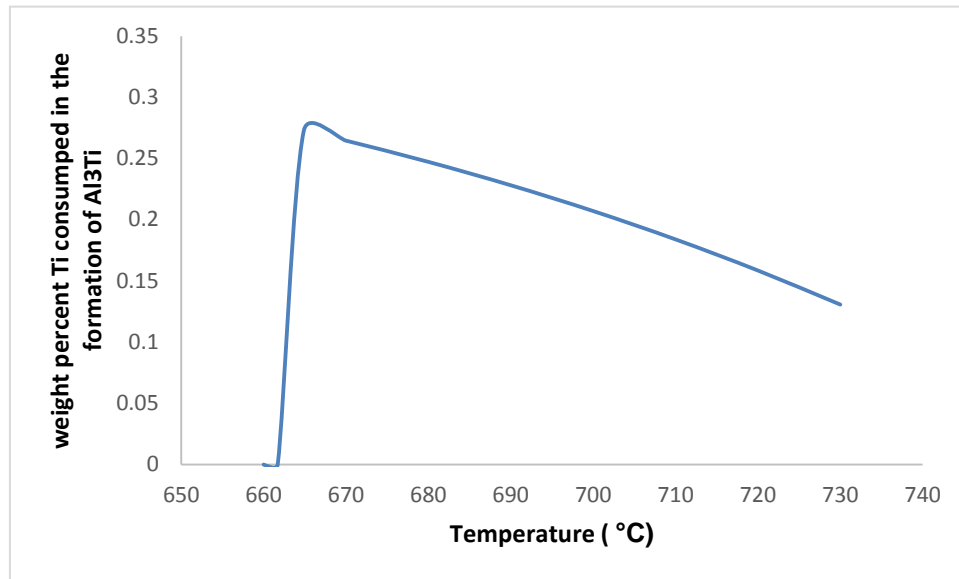


**Figure 5-2 The weight percent of Ti consumed in the formation of Al3Ti predicted by ThermoCalc in Al-0.4 wt.% Ti alloy.**

The results contradict Raeiszadeh[28], who showed that the addition of Ti did not change the consumption rate of the entrapped atmosphere of the blind hole. However, the author used a much smaller amount of Ti (0.1 wt.%) compared with this work (0.4 wt.%) and the amount might affect the formation of Ti containing-oxide in the aluminium melt.

For other element additions into CP-Al, little difference was found in terms of the oxide layer formed (16mm +/- 3mm), and the difference in the sample height could be due to experimental error, e.g. variation in the hydrogen content in the melt and the variability of the purity of the transition metal addition.

The addition of Mo tended to form a different type of oxide on the sample surface, which showed a nodule shape (see Figure 4-12). Salas et al.[77] also found a similar oxide in an Al-Mg oxide and the author suggested the nodule was formed by the liquid metal penetrating through the rupture points of the existing oxide and reacting with the atmosphere.

### 5.1.2.2 *The oxide layer on 2L99 alloy*

Silva [157]suggested that while the Mg content of an Al alloy is between 0.15-1.5 wt.%, the most favoured reactant between the aluminium melt and oxygen produces $MgAl_2O_4$. As the Mg content in 2L99 alloy is 0.35 wt.%, the oxide probably formed spinel ($MgAl_2O_4$). This is also confirmed by a number of researchers, who suggested that while the Mg content was small, the oxide formed would be spinel[73, 74].

The bubble trapping experiment suggested that the 2L99 alloy had the lowest consumption rate of the entrapped atmosphere. This could be due to the thickness of the oxide layer or its strength. Hinton[151] suggested that the thickness of the oxide layer on 2L99 alloy was twice as much as CPAl (0.35 μm) after holding the melt for 1h. The liquid metal, might take a longer time to penetrate this surface layer through microchannels in the oxide. In addition, thick oxide might suggest a higher strength of the surface film which adds to the difficulty for rupture of the oxide during the experiment. The PBR for $MgAl_2O_4$//Al is 1.15, which suggested a protective oxide layer might be formed.

For Ti-addition into 2L99, a porous structured Ti containing oxide was found on the sample surface. Such oxide was present in relatively small areas (with a size of 0.1-0.5 mm$^2$, and it constituted only 0.1%~0.4% of the whole sample surface area). A high Si, O and Ti content was detected by EDX (12%, 35% and 15%, respectively) but the Mg content was shown to be

stable at around 0.9 wt.% for the oxide area with or without Ti pickup. This might suggest that the Ti- containing oxide layer could constitute a mixture of both spinel and Ti-related oxide.

This Ti-containing oxide layer was shown to have a porous structure, which might be supposed to accelerate the consumption of the entrapped atmosphere; however the results suggested that the height of the liquid metal in the blind hole was not affected with the addition of Ti (see Figure 4-13). This might be due to only small areas of the Ti-containing oxide forming during the gas-metal reaction, which means that a Ti-containing oxide was not formed preferentially to spinel ($MgAl_2O_4$).

For the Mo addition into 2L99, sample height measurements suggested that 60% more gas was consumed compared with the experiment using 2L99 alloy only. This was also confirmed by SEM investigation which revealed a nitride on the surface layer (see Figure 4-31). This layer consisted of particles of about 500nm. The distribution of the particles was inhomogeneous rather than a continuous layer, and microchannel might exist between the particles to make it possible for the continuous nitration of the surface layer.

SEM investigation of the cross-section of the sample suggested that a number of Al-Si-Mo intermetallic phases were seen on the wetted side of the oxide film (the side in contact with the liquid metal). Some researchers [158, 159]suggested that, at the Al-rich corner of the Al-Si-Mo system a phase, $Mo(Al,Si)_2$, might be formed at a temperature of 850K-1100K. EDX analysis also suggested that the ratio Mo:(Si, Al) was roughly 0.5:1. (see Table 4-53, Mo:(Si,Al) was $0.498 \pm 0.008$:1). The intermetallic phase is likely to nucleate on the wetted sides of the surface oxide layer or bi-films in the melt as those consist of the majority solid in the melt at the temperature.

**Table 4-53 summary of the quantified EDX analysis of Mo containing intermetallic compound**

| | Concentration of Mo containing compound (at.) | | | |
|---|---|---|---|---|
| | Figure 4-70X1 | Figure 4-71 X2 | Figure 4-79 X1 | Figure 4-83 X2 |
| Al | 15.77 | 20.7 | 18.08 | 15.77 |
| Si | 47.65 | 46.15 | 48.94 | 50.3 |
| Mo | 31.13 | 33.15 | 32.98 | 33.84 |
| O | 5.45 | | | |

A number of researchers have confirmed that $MoSi_2$, when exposed to air at a low temperature (<1000 °C) is likely to experience 'pest' oxidization with Mo continuously reacting with oxygen to form Mo oxide, causing a rapid volume change of the intermetallic phase to break it into smaller pieces[160-162]. This is due to the fact that a protective $SiO_2$ layer, which is supposed to be formed at higher temperature and to cover the surface of the $MoSi_2$, will not be formed at a lower temperature due to the reduced activity of Si. However, with the addition of Al, $Mo(Si, Al)_2$ can become stabilized due to the high activity of Al in the $Mo(Si, Al)_2$ phase, which would migrate to the surface of the intermetallic phase and easily form a protective $Al_2O_3$[163-165]. If Mg is present in the area, a spinel might be formed.

Therefore, Al in the intermetallic structure (growing on the sides of the bi-film) might migrate to the upper surface (the surface in contact with the spinel layer) and react with oxygen supplied by the microchannels in the spinel layer. A layer of $Al_2O_3$ would then be formed between the intermetallic phase and the spinel layer which would introduce stress into the existing oxide and cause the oxide to rupture locally. As more intermetallic phase nucleated with the cooling of the liquid metal, more rupture points would be created and

more metal would then be able to react with the entrapped atmosphere and consume it. Large ruptures might even tear oxide film defects into smaller sizes.

For the experiment with Sc addition into 2L99, much more liquid metal rose up into the blind hole (which constituted 87.5% of the volume), compared to other element additions. Islands of oxide could still be seen on the sample surface (see Figure 4-22), which could come from the oxide formed in the previous stage, when the main reaction was between entrapped oxygen and liquid metal. The white spots, which contained a high Mg and oxygen content, are possibly spinel particles. Nitride particles were also observed forming a nitride layer. Microchannels might exist between the nitride particles to provide a chance for the reaction between the entrapped atmosphere and the liquid metal.

Sc peaks were detected with both oxide and nitride. Cross-section investigation (see Figure 4-25) suggested that Sc was present in three forms, Sc dissolved in the aluminium melt, the Al-Sc intermetallic compound ($ScAl_3$), which might nucleate on the sides of the sample surface and a Sc-containing oxide layer. The Sc containing oxide layer was found to be permeable (see Figure 4-28), which might allow the liquid metal to penetrate through the surface layer and accelerate the consumption of the entrapped atmosphere.

### 5.1.2.3  The oxide layer formed on Al-5Mg alloy

Al-5Mg had the highest sample depth among all three alloys, with nitride found in all the samples (see Figure 4-37, 4-42 and 4-43) which suggested that the majority of the oxygen in the entrapped atmosphere was depleted rapidly.

Figure 4-42 showed a smooth oxide layer, with a high Mg peak detected by EDX, which appeared ruptured, allowing newly formed nitride to grow on the existing oxide. A high Mg

peak detected could possibly be due to an oxide layer that contains more Mg, probably MgO. From a thermodynamic point of view [157], as shown in Equations 47 to 49, at a temperature of 725 °C, MgO, with a Gibbs Free Energy of -990.27 kJmol$^{-1}$ could be formed preferentially to MgAl$_2$O$_4$ (-924.5 kJ*mol$^{-1}$) and Al$_2$O$_3$ (-874.2 kJmol$^{-1}$). The Pilling-Bedworth ratio of MgO// liquid Al is 0.84 which suggested a porous, less protective oxide layer and suggests continuous thickening of the oxide layer with time.

$$2Mg(l) + O_2 = 2MgO(s)$$
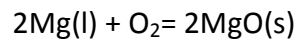
$$\Delta G^0 = -125126 - 2T*\log T + 225.3\ T\ Jmol^{-1} \quad\quad (47)$$

$$1/2Mg\ (l) + Al\ (l) + O_2\ (g) = 1/2\ MgAl_2O_4(s)$$
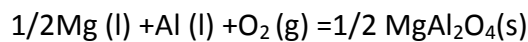
$$\Delta G^0 = -1169585 - 8.4T \log T + 245.6T\ Jmol^{-1} \quad\quad (48)$$

$$4/3\ Al\ (l) + O_2\ (g) = 2/3\ Al_2O_3$$
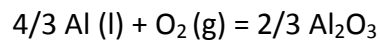
$$\Delta G^0 = -1130718 - 10.5\ T \log T + 257\ T\ J\ mol^{-1} \quad\quad (49)$$

Two forms of nitrides were observed on the sample surface: a feather-like nitride and a particle shaped-nitride (see Figure 4-37 and 4-39). The feather-like nitride resembled those found with commercial purity aluminium, and could be AlN. As the formation of Mg$_2$N$_3$ is less likely due to a much higher Gibbs Free Energy (-257.14 kJ mole$^{-1}$[153]) compared with AlN (-423.5 kJmole$^{-1}$[153]), the particle-like nitride could still be AlN but with a different morphology.

The experiments suggested that the addition of Ti, Zr and Mo have no effect on the formation of oxide. This might due to the fact that the Mg in the Al melt is so active that the other element additions have no chance to participate in the formation of an oxide.

## 5.2 The experiment to determine the position of the double oxide film defects by 4-point bend test

In a 4-point bend test, the sample with the bottom part placed under the maximum load appeared to have a higher mean value for the Ultimate Bend Strength, compared with the samples with their top part placed under the maximum load. A lower standard deviation was also seen for the former compared with the latter.

The Weibull analysis suggested that for the sample with the top part placed under the maximum load, a bi-modal distribution occurred, which might be caused by more than one type of defect, which according to Campbell [1], could be young oxide film defects and old oxide film defects. A young oxide film defect was formed during the liquid metal transfer or pouring process and an old oxide film type defect was formed in the previous melt and was carried into the current casting. The old oxide film defect is usually a thicker oxide film and the defect is larger in size, thus they cause a more detrimental effect on the mechanical properties, which lead to a low Weibull modulus of the casting.

For the sample with the bottom part placed under the maximum load, the high Weibull moduli, position parameter and the good curve fitting for the Weibull distribution suggested that, for the majority of the samples, there was a similar reason for the failure of the sample. This might be largely attributed to the limitation of the material itself.

The experiment suggested that oxide film defects are mainly concentrated at the upper part of the Bend test bars, due to floatation of the bi-film defect during casting. The result is

consistent with the finding from Raizadeh[155], who suggested that, with sufficient holding time in the liquid state double oxide film defects in the melt might float to the top surface, reducing the number of bi-film defects in the melt and improving the Weibull moduli of the casting. However, this floatation happened during the metal pouring and solidification process, which was about 60s, which suggested that floatation was quite rapid (with an average speed of 0.17mm/s).

## 5.3 The mechanical properties for different element additions into 2L99 alloy

### 5.3.1 2L99 castings without element addition

The results of the mechanical property tests suggested that precipitation heat-treatment doubled the mean value of UTS for 2L99 castings from 145 MPa to 271 MPa. The Weibull modulus of UTS of the tensile test bars was also increased, from 8 to 18.

For the results without heat-treatment, Bangykhan[11] did a similar experiment with A356 alloy, where the author kept the Fe content low, with a low H content and high oxide film defect content. The Weibull modulus of UTS was 7, which was consistent with results obtained here. For the results with T6 heat-treatment, a similar result was reached by Yang [166], who suggested that T6 heat-treated 2L99 castings had a Weibull moduli of 18.

SEM images suggested that the size and morphology of the oxide film defect was not changed under different casting conditions (see Figure 4-49), which suggested that the shift of the Weibull modulus by heat-treatment might simply be caused by an increase in the mean value of the UTS value. Tiryakioglu and Campbell [167] suggested that such shifts in the mean value could lead to an increase in the Weibull moduli.

The use of the roll-over technique was supposed to minimise the formation of shrinkage porosity in the solidified test bar. However, the results suggested that the roll-over did not significantly alter the mechanical properties of the 2L99 alloy castings. This work is also consistent with the results of Bangyikhan [11] who reached a similar conclusion when the roll-over device was used. However, Yang et al. [168] suggested in his modelling that, for the casting without rollover, the formation of micro-shrinkage inside the test bar is possible for the same mould used in this experiment, which might affect mechanical properties. The similar result for the castings with and without use of the roll-over, obtained in this work, suggested that the shrinkage porosity formed inside the test bar has a less detrimental effect on the 2L99 alloy casting compared with double oxide film defects.

For the 2L99 alloy without heat-treatment or roll over, the mean value of elongation was 1.55%. This number reduced to 1.39% when heat-treatment was used and increased to 1.90 when both heat-treatment and roll-over were used. The mean value of %Elongation was therefore variable which suggested a larger sample size was needed for clearer results.

A high magnification image of the spinel layer (Figure 4-51), observed  on the fracture surface of 2L99 castings, showed that there were some oxide particles (of size 500 nm) on the fracture surface. Smaller sized particles were also seen between the larger ones.  It is possible that these particles were formed by liquid metal penetrating through the existing oxide layer, and reacting with the entrapped atmosphere. It is also possible that more oxide particles grew on the surface with time which thickened the existing oxide layer.

Rupture of the oxide film defect might also occur when promoted the reaction between the entrapped gas and liquid melt. This rupture could be caused by:

(i) The non-uniform growth of the oxide particle, which might introduce stress to the oxide layer and lead to its rupture. The investigation of the cross-section of the tensile test bar (Figure 4-57) suggested that the thickness of the oxide layer in one bifilm defect varied from 50nm to a few hundred nm with newly formed particles growing on the un-wetted side. This variable thickness of the oxide layer could be the result of non-uniform growth of the oxide particles.

(ii) The nucleation and transformation of intermetallic phases growing on the wetted side of the oxide film, introducing stress, (e.g., Fe-containing intermetallic phases transform between $\beta$-AlFeSi to $\pi$-Al$_8$FeMg$_3$Si$_6$, and the Al-Si-Ti intermetallic phase, as mentioned earlier).

(iii) The Si phase growing on the wetted side of the bi-film defect and introducing extra stress [34].

(iv) The growth of aluminium dendrites meeting with a free floating-oxide film defect during solidification. The oxide film defect may then be suspended between the tips of the dendrite fronts, and the advance of the solidification front will introduce stress into the oxide layer.

However, for all the cases mentioned above, the consumption of the entrapped atmosphere may not be significant. Nitride was not discovered on the fracture surfaces examined, suggesting the bifilms were still in the oxygen consumption stage and there is possibly not much change in the size of the bi-film defect due to the consumption of the entrapped gas. The mechanical properties of the tensile test bar, in turn, would not be significantly affected.

### 5.3.2 The effect of a Mo addition into 2L99 on mechanical properties

Tensile test results from the Mo addition into the 2L99 alloy, suggested that, with a 0.4 wt.% Mo addition, an improvement in the Weibull moduli of the UTS occurred in all three casting conditions (casting without heat-treatment (156.2%), casting with a T6 heat-treatment (92.8%), casting with heat-treatment and roll over(110.0%)). The increase in the Weibull moduli was accompanied with an improvement in the mean value of the UTS and the %Elongation in all three cases, also. These experimental results suggested that the addition of Mo reduced the scatter of mechanical properties in 2L99 alloy and improved its reproducibility.

The fracture surfaces show both oxides and nitrides, which suggested that the entrapped nitrogen was also in the process of being consumed, after the oxygen. This suggested an accelerated consumption of the entrapped atmosphere.

#### 5.3.2.1 The effect of occurrence of Mo affected oxide on the fracture surface of 2L99 casting on tensile strength

15% of the fracture surfaces examined (3/20) from 2L99 +Mo were found to contain oxides with morphology or composition different from the oxide in the Mo free 2L99 castings.

A highly wrinkled oxide surface with a higher oxygen content was observed (Figure 4-70, (about 40 at.% compared to about 10 at.% in a "normal" oxide layer). This constituted typically about 5% of the whole fracture surface (see Figure 4-69) and was likely to be a factor leading to the facture of the test bar. No Mo peaks were detected, but an Al-Mo-Si intermetallic phase was observed perhaps nucleated on the sides of the oxide (Figure 4-70). (A possible role for the Al-Mo-Si phase was described in 5.1.2.2).

The oxide in Figure 4-74, which showed a Mo-peak in the EDX analysis of the oxide layer, with a surface area of about 0.1 mm$^2$, occupied about 0.2% of the fracture surface. The morphology of this defect suggested that they might be pores. Mo-containing oxide was detected on the internal wall of this pore, which suggested that this pore may have been an inflated double oxide film defect. The detection of Mo on the oxide suggested that Mo might participate in the oxide-forming reaction in some way.

### 5.3.2.2 *The effect of nitride occurring on the fracture surface on the tensile test bar*

15% of the fracture surfaces examined (3/20) in the 2L99+Mo casting were found to contain nitride, which suggested that the oxygen in the double oxide film defect might be largely consumed. Such a nitride was not found on fracture surfaces from the 2L99 alloy. The nitride on the fracture surfaces has been shown in Figure 4-77, 4-81 and 4-90, with areas of 5.6mm$^2$, 0.88mm$^2$, and 0.02mm$^2$, which accounted for 16%, 2.5% and 0.06% of the fracture surface respectively. In the first two samples a direct effect on mechanical properties was likely due to their large size, while the last one (Figure 4-90) was shown to be in the middle of a spinel layer, which might be a region where the nitride formed which resealed the rupture of the oxide layer.

SEM suggested that the nitride observed was of two forms, a tooth-like nitride (Figure 4-80 X1 and Figure 4-86 X1) and a particle nitride (Figure 4-87 X2 and Figure 4-93). The tooth-like nitride was also confirmed in Figure 4-97 to Figure 4-99 by TEM. The particulate aluminium nitride was also shown in Figure 4-94, after FIB milling, and Figure 4-101, by TEM. A cross-section of the fracture surface suggested that the nitride layer, (either particle or tooth-like morphology) were quite permeable, which probably was the reason for the accelerated consumption of the entrapped gas and the formation of nitride.

However, hydrogen in the aluminium melt might also penetrate through the oxide layer and inflate a bi-film defect. An increased hydrogen diffusion rate through a nitride layer (compared to an oxide layer) was observed by Gerrard and Griffiths[51]. As the Weibull moduli of the UTS of castings are quite sensitive to the size and orientation of double oxide film defects, a noticeable increase in the Weibull moduli for both UTS and %Elongation in 2L99 castings with the addition of Mo, suggested that the beneficial effect caused by increased consumption of entrapped atmosphere outweighed the drawback caused by inflation of the oxide film defect by hydrogen.

A whisker-like Al-Si phase was also observed, on Figure 4-86 and 4-97, located on the un-wetted side of an oxide layer. The formation of this phase can be described as follows:

While the oxide layer was ruptured locally and the size of the rupture was large, liquid metal might penetrate through the oxide layer at the rupture point and sit on the un-wetted side of the oxide film. The rupture point of the oxide layer might then be resealed by newly formed oxide/ nitride, and the entrapped liquid metal will react with the atmosphere which forms oxide/nitride on its surface. During this time, the entrapped liquid metal might solidify which precipitate needle shaped Si with Al surrounded.

Spinel phase on a nitride-containing fracture surface was observed in two forms: both particle shaped (fine (Figure 4-100) and coarse (Figure 4-89)) and also as whiskers (Figure 4-91, Figure 4-87 (b)). EDX and TEM analysis confirmed that these phases are possibly spinel. The whisker-spinel might be formed by evaporated Mg reacting with aluminium and entrapped oxygen, or formed by evaporated spinel deposited as a whisker structure. El-sayed [92] suggested that the nature resealing of the spinel layer, as described in 2.1.3, is an exothermic process, which could increase the local temperature to as high as 5000K. This

heat might provide head to the evaporation of Mg and spinel. However, the range for this heat generation was as localized as 2nm, which estimated by the author. This made it difficult for such a whisker to appear on fracture surface easily. However, for the Mo containing casting, a Mo containing intermetallic compound was observed nucleating on the sides of the double oxide film defect. Al in the $Mo(Si,Al)_2$ might migrate to the side near to the spinel layer and oxidised as described in 5.1.2.2. This oxidation process is also exothermic which could generate much more heat in a wider area (possible in μm) and this would be sufficient to provide heat for the formation of spinel in larger area.

As mentioned in Section 4.3.3, the nitride containing surface layer might contain a duplex oxide/nitride layer. Nitride particles, of size 1-2 μm, were seen growing on the Al matrix, which consist of the bottom surface layer. Spinel layer, with the morphology of particles or whiskers, was seen grew on the top of the nitride layer. This duplex surface layer was permeable and the thickness could vary from hundreds of nm to tens of μm.

One of the beneficial effects of the depletion of the entrapped atmosphere is that the unwetted oxide surfaces might have a chance to bond together, reducing the detrimental effect of the double oxide film defect [30]. Figure 4-88 shows a flat area, composed of aluminium. SEM examination suggested that this area was higher in position compared with other areas, which means that this area could be an area where bonding happened. Because of the consumption of the entrapped atmosphere, the distance between the two un-wetted oxide layers was gradually reduced, and finally contact occurred at several points.

### 5.3.2.3 The effect of Mo addition on the grain size of CPAl and 2L99 alloy

The experiment was conducted to see if Mo addition will affect the grain size of the CPAl and 2L99 alloy. It will also try to investigate if Mo conflicted with $TiB_2$ in achieving a desirable grain refining effect in Al alloys. With 0.4 wt.% Mo addition into commercial pure aluminium, a weak grain refinement effect was seen, with grains in the central part of the sample refined to 565 μm, compared to 2014 μm, consistent with the results from Mondolfo [147] who suggested that a Mo addition improves mechanical properties ( Young's modulus was Improved by 3% for every 1% of Mo addition) by slightly refining the grain size. Magdalena [150] also suggested that a 1% Mo addition into commercial pure aluminium led to the formation of a smaller sized equiaxed grains. There are several reasons how the refinement of grain size could occur:

1.      For a Mo addition into commercial pure aluminium, the calculated grain restriction factor (Q=m (k-1)) and supercooling parameter (P: m (k-1)/k)(see section 2.6)[169] are 7.5 and 3.0 respectively.  These numbers were much lower that the relative value with a Ti addition, so a weak grain refining effect can still be expected.

2.      The Al-Mo phase diagram suggested that the most stable intermetallic phase at this temperature could be $Al_{12}Mo$. Due to the fast cooling rate, a small amount of $Al_4Mo$ and $Al_5Mo$ intermetallic phase may still be expected. The calculated lattice mismatch (shown in Equation 13 [170].) for $Al_{12}Mo$//Al, $Al_4Mo$//Al, and $Al_5Mo$//Al are -81.28%, -87.01% and -97.08% respectively. When the lattice mismatch is within ±20%, it is supposed that the phase may act as a potent substrate for the nucleation of Al. All of the intermetallic phases formed here can serve as potent nucleation points, promoting the nucleation, although $Al_5Mo$ should be the most potent.

$$\delta = \frac{d_\beta - d_\alpha}{d_\alpha} \qquad\qquad （50）$$

δ: lattice mismatch

$d_\beta$: interplanar spacing for the phase

$d_\alpha$: interplanar spacing for the matrix

3.　　The process of the addition of Mo into commercial pure aluminium can introduce oxide inclusions into aluminium melt. The 15s stirring during the addition of the Al-10Mo alloy into the aluminium melt could add to the amount of oxide in the aluminium melt. According to Honiton[151], γ and α state alumina have a lattice mismatch of -6% and 17.54% respectively, which are all within ± 20%, which suggests that alumina can be a suitable site for the nucleation of aluminium grains and thus might have a grain refinement effect.

However, the results also suggested the addition of Mo had no effect on the grain size of 2L99, which might be due to the different intermetallic phases formed in the aluminium melt, which did not serve as a good substrate for nucleation of primary aluminium grains and eutectic grains.

### 5.3.2.4　Summary

The Mo addition increased the Weibull moduli of both the UTS and the %Elongation of 2L99 alloy.  Both oxide and nitride were found on test bar fracture surfaces, which suggested that the consumption of the entrapped atmosphere in a bifilm had been accelerated. This has been attributed to a permeable oxide/nitride layer being formed. The formation of Mo-

containing oxide and the role of intermetallic phases might also have changed the morphology of the oxide/nitride layer in the double oxide film defect.

### 5.3.3    The effect of modifier additions into 2L99 alloy

The addition of modifiers are supposed to modify the coarse, plate-like Si phase into a fine coral-like, or fibrous structure, which reduces the effect of brittle Si phase on the mechanical properties of Al-Si alloy.

2 set of castings were conducted, both high and low bifilm defect content. For the casting with low bi-film defect content, a redesigned mould was used, shown in Figure 3-3, with the aim of reducing the turbulence during the casting process. A 20 ppm filter was placed in the running system to filter out bifilm defects formed during the earlier stage of metal melting and pouring. It also slows down the velocity of the liquid metal entering the running system. The use of this mould in the casting will tend to have lower bifilm defects entering the casting compared with the castings with mould shown in Figure 3-2.

The mechanical property tests showed that the addition of the modifiers Ba, Sr and Na into the casting with a high oxide film defect content did not significantly improve the UTS or %Elongation of 2L99 alloy, as shown in Table 4-22. This is contradictory to previous research work, which suggested a significant improvement in %Elongation of the modified 2L99 alloy[171, 172]. However, with the reduced double oxide film defect, the 2L99 casting showed significant improvement in the mean value of %Elongation (4.51%) compared with the unmodified casting (1.88%).

For the casting with a high oxide film defect, the Ba addition did not significantly alter the mean value or the Weibull moduli of both UTS and %Elongation, as shown in Table 4-22 and

Figure 4-59, compared with corresponding results from 2L99 alloy. While the addition of Sr and Na showed a 10% decrease in the mean value of the UTS (decreased from 267.6MPa to around 250 MPa) and the Sr addition significantly decreased the Weibull moduli of the UTS statistically (from 16.1 to 8.8).

This reduction in the mechanical properties of the alloy could be attributed to the effect of high double oxide film defect content in the castings combined with modifier additions, which would reduce tensile properties, if this effect outweighed the beneficial effect from the modification addition.

Campbell and Green [173] suggested that for an Al-Si alloy modified by Sr, the Weibull modulus of the UTS was significantly improved from 19.7 to 37.7. The casting they used was bottom-filled with a 20 ppm filter with the aim to filter out the pre-formed bifilm defects and reduce the velocity of the liquid metal in the running system. In this work, for the castings with reduced oxide film defect, the same result was found which showed that the Weibull modulus of the UTS was improved from 22 to 42.

Previous researchers[101, 102] suggested that, with a modifier addition, the hydrogen content in the melt might be increased, either by the stirring process which would continuously break the surface film, removing the barrier for the passage of hydrogen into the liquid metal, or the modifier additions might change the continuous oxide layer into a permeable morphology which promoted hydrogen penetration [101, 102]. Campbell[34] further stated that the increased hydrogen content in the melt might result in more hydrogen diffusing into the entrapped atmosphere into the bi-film defects, expanding their size.

However, in this work, no permeable oxide layer was observed in the bi-film defects discovered on the fracture surfaces of the tensile test bars. EDX did not detect any modifier elements in the oxide film, which suggested that they were not affecting the oxide forming process, or the oxide affected by the modifiers were present in a small amount which was not detected on the fracture surface. In either case, the modifier addition would not introduce oxide films which would increase the hydrogen content in the melt. In addition, LECO hydrogen content analysis suggested that the hydrogen content for the casting with or without a modifier addition was not changed significantly (see Table 4-20).

The other type of defect discovered on the fracture surface was small sized porosity. SEM investigation suggested that this type of defect accounted for the failure of the test bar with good (No. 23) mechanical properties in a Sr-modified casting and both good (No. 11) and middle (No. 10) mechanical properties in a Na-modified casting. The internal walls of these pores showed aluminium dendrites, and no oxide was detected (see Figure 4-62 (e) and (f)). They could therefore be very small shrinkage, or hydrogen porosity. It is also possible that they are young oxide film defects, (with a very thin oxide thickness, with a short lifetime before solidification), but which were expanded by the hydrogen content in the melt.

Fuoco[105] suggested that the addition of modifiers reduced the mobility and feeding of the liquid metal during solidification. Campbell [34] suggested that without modifier additions, Si was likely to nucleate on a bi-film which would stretch the oxide film defect and restrain its movement. However with the addition of a modifier, this nucleation site may be poisoned. The free floating oxide will then more easily to trap hydrogen from the melt which would cause its expansion. They might also be suspended between the aluminium dendrites which affect the advancing of the solidification front. The liquid metal trapped

between the aluminium dendrites and bifilm defect will solidified isolated from the bulk liquid metal and thus creating shrinkage porosity locally or expand the existing oxide film defect.

Optical microscopy suggested that, with the addition of modifiers, the modification effect was not strong, which suggested that the effect of modification was reduced by the presence of double oxide film defects. SEM examination suggested that Ba- and Sr-containing intermetallic compounds nucleated on the sides of bifilm defects (see Figure 4-63 to 64). This reduces the effective concentration for Si modification.

### 5.3.4 The effect of Ti additions on the mechanical properties of 2L99 alloy

The Ti content added to the 2L99 castings in this work was up to 0.4 wt. %. To investigate its effect on double oxide film defects, compared with 2L99, (with 0.15 wt.% Ti content), tensile test results, (see Table 4-45), suggested that this addition caused a slight decrease in the mean value of UTS, but the %Elongation was decreased by about 30%. The statistical comparison (Table 4-47) suggested that increasing Ti to 0.4% had no effect on the Weibull moduli of both the UTS and %Elongation of 2L99.

The work here confirms the possibility of the formation of a Ti-related oxide, consistent with the thermodynamic calculation (see Appendix I). SEM investigation of a fracture surface of a 2L99+Ti test bar suggested the presence of Ti-containing oxide particles, which changed the morphology of the surface layer (see Figure 4-125). Spinel was present in the form of either particles or with a grass shaped morphology which formed a porous surface layer, This bi-film defect constitute 5% of the whole fracture surface which is likely to affect the mechanical properties of the tensile test bar.

However, only one of the samples (1/10) examined, contained an oxide like this. (Ti containing particles are also shown in Figure 4-127 and 124 with a size of 2um, however, there was only one such particle observed in the region). This suggested that the formation of a Ti-containing oxide was difficult and, might not be sufficient to affect the mechanical properties of the entire casting.

It was supposed that the slight decrease in the mean value of UTS (2.5%) was caused by an increase in an AlSiTi intermetallic compound, which had been observed by a number of authors [174, 175]. They were reported to be formed preferentially in a hypoeutectic Al-Si melt and holding at long time. These intermetallic phases are present with blocky or flake morphology, and size could be a few hundred μm, which might have a negative effect on the mechanical properties. The oxide introduced during the transition metal addition, and the old oxide films from the masteralloy, might combine to affect the mechanical properties of the casting.

### 5.3.5   The effect of Mn addition on the mechanical properties of 2L99 casting

Tensile test results suggested that the Mn addition decreased the mean value of the UTS by about 10%( from 267.6 MPa to 247.4 MPa), and the %Elongation by 50% ( from 1.9% to 0.78%). However, the comparison of the Weibull moduli for both UTS and %Elongation for 2L99 castings, with and without the addition of Mn suggested no significant difference existed, although the addition of Mn reduced the Weibull moduli from 16.1 to 11.7.

Fig. 4-133 showed a large Al-Mn-Si intermetallic phase, of size 300 μm, observed on the fracture surface. Warmuzek et al. [120], suggested that the addition of Mn resulted in the formation of a number of  intermetallic phases, namely $Al_6Mn$, $Mn_{12}Si_7Al_5$, in the Al-Si alloy.

As intermetallic phases are present of a relatively large size, the brittleness of these phases might cause a decrease in the mean UTS and %Elongation values. The amounts of intermetallic phase would increase with increased amount of Mn addition into the aluminium melt, and thus decrease UTS values.

Hwang et al. [176] suggested that Mn additions have an effect on the formation of Fe-rich intermetallic phases. He pointed out the optimum Mn:Fe ratio is 0.6. At this addition rate, the needle like β-Al-Fe-Si phase, which is supposed to be the main detrimental Fe-containing intermetallic phase, are mostly converted to α-Al-(Fe,Mn)-Si phase with Chinese-script morphology which is less detrimental to mechanical properties. As the Fe content in this work was about 0.1 wt.%, the addition rate for Mn was far above the 0.6 ratio. According to Hwang, the presence of excess Mn will lead to an iron-containing polyhedral phase which would have a negative effect on mechanical properties.

In summary, the presence of the Mn-containing intermetallic phase, and the oxide film defects introduced during the addition, may be the main causes for the reduction in mechanical properties of the castings.

### 5.3.6 The effect of W addition on the mechanical properties of 2L99 casting

Table 4-43 suggested that a W addition of 0.4% increased the mean value of UTS by about 10% (from 267.6 MPa to 288.8 MPa), and for %Elongation about 20% (from 1.9% to 2.26%). Analysis suggested a statistically significant improvement in the Weibull moduli of UTS compared with 2L99 alloy.

SEM examination, shown Figure 4-114 to 117, suggested that there was no significant difference in the composition of the double oxide film defects formed, however spinel

particles, of size 500nm-3μm, were commonly observed on the facture surface. It is possible that the oxide layer in the 2L99+W casting consisted of large amount of oxide particles with a nonuniform size.

A thin oxide film was discovered (200nm, see Figure 4-119) with W-containing particles (350nm) precipitated into the oxide formation, or nucleated on the oxide film. This oxide particle might play a part in the formation of a crack in the double oxide films.

W-containing intermetallic compounds, as shown in Figure 4-117 to 118, were seen growing on the sides of the bifilm defect. Like the Mo-containing intermetallic compound, a high Si peak was detected, suggesting $WSi_2$.

$WSi_2$ is quite dense (9.3g/cm$^3$) and these high-density intermetallic compounds might nucleate on the oxide film (as this accounts for the majority solid in the liquid solution), which might then result in the sinking of the oxide films, instead of their floating upwards. This might explain why the oxide observed in Figure 4-114X3 was quite small, even though it was associated with relatively poor mechanical properties. The reduced number of double oxide film defects could lead to improvements in mechanical properties of the casting. Such a settling phenomenon was also suggested by Cao and Campbell[177].

## 5.4  Summary

This research work was aimed at deactivating the double oxide film defect which formed inside the aluminium alloys by a transition elements addition method. The transition metal additions might affect the structure of an oxide layer in a double oxide film defect and might accelerate the consumption of the entrapped atmosphere in this defect and reduce its size in the casting component.

A bubble trap experiment was initially used to investigate the transition metal additions on the consumption of the internal atmosphere in a trapped bubble. It was discovered that the addition of Sc and Mo have accelerated the consumption of the entrapped atmosphere in the trapped bubble in Al-7Si-0.35Mg Alloy. Nitride was found on the sample surface of both cases while in the case of 2L99 without elements addition, no nitride was discovered.

Tensile test suggested that the addition of Mo and W has significantly improved the Weibull moduli of UTS. Nitride was found on the fracture surface of Mo containing test bar. SEM and EDX analysis have suggested that the surface layer contains a duplex oxide/nitride layer. A nitride layer which mainly consists of nitride particles was seen on the bottom layer while the spinel layer, which mainly consists of particles and whiskers, formed the top layer. This duplex layer is permeable which allows continues reaction of the entrapped atmosphere of the entrapped gas and the bulk liquid aluminium.

This effect was attributed to the intermetallic compound nucleation on the side of the bi-film defect. The oxidation of this intermetallic compound might introduce stress and heat on the spinel layer it nucleated which might crack or evaporate the oxide layer.

The improvement of W addition on Weibull moduli might be attributed to the W containing intermetallic, which nucleated on the sides of the bi-film and settled to the bottom of the casting due to the high density of this intermetallic compound.

Modifier additions were also found to have a negative effect on the mechanical properties when the bi-film defect content in the casting was too high. The modifier additions tend to aggravate the effect of double oxide film defect. However, when the bi-film defect content was low, the modifier addition tended to improve the mechanical properties significantly.

For Ti and Mn addition into 2L99, a negative effect was seen on the mechanical properties. This might due to the oxide film defect introduced during master alloy preparation and addition process or stirring process.

A four point bend test also confirms that the bi-film defect in the casting might be able to float upward to the top surface of the mould during the liquid metal transfer and solidification.

# Chapter 6 Conclusions

## 6.1 The bubble trapping experiment

This work compared the consumption rate of the entrapped atmosphere in three different alloys and with several element additions as an analogy of the consumption of the entrapped atmosphere in double oxide film defects.

In the bubble trapping experiment, commercial purity Al alloy showed a consumption rate of the entrapped atmosphere that was, between that for 2L99 alloy (20% smaller) and Al-5Mg alloy (55% greater). Addition of Ti reduced the consumption rate of the bubble in commercial purity aluminium alloy by 55%, and for the 2L99 alloy, Mo and Sc addition improved the consumption rate of the entrapped atmosphere by 33% and 133%, respectively. No element addition was found to affect the consumption rate of the entrapped atmosphere in Al-5Mg alloy.

SEM/EDX analysis of the sample surfaces suggested that 2 types of nitride were found on the sample surface of commercial purity aluminium, with either a granular or a feather-like morphology.

For the experiment with 2L99 alloy, small areas of Ti containing oxide ($0.1-0.3mm^2$) were found on the fracture surface of the 2L99+Ti alloy with porous morphology. However, this was not associated with an increased consumption rate of the entrapped atmosphere, which could be due to the area of the Ti containing oxide being too small to effectively change the consumption rate. Mo and Sc were found to change the morphology and composition of the oxide surface over large areas and a granular nitride occurred on both of the sample fracture surfaces.

For the Al-Mg alloy, both feather-like nitride and granular nitride were both observed. No element addition was found that affected the oxide/nitride composition or morphology.

The results from this work can only be a guideline as in the real casting process solidification times are usually much shorter, (around 60s for a sand casting), and the bifilm defect sizes are much smaller, compared to this work. Therefore it would be necessary to explore the effect of different elements additions on double oxide film defects and mechanical properties of the casting in real casting conditions, shown in the following experiments.

## 6.2   An experiment to determine the position of the double oxide film defects

Four point bend test result suggested that the testbars with their top surface placed under maximum load have a 25% lower mean value and 65.8% higher deviation of UBS (Ultimate Bend Strength), compared with testbars with their bottom surface under the maximum load. In addition, a bi-modal distribution was shown by the Weibull plot of the UBS for the testbars with their top part placed under the maximum load.

For the group of samples with the top surface placed under the maximum load, the low mean value and bi-modal distribution of UBS could be due to the presence of double oxide film defects which formed during the casting process and floated upwards to the top surface of the sample during the solidification process. Fracture surface analysis also confirmed that oxide film defects were found near the top surface.

This experiment confirmed the hypothesis that oxide film defect may float upwards to the surface in the aluminium melt during liquid metal transfer and solidification. This provides

another piece of evidence that holding the aluminium alloy melt for a period of time might allow the floatation of the oxide film defect and thus physically remove oxide film defect from the bulk liquid metal.

## 6.3 The effect of different element additions to 2L99 alloy on mechanical properties

### 6.3.1 The effect of different casting approaches

Tensile testing suggested that a T6 heat-treatment shifted the mean value of the UTS from 145 MPa to 271 MPa. The Weibull modulus of the UTS was also increased from 8 to 18. Statistical analysis suggested that the improvement was significant. However, the use of a roll-over device to reduce the formation of shrinkage porosity in the casting did not further improve the mean value or Weibull modulus of the UTS.

For %Elongation, a T6 heat-treatment reduced the mean value from 1.55% to 1.39%. This increased to 1.9% with the use of roll-over. The Weibull moduli of %Elongation of 2L99 alloy in three different casting conditions (without T6 heat-treatment, with T6 heat treatment; with both T6 heat-treatment and the use of the roll-over device) were 2.56, 3 and 2.55, respectively, which was shown to be not statistically significant. The variability of the results suggested that a larger sample size is needed to detect any difference.

A high magnification SEM image of an oxide layer of a double oxide film defect discovered on the fracture surface of 2L99 alloy suggested that the oxide layer was non-uniform in thickness, ranging from tens of nanometres to about 500 nm.

### 6.3.2 The effect modifier additions (Sr, Ba and Na) on the mechanical properties of 2L99 alloy

For castings with a high number of bifilm defects, a Ba addition did not affect the mechanical properties of the 2L99 alloy. The mean value of the UTS was unchanged but the %Elongation was decreased by 9 %. The Weibull moduli for UTS and %Elongation were not affected either. SEM images of the fracture surfaces suggested that, for the +Ba casting, the morphology of the oxide layer in the double oxide film defect was unchanged, (for 2L99 alloy). The Optical Microscopy image showed that the Si morphology was not modified with the Ba addition. It is possible that a higher Ba composition would be required to achieve a desirable modification effect.

Bimodal distributions of the mechanical properties were found in the case of Na additions into 2L99 with a high bifilm defect content. A decrease of 7% in the UTS and 15% in %Elongation of the mean value was seen. Statistical analysis suggested that no significant difference existed in the Weibull moduli of the UTS between 2L99 and 2L99+Na. Examination of fracture surfaces suggested that both porosity and bi-film defects were present on the fracture surfaces, which might be the reason for the bimodal distribution of the mechanical properties.

For Sr-modified 2L99 alloy, with a high bifilm defect content, a decrease of 49% in the Weibull moduli of the UTS was seen, which proved to be significantly lower compared with 2L99 alloy without modifier addition. The mean value of the UTS was 7% lower and the %Elongation was decreased by 5%, compared with 2L99 castings. Sr-containing intermetallic compounds were seen on the sides of the bifilm defects. However, for castings with low bifilm defect content, the addition of Sr significantly improved the Weibull modulus for both UTS and %Elongation. The mean value for %Elongation was also improved by 3 times.

The results therefore suggested that the positive effect of modifier additions on the mechanical properties of 2L99 alloy castings was not significant unless the bifilm defect content in the casting was low.

### 6.3.3 The effect of Mo additions on the mechanical properties of 2L99 alloy

With 0.4 wt.% Mo addition to 2L99 alloy, the Weibull moduli of the UTS for the unheat-treated castings, heat-treated castings and casting with heat-treatment and roll over, were improved by 156 %, 95 % and 110 % respectively, compared with the corresponding castings without Mo addition. The corresponding %Elongation was improved by 68 %, 33 % and 18 %, respectively. Statistical analysis suggested that the improvement in the Weibull moduli of the UTS in all three experimental conditions was statistically meaningful. For the %Elongation, only the improvement in the unheat-treated experimental condition was statistically meaningful, while in the case of the other two experimental conditions it was not statistically meaningful.

20% of the samples examined (3 out of 15) showed granular nitride occurring on the fracture surface of 2L99+Mo casting. The occurrence of nitride on the fracture surface is unique and suggested that the consumption of the internal atmosphere trapped in the double oxide film defect might have been accelerated, compared with Mo free casting. Majority of the entrapped oxygen might be consumed, and bonding between the un-wetted sides of the oxide film in the bifilm defect might even have occurred at a few points (one such bonding point was observed). The reduced volume of the double oxide film defect and the bonding effect should have had a beneficial effect on mechanical properties.

The SEM image of the cross-section of the bifilm defects suggested that, in a Mo containing casting, the thickness of the nitride layer on a fracture surface can be as thick as 13.6 μm, which was much thicker than an oxide layer detected in an oxide film defect in a 2L99 casting, which could range from 50nm to 500nm. The morphology of the nitride layer was permeable, which might allow the internal atmosphere to penetrate through the surface layer to more easily react with the surrounding liquid metal, and thus accelerate its consumption rate. This might reduce the size of the bifilm defect.

TEM analysis suggested that the nitride layer discovered on the fracture surface of a 2L99+Mo testbar consisted of a duplex layer. Nitride particles were seen at the bottom of the layer, and fine sized spinel particles or whiskers were seen at the top of the layer.

TP-1 tests suggested a slight grain refinement effect for the Mo addition in commercial purity Al and $TiB_2$-refined commercial purity Al. It was suggested that an intermetallic phase formed ($Al_4Mo$ or $Al_{12}Mo$) and that oxide inclusions introduced by the addition of the masteralloy, and from materalloy itself, served as a good substrate for the nucleation of Al grains. A grain restriction factor calculation for a Mo-containing Al melt also suggested a slight grain refinement effect in commercial purity Al. However, such a grain refinement effect was not seen in 2L99 alloy, which could be due to the fact that $Mo(Si,Al)_2$, the intermetallic phase formed in this alloy, is less favoured as a nucleation substrate for Al and Al-Si eutectic grains. This experiment also suggested that the Mo addition did not interfere with the addition of grain refiner and affect the grain refinement effect of $TiB_2$ in the alloy.

### 6.3.4   The effect W additions on the mechanical properties of 2L99 alloy

0.4 wt.% W addition into 2L99 alloy showed an increase of the Weibull moduli of the UTS by 91 %, and of the %Elongation by 13 %. Statistical analysis suggested a beneficial effect on the Weibull moduli of the UTS by the W addition. However, no statistically valid beneficial effect was concluded from the Weibull moduli of %Elongation. The mean value of the UTS and %Elongation for a W addition into 2L99 alloy showed a 10 % and 19 % increase, respectively.

A W-containing intermetallic phase was found on the sides of double oxide film defects. EDX analysis suggested that the W:(Si,Al) ratio was 1:2, which suggested $WSi_2$ but with Al in the lattice. $WSi_2$ is dense (9.2 g/cm$^3$) and may drag an attached oxide film to the bottom of the liquid metal, which would lead to a reduction in the detrimental effects of oxide film defects on casting properties.

### 6.3.5 The effect of Ti additions on the mechanical properties of 2L99 alloy

With 0.4 wt.% Ti addition to 2L99, the Weibull moduli of the UTS was decreased by 30% and for %Elongation was decreased by 17 %. However, statistical analysis suggested that there was insufficient data to statistically differentiate between the Weibull moduli of the two alloys, (2L99 with and without Ti). The mean value of tensile properties suggested that the Ti addition caused a 41% decrease in %Elongation and had no effect on UTS. It is supposed that the oxide film from the masteralloy and the stirring process during masteralloy addition, as well as the Ti-containing intermetallic phases present, decreased the mean value of %Elongation and caused an increase in the variation in mechanical properties.

Ti-containing particles were found occasionally on the fracture surfaces but their size was so small (2μm) that they probably did not affect mechanical properties. Large areas of Ti-

containing oxide were also found on just one sample. A porous oxide was occasionally observed, which suggested a beneficial effect on mechanical properties due to the consumption of interior atmosphere of the bifilms might occur. However, as only one sample, (out of ten examined), was found with such an oxide, the mechanical properties of the entire casting can hardly have been affected.

### 6.3.6    The effect of Mn additions on the mechanical properties of 2L99 alloy

The addition of Mn to 2L99 alloy led to a 28 % decrease in the Weibull moduli and a 9 % decrease in %Elongation. Statistical analysis suggested no difference between the two alloys (2L99 and 2L99+Mn) for the Weibull moduli of both the UTS and %Elongation. However, the mean value for the UTS and %Elongation was decreased by 8 %. It is suggested that this decrease was caused by the formation of large Mn-containing intermetallic phases and increased bifilm defect content in the casting due to the alloying addition. SEM analysis of the fracture surface suggested that the morphology and structure of the oxide layers were not changed, compared with 2L99 alloy without addition.

### 6.3.7    Summary

These experiments suggested that the addition of Mo and W significantly improved the Weibull moduli of the UTS for 2L99 alloy. For Mo containing castings, the structure of surface layers on the bifilm defects of some testbars are changed, with a nitride occurring on the surface. This suggested that the majority of the entrapped oxygen in the defect had been consumed which reduced the size of the defect and led to an associated improvement in mechanical properties. For W containing casting, dense W-containing intermetallic compound might nucleate on the sides of the bifilm defect and drag the attached oxide film

to the bottom of the liquid metal, which would also lead to a reduced effect of oxide film defects on casting properties.

For the modifier containing castings, an improvement on the Weibull moduli was only be achieved while the bifilm defect content in the casting was low. For castings with high bifilm defect content, the addition of the modifier was detrimental to mechanical properties.

No improvement on Weibull moduli of the UTS or %Elognation was achieved for Ti or Mn addition, which might be due to their weak effects on double oxide film defect. In addition, the formation of intermetallic compounds and more oxide film defects introduced during the alloy addition process, might have a negative effect on the mechanical properties of castings.

# Chapter 7   Future Work

1. In this work, the element addition and their effect on double oxide film defects has been demonstrated. However, this has been shown to be effective in sand cast alloys with a moderate cooling rate. This means that newly formed oxide film defects probably have about a one-minute life time before solidification. The effect of the element additions in castings with shorter cooling times, (e.g., in low pressure and high pressure die castings) or prolonged solidification time, (e.g., the use of a ceramic mould), remain unknown and need to be further investigated.

2. A changed mould design and a different morphology of the casting, (e.g., a thin-walled section casting), might affect the behaviour of the double oxide film defects in the castings, (with less flexibility and less orientation option of the castings). The effect of the transition metal additions on double oxide film defects, (which would be reflected in mechanical properties), might also be affected.

3. The amount of elemental additions used in this work (0.4 wt.%) might not be at the optimal to deactivate double oxide film defects in Al alloy castings. More casting work is required for the optimum addition rate to be established. Mo and W addition was found, in this work, to improve the Weibull moduli of UTS. However, these elements might form intermetallic compounds which impair the mechanical properties of a casting. To find the balance point between these two effects, it would be necessary to explore the effect of the elements additions at lower concentrations compared to those used in this work (i.e., 0.05 wt.%-0.4 wt.%).

4. More experimental work is needed to explore possibly cheaper and more effective alternatives which can be used commercially in industry. For instance, Cr, which is in

the same main group in the Periodic Table as Mo and W, but with a cheaper price, is worth exploring. In addition, Sc was found to significantly increase the consumption rate of the entrapped atmosphere in the bubble trapping experiment and this transition element addition could also be investigated in more detail. Sc is an expensive element to be added into aluminium melt. However, if this element addition could alleviate the detrimental effect of double oxide film defects on mechanical properties at a relatively low concentration of addition, it could still be of commercial value. This will be related to a significant decrease in the safety factor that is applied to a casting during component design, which might be a more economic option for industry.

5. Hypotheses for the effects of the $Mo(Si,Al)_2$, and $W(Si,Mo)_2$ on double oxide film defects has been suggested. However more thermodynamic and TEM evidence is needed for the prediction of the lifetime and stability of these intermetallic phases during casting.

# Reference

1.      Campbell, J., *Castings*. 2001, Elsevier.

2.      Fox, S and Campbell, J*., Visualisation of Oxide Film Defects During Solidification of Aluminium Alloys.* Scripta Mater., 2000. **43**(10): p. 881-886.

3.      Sleppy, W.C., *Oxidation of Molten High‐purity Aluminum in Dry Oxygen.* J. Electrochem. Soc., 1961. **108**(12): p. 1097-1102.

4.      J. Runyoro, S.M.A. Boutorati, and J. Campbell, *Critical Gate Velocities for Film-Forming Casting alloys: a Basic for Process Specification.* AFS Trans., 1992(37): p. 225-234.

5.      Griffiths, W.D. and N.-W. Lai, *Double Oxide Film Defects in Cast Magnesium Alloy.* Metallurgical and Materials Transactions A, 2007. **38**(1): p. 190-196.

6.      Dispinar, D. and J. Campbell, *Supercooling of metal in fine filters.* Journal of Materials Science, 2007. **42**(24): p. 10296-10298.

7.      Lai, N.-W., *Critical Ingate Velocity in Mg and Al alloy*. 2004, PhD thesis, School of Metallurgy and Materials, University of Birmingham: Birmingham.

8.      Campbell, J., *Chapter 2 - Entrainment*, in *Complete Casting Handbook*. 2011, Butterworth-Heinemann: Oxford. p. 19-103.

9.      Cao, X. and J. Campbell, *Oxide Inclusion Defects in Al-Si-Mg Cast Alloy.* Canadian Metallurgical Quarterly, 2005. **44**(4): p. 435-448.

10.     Divandari, M. and J. Campbell, *Oxide film characteristics of Al–7Si–Mg alloy in dynamic conditions in casting.* International Journal of Cast Metals Research, 2004. **17**(3): p. 182-187.

11.     Bangyikhan, K., *Effects of oxide film, Fe-rich phase, porosity and their interactions on tensile properties of cast Al-Si-Mg alloys*, in *Metallurgy and Materials*. 2005, University of Birmingham.

12.     Divandari, M. and J. Campbell, *Morphology of oxide films of Al–5Mg alloy in dynamic conditions in casting.* International Journal of Cast Metals Research, 2005. **18**(3): p. 187-192.

13.     Halvaee, A.C., J. Campbell, *Critical mold entry velocity for aluminiumn bronze casting.* AFS Trans., 1997(105): p. 35-46.

14.     Byczynski, G.E., *The strength and fatigue performance of 319 aluminium alloy castings / by Glenn Edwin Byczynski*. 2002, Thesis (Ph.D) - University of Birmingham, School of Metallurgy and Materials, Faculty of Engineering : Birmingham.

15.     Griffiths, W.D. and N.W. Lai, *Double Oxide Film Defects in Cast Magnesium Alloy.* Metallurgical and Materials Transactions A, 2007. **38**(1): p. 190-196.

16.     Wang, L., Rhee, H., Felicelli, S., Sabau, A., Berry, J., *Oxide Film and Porosity Defects in Magnesium Alloy AZ91*. in *Shape Casting: The 3rd International Symposium, eds. J. Campbell, PN Crepeau and M. Tiryakioglu, TMS, Warrendale, PA*. 2009.

17.     Mirak, A.R., Divandari, M., Boutorabi, SMA and Campbell, J., *Oxide film characteristics of AZ91 magnesium alloy in casting conditions.* International Journal of Cast Metals Research, 2007. **20**(4): p. 215-220.

18.     Campbell, J. and M. Tiryakioğlu, *Bifilm Defects in Ni-Based Alloy Castings.* Metallurgical and Materials Transactions B, 2012. **43**(4): p. 902-914.

19.     Divandarilr, M. and J. Campbell, *A New Technique for the Study of Aluminum Oxide Films.*

20.     Divandari, M. and J. Campbell, *Mechanisms of bubble trail formation in castings.* Trans. AFS, 2001. **109**: p. 433-442.

21.     Cox, M., Wichins, M., Kuang, J.P., Harding, R.A. and Campbell, J., *Effect of top and bottom filling on reliability of investment castings in Al, Fe, and Ni based alloys.* Materials Science and Technology, 2000. **16**(11-12): p. 1445-1452.

22.     Dai, X., Yang, X., Campbell, J., and Wood, J., *Effects of runner system design on the mechanical strength of Al–7Si–Mg alloy castings.* Materials Science and Engineering: A, 2003. **354**(1–2): p. 315-325.

23.     Aubrey, L.S.S., Schmahl, J. R. and Cummings, M.A., *Application of Advanced Reticulated Ceramic Foam Filter Technology to Prodice Clean Steel Castings.* AFS Trans., 1993(101): p. 59-69.

24.     Sirrell, B.C., J. Campbell, *Mechanism of filtration in reduction of casting defects due to surface turbulence during mould filling.* AFS Trans., 1990(105): p. 645-654.

25.     J. Bäckman, I.L. Svensson, and Y. Maeda, *Influence of filter on the mould filling of aluminium melts in vacuum-sealded moulds.* 1999.

26.     A. Ardekhani and R. Raiszadeh, *Removal of Double Oxide Film Defects by Ceramic Foam Filters.* Journal of Materials Engineering and Performance, 2012. **21**(7): p. 1352-1362.

27.     Nyahumwa, C., Green, N.R., Campbell, J., *Effect of mold-filling turbulence on fatigue properties of cast aluminum alloys*. Transactions of the American Foundrymen's Society, Vol 106. Vol. 106. 1998, Des Plaines: Amer Foundrymens Soc. 215-223.

28.     Raeiszadeh, R., *A Method to Study the Behaviour of Double Oxide Film Defects in Aluminium Alloy.* PhD Thesis, 2005, School of Metallurgy and Materials, University of Birmingham.

29.     El-Sayed, M., *Double Oxide Film Defects and Mechanical Properties in Aluminium Alloys*. PhD thesis, 2012, School of Metallurgy and Materials, University of Birmingham.

30.     Aryafar, M., R. Raiszadeh, and A. Shalbafzadeh, *Healing of double oxide film defects in A356 aluminium melt.* Journal of Materials Science, 2010. **45**(11): p. 3041-3051.

31.    Amirinejhad, S., R. Raiszadeh, and H. Doostmohammadi, *Study of double oxide film defect behaviour in liquid Al–Mg alloys.* International Journal of Cast Metals Research, 2013. **26**(6): p. 330-338.

32.    Najafzadeh Bakhtiarani, F. and R. Raiszadeh, *The behaviour of double oxide film defects in Al–4.5 wt% Mg melt.* Journal of Materials Science, 2011. **46**(5): p. 1305-1315.

33.    T.C. Totemeier, W.F. Gale, *Smithells Metals Reference Book*.(8$^{th}$ Ed.) 1999, Butterworth-Heinemann: Oxford.

34.    Campbell, J. and M. Tiryakioğlu, *Review of effect of P and Sr on modification and porosity development in Al–Si alloys.* Materials Science and Technology, 2010. **26**(3): p. 262-268.

35.    Dahle, A.K., Nogita, K., McDonald, S.D., Dinnis, C., Lu, L., *Eutectic modification and microstructure development in Al–Si Alloys.* Materials Science and Engineering: A, 2005. **413–414**: p. 243-248.

36.    Cao, X., *Heat treatment of liquid metal: precipitation and sedimentation processing of liquid Al-11.5 Si-0.4 Mg alloy*. PhD thesis, 2001, School of Metallurgy and Materials, University of Birmingham.

37.    Lu, L. and A.K. Dahle, *Iron-rich intermetallic phases and their role in casting defect formation in hypoeutectic Al–Si alloys.* Metallurgical and Materials Transactions A, 2005. **36**(13): p. 819-835.

38.    Cao, X. and J. Campbell, *The nucleation of Fe-Rich phases on oxide films in Al-11.5Si-0.4Mg cast alloys.* Metallurgical and Materials Transactions A, 2003. **34**(7): p. 1409-1420.

39.    Cao, X. and J. Campbell, *The solidification characteristics of Fe-rich intermetallics in Al-11.5Si-0.4Mg cast alloys.* Metallurgical and Materials Transactions A, 2004. **35**(5): p. 1425-1435.

40.    Cao, X. and J. Campbell, *Morphology of βAl$_5$FeSi Phase in Al-Si Cast Alloys.* Materials Transation, 2006. **47**(5): p. 1303-1312.

41.    Backenrud, L., E. Krol, and J. Tamminem, *Solidification Characteristics of Aluminium Alloys*, in *AFS*. 1990, Volume. p. 71-84.

42.    D.E.J.Talbot, *Effect of Hydrogen in Aluminium, Magnesium, Copper and their alloys.* International Metallurgical Review, 1975(20): p. 166-184.

43.    Talbot, D.E.J., *Effects of Hydrogen in Aluminium and its Alloys*. 2004, Maney Publishing for IOM3, the Institute of Materials, Minerals and Mining.

44.    Jakse, N. and A. Pasturel, *The hydrogen diffusion in liquid aluminum alloys from ab initio molecular dynamics.* The Journal of Chemical Physics, 2014. **141**(9): p. 094504.

45.    Ransley, C. and H. Neufeld, *The solubility of hydrogen in liquid and solid aluminium.* Journal of the Institute of Metals, 1948. **74**(12): p. 599-620.

46.    Zhou, J., Shivkumar., and Apelian, D., *Modeling of microstructure evolution and microporosity formation in cast aluminium alloys.* AFS Trans., 1990. **98**: p. 871-878.

47.     Elsayed, M.A., Griffiths, W.D., *Hydrogen, bifilms and mechanical properties of Al castings.* International Journal of Cast Metals Research, 2014. **27**(5): p. 282-287.

48.     Atwood, R.C., Sridhar, S., Zhang, W., Lee, P.D., *Diffusion-controlled growth of hydrogen pores in aluminium–silicon castings: in situ observation and modelling.* Acta Materialia, 2000. **48**(2): p. 405-417.

49.     Fisher, J.C., *The Fracture of Liquids.* Journal of Applied Physics, 1948. **19**(11): p. 1062-1067.

50.     Weigel, J. and E. Fromm, *Determination of hydrogen absorption and desorption processes in aluminum melts by continuous hydrogen activity measurements.* Metallurgical Transactions B, 1990. **21**(5): p. 855-860.

51.     Gerrard, A.J. and W.D. Griffiths, *The Formation of Hydrogen Related Porosity by Double Oxide Film Defects in Al Alloys*, in *Shape Casting: 5th International Symposium 2014*. 2014, John Wiley & Sons, Inc. p. 269-276.

52.     Weibull, W., *A Statistical Distribution Function of Wide Application.* Journal of Applied Mechanics-Transactions of the Asme, 1951. **18**(3): p. 293-297.

53.     Hallinan, A.J., *A review of the Weibull distribution.* Journal of Quality Technology, 1993. **25**(2): p. 85-93.

54.     Campbell, J., *Chapter 9 - Properties of castings*, in *Complete Casting Handbook*, J. Campbell, Editor. 2011, Butterworth-Heinemann: Oxford. p. 499-597.

55.     Green, N.R. and J. Campbell, *Statistical distributions of fracture strengths of cast Al₇SiMg alloy.* Materials Science and Engineering: A, 1993. **173**(1): p. 261-266.

56.     Sullivan, J.D. and P.H. Lauzon, *Experimental probability estimators for Weibull plots.* Journal of Materials Science Letters, 1986. **5**(12): p. 1245-1247.

57.     Lawless, J.F., *Statistical models and methods for lifetime data*. Vol. 362. 2011: John Wiley & Sons.

58.     Kromp, A.K., *Statistical properties of Weibull estimators.* J. Materials Science, 1991. **26**: p. 6741-6752.

59.     Tiryakioğlu, M. and D. Hudak, *Unbiased estimates of the Weibull parameters by the linear regression method.* Journal of Materials Science, 2008. **43**(6): p. 1914-1919.

60.     Tiryakioğlu, M., D. Hudak, and G. Ökten, *On evaluating Weibull fits to mechanical testing data.* Materials Science and Engineering: A, 2009. **527**(1–2): p. 397-399.

61.     Tiryakioğlu, M., *Weibull Analysis of Mechanical Data for Castings II: Weibull Mixtures and Their Interpretation.* Metallurgical and Materials Transactions A, 2015. **46**(1): p. 270-280.

62.     Nayhumwa, C., N. Green, and J. Campbell, *Influence of casting technique and hot isostatic pressing on the fatigue of an Al-7Si-Mg alloy.* Metallurgical and Materials Transactions A, 2001. **32**(2): p. 349-358.

63. Cox, M., Wickins, M., Kuang, J.P., Harding, R.A., and Campbell, J. , *Effect of top and bottom filling on reliability of investment castings in Al, Fe and Ni based alloys.* Materials Science and Technology, 2000. **16**: p. 1445-1452.

64. Hudak, D. and M. Tiryakioğlu, *On comparing the shape parameters of two Weibull distributions.* Materials Science and Engineering: A, 2011. **528**(27): p. 8028-8030.

65. Fuoco, R., Correa, E.R., *Characterization of Some Types of Oxide Inclusions in Aluminum Alloy Castings (99-85).* AFS Trans., 1999: p. 287-294.

66. Impey, S., D. Stephenson, and J. Nicholls. *The influence of surface preparation and pretreatments on the oxidation of liquid aluminum and aluminum magnesium alloys*. in *Proc. 2nd Int. Conf. on the Microscopy of Oxidation, Selwyn College, The University of Cambridge*. 1993.

67. Wightman, G. and D. Fray, *The dynamic oxidation of aluminum and its alloys.* Metallurgical Transactions B, 1983. **14**(4): p. 625-631.

68. Impey, S.A., D.J. Stephenson, and J.R. Nicholls, *Mechanism of scale growth on liquid aluminium.* Materials Science and Technology, 1988. **4**(12): p. 1126-1132.

69. S. Impey, D.J. Stephenson and J.R. Nicholls, *A Study of the Effect of Magnisium Additions on The Oxide Growth Morphologies on Liquid Aluminium Alloys,* in *Int. Conf. on the microscopy of oxidation*. 1990: University of Cambridge. p. 238-244.

70. Cochran, C.N., D.L. Belitskus, and D.L. Kinosz, *Oxidation of aluminum-magnesium melts in air, oxygen, flue gas, and carbon dioxide.* Metallurgical Transactions B. **8**(1): p. 323-332.

71. Silva, M. and D. Talbot, *Oxidation of liquid aluminum–magnesium alloys.* Essential Readings in Light Metals, Cast Shop for Aluminum Production, 2013. **3**: p. 137.

72. SILVA, M.P., Oxidation of Aluminium -Magnisium Alloys at Elevated Temperature in the Solid, Semi-Liquid and Liquid States, PhD thesis, Department of Technology, 1987, Brunel.

73. Belitskus, D.L., *Effect of $H_3BO_3$, $BCl_3$, and $BF_3$ pretreatments on oxidation of molten Al-Mg alloys in air.* Oxidation of Metals. **8**(5): p. 303-307.

74. Haginoya, I. and T. Fukusako, *Oxidation of Molten Al-Mg Alloys.* Transactions of the Japan Institute of Metals, 1983. **24**(9): p. 613-619.

75. Field, D.J., G.M. Scamans, and E.P. Butler, *The high temperature oxidation of Al-4.2 Wt Pct. Mg alloy.* Metallurgical Transactions A, 2013. **18**(3): p. 463-472.

76. S. Impey, D.J. Stephen, and J.R. Nicholls, *A study of the Effect of Magnisium Additions on the Oxide Growth Morphologies on Liquid Aluminium Alloys*, in *Int. Conf. on Microscopy of Oxidation*. 1990: Univ. Cambridge. p. 238-244.

77. Salas, O., Ni, H., Jayaram, V., Vlach, K. C., Levi, C. G.,*Nucleation and growth of $Al_2O_3$/metal composites by oxidation of aluminum alloys.* Journal of Materials Research, 1991. **6**(09): p. 1964-1981.

78.     K. H. Kim, N. R. Green, W. D. Griffiths, *Focused Ion Beam Milling and Imaging: An Advanced Method to Detect Fine Inclusions in Cast Aluminium Alloys.* Materials Science Forum, 2013. **765**: p. 150-154.

79.     Kim, K., *Detection of a Layer of $Al_2O_3$ at the Interface of $Al/MgAl_2O_4$ by High-Resolution Observation Using Dual-Beam FIB and TEM.* Metallography, Microstructure, and Analysis, 2014. **3**(3): p. 233-237.

80.     Kim, K., *Formation of endogenous MgO and $MgAl_2O_4$ particles and their possibility of acting as substrate for heterogeneous nucleation of aluminum grains.* Surface and Interface Analysis, 2015. **47**(4): p. 429-438.

81.     Zheng, Q., B. Wu, and R.G. Reddy, *In-Situ Processing of Al Alloy Composites.* Advanced Engineering Materials, 2003. **5**(3): p. 167-172.

82.     Aghajanian, M.K., Rocazella, M. A., *The fabrication of metal matrix composites by a pressureless infiltration technique.* Journal of Materials Science, 1991. **26**(2): p. 447-454.

83.     Nagendra, N., B.S. Rao, and V. Jayaram, *Microstructures and properties of $Al_2O_3/Al–AlN$ composites by pressureless infiltration of Al-alloys.* Materials Science and Engineering: A, 1999. **269**(1–2): p. 26-37.

84.     Swaminathan, S., B. Srinivasa Rao, and V. Jayaram, *The influence of oxygen impurities on the formation of AlN–Al composites by infiltration of molten Al–Mg.* Materials Science and Engineering: A, 2002. **337**(1–2): p. 134-139.

85.     Scholz, H. and P. Greil, *Nitridation reactions of molten Al-(Mg, Si) alloys.* Journal of Materials Science, 1991. **26**(3): p. 669-677.

86.     Swaminathan, S., B. Srinivasa Rao, and V. Jayaram, *The production of AlN-rich matrix composites by the reactive infiltration of Al alloys in nitrogen.* Acta Materialia, 2002. **50**(12): p. 3095-3106.

87.     Zheng, Q. and R.G. Reddy, *Mechanism of in situ formation of AlN in Al melt using nitrogen gas.* Journal of Materials Science, 2004. **39**(1): p. 141-149.

88.     Hou, Q., R. Mutharasan, and M. Koczak, *Feasibility of aluminium nitride formation in aluminum alloys.* Materials Science and Engineering: A, 1995. **195**: p. 121-129.

89.     Ye, H.Z., X.Y. Liu, and B. Luan, *In situ synthesis of AlN in Mg–Al alloys by liquid nitridation.* Journal of Materials Processing Technology, 2005. **166**(1): p. 79-85.

90.     Sercombe, T.B. and G.B. Schaffer, *On the role of magnesium and nitrogen in the infiltration of aluminium by aluminium for rapid prototyping applications.* Acta Materialia, 2004. **52**(10): p. 3019-3025.

91.     Kumari, S.S.S., U.T.S. Pillai, and B.C. Pai, *Synthesis and characterization of in situ Al–AlN composite by nitrogen gas bubbling method.* Journal of Alloys and Compounds, 2011. **509**(5): p. 2503-2509.

92. El-Sayed, M.A., *Double Oxide Film Dfects and Mechanical Properties in Aluminium Alloy*. 2012, PhD thesis, School of Metallurgy and Materials, University of Birmingham.

93. Aladar, P., *Alloy*. 1921, US Patent, US1387900 A.

94. Emadi, D., J.E. Gruzleski, and J.M. Toguri, *The effect of Na and Sr modification on surface tension and volumetric shrinkage of A356 alloy and their influence on porosity formation.* Metallurgical Transactions B, 1993. **24**(6): p. 1055-1063.

95. Griffiths, W. D., Jolly, M. R., Kaettlitz, W., Kendrick, R., *Effect of simultaneous additions of sodium and strontium on the modification of aluminum silicon alloy.* Light Met, 1990. **1047**.

96. Gruzleski, J. E. and B. M. Closset, *The treatment of liquid aluminum-silicon alloys*. 1990: Amer Foundry Society.

97. Flood, S.C. and J.D. Hunt, *Modification of Al-Si eutectic alloys with Na.* Metal Science, 1981. **15**(7): p. 287-294.

98. Knuutinen, A., Nogita, K., McDonald, S. D., Dahle and A. K., *Modification of Al–Si alloys with Ba, Ca, Y and Yb.* Journal of Light Metals, 2001. **1**(4): p. 229-240.

99. Nogita, K., S.D. McDonald, and A.K. Dahle, *Eutectic Modification of Al-Si Alloys with Rare Earth Metals.* Materials Transation, 2004. **45**(2): p. 323-326.

100. Lu, S.-Z. and A. Hellawell, *The mechanism of silicon modification in aluminum-silicon alloys: Impurity induced twinning.* Metallurgical Transactions A, 1987. **18**(10): p. 1721-1733.

101. Jacob, S., *Modification of the Alloy Al-7Si-0.6Mg by Sodium, Antimony and Strontium.* Fonderie, 1977(363): p. 13-25.

102. Denton, J.R. and J.A. Spittle, *Solidification and susceptibility to hydrogen absorption of Al–Si alloys containing strontium.* Materials Science and Technology, 1985. **1**(4): p. 305-311.

103. Shahani, H., *Effect of hydrogen on the shrinkage porosity of Al-Cu and Al-Si alloys.* Scand. J. Metallurgy, 1985(14): p. 306-312.

104. R. Fuoco, E.R.C.a.M.d.A.B., *Effects of grain refinement on feeding mechanisms in A356 aluminium alloy.* AFS Trans., 1998(106): p. 401–409.

105. R. Fuoco, E. R. Correa and H. Goldenstein, *Effect of modification treatment on microporosity formation in 356 Al alloy, Part I: interdendritic feeding evaluation.* AFS Transactions, 1996(104): p. 1151-1157.

106. Iwahori, H., Yonekura, K., Yamamoto, Y. and Nakamura, M., *Feedability and Segregation of Al-Si-Cu Alloys.* The Journal of the Japan Foundrymens's Society, 1989. **61**(10): p. 730-735.

107. Emadi, D., J. Gruzleski, and M. Pekguleryuz, *Melt oxidation behavior and inclusion content in unmodified Al-Si and Sr.* Transactions of the American Foundrymen's Society, 1996. **104**: p. 763-768.

108.    S. Jacob, M.G., G. Laslaz, P. Meyer, P. H. Guerin and R. Adam *the Actual Situation in the Use of Sodium, Strontium, and Antimony in Aluminum-Silicon Castings.* Hommes et Fonderie, 1995(258): p. 45-54.

109.    Lee, P.D. and S. Sridhar, *Direct observation of the effect of strontium on porosity formation during the solidification of aluminium-silicon alloys.* International Journal of Cast Metals Research, 2000. **13**(4): p. 185-198.

110.     ASM Handbook Committee, *ASM Handbook, Volume 04 - Heat Treating*. 1991, ASM International.

111.    Hollingsworth, E. H., *Metal Handbook*. Corrosion of aluminum and aluminum alloy. Vol. 13. 1987: ASM International.

112.    Kammer, C., *Aluminium Handbook Volumn 1: Fundamentals and Materials*. 1999.

113.    Nafsin, N. and H. Rashed, *Effects of Copper and Magnesium on Microstructure and Hardness of Al-Cu-Mg Alloy.* International Journal of Engineering and Technology, 2013. **2**.

114.    Zeren, M., *Effect of copper and silicon content on mechanical properties in Al–Cu–Si–Mg alloys.* Journal of Materials Processing Technology, 2005. **169**(2): p. 292-298.

115.    Sharma, K., *Effect of magnesium on strength and microstructure of Aluminium Copper Magnesium Alloy.* Internation Journal of Scientific & Engineering Research, 2012. **3**(2): p.1-4.

116.    Shabestari, S.G. and H. Moemeni, *Effect of copper and solidification conditions on the microstructure and mechanical properties of Al–Si–Mg alloys.* Journal of Materials Processing Technology, 2004. **153–154**: p. 193-198.

117.    Nam, S.W. and D.H. Lee, *The effect of Mn on the mechanical behavior of Al alloys.* Metals and Materials, 2000. **6**(1): p. 13-16.

118.    Warmuzek, M., K. Rabczak, and J. Sieniawski, *The course of the peritectic transformation in the Al-rich Al–Fe–Mn–Si alloys.* Journal of Materials Processing Technology, 2005. **162–163**: p. 422-428.

119.    R. S. Rana, R.P., and S Das, *Reviews on the Influences of Alloying elements on the Microstructure and Mechanical Properties of Aluminum Alloys and Aluminum Alloy Composites.* International Journal of Scientific and Research, 2012. **2**(6): p. 1-7.

120.    Warmuzek, M., Sieniawski, J., Wicher, K. and Mrowka, G., *The study of the distribution of the transition metals and Si during primary precipitation of the intermetallic phases in Al–Mn–Si alloys.* Journal of Materials Processing Technology, 2006. **175**(1–3): p. 421-426.

121.    Davis, J.R., *Corrosion of aluminum and aluminum alloys*. 1999: Asm International.

122.    Bourkhina, A.N., *Aluminum alloy with improved tribological characteristics*. 1999, US Patent US5925315.

123.    Kawahara, H., et al., *Aluminum alloy, cast article of aluminum alloy, and method for producing cast article of aluminum alloy*. 2001, Patent, EP1477577 A4.

124.    Magusa, S., Satake, I., Fujimoto, K., *Aluminium alloy for casting with superoir heat resistence*. 1983, Japan Patent, JPS58100654 A.

125.    Ahmad, Z., *The properties and application of scandium-reinforced aluminum.* JOM. **55**(2): p. 35-39.

126.    Tack, W.T. and I.L.H. Hansson, *Aluminum alloys containing scandium with zirconium additions*. 1997, US Patent, US5620652 A.

127.    Shaw, B., Davis, D. A., Fritz, T. L., and Moshier, W. C, *The influence of Tungsten alloying additions on the passivity of Aluminum.* Journal of the Electrochemical Society, 1991. **138**(11): p. 3288-3295.

128.    Rohatgi, P.K., J.A.E. Bell, and T.F. Stephenson, *Aluminum-base metal matrix composite*. 2001, US Patent, US4946500 A.

129.    Gronostajski, J. and A. Matuszak, *The recycling of metals by plastic deformation: an example of recycling of aluminium and its alloys chips.* Journal of Materials Processing Technology, 1999. **92–93**: p. 35-41.

130.    A, C., *Grain Refinement and its Effects in Non-Feooous Casting Alloys.* Foundry Trade Journal, 1952. **93**: p. 695.

131.    McCartney, D.G., *Grain refining of aluminium and its alloys using inoculants.* International Materials Reviews, 1989. **34**(1): p. 247-260.

132.    Jones, G.P. and J. Pearson, *Factors affecting the grain-refinement of aluminum using titanium and boron additives.* Metallurgical Transactions B, 1976. **7**(2): p. 223-234.

133.    Davies, I.G., J.M. Dennis, and A. Hellawell, *The nucleation of aluminum grains in alloys of aluminum with titanium and boron.* Metallurgical Transactions, 1970. **1**(1): p. 275-280.

134.    Guzowski, M.M., G.K. Sigworth, and D.A. Sentner, *The role of boron in the grain.* Metallurgical Transactions A. **18**(5): p. 603-619.

135.    P. S. Mohanty, F. H. Samuel and J. E. Gruzleski, *Mechanism of Grain Refinement in Aluminum*, in *Int. Conf Light Metals*. 1994, The Minerals, Metals & Materials Society: Warrendale, PA. p. 1039-46.

136.    Maxwell, I. and A. Hellawell, *The constitution of the system Al-Ti-B with reference to aluminum-base alloys.* Metallurgical Transactions, 1972. **3**(6): p. 1487-1493.

137.    Maxwell, I. and A. Hellawell, *A simple model for grain refinement during solidification.* Acta Metallurgica, 1975. **23**(2): p. 229-237.

138.    Cornish, A. J., *The Influence of Boron on the Mechanism of Grain Refinement in Dilute Aluminium-Titanium Alloys.* Metal Science, 1975. **9**(1): p. 477-484.

139.    J. A. Marc Antonio, L. F. Mondo Lfo, *Grain refinement in aluminum alloyed with titanium and boron.* Met. Trans. B, 1971. **2**(2): p. 465-471.

140. P. S. Mohanty, F. H. Samuel, J. E. Gruzleski, *Studies on addition of inclusions to molten aluminum using a novel technique.* Met. Trans. B, 1995. **26**(1): p. 103-109.

141. Schumacher, P. and A.L. Greer, *NATO-Advanced Research Workshop on Undercooled Metallic Melts: Properties, Solidification and Metastable Phases Heterogeneously nucleated α-Al in amorphous aluminium alloys.* Materials Science and Engineering: A, 1994. **178**(1): p. 309-313.

142. Li, H.,Sritharan, T., Lam, Y. M., Leng, N. Y., *Effects of processing parameters on the performance of Al grain refinement master alloys AlTi and AlB in small ingots.* Journal of Materials Processing Technology, 1997. **66**(1-3): p. 253-257.

143. Spittle, J. A. and S. Sadli, *Effect of alloy variables on grain refinement of binary aluminium alloys with Al–Ti–B.* Materials Science and Technology, 1995. **11**(6): p. 533-537.

144. Young, D. K., Dunville, B. T., Setzer, W. C., Koch, F. P., *A Survey of Grain Refiners for Hypoeutectic Al-Si Alloys.* Light Met, 1991: p. 1115-1121.

145. Easton, M. and D. StJohn, *Grain refinement of aluminum alloys: Part I. the nucleant and solute paradigms-a review of the literature.* Metallurgical and Materials Transactions A, 1999. **30**(6): p. 1613-1623.

146. Greer, A.L., Bunn, A. M., Tronche, A., Evams, P. V., Bristow, D. J., *Modelling of inoculation of metallic melts: application to grain refinement of aluminium by Al–Ti–B.* Acta Materialia, 2000. **48**(11): p. 2823-2835.

147. Mondolfo, L., F., *Aluminum Alloys: Structure and Properties*. 1976: Butterworth.

148. NL, R.M.C., *Aluminium Grain Refinement by Nb, Zr and Ti Additions and Their Effect on Mechanical and Electrical Properties*, in *Solidification Processing 1987*. 1987: sheffield. p. 153.

149. Arjuna Rao, A., B.S. Murty, and M. Chakraborty, *Influence of chromium and impurities on the grain- refining behavior of aluminum.* Metallurgical and Materials Transactions A, 1996. **27**(3): p. 791-800.

150. Nowak, M., Development of Niobium-Boron Grain Refiner for Aluminium-Silicon Alloys, PhD thesis, in *Brunel Centre for Advanced Solidification Technology*. 2011, Brunel University. p. 51-60.

151. Hinton, E., *The oxidation of Liquid Aluminium and the Potential for the Oxides in Grain Refinement of Aluminium Alloys*. PhD thesis, 2015, University of Birmingham. p. 56-82.

152. *Standard Test Methods for Tension Testing of Metallic Materials*. 2012, ASTM International.

153. Ramin, R., *A Method to Study the Behaviour of Double Oxide Film Defects in Aluminium Alloys*. PhD thesis, 2005, University of Birmingham. p. 110-111.

154. Sklyarchuk, V., Yakymovych, A., Eckert, S., Gerbeth, G., Eigenfeld, K., *Structure Sensitive Properties of Liquid Al–Si Alloys.* International Journal of Thermophysics, 2009. **30**(4): p. 1400-1410.

155. Raiszadeh, R. and W.D. Griffiths, *The behaviour of double oxide film defects in liquid Al alloys under atmospheric and reduced pressures.* Journal of Alloys and Compounds, 2010. **491**(1–2): p. 575-580.

156. Pilling, N., Bedworth, R.E., *The oxidation of metals at high temperatures*. J. Inst. Met, 1923. **29**: p. 529-591.

157. D.E.J.Talbot and M.P. Silva *oxidation of liquid aluminium magnesium alloy*. in *Tech. Sessions, TMS Light Metals Comettee, 118th Ann. Meeting*. 1989. Las Vegas.

158. Liu, Y., G. Shao, and P. Tsakiropoulos, *Thermodynamic reassessment of the Mo–Si and Al–Mo–Si systems.* Intermetallics, 2000. **8**(8): p. 953-962.

159. Guo, C., Li, C., Masset, P. J., Du, Z., *A thermodynamic description of the Al–Mo–Si system.* Calphad, 2012. **36**: p. 100-109.

160. C. G. McKamey, P. F. Tortorelli, J. H. DeVan, and C. A. Carmichae, *A study of pest oxidation in polycrystalline MoSi$_2$.* J. Mater. Res, 1992. **7**(10): p. 2747-2755.

161. Chen, J., Li, C., Fu, Z., Tu, X., Sundberg, M.,, *Low temperature oxidation behavior of a MoSi$_2$-based material.* Materials Science and Engineering: A, 1999. **261**(1–2): p. 239-244.

162. Hansson, K., Halvarsson, M., Tang, J. E., Pompe, R., Sundberg, M., Svensson, J. E., *Oxidation behaviour of a MoSi$_2$-based composite in different atmospheres in the low temperature range (400–550 °C).* Journal of the European Ceramic Society, 2004. **24**(13): p. 3559-3573.

163. Ingemarsson, L., Halvarsson, M., Engkvist, J., Jonsson, T., *Oxidation behavior of a Mo (Si, Al)$_2$-based composite at 300–1000 °C.* Intermetallics, 2010. **18**(4): p. 633-640.

164. Nanko, M., Kitahara, A., Ogura, T., Ksmata, H., Maruyama, T., *Formation of Mo(Si, Al)$_2$ layer on Mo dipped in Al melt saturated with Si and the effects of transition metals added in the melt.* Intermetallics, 2001. **9**(7): p. 637-646.

165. R. Mitra, V.V.R. Rao, A. Venugopal Rao, *Effect of small aluminum additions on microstructure and mechanical properties of molybdenum di-silicide.* Intermetallics, 1999(7): p. 213-232.

166. Y.Yang, *Modelling of the effects of entrainment defects on mechanical properties in Al-Si-Mg alloy castings*. 2014, PhD thesis, School of Metallurgy and Materials, University of Birmingham.

167. Tiryakioğlu, M. and J. Campbell, *Weibull Analysis of Mechanical Data for Castings: A Guide to the Interpretation of Probability Plots.* Metallurgical and Materials Transactions A, 2010. **41**(12): p. 3121-3129.

168. Griffiths, W. D., and Yang, Y., *Double Oxide Film Defects in Al Alloys*, in *M5 Advanced Materilas conference*. 2015: University of Loughborough.

169. Easton, M.A. and D.H. StJohn, *A model of grain refinement incorporating alloy constitution and potency of heterogeneous nucleant particles.* Acta Materialia, 2001. **49**(10): p. 1867-1878.

170. Porter, D.A. and Easterling, K.E., *Phase Transformation in Metals and Alloys*. 2009: Taylor & Francis Group.

171. Suárez-Peña, B. and J. Asensio-Lozano, *Microstructure and mechanical property developments in Al–12Si gravity die castings after Ti and/or Sr additions.* Materials Characterization, 2006. **57**(4–5): p. 218-226.

172. Yilmaz, F. and R. Elliott, *The microstructure and mechanical properties of unidirectionally solidified Al–Si alloys.* Journal of Materials Science, 1989. **24**(6): p. 2065-2070.

173. Green, N. and J. Campbell, *Influence of Oxide Film Filling Defects on the Strength of Al-7Si-Mg Alloy Castings (94-114).* Transactions of the American Foundrymen's Society, 1994. **102**: p. 341-348.

174. Chen, X.G. and M. Fortier, *TiAlSi intermetallic formation and its impact on the casting processing in Al–Si alloys.* Journal of Materials Processing Technology, 2010. **210**(13): p. 1780-1786.

175. Ghomashchi, R., *The evolution of AlTiSi intermetallic phases in Ti-added A356 Al–Si alloy.* Journal of Alloys and Compounds, 2012. **537**: p. 255-260.

176. Hwang, J.Y., H.W. Doty, and M.J. Kaufman, *The effects of Mn additions on the microstructure and mechanical properties of Al–Si–Cu casting alloys.* Materials Science and Engineering: A, 2008. **488**(1–2): p. 496-504.

177. Cao, X. and J. Campbell, *Effect of precipitation and sedimentation of primary α-Fe phase on liquid metal quality of cast Al–11.1Si–0.4Mg alloy.* International Journal of Cast Metals Research, 2004. **17**(1): p. 1-11.

178. Yildirim, M., M.V. Akdeniz, and A.O. Mekhrabov, *Microstructural Investigation and Phase Relationships of Fe-Al-Hf Alloys.* Metallurgical and Materials Transactions A, 2014. **45**(8): p. 3412-3421.

179. Gaydosh, D.J., S.L. Draper, and M.V. Nathal, *Microstructure and tensile properties of Fe-40 At. pct Al alloys with C, Zr, Hf, and B additions.* Metallurgical Transactions A, 1989. **20**(9): p. 1701-1714.

180. Murray, J., A. McAlister, and D. Kahan, *The Al-Hf (aluminum-hafnium) system.* Journal of phase equilibria, 1998. **19**(4): p. 376.

181. *Standard Test Procedure for Aluminium Alloy Grain Refiners*. 2012, Aluminium Association.